NQ

7 | 2 | 3 | 7 | 4

U M I

INFORMATION TO USERS

This manuscript has been reproduced from the microfilm master. UMI films the text directly from the original or copy submitted. Thus, some thesis and dissertation copies are in typewriter face, while others may be from any type of computer printer.

The quality of this reproduction is dependent upon the quality of the copy submitted. Broken or indistinct print, colored or poor quality illustrations and photographs, print bleedthrough, substandard margins, and improper alignment can adversely affect reproduction.

In the unlikely event that the author did not send UMI a complete manuscript and there are missing pages, these will be noted. Also, if unauthorized copyright material had to be removed, a note will indicate the deletion.

Oversize materials (e.g., maps, drawings, charts) are reproduced by sectioning the original, beginning at the upper left-hand corner and continuing from left to right in equal sections with small overlaps.

USE OF THE FINITE DIFFERENCE TIME DOMAIN METHOD TO STUDY BROADBAND ANTENNAS FOR MILLIMETER WAVE POINT-TO-POINT AND POINT-TO-MULTIPOINT COMMUNICATIONS

By

CHEN WU
B. Eng., M. Eng.

A Thesis
Submitted to the School of Graduate Studies
in Partial Fulfillment of the Requirements
for the Degree Doctor of Philosophy

USE OF FDTD METHOD TO STUDY

BROADBAND MILLIMETER WAVE ANTENNAS

DOCTOR OF PHILOSOPHY (2000)   McMASTER UNIVERSITY

Electrical and Computer Engineering   Hamilton, Ontario

TITLE: USE OF THE FINITE DIFFERENCE TIME DOMAIN
METHOD TO STUDY BROADBAND ANTENNAS FOR
MILLIMETER WAVE POINT-TO-POINT AND POINT-
TO-MULTIPOINT COMMUNICATIONS

AUTHOR: Mr. Chen Wu
B. Eng., (The East China Normal University)
M. Eng., (The East China Normal University)

SUPERVISOR: Dr. John Litva
Professor, Department of Electrical and Computer Engineering
Director, Communications Research Laboratory, McMaster University
Fellow, I.E.E.E.

NUMBER OF PAGES: xiv, 182

Abstract

This thesis presents an in-depth investigation of new broadband millimeter wave antennas, which can be used in millimeter wave point-to-point and point-to-multipoint communications.

A very powerful design tool – the Finite Difference Time Domain (FDTD) method is presented in its regular uniform grid form, which is referred to as Yee's method, its non-uniform grid form, and its General Curvilinear Coordinate (GCC) form. Accompanying formulas are presented in each case. The advantages of these different formulas are discussed, their use for solving different complex electromagnetic problems is demonstrated, as well.

Different absorbing boundary conditions (ABC) are used to design antennas, their beam forming networks and transitions, for example Mur's first order ABC, Litva's dispersive ABC and Modified Perfect Matched Layers (M-PML). Here Litva's ABC is presented in detail, and some case studies are given to prove that it is a very good ABC for printed circuit applications.

A research based FDTD 3-Dimensional Structure Simulator (FDTD 3D SS) is used to design these new wide-band antennas and transitions. More than 500 simulations have been calculated for this study within less than a year. It is obvious that the designs would not be so successful if we were not able to use this 3-dimensional structure simulator. A list of structures, which were studied using the FDTD method in the past few years, is given in Appendix A, as well.

The Tapered Slot Antennas (TSA) and different type feed structures for TSA are reviewed in Chapter 2. As a member of the class of traveling wave antennas, the TSA's are wide-band elements with very good directivities. Based on the Suspended Microstrip Line (SML) and the Inverted Microstrip Line (IML), three new feed structures have been developed, by using FDTD 3D SS, for millimeter wave wide-band applications. They are:

1. five-piece assembled SML fed slot line coupled Linear Tapered Slot Antenna (LTSA),

2. three-piece assembled IML-to-CDS (Coplanar Double Strips) fed LTSA, and

3. SML fed 'Hockey Stick' slot coupled LTSA.

The hardware designs are presented in Chapter 3. The reasons for these designs are: to verify the FDTD designs that are given in Chapter 2, and to investigate how these elements work in array environments. The hardware includes:

1. 1 x n (n = 1, 4, 8, 16, 32) five-piece assembled SML fed slot line coupled LTSA linear arrays,

2. 1 x 16 three-piece assembled IML-to-CDS fed LTSA linear array,

3. 32 x 32 five-piece assembled SML fed slot line coupled LTSA array,

4. 4 x 4 SML fed 'Hockey Stick' slot coupled LTSA array,

5. 16 x 16 SML fed 'Hockey Stick' slot coupled LTSA array.

All these arrays show good measured results. The SML fed 'Hockey Stick' slot coupled LTSA design has proven itself to be the simplest concept not only from the design point of view, but also from the manufacturing point of view.

The Vivaldi antenna, which belongs to the traveling wave antenna category and shares the same features as TSA, is used as a very short element (antenna length $L < \lambda_o/2$) to design an 120-degree-vertical-polarization sector antenna. The experimental study shows that the design gives very good results and meets the specifications in real applications. It has a potential to be used as a sector antenna with different horizontal beam-widths. This design shows antenna engineers a novel approach to design sector antennas without worrying about the antenna input impedance bandwidth.

Acknowledgement

Contents

List of Figures

List of Tables

Chapter 1 . A Powerful Design Tool - The Finite Difference Time Domain Method and The 3-Dimensional Structure Simulator

1.1 The Regular FDTD Method

1.1.1 Introduction

The regular Finite Difference Time Domain Method (FDTD) is formulated using a central difference discretization of Maxwell's curl equations in both time and space domain. This technique has undergone rapid development since 1966 [1]. In this thesis, the FDTD method is used to investigate Tapered Slot Antenna (TSA) elements and arrays, which can be used in millimeter wave and sub-millimeter wave point-to-point and point-to-multipoint communications. After ten years of continuous development and application of the FDTD method to solve electromagnetic problems, especially for antennas and microwave circuits, we found that this numerical method is accurate, remarkably robust, flexible, and provides wideband information. The method is very easily incorporated with advanced digital signal processing (DSP) methods and other methods, for example neural networks, to explore electromagnetic wave interaction on the surrounding environment [2] [3] [4] [5] [6] [7].

1.1.2 Maxwell's Curl Equations

Let us consider a region of space that is source-free and has constitutive electrical parameters that are independent of time. Maxwell's curl equations are given by,

$$\frac{\partial \mathbf{H}}{\partial t} = -\frac{1}{\mu}\left[\nabla \times \mathbf{E} + \rho^{'}\mathbf{H}\right] \qquad (1.1)$$

$$\frac{\partial \mathbf{E}}{\partial t} = \frac{1}{\varepsilon}\left[\nabla \times \mathbf{H} - \sigma\mathbf{E}\right] \qquad (1.2)$$

where $\mathbf{E}$ is the electric field in Volts/meter; $\mathbf{H}$ is the magnetic field in Amperes/meter; ε is the electrical permittivity in Farads/meter; σ is the electrical conductivity in Siemens/meter; μ is magnetic permeability in Henrys/meter; and $\rho^{'}$ is an equivalent magnetic resistivity in Ohms/meter. The magnetic resistivity term is provided to yield symmetric curl equations, and to allow for the possibility of a magnetic field loss mechanism. In order to ensure the uniqueness for the solution of these Maxwell's equations, the following conditions must be satisfied,

1. The initial condition for the fields must be satisfied on the whole domain of interest, that is, $\mathbf{E}(\mathbf{r}, t = 0)$ and $\mathbf{H}(\mathbf{r}, t = 0)$, where $\mathbf{r}$ is the position vector, must be given everywhere inside the computational domain.

2. The tangential components of $\mathbf{E}$ and $\mathbf{H}$ on the boundary of the domain of interest must be given for all $t > 0$. For the boundary conditions, the wave at infinity must be of an outgoing type.

Expanding the curl operator and assuming that ε, σ, μ, $\rho^{'}$ are isotropic. We have the following system of scalar equations in rectangular coordinate system (x, y, z),

$$\frac{\partial H_x}{\partial t} = \frac{1}{\mu}\left(\frac{\partial E_y}{\partial z} - \frac{\partial E_z}{\partial y} - \rho^{'}H_x\right) \qquad (1.3)$$

$$\frac{\partial H_y}{\partial t} = \frac{1}{\mu}\left(\frac{\partial E_z}{\partial x} - \frac{\partial E_x}{\partial z} - \rho^{'}H_y\right) \qquad (1.4)$$

$$\frac{\partial H_z}{\partial t} = \frac{1}{\mu}\left(\frac{\partial E_x}{\partial y} - \frac{\partial E_y}{\partial x} - \rho^{'}H_z\right) \qquad (1.5)$$

$$\frac{\partial E_x}{\partial t} = \frac{1}{\varepsilon}\left(\frac{\partial H_z}{\partial y} - \frac{\partial H_y}{\partial z} - \sigma E_x\right) \tag{1.6}$$

$$\frac{\partial E_y}{\partial t} = \frac{1}{\varepsilon}\left(\frac{\partial H_x}{\partial z} - \frac{\partial H_z}{\partial y} - \sigma E_y\right) \tag{1.7}$$

$$\frac{\partial E_z}{\partial t} = \frac{1}{\varepsilon}\left(\frac{\partial H_y}{\partial x} - \frac{\partial H_x}{\partial z} - \sigma E_z\right) \tag{1.8}$$

The system of six coupled partial differential equations forms the basis of the regular FDTD algorithm of electromagnetic wave interactions with general three-dimensional structures.

1.1.2 The Yee Algorithm

In 1966 [1], Yee introduced a set of finite-difference equations for the system of (1.3) to (1.8). Following Yee's notation, we denote a space point in a rectangular mesh as,

$$(i, j, k) = (i\Delta x, j\Delta y, k\Delta z) \tag{1.9}$$

and any function of space and time as,

$$F^n(i, j, k) = F(i\Delta x, j\Delta y, k\Delta z, n\Delta t) \tag{1.10}$$

where Δx, Δy, Δz are, respectively, the mesh space increments in the x, y, and z coordinate directions. Δt is the time increment, and i, j, k and n are integers. Yee used centered finite-difference expressions for the space and time derivatives that are both simply programmed and of second-order accuracy in the space and time increments, respectively,

$$\frac{\partial F^n(i, j, k)}{\partial x} = \frac{F^n\left(i+\frac{1}{2}, j, k\right) - F^n\left(i-\frac{1}{2}, j, k\right)}{\Delta x} + O(\Delta x^2) \tag{1.11}$$

$$\frac{\partial F^n(i, j, k)}{\partial t} = \frac{F^{n+\frac{1}{2}}(i, j, k) - F^{n-\frac{1}{2}}(i, j, k)}{\Delta t} + O(\Delta t^2) \tag{1.12}$$

To achieve second-order accuracy of (1.11), and to realize all of the required space derivatives of the system of equations (1.3) to (1.8), we will position the components of **E** and **H** about a cell as shown in Figure 1.1. Note that the numbering of the **E** and **H** components, as illustrated in this figure, is different from Yee's original paper [1]. The differences are due to programming considerations.

In order to achieve second-order accuracy of (1.12) in the time domain, we evaluate **E** and **H** at alternate half time steps and assume the numbering scheme illustrated in Figure 1.1. The repetitive arrangement of the cells fills the computation domain with a finite-difference mesh. Every component of **H** can be obtained by the loop integral of **E** using the four surrounding **E** nodal values according to Maxwell's curl equation. A similar approach holds for the calculation of **E**.

In this algorithm, contiguous **E** and **H** nodes are separated by one-half of a space step. The instants of time, when the **E** or **H** fields are calculated, are also off by half a time step. To be more specific, if the components of **E** are calculated at $n\Delta t$, where Δt is the time increment and n is any non-negative integer, the components **H** are calculated at $(n+1/2)\Delta t$. For this reason the algorithm is called the leapfrog method.

To summarize, for a homogeneous region of space, the discretization of Maxwell's curl equations (1.3) to (1.8) with $\rho' = \sigma = 0$ using this scheme leads to the following equations,

$$E_x^{n+1}(i,j,k) = E_x^n(i,j,k) + \frac{\Delta t}{\varepsilon} \cdot \left[\frac{H_z^{n+1/2}(i,j+1,k) - H_z^{n+1/2}(i,j,k)}{\Delta y} \right.$$

$$\left. - \frac{H_y^{n+1/2}(i,j,k+1) - H_y^{n+1/2}(i,j,k)}{\Delta z} \right] \qquad (1.13)$$

$$E_y^{n+1}(i,j,k) = E_y^n(i,j,k) + \frac{\Delta t}{\varepsilon} \cdot \left[\frac{H_x^{n+1/2}(i,j,k+1) - H_x^{n+1/2}(i,j,k)}{\Delta z} \right.$$

$$\left. - \frac{H_z^{n+1/2}(i+1,j,k) - H_z^{n+1/2}(i,j,k)}{\Delta x} \right] \qquad (1.14)$$

$$E_z^{n+1}(i,j,k) = E_z^n(i,j,k) + \frac{\Delta t}{\varepsilon} \cdot \left[\frac{H_y^{n+1/2}(i+1,j,k) - H_y^{n+1/2}(i,j,k)}{\Delta x} \right.$$

$$\left. - \frac{H_x^{n+1/2}(i,j+1,k) - H_x^{n+1/2}(i,j,k)}{\Delta y} \right] \tag{1.15}$$

$$H_x^{n+1/2}(i,j,k) = H_x^{n-1/2}(i,j,k) - \frac{\Delta t}{\mu} \cdot \left[\frac{E_z^n(i,j,k) - E_z^n(i,j-1,k)}{\Delta y} \right.$$

$$\left. - \frac{E_y^n(i,j,k) - E_y^n(i,j,k-1)}{\Delta z} \right] \tag{1.16}$$

$$H_y^{n+1/2}(i,j,k) = H_y^{n-1/2}(i,j,k) - \frac{\Delta t}{\mu} \cdot \left[\frac{E_x^n(i,j,k) - E_x^n(i,j,k-1)}{\Delta z} \right.$$

$$\left. - \frac{E_z^n(i,j,k) - E_z^n(i-1,j,k)}{\Delta x} \right] \tag{1.17}$$

$$H_z^{n+1/2}(i,j,k) = H_z^{n-1/2}(i,j,k) - \frac{\Delta t}{\mu} \cdot \left[\frac{E_y^n(i,j,k) - E_y^n(i-1,j,k)}{\Delta x} \right.$$

$$\left. - \frac{E_x^n(i,j,k) - E_x^n(i,j-1,k)}{\Delta y} \right] \tag{1.18}$$
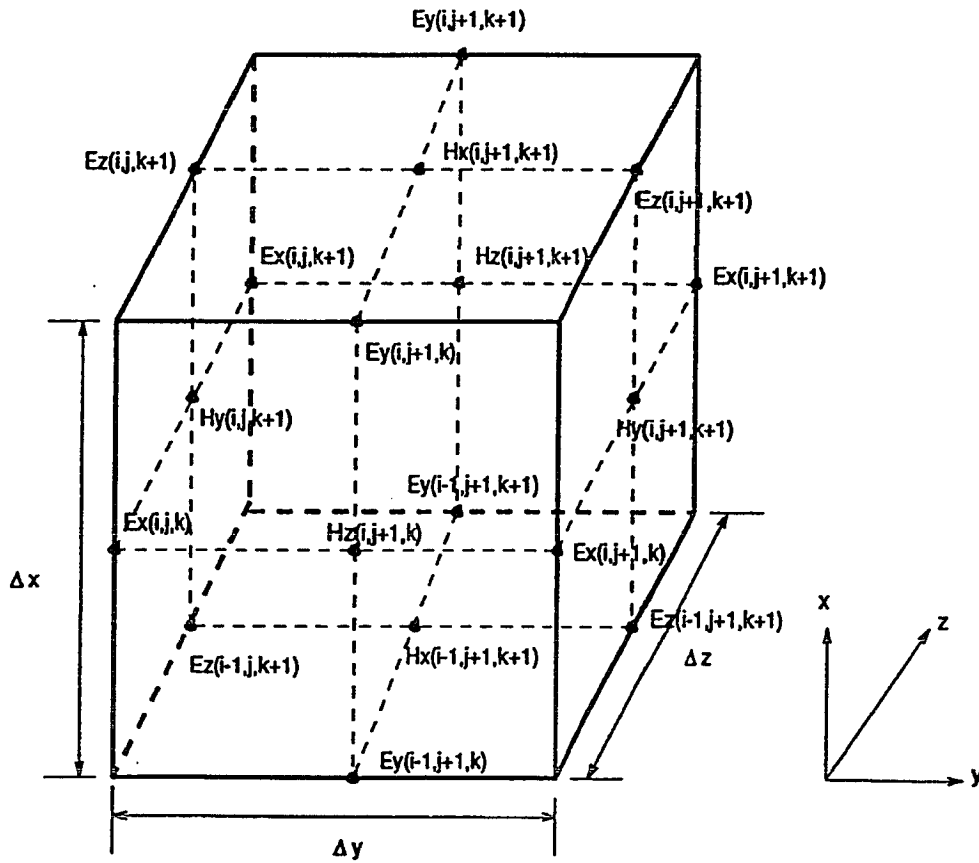
Figure 1.1 Yee's grid showing the position of E and H field locations.

1.1.4 The Advantage of Using the FDTD Method

The FDTD algorithm has several advantages over other schemes for the calculation of time domain fields.

1. The central difference nature of the leapfrog method makes it a relatively accurate method since it has second-order accuracy in both the time and space domain compared to some first-order schemes.

2. There is no need for special treatment on the edge of a metal surface if the tangential E components are arranged to lie on this surface.

3. The leapfrog algorithm has the unique characteristic that the numerical scheme has no dissipation and only a very small amount of dispersion.

Because the FDTD method is a time domain method, it is very easy to get wideband frequency domain information by simply applying the Fourier Transformation.

1.1.5 A Detailed Analysis of the Yee's Mesh

Care must be exercised when using Yee's grid, which is shown in Figure 1.1 to calculate the **E** and **H** fields. A simplification of the field locations in the x, y, and z directions is illustrated in Figure 1.2. From Figure 1.2 one can define where the absorbing boundary conditions (ABC) are applied around the computational domain and precisely locate the metal or dielectric edges or surface inside the computational domain. Using this simplified 2D sketch of Yee's mesh, we can show how to calculate the values of the **E** and **H** fields at the nodes of Yee's grid.
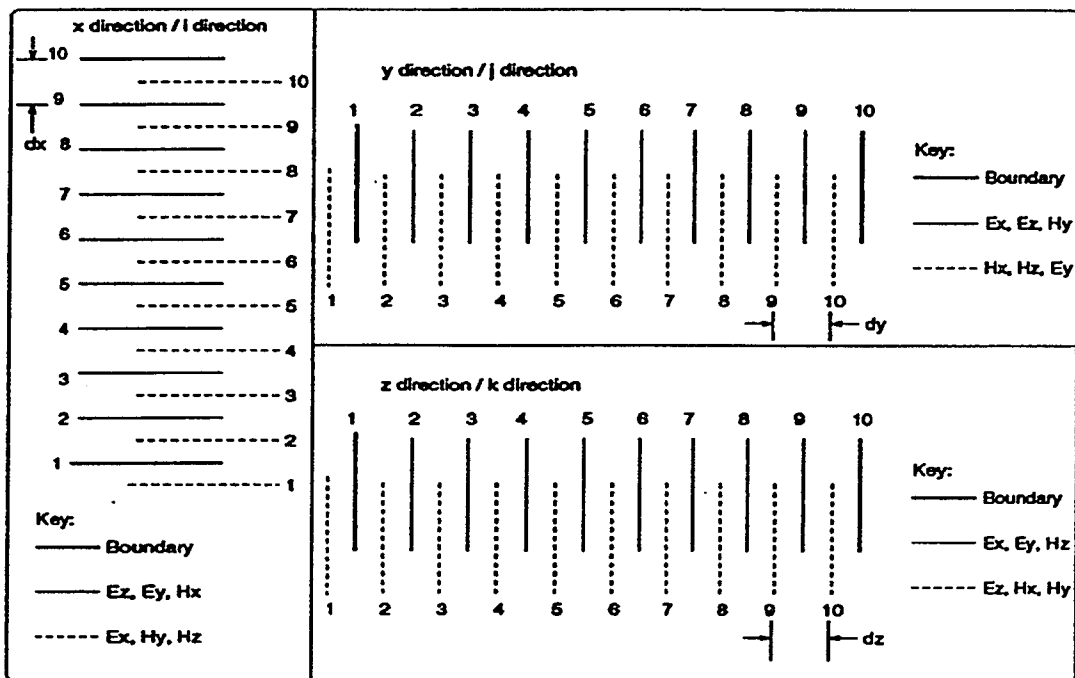
Figure 1.2 A 2D mesh diagram showing the location of E and H fields in x, y, and z directions, respectively.

1.1.6 The Stability Condition

There is a stability condition that applies to each finite difference scheme. When invoked, the condition guarantees that the numerical error generated at each time step does not grow with time. The stability criterion of Yee's algorithm is the well known Courant-Friedrichs-Lewy condition, often simply called the *Courant condition*,

$$v_{max} \cdot \Delta t \leq \frac{1}{\sqrt{\Delta x^{-2} + \Delta y^{-2} + \Delta z^{-2}}} \qquad (1.19)$$

where v_{max} is the maximum signal phase velocity in the configuration being simulated.

1.1.7 The Excitations

The Gaussian Pulse Excitation

A Gaussian pulse is usually used as the source of excitation because its smooth Gaussian shaped waveform in time and in the spectral domain can provide information from dc to the desired frequency simply by adjusting the width of the pulse.

An ideal Gaussian pulse, which propagates in +x direction, for example, has the following expression,

$$g(t,x) = \exp\left[\frac{\left(t - t_0 - \frac{x - x_0}{v}\right)^2}{T^2}\right] \qquad (1.20)$$

where v is the velocity of the pulse in the specific medium, and the pulse has its maximum at x = x_0 when t = t_0. T is a constant.

The Fourier transform of the above Gaussian pulse has the following form in the frequency domain,

$$G(f) \propto \exp[-\pi^2 T^2 f^2].$$

Equation (1.20) was redefined for ease of implementation to be,

$$g = \exp\left[-\left(\frac{t_0}{t_c}\right)^2\right]$$

(1.21)

where $t_0 = n_0 \cdot \Delta t$. This means that the pulse will reach its maximum magnitude after n_0 time steps, and $t_c = n_1 \Delta t$. n_1 is a non-negative integer. The steps used when implementing this equation are, as follows;

1. The space discretization intervals Δx, Δy and Δz have to be chosen fine enough to represent the smallest dimension of the structure.

2. The time discretization interval Δt has to be chosen small enough to meet the stability criterion.

3. The Gaussian pulse must be wide enough to contain enough space and time divisions so that good resolution can be achieved. At the same time, the spectrum of the pulse must be wide enough, or the pulse must be narrow enough, to maintain a substantial energy level within the frequency range of interest. One can change n_1 in order to realize this step.

A Sinusoid Wave Modulated Gaussian Pulse Excitation

In some applications, such as wave propagation in a waveguide there is a cutoff frequency. One would like to be able to shift the maximum point of the spectrum to the frequency (f_0). This can be realized by using a sinusoidal wave, which is modulated with a Gaussian pulse.

An ideal signal, i.e. a sinusoidal wave modulated with a Gaussian pulse, which propagates in the +x direction, can be expressed as,

$$g(t,x) = \sin(2\pi f_0 t)\exp\left[\frac{\left(t-t_0-\frac{x-x_0}{v}\right)^2}{T^2}\right]$$

(1.22)

The spectrum of (1.22) achieves its maximum magnitude at the frequency f_0. The computer program implementation uses the following form,

9

$$g = \sin(2\pi f_0 t)\exp\left[-\left(\frac{t_0}{t_c}\right)^2\right] \qquad (1.23)$$

Again by changing n_1, one can control the width of the pulse in both the time and space domains in order to obtain good resolution during simulations, and to avoid having large frequency components falling below the cutoff frequency. From Figure 1.3 and Figure 1.4, it can be observed that the spectrum of the pulse has a very small magnitude when the frequency is less than 21.2 GHz. The main frequency components of the pulse fall between from 26.5 and 40 GHz, which is the standard WR28 waveguide frequency band.
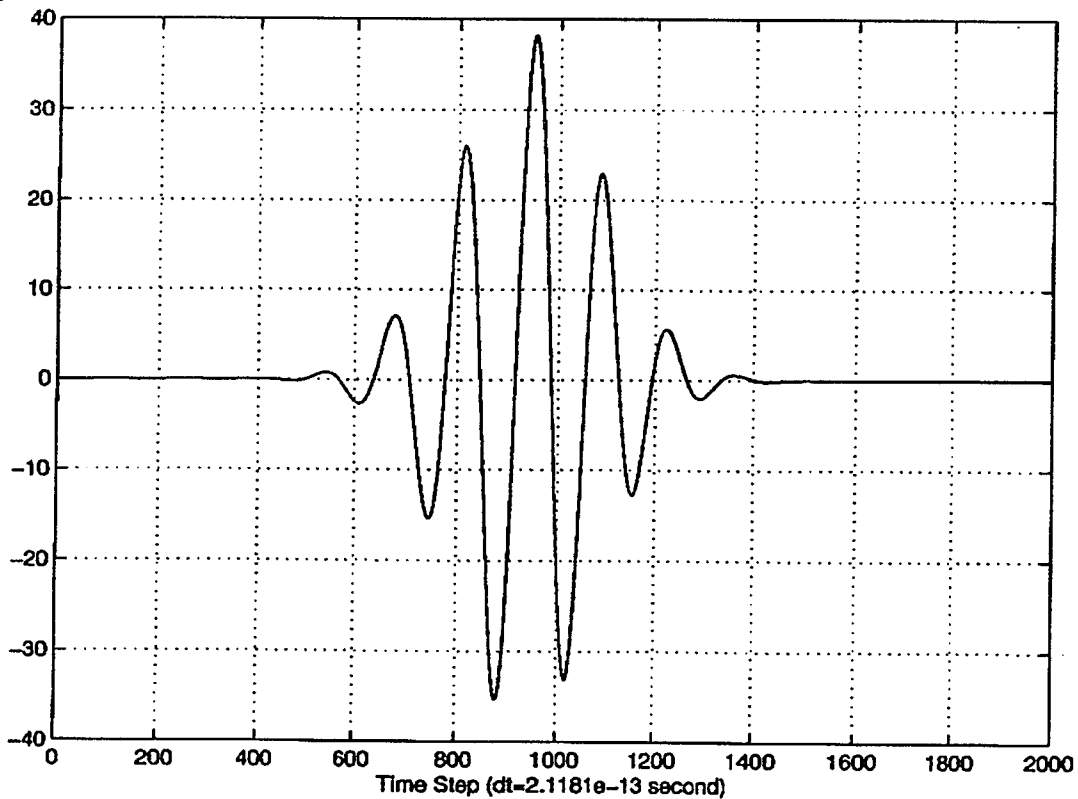
Figure 1.3 A sinusoidal wave modulated with a Gaussian pulse $f_0 = 33.25$GHz, $n_0 = 800$, $t_c = 200\Delta t$.

10
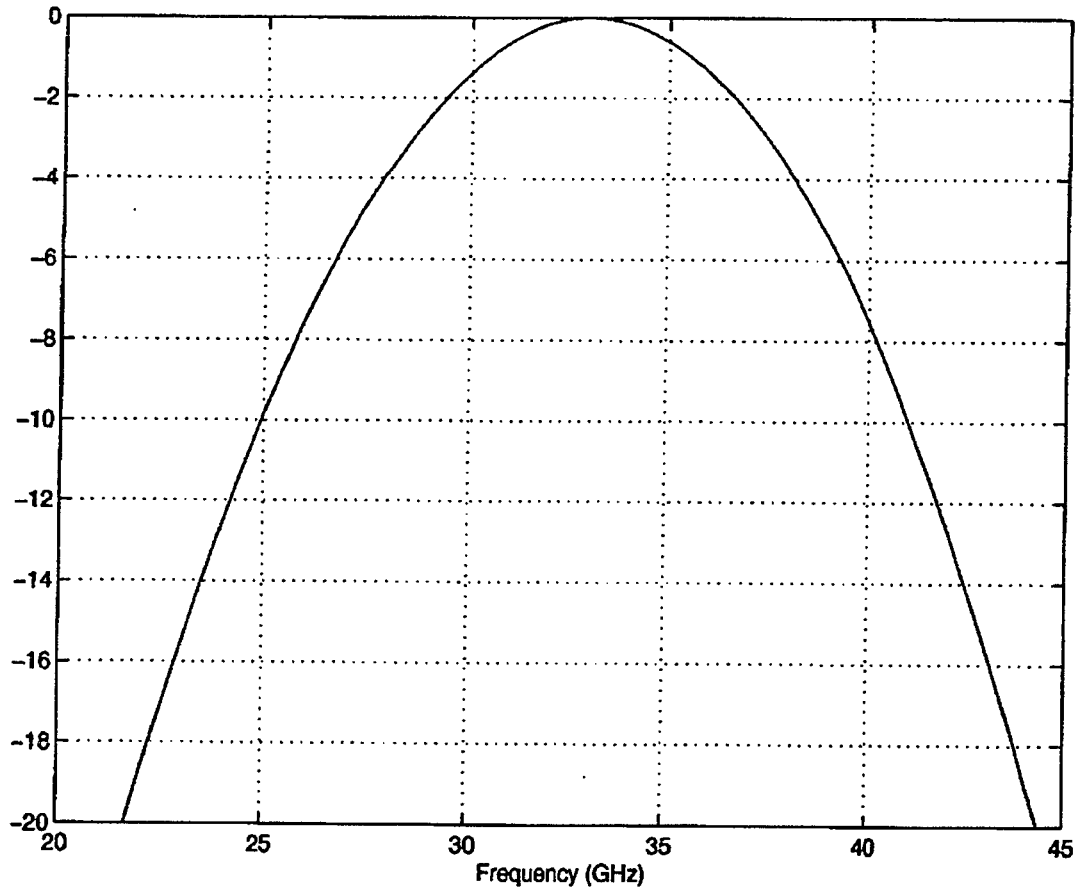
Figure 1.4 The spectrum of the pulse in Figure 1.3.

1.2 Non-orthogonal FDTD Method

1.2.1 Introduction

Problems arise when the FDTD algorithm is used to simulate structures involving, (1) complicated shapes, and (2) curved boundaries. When small or fine details are present in a large complicated structure, a very fine mesh is needed to represent these details. This leads to a less efficient use of computer memory and an increase in the overall computational time. To resolve (2), a curved boundary is approximated by using 'staircasing' which often leads to more complicated implementations.

To overcome these two major problems with the regular FDTD method, an FDTD in General Curvilinear Coordinate or FDTD-GCC method has been developed. This method is also referred to as a Non-orthogonal method because the FDTD mesh is composed of hexahedral, i.e. non-orthogonal cells.

The use of a non-orthogonal or non-regular mesh in the FDTD algorithm can increase its efficiency because a fine mesh can be used in regions with fine structure and a coarse mesh in regions where fine details are absent. The use of a non-orthogonal mesh for 2-D problems can be found in [8] and [9] for the analysis of open dielectric structures.

A non-orthogonal mesh for modeling 3D square coaxial waveguides is very useful because the discontinuities are often confined to limited regions of the total structure. This allows for large savings in memory and computation time. Figure 1.5 illustrates the benefits of applying the FDTD method in general curvilinear coordinates.

An another big advantage of using an FDTD in General Curvilinear Coordinate is that one can flexibly combine several different orthogonal coordinate systems in a computational domain. For example [10], in Figure 1.6 is shown a square-coaxial Rat-race coupler. To simulation the structure, we developed the non-orthogonal mesh that is shown in Figure 1.7. It is very clear that the two orthogonal coordinate systems shown in the figure, i.e. rectangular and cylindrical coordinate systems have been merged together. The use of GCC is limited to small regions, namely those that are located at the interface between rectangular and cylindrical coordinates. The simulated results (solid line) obtained with FDTD are compared against measured (dashed line) for a 3dB Rat-race coupler [11] are shown in Figures 1.8, 1.9, 1.10 and 1.11.
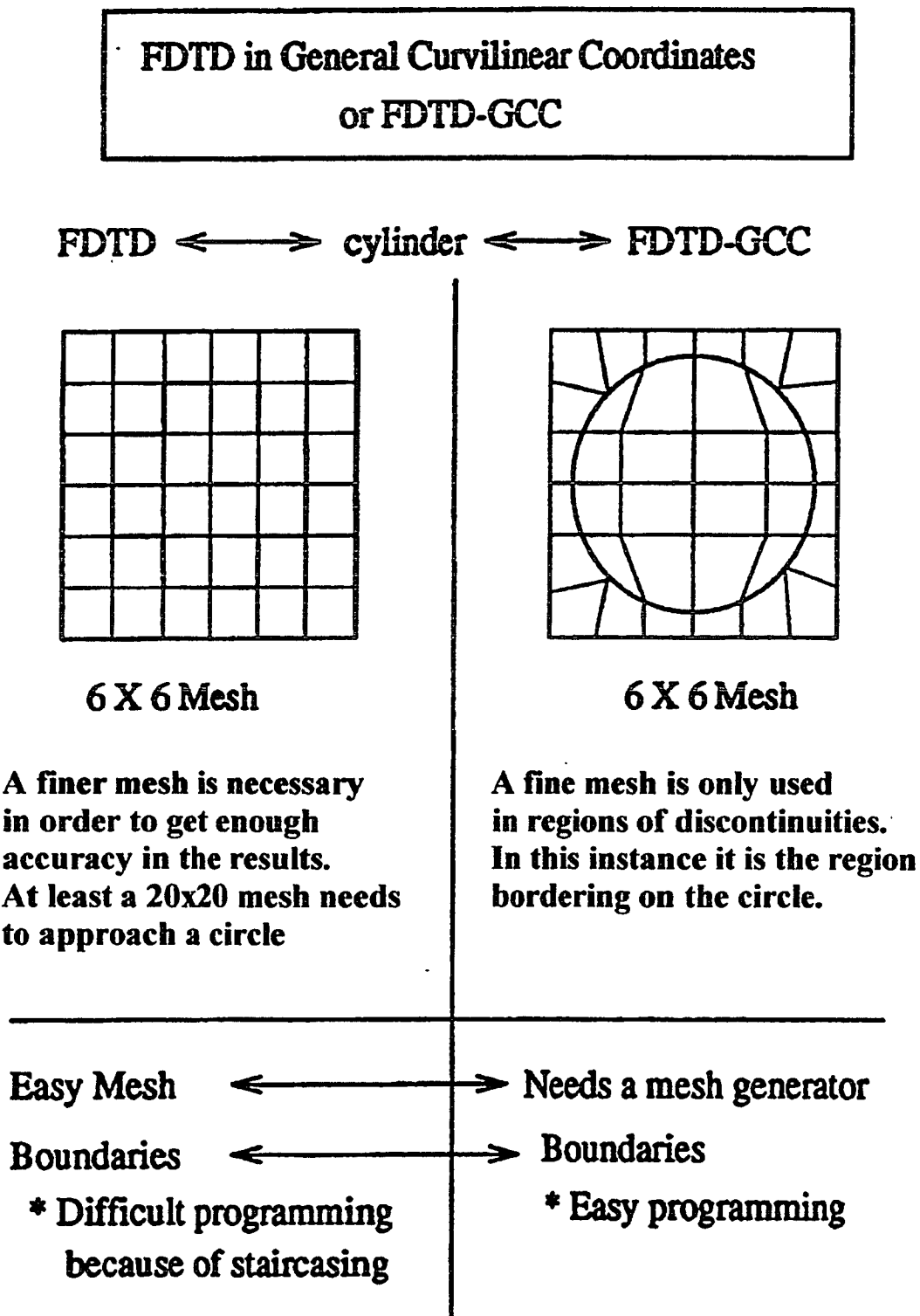
Figure 1.5 Benefits of applying the FDTD in GCC.
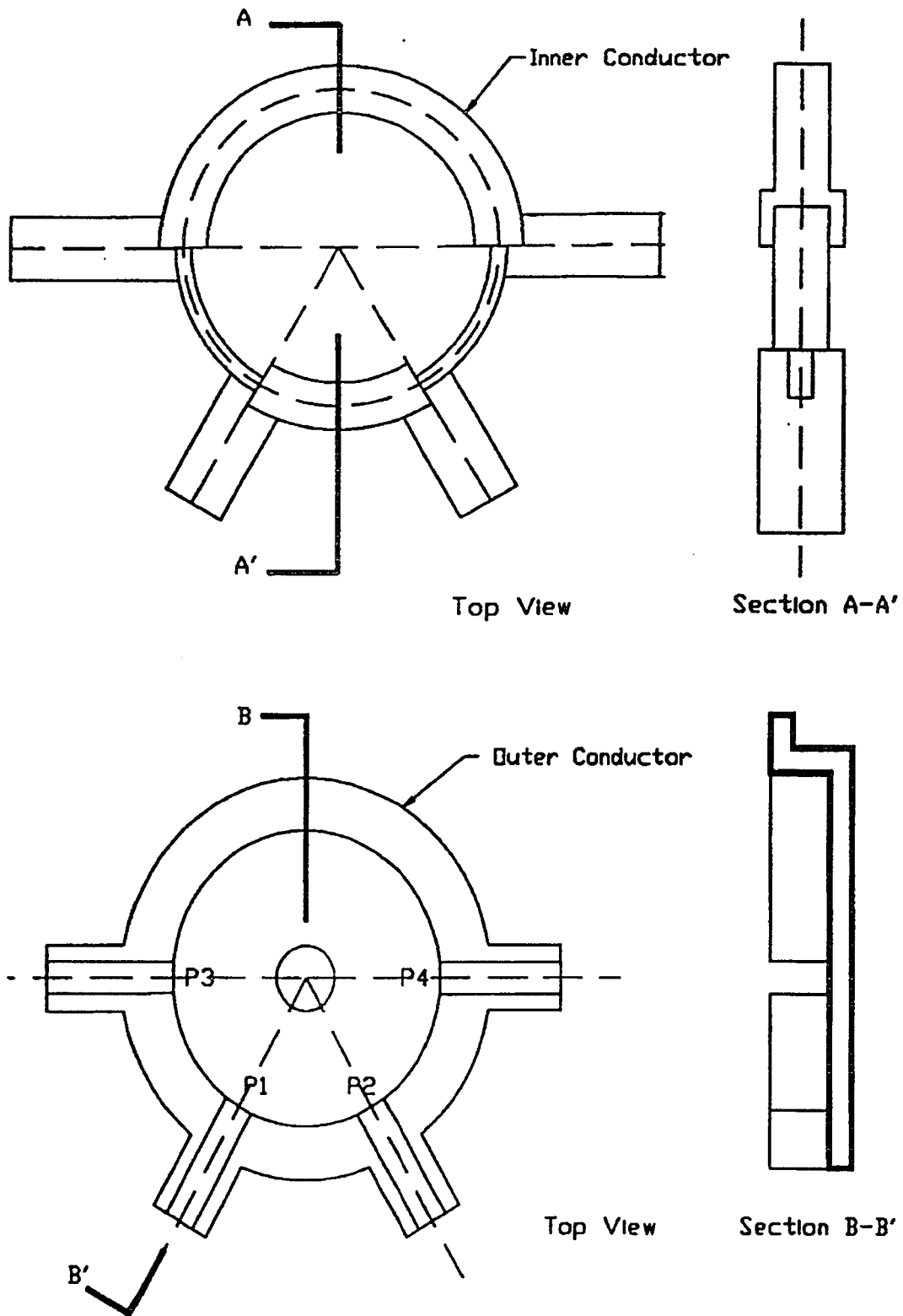
Figure 1.6 The square-coaxial waveguide Rat-race coupler.
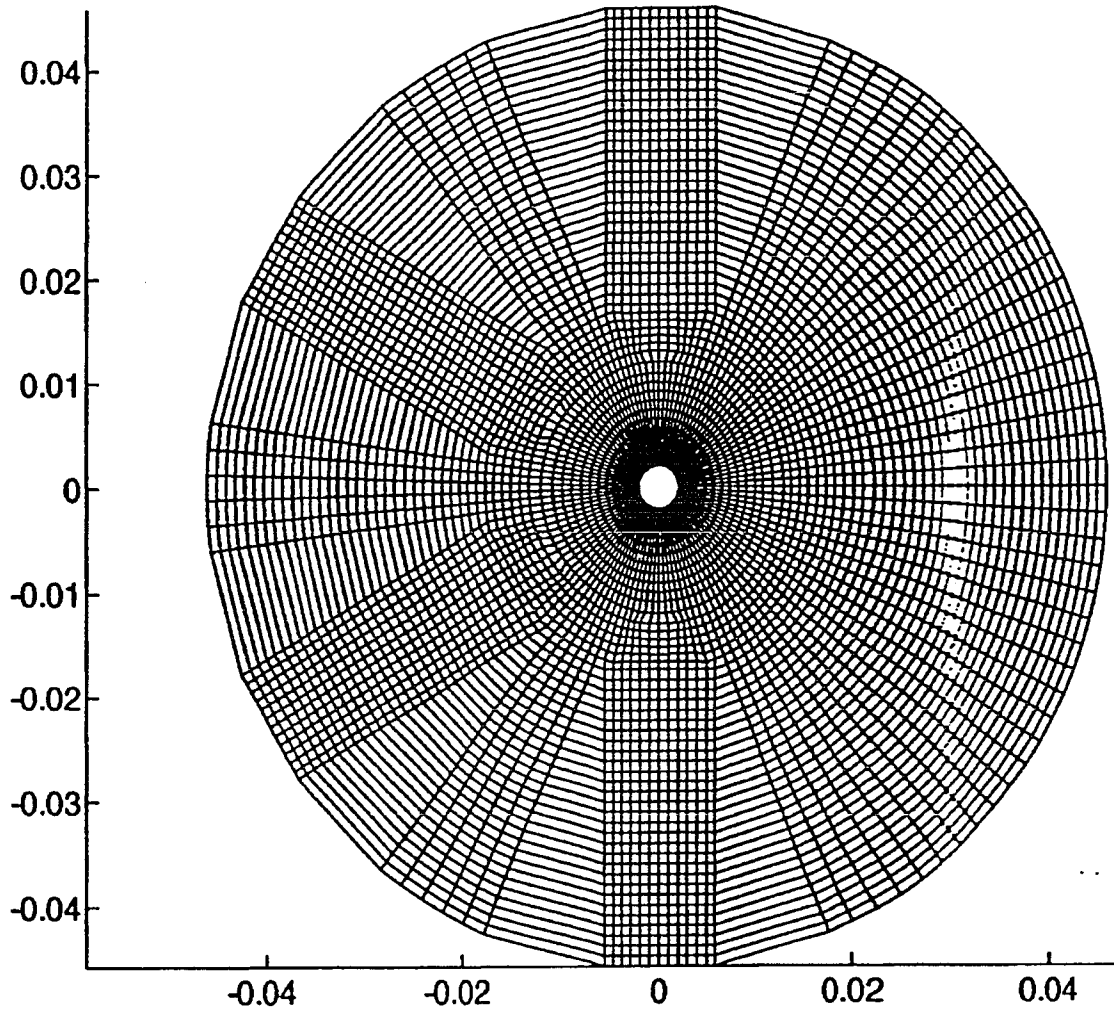
Figure 1.7 The GCC mesh for the Rat-race coupler.
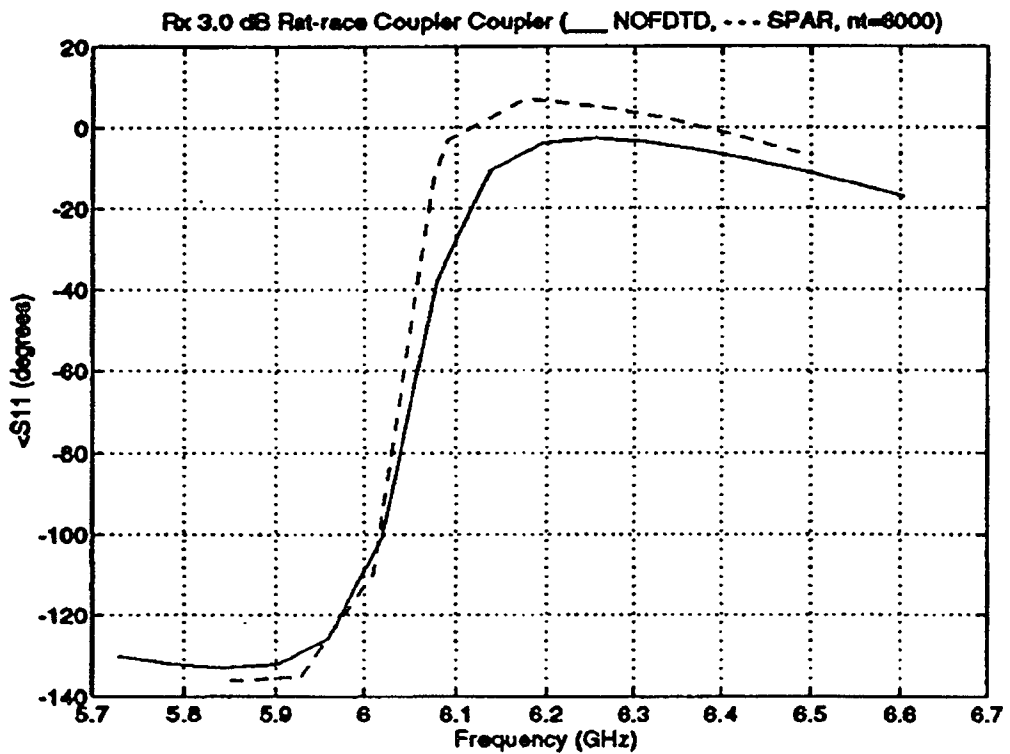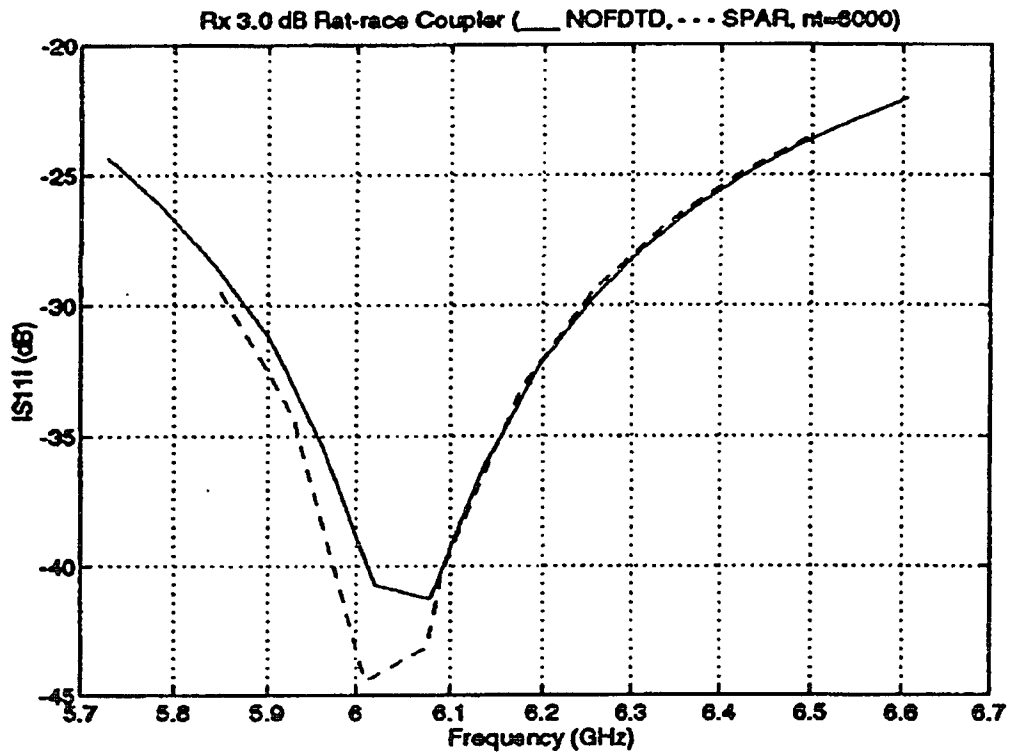
Figure 1.8 S11 for a 3dB Rat-race coupler.
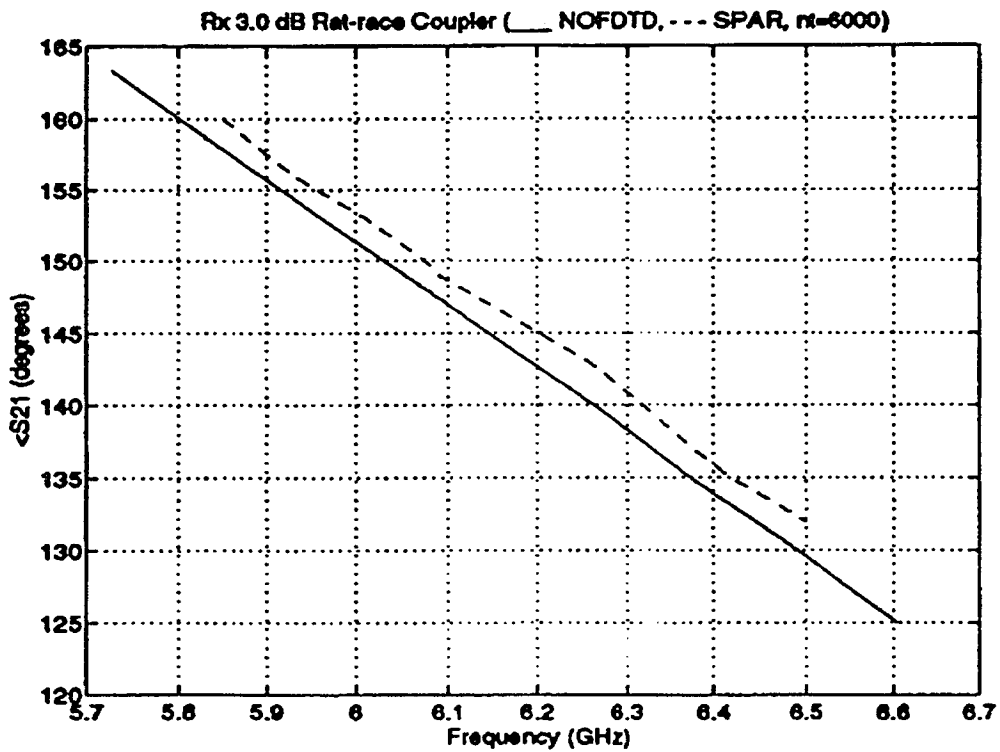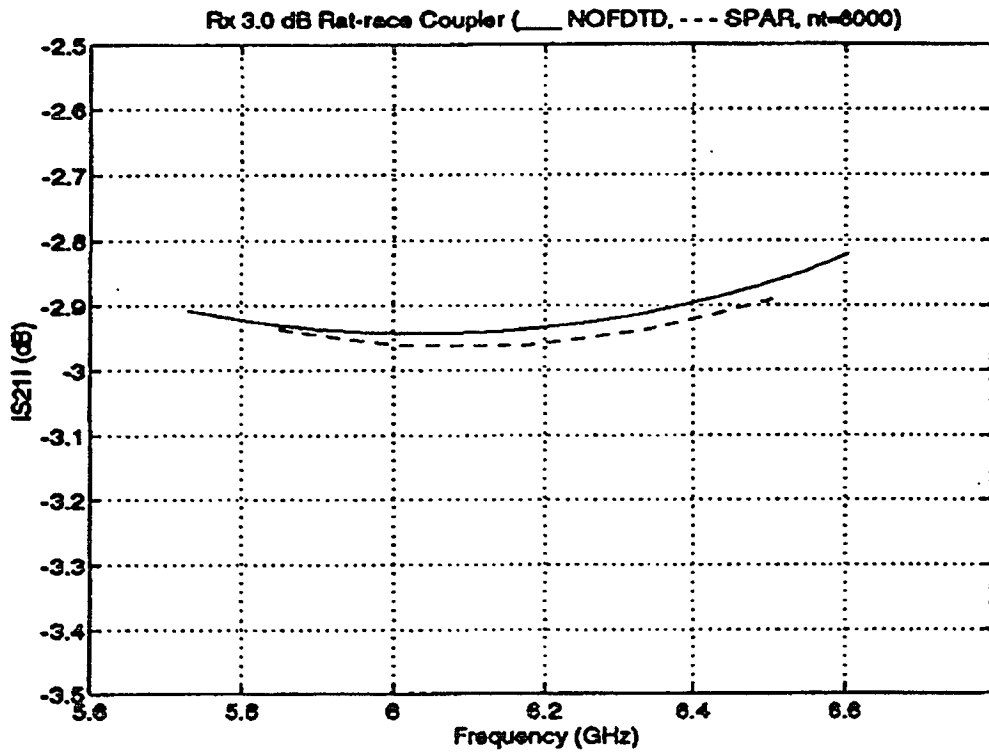
Figure 1.9 S21 for a 3dB Rat-race coupler.
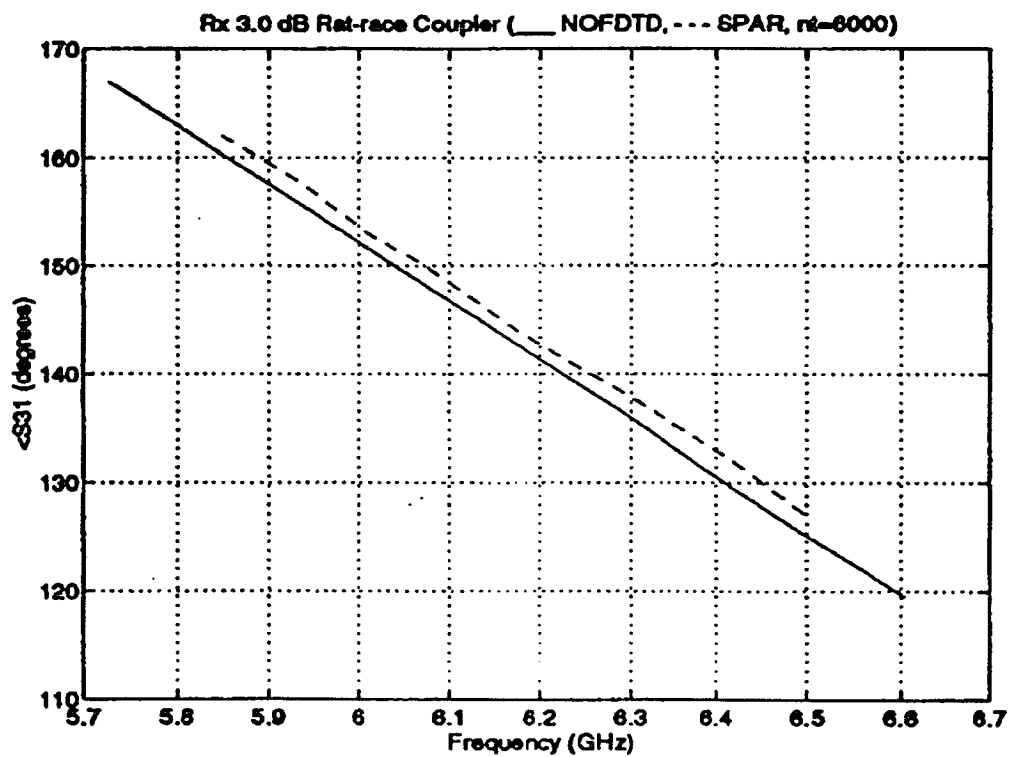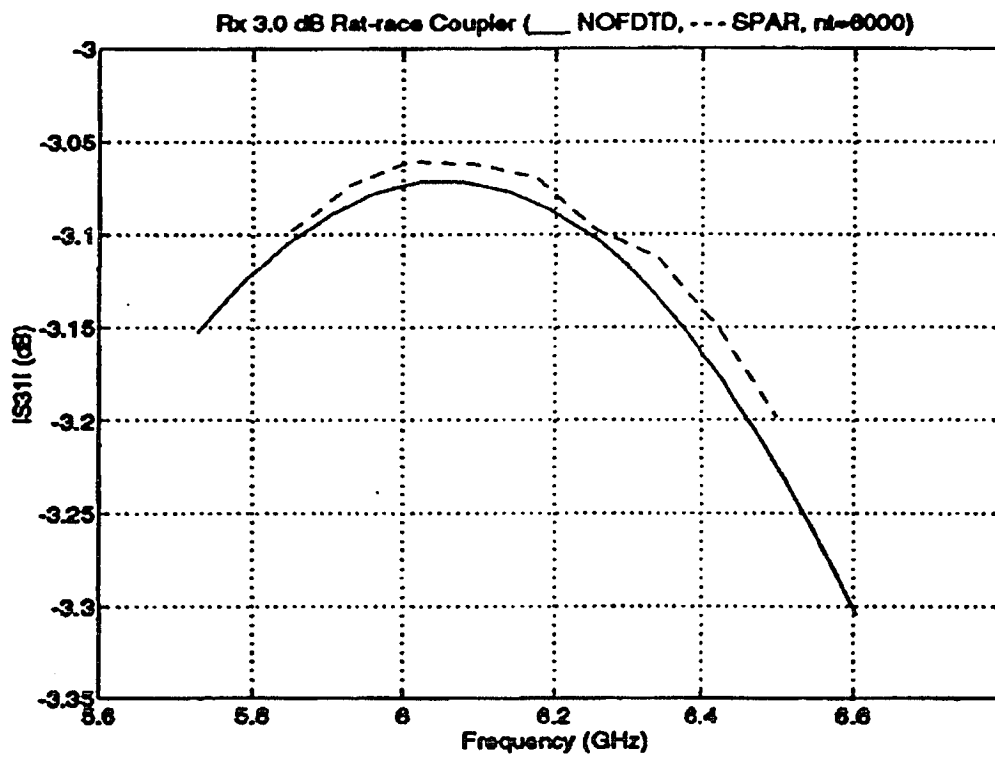
Figure 1.10 S31 for a 3dB Rat-race coupler.
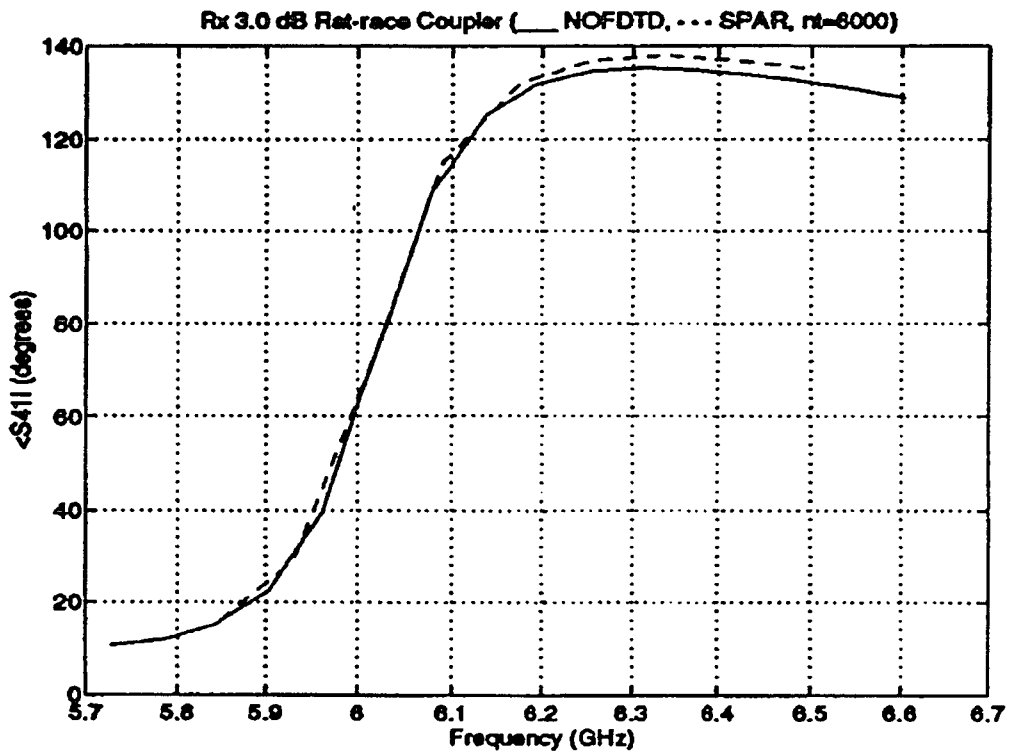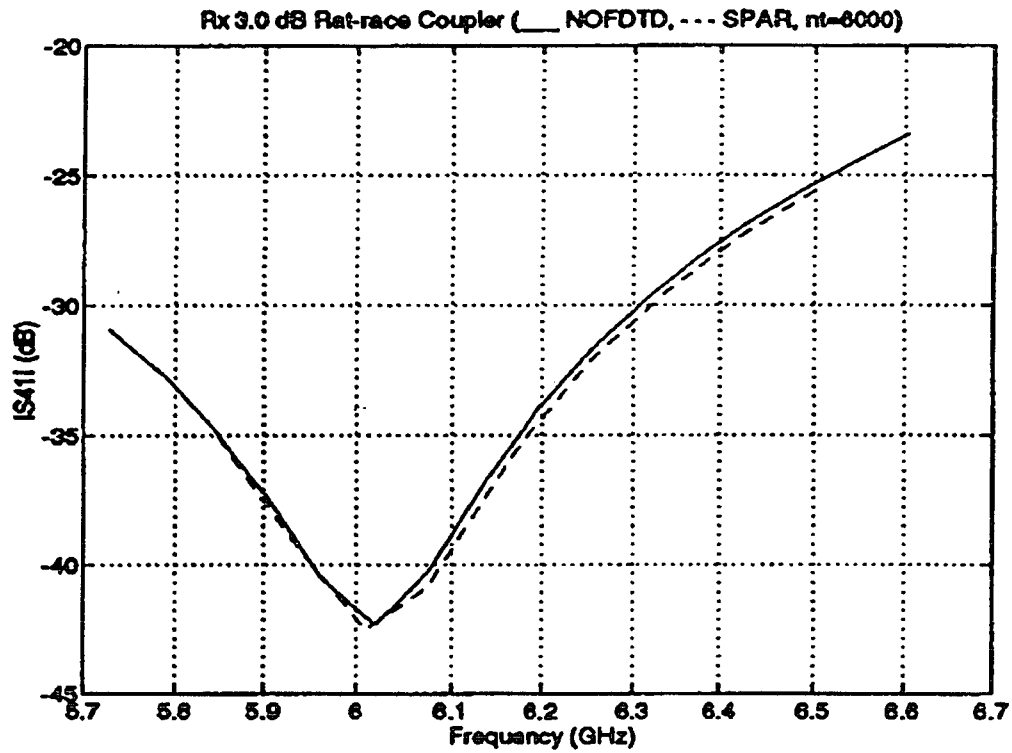
Figure 1.11 S41 for a 3dB Rat-race coupler.

1.2.2 Formulation of the FDTD in GCC

A comparison is made in Figure 1.12 between orthogonal and non-orthogonal FDTD grids in three dimensions. It diagrammatically shows the changes that are required in going from Cartesian coordinates to a general curvilinear coordinates system. Also, in a manner similar to the orthogonal FDTD method, the locations of both **E** and **H** nodes are displaced in space by one-half a space step. The time instants when the **E** or **H** fields are calculated are also offset by half a time step.

1.2.3 From Orthogonal to Non-orthogonal Coordinate Systems

Figure 1.13 shows a transform from a Cartesian (orthogonal) to a general curvilinear (non-orthogonal) coordinate system. At each point of the mesh $r(u^1, u^2, u^3)$, we have the new basis vectors,

$$A_l(u^1, u^2, u^3) = \frac{dr(u^1, u^2, u^3)}{du^l} \qquad l=1, 2, 3. \tag{1.24}$$

where **r** is a displacement vector, whose magnitude is equal to the distance between the origin of the GCC and a point (u^1, u^2, u^3) in the GCC, and its direction is from the origin to (u^1, u^2, u^3). A_1, A_2, A_3 are not necessarily orthogonal (for example: $A_1 \cdot A_2 \neq O$). At each point we can define the reciprocal basis vectors,

$$A^1 = (A_2 \times A_3)/V \tag{1.25a}$$

$$A^2 = (A_3 \times A_1)/V \tag{1.25b}$$

$$A^3 = (A_1 \times A_2)/V \tag{1.25c}$$

where V is a volume. It is defined by $V= A_1 \cdot (A_2 \times A_3)$. Then $A^i \cdot A_j = \delta_{ij}$. (If i = j, δ_{ij} = 1 and If i $\neq$ j, δ_{ij} = 0, i, j=1, 2, 3)

Then the field can be expressed in two bases,

$$E = E^i \cdot A_i \tag{1.26a}$$

where E^i is the contravariant component of **E** field and,

$$\mathbf{E} = E_j \cdot \mathbf{A}^j \qquad (1.26b)$$

where E_j is the covariant component of **E** field. $\mathbf{E} \cdot \mathbf{A}_l = E_l$, the l covariant component of the electric field. $\mathbf{H} \cdot \mathbf{A}^k = H^k$, the k contravariant component of the magnetic field.

The covariant field components E_i are obtained through the contravariant E^j by,

$$E_i = g_{ij} \cdot E^j \qquad (1.27)$$

where $g_{ij} = \mathbf{A}_i \cdot \mathbf{A}_j$ is the tenser metric [12] of the new coordinates.
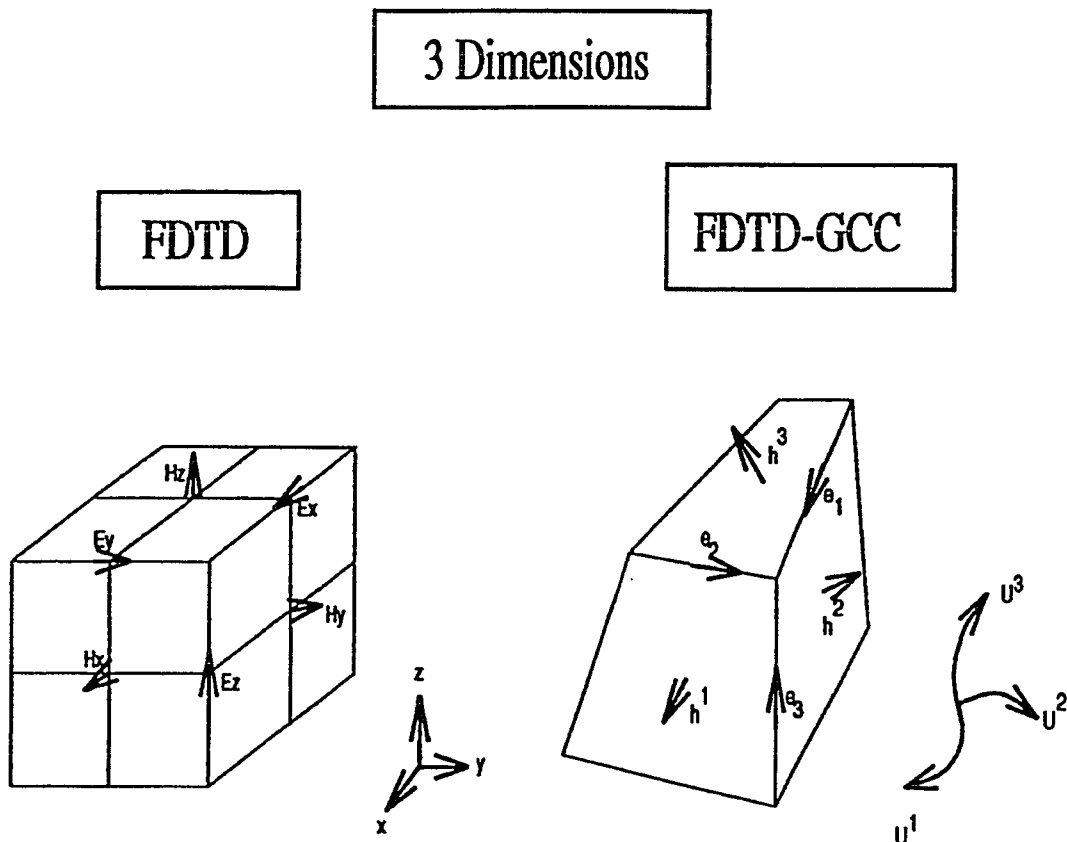
Figure 1.12 A comparison of orthogonal and non-orthogonal three-dimensional grids.
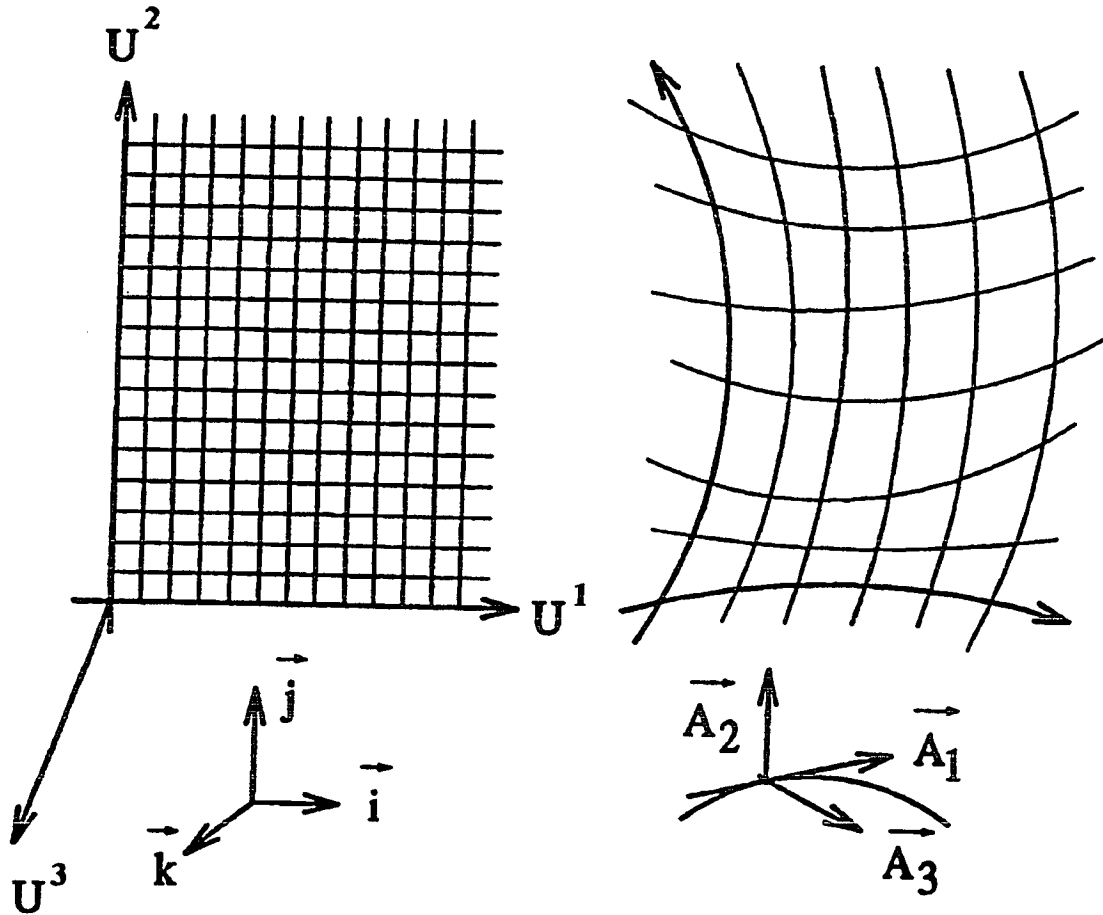
Figure 1.13 The transform from orthogonal the non-orthogonal coordinate systems.

1.2.4 Maxwell Equations in Integral Form

The non-orthogonal FDTD algorithm can be easily derived from Maxwell's equations for an isotropic media in integral form [12]. The FDTD-GCC starts from the Maxwell equations in integral form,

$$-\mu \int \frac{\partial \mathbf{H}}{\partial t} \, d\mathbf{S} = \int_c \mathbf{E} \cdot d\mathbf{l} \qquad \text{(Faraday's law)} \qquad (1.28)$$

$$\varepsilon \int \frac{\partial \mathbf{E}}{\partial t} \cdot d\mathbf{S} = \int_c \mathbf{H} \cdot d\mathbf{l} \qquad \text{(Ampere's law)} \qquad (1.29)$$

These equations are enforced cell by cell in the general curvilinear coordinates system. For the surface enclosed by the four coordinate lines as shown in Figure 1.14, we derive the following expression by obtaining a finite difference approximation of Ampere's law for the contravariant component of the magnetic field $H^1 = \mathbf{H} \cdot \mathbf{A}^1$, at the instant n + 1/2,

$$
-\mu \frac{\mathbf{H}^{n+1/2}\left(u^1,u^2,u^3\right) - \mathbf{H}^{n-1/2}\left(u^1,u^2,u^3\right)}{\Delta t} \cdot \frac{\mathbf{A}^1}{\left|\mathbf{A}^1\right|} \cdot S\bigg|_{\left(u^1,u^2,u^3\right)}
$$

$$
= \mathbf{E} \cdot \left[\mathbf{A}_3\left(u^1,u^2+1/2,u^3\right) - \mathbf{A}_3\left(u^1,u^2-1/2,u^3\right)\right]
$$

$$
- \mathbf{E} \cdot \left[\mathbf{A}_2\left(u^1,u^2,u^3+1/2\right) - \mathbf{A}_2\left(u^1,u^2,u^3-1/2\right)\right]
$$

(1.30)

where,

$$
S\bigg|_{\left(u^1,u^2,u^3\right)} \approx \left|\mathbf{A}_2 \times \mathbf{A}_3\right|_{\left(u^1,u^2,u^3\right)} = \sqrt{\left(\mathbf{A}_2 \times \mathbf{A}_3\right) \cdot \left(\mathbf{A}_2 \times \mathbf{A}_3\right)}\bigg|_{\left(u^1,u^2,u^3\right)}
$$

(1.31)

Simplifying,

$$
H^1\left(u^1,u^2,u^3\right)^{n+1/2} = H^1\left(u^1,u^2,u^3\right)^{n-1/2} - \frac{\Delta t}{\mu V\left(u^1,u^2,u^3\right)} \cdot
$$

$$
\left[E_3\left(u^1,u^2+1/2,u^3\right)^n - E_3\left(u^1,u^2-1/2,u^3\right)^n \right.
$$

$$
\left. - E_2\left(u^1,u^2,u^3+1/2\right)^n + E_2\left(u^1,u^2,u^3-1/2\right)^n \right]
$$

(1.32a)

For H^2 and H^3 one can have,

$$
H^2\left(u^1,u^2,u^3\right)^{n+1/2} = H^2\left(u^1,u^2,u^3\right)^{n-1/2} - \frac{\Delta t}{\mu V\left(u^1,u^2,u^3\right)} \cdot
$$

$$
\left[E_1\left(u^1,u^2,u^3+1/2\right)^n - E_1\left(u^1,u^2,u^3-1/2\right)^n \right.
$$

$$
\left. - E_3\left(u^1+1/2,u^2,u^3\right)^n + E_3\left(u^1-1/2,u^2,u^3\right)^n \right]
$$

(1.32b)

$$
H^3\left(u^1,u^2,u^3\right)^{n+1/2} = H^3\left(u^1,u^2,u^3\right)^{n-1/2} - \frac{\Delta t}{\mu V\left(u^1,u^2,u^3\right)} \cdot
$$

$$\left[E_2\left(u^1 + 1/2, u^2, u^3\right)^n - E_2\left(u^1 - 1/2, u^2, u^3\right)^n \right.$$
$$\left. - E_1\left(u^1, u^2 + 1/2, u^3\right)^n + E_1\left(u^1, u^2 - 1/2, u^3\right)^n \right] \qquad (1.32c)$$

where $\mathbf{u} = (u^1, u^2, u^3)$ are the generalized curvilinear coordinates, $\{A_i\}_{i=1,2,3}$, is the curvilinear bases that is defined by the mesh, and $\{A^j\}_{j=1,2,3}$ is the dual bases [12] [13] [14] [15]. $E_i = \mathbf{E} \cdot A_i$, and $H^j = \mathbf{H} \cdot A^j$, are the covariant and contravariant components of the electric and magnetic field, respectively. Note, the volume of the non-orthogonal cell can be reduced to the form,

$$V\left(u^1, u^2, u^3\right) = |A_1| |S| \big|_{(u^1, u^2, u^3)}$$

$$= \sqrt{A_1 \cdot A_1} \sqrt{(A_2 \times A_3) \cdot (A_2 \times A_3)} \big|_{(u^1, u^2, u^3)}$$

$$= \sqrt{\left[A_1 \cdot (A_2 \times A_3)\right] \cdot \left[A_1 \cdot (A_2 \times A_3)\right]} \big|_{(u^1, u^2, u^3)}$$

$$= A_1 \cdot (A_2 \times A_3) \big|_{(u^1, u^2, u^3)}$$

$$= \sqrt{g} \big|_{(u^1, u^2, u^3)} \qquad (1.33)$$

Similarly, we derive the following expression by obtaining a finite difference approximation to Faraday's law for the contravariant component of the electric field $E^1 = \mathbf{E} \cdot A^1$, at the instant n+1,

$$E^1\left(u^1, u^2, u^3\right)^{n+1} = E^1\left(u^1, u^2, u^3\right)^n + \frac{\Delta t}{\varepsilon V\left(u^1, u^2, u^3\right)} \cdot$$

$$\left[H_3\left(u^1, u^2 + 1/2, u^3\right)^{n+1/2} - H_3\left(u^1, u^2 - 1/2, u^3\right)^{n+1/2} \right.$$
$$\left. - H_2\left(u^1, u^2, u^3 + 1/2\right)^{n+1/2} + H_2\left(u^1, u^2, u^3 - 1/2\right)^{n+1/2} \right] \qquad (1.34a)$$

The other $\mathbf{E}$ field components, E^2 and E^3 are derived in the same way. They are,

$$E^2\left(u^1,u^2,u^3\right)^{n+1} = E^2\left(u^1,u^2,u^3\right)^n + \frac{\Delta t}{\varepsilon V\left(u^1,u^2,u^3\right)} \cdot$$

$$\left[H_1\left(u^1,u^2,u^3+1/2\right)^{n+1/2} - H_1\left(u^1,u^2,u^3-1/2\right)^{n+1/2} \right.$$
$$\left. - H_3\left(u^1+1/2,u^2,u^3\right)^{n+1/2} + H_3\left(u^1-1/2,u^2,u^3\right)^{n+1/2}\right] \qquad (1.34b)$$

$$E^3\left(u^1,u^2,u^3\right)^{n+1} = E^3\left(u^1,u^2,u^3\right)^n + \frac{\Delta t}{\varepsilon V\left(u^1,u^2,u^3\right)} \cdot$$

$$\left[H_2\left(u^1+1/2,u^2,u^3\right)^{n+1/2} - H_2\left(u^1-1/2,u^2,u^3\right)^{n+1/2} \right.$$
$$\left. - H_1\left(u^1+1/2,u^2,u^3\right)^{n+1/2} + H_1\left(u^1-1/2,u^2,u^3\right)^{n+1/2}\right] \qquad (1.34c)$$

As a final step in our formulation, we need to convert the contravariant components of E into its covariant components, in order to calculate the contravariant components of H, and vice verse. This can be accomplished by noting that the original bases A_i are related to the dual bases through the tenser metric [12], according to,

$$\mathbf{A}_i = \sum_j g_{ij}\mathbf{A}^j, \qquad \text{and} \qquad g_{ij} = \mathbf{A}_i \cdot \mathbf{A}_j \qquad (1,35)$$

Thus, the covariant components of H can be obtained from the contravariant components of H as follows,

$$A_1 = \sum_{j=1}^{3} g_{1j}A^j, \qquad A_2 = \sum_{j=1}^{3} g_{2j}A^j, \qquad A_3 = \sum_{j=1}^{3} g_{3j}A^j. \qquad (1.36)$$

By using an approximation technique whereby the neighboring values are averaged [15], we derive the finite difference approximation of equation (1.36). These results are used to convert the contravariant components of E^i and H^i to the covariant components of E_i and H_i, we have,

$$E_1\left(u^1,u^2,u^3\right)= g_{11}E^1\left(u^1,u^2,u^3\right)$$

$$+\frac{g_{12}}{4}\left[E^2\left(u^1+1/2,u^2-1/2,u^3\right)+E^2\left(u^1-1/2,u^2-1/2,u^3\right)\right.$$

$$+E^2\left(u^1-1/2,u^2+1/2,u^3\right)+E^2\left(u^1+1/2,u^2+1/2,u^3\right)\right]$$

$$+\frac{g_{13}}{4}\left[E^3\left(u^1+1/2,u^2,u^3-1/2\right)+E^3\left(u^1-1/2,u^2,u^3-1/2\right)\right.$$

$$+E^3\left(u^1-1/2,u^2,u^3+1/2\right)+E^3\left(u^1+1/2,u^2,u^3+1/2\right)\right] \qquad (1.37)$$

$$E_2\left(u^1,u^2,u^3\right)= g_{22}E^2\left(u^1,u^2,u^3\right)$$

$$+\frac{g_{21}}{4}\left[E^1\left(u^1+1/2,u^2-1/2,u^3\right)+E^1\left(u^1-1/2,u^2-1/2,u^3\right)\right.$$

$$+E^1\left(u^1-1/2,u^2+1/2,u^3\right)+E^1\left(u^1+1/2,u^2+1/2,u^3\right)\right]$$

$$+\frac{g_{23}}{4}\left[E^3\left(u^1,u^2+1/2,u^3-1/2\right)+E^3\left(u^1,u^2-1/2,u^3-1/2\right)\right.$$

$$+E^3\left(u^1,u^2-1/2,u^3+1/2\right)+E^3\left(u^1,u^2+1/2,u^3+1/2\right)\right] \qquad (1.38)$$

$$E_3\left(u^1,u^2,u^3\right)= g_{33}E^3\left(u^1,u^2,u^3\right)$$

$$+\frac{g_{31}}{4}\left[E^1\left(u^1-1/2,u^2,u^3+1/2\right)+E^1\left(u^1-1/2,u^2,u^3-1/2\right)\right.$$

$$+E^1\left(u^1+1/2,u^2,u^3-1/2\right)+E^1\left(u^1+1/2,u^2,u^3+1/2\right)\right]$$

$$+\frac{g_{32}}{4}\Big[E^2\big(u^1,u^2+1/2,u^3-1/2\big)+E^2\big(u^1,u^2-1/2,u^3-1/2\big)$$

$$+E^2\big(u^1,u^2-1/2,u^3+1/2\big)+E^2\big(u^1,u^2+1/2,u^3+1/2\big)\Big]$$

<div style="text-align:right">(1.39)</div>

$$H_1\big(u^1,u^2,u^3\big)=g_{11}H^1\big(u^1,u^2,u^3\big)$$

$$+\frac{g_{12}}{4}\Big[H^2\big(u^1+1/2,u^2-1/2,u^3\big)+H^2\big(u^1-1/2,u^2-1/2,u^3\big)$$

$$+H^2\big(u^1-1/2,u^2+1/2,u^3\big)+H^2\big(u^1+1/2,u^2+1/2,u^3\big)\Big]$$

$$+H^3\big(u^1-1/2,u^2,u^3+1/2\big)+H^3\big(u^1+1/2,u^2,u^3+1/2\big)\Big]$$

<div style="text-align:right">(1.40)</div>

$$H_2\big(u^1,u^2,u^3\big)=g_{22}H^2\big(u^1,u^2,u^3\big)$$

$$+\frac{g_{21}}{4}\Big[H^1\big(u^1+1/2,u^2-1/2,u^3\big)+H^1\big(u^1-1/2,u^2-1/2,u^3\big)$$

$$+H^1\big(u^1-1/2,u^2+1/2,u^3\big)+H^1\big(u^1+1/2,u^2+1/2,u^3\big)\Big]$$

$$+\frac{g_{23}}{4}\Big[H^3\big(u^1,u^2+1/2,u^3-1/2\big)+H^3\big(u^1,u^2-1/2,u^3-1/2\big)$$

$$+H^3\big(u^1,u^2-1/2,u^3+1/2\big)+H^3\big(u^1,u^2+1/2,u^3+1/2\big)\Big]$$

<div style="text-align:right">(1.41)</div>

$$H_3\big(u^1,u^2,u^3\big)=g_{33}H^3\big(u^1,u^2,u^3\big)$$

$$+\frac{g_{31}}{4}\Big[H^1\big(u^1-1/2,u^2,u^3+1/2\big)+H^1\big(u^1-1/2,u^2,u^3-1/2\big)$$

$$+ H^1\left(u^1 + 1/2, u^2, u^3 - 1/2\right) + H^1\left(u^1 + 1/2, u^2, u^3 + 1/2\right)\Big]$$

$$+ \frac{g_{32}}{4}\Big[H^2\left(u^1, u^2 + 1/2, u^3 - 1/2\right) + H^2\left(u^1, u^2 - 1/2, u^3 - 1/2\right)$$

$$+ H^2\left(u^1, u^2 - 1/2, u^3 + 1/2\right) + H^2\left(u^1, u^2 + 1/2, u^3 + 1/2\right)\Big] \tag{1.42}$$
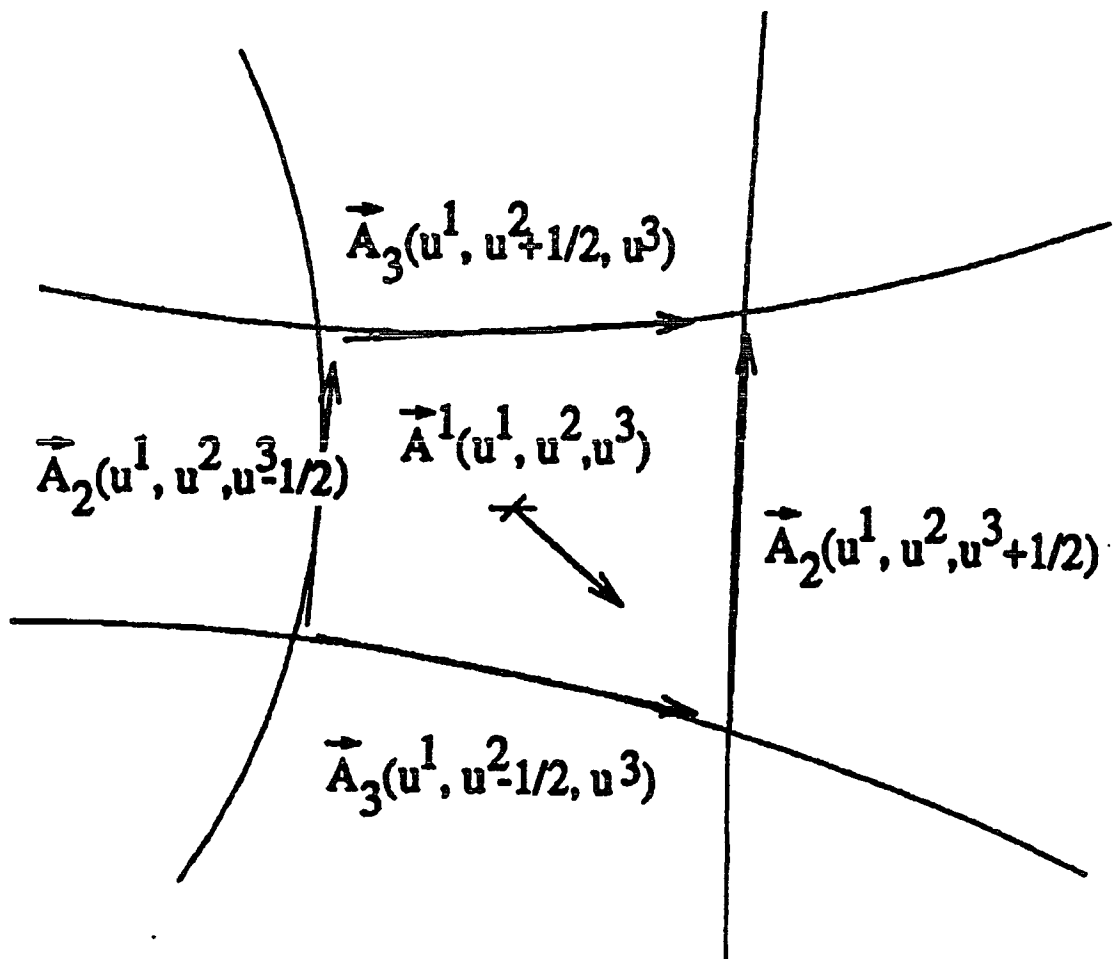
Figure 1.14 General curvilinear coordinate system.

28

1.2.5 The Stability Condition

The use of a non-orthogonal mesh results in a truncation error that is of first order. However, globally, the accuracy of the solution is second order. This is called supra-convergence [16] [17]. No special treatment is performed at the boundaries between regions of different sized cells, thus, some numerical reflections will occur. However, the numerical dispersion can be kept to within reasonable bounds by using a finer mesh, relative to a wavelength, in each region.

The stability condition can be demonstrated to be [15] [20],

$$\Delta t \leq \min \left[\frac{1}{c\sqrt{\sum_{i=1,j=1}^{3,3} g^{ij}}} \right] \qquad (1.43)$$

1.3 The Orthogonal Non-uniform FDTD Method

1.3.1 Introduction

The regular FDTD method has been shown to exhibit second-order accuracy in both time and space as long as a uniform mesh is used in both of these dimensions. This conclusion follows directly from the fact that the processing is based on centered differences. However, the power of the regular FDTD method is lost when we try to analyze devices in which small details or curved edges are involved inside big regions where strong field variations are expected. Often, when modeling a structure, one is forced to reduce the cell size, thereby increasing the requirements for computer memory and computation time. Although the non-orthogonal FDTD method can easily model curved or oblique boundaries and use different cell sizes to simulate small details in a large structure [15] [18], a big drawback of this method is that it needs 12-field components. When simulations are carried out, this usually means the algorithm requires more memory and large computational time.

The use of an orthogonal non-uniform mesh with the FDTD algorithm can increase its efficiency because a fine mesh can be used in regions where fine details prevail and a coarse mesh in regions where fine details are absent. This is a useful technique for modeling microwave devices because the discontinuities are often confined to limited regions of the total device. This allows for large savings in memory and computational time.

The work of Manteuffel and White [17] on the numerical solutions of scalar boundary value problems, using orthogonal non-uniform meshes, shows that for many common difference schemes, the accuracy is second-order in spite of the first-order truncation error. The second order accuracy requires no restrictions on the characteristics of the orthogonal non-uniform grid. Monk and Suli [16] proved that the FDTD scheme is also second-order convergent regardless of the mesh non-uniformity. The demonstration of the second-order properties was based on a pervious work on finite volume approximations for the Poisson equation [19] and used the fact that Yee's scheme is also a finite volume scheme. The proof also used the assumption of Dirichlet homogeneous boundary conditions. In a recent work, Navarro, Sangary and Litva [20] carried out a numerical investigation of the accuracy of the orthogonal non-uniform FDTD method. The results obtained from the FDTD simulations are compared with analytical values for different boundary conditions. Navarro *et al* showed that the use of orthogonal non-uniform grids with FDTD yields numerical values of the fields that have second-order accuracy.

1.3.2 The FDTD-GCC Algorithm Used on Orthogonal Non-uniform Mesh

Orthogonal coordinate systems are special cases of the GCC. From the FDTD-GCC one can easily derive the FDTD algorithm on an orthogonal non-uniform grid. Equation (1.27) contains a non-zero tensor matrix $\{g_{ij}\}$, $(i, j = 1, 2, 3)$. In the orthogonal coordinate system, $g_{ij} = 0$, when $i \neq j$. Then the covariant field components and contravariant components of $\mathbf{E}$ and $\mathbf{H}$ fields from (1.37) to (1.42) have following simple relations,

$$E_1 = g_{11}E^1, \quad E_2 = g_{22}E^2, \quad E_3 = g_{33}E^3 \tag{1.44a}$$

$$H_1 = g_{11}H^1, \quad H_2 = g_{22}H^2, \quad H_3 = g_{33}H^3 \tag{1.44b}$$

By combining (1.32) and (1.34) with (1.44) one has the FDTD algorithm on an orthogonal non-uniform grid,

$$H_1\left(u^1,u^2,u^3\right)^{n+1/2} = H_1\left(u^1,u^2,u^3\right)^{n-1/2} - \frac{g_{11}\left(u^1,u^2,u^3\right)\Delta t}{\mu V\left(u^1,u^2,u^3\right)} \cdot$$

$$\left[E_3\left(u^1,u^2+1/2,u^3\right)^n - E_3\left(u^1,u^2-1/2,u^3\right)^n \right. \\ \left. - E_2\left(u^1,u^2,u^3+1/2\right)^n + E_2\left(u^1,u^2,u^3-1/2\right)^n\right] \tag{1.45}$$

$$H_2\left(u^1,u^2,u^3\right)^{n+1/2} = H_2\left(u^1,u^2,u^3\right)^{n-1/2} - \frac{g_{22}\left(u^1,u^2,u^3\right)\Delta t}{\mu V\left(u^1,u^2,u^3\right)} \cdot$$

$$\left[E_1\left(u^1,u^2,u^3+1/2\right)^n - E_1\left(u^1,u^2,u^3-1/2\right)^n \right. \\ \left. - E_3\left(u^1+1/2,u^2,u^3\right)^n + E_3\left(u^1-1/2,u^2,u^3\right)^n\right] \tag{1.46}$$

$$H_3\left(u^1,u^2,u^3\right)^{n+1/2} = H_3\left(u^1,u^2,u^3\right)^{n-1/2} - \frac{g_{33}\left(u^1,u^2,u^3\right)\Delta t}{\mu V\left(u^1,u^2,u^3\right)} \cdot$$

$$\left[E_2\left(u^1+1/2,u^2,u^3\right)^n - E_2\left(u^1-1/2,u^2,u^3\right)^n \right. \\ \left. - E_1\left(u^1,u^2+1/2,u^3\right)^n + E_1\left(u^1,u^2-1/2,u^3\right)^n\right] \tag{1.47}$$

and for **E** field components,

$$E_1\left(u^1,u^2,u^3\right)^{n+1} = E_1\left(u^1,u^2,u^3\right)^n + \frac{g_{11}\left(u^1,u^2,u^3\right)\Delta t}{\varepsilon V\left(u^1,u^2,u^3\right)} \cdot$$

$$\left[H_3\left(u^1,u^2+1/2,u^3\right)^{n+1/2} - H_3\left(u^1,u^2-1/2,u^3\right)^{n+1/2} \right. \\ \left. - H_2\left(u^1,u^2,u^3+1/2\right)^{n+1/2} + H_2\left(u^1,u^2,u^3-1/2\right)^{n+1/2}\right] \tag{1.48}$$

$$E_2\left(u^1,u^2,u^3\right)^{n+1} = E_2\left(u^1,u^2,u^3\right)^n + \frac{g_{22}\left(u^1,u^2,u^3\right)\Delta t}{\varepsilon V\left(u^1,u^2,u^3\right)} \cdot$$

$$\left[H_1\left(u^1,u^2,u^3+1/2\right)^{n+1/2} - H_1\left(u^1,u^2,u^3-1/2\right)^{n+1/2} \right.$$
$$\left. - H_3\left(u^1+1/2,u^2,u^3\right)^{n+1/2} + H_3\left(u^1-1/2,u^2,u^3\right)^{n+1/2} \right] \qquad (1.49)$$

$$E_3\left(u^1,u^2,u^3\right)^{n+1} = E_3\left(u^1,u^2,u^3\right)^n + \frac{g_{33}\left(u^1,u^2,u^3\right)\Delta t}{\varepsilon V\left(u^1,u^2,u^3\right)} \cdot$$

$$\left[H_2\left(u^1+1/2,u^2,u^3\right)^{n+1/2} - H_2\left(u^1-1/2,u^2,u^3\right)^{n+1/2} \right.$$
$$\left. - H_1\left(u^1+1/2,u^2,u^3\right)^{n+1/2} + H_1\left(u^1-1/2,u^2,u^3\right)^{n+1/2} \right] \qquad (1.50).$$

The system consisting of (1.45) to (1.50) is another form of Yee's formulation, but in this case the mesh can be non-uniform. Since $E_i = \mathbf{E} \cdot \mathbf{A}_i$ and $H_i = \mathbf{H} \cdot \mathbf{A}_i$, (i = 1, 2, 3) and letting $(u^1, u^2, u^3) =$ (x, y, z), from Figure 1.14 and Figure 1.15 one can obtain,

$$E_1 = E_x dx(i), \quad E_2 = E_y dy(j), E_3 = E_z dz(k) \qquad (1.51a)$$

$$H_1 = H_x dx(i), H_2 = H_y dy(j), H_3 = H_z dz(k) \qquad (1.51b)$$

where dx(i), dy(j) and dz(k) are the mesh size in x, y and z directions, and E_x, E_y, E_z H_x, H_y and H_z are $\mathbf{E}$ and $\mathbf{H}$ field components. Finally, equations (1.45) to (1.50) can be written as,

$$H_x^{n+1/2}(i,j,k) = H_x^{n-1/2}(i,j,k) - \frac{\Delta t}{\mu}\left[\frac{E_z^n(i,j+1/2,k) - E_z^n(i,j-1/2,k)}{\Delta y(j)} \right.$$

$$\left. - \frac{E_y^n(i,j,k+1/2) - E_y^n(i,j,k-1/2)}{\Delta z(k)} \right] \qquad (1.52)$$

$$H_y^{n+1/2}(i,j,k) = H_y^{n-1/2}(i,j,k) - \frac{\Delta t}{\mu}\left[\frac{E_x^n(i,j,k+1/2) - E_x^n(i,j,k-1/2)}{\Delta z(k)} \right.$$

$$\left. - \frac{E_z^n(i+1/2,j,k) - E_z^n(i-1/2,j,k)}{\Delta x(i)} \right] \qquad (1.53)$$

$$H_z^{n+1/2}(i,j,k) = H_z^{n-1/2}(i,j,k) - \frac{\Delta t}{\mu}\left[\frac{E_y^n(i+1/2,j,k) - E_y^n(i-1/2,j,k)}{\Delta x(i)}\right.$$

$$\left. - \frac{E_x^n(i,j+1/2,k) - E_z^n(i,j-1/2,k)}{\Delta y(j)}\right] \tag{1.54}$$

$$E_x^{n+1}(i,j,k) = E_x^n(i,j,k) + \frac{\Delta t}{\varepsilon}\left[\frac{H_z^{n+1/2}(i,j+1/2,k) - H_z^{n+1/2}(i,j-1/2,k)}{\Delta y(j)}\right.$$

$$\left. - \frac{H_y^{n+1/2}(i,j,k+1/2) - H_y^{n+1/2}(i,j,k-1/2)}{\Delta z(k)}\right] \tag{1.55}$$

$$E_y^n(i,j,k) = E_y^n(i,j,k) + \frac{\Delta t}{\varepsilon}\left[\frac{H_x^{n+1/2}(i,j,k+1/2) - H_x^{n+1/2}(i,j,k-1/2)}{\Delta z(k)}\right.$$

$$\left. - \frac{H_z(i+1/2,j,k)^{n+1/2} - H_z(i-1/2,j,k)^{n+1/2}}{\Delta x(i)}\right] \tag{1.56}$$

$$E_z^n(i,j,k) = E_z^n(i,j,k) + \frac{\Delta t}{\varepsilon}\left[\frac{H_y^{n+1/2}(i+1/2,j,k) - H_y^{n+1/2}(i-1/2,j,k)}{\Delta x(i)}\right.$$

$$\left. - \frac{H_x^{n+1/2}(i,j+1/2,k) - H_z^{n+1/2}(i,j-1/2,k)}{\Delta y(j)}\right] \tag{1.57}$$

where $g_{11} = \Delta x(i)\cdot\Delta x(i)$, $g_{22} = \Delta y(j)\cdot\Delta y(j)$, $g_{33} = \Delta z(k)\cdot\Delta z(k)$ and $V = \Delta x(i)\Delta y(j)\Delta z(k)$ are used.
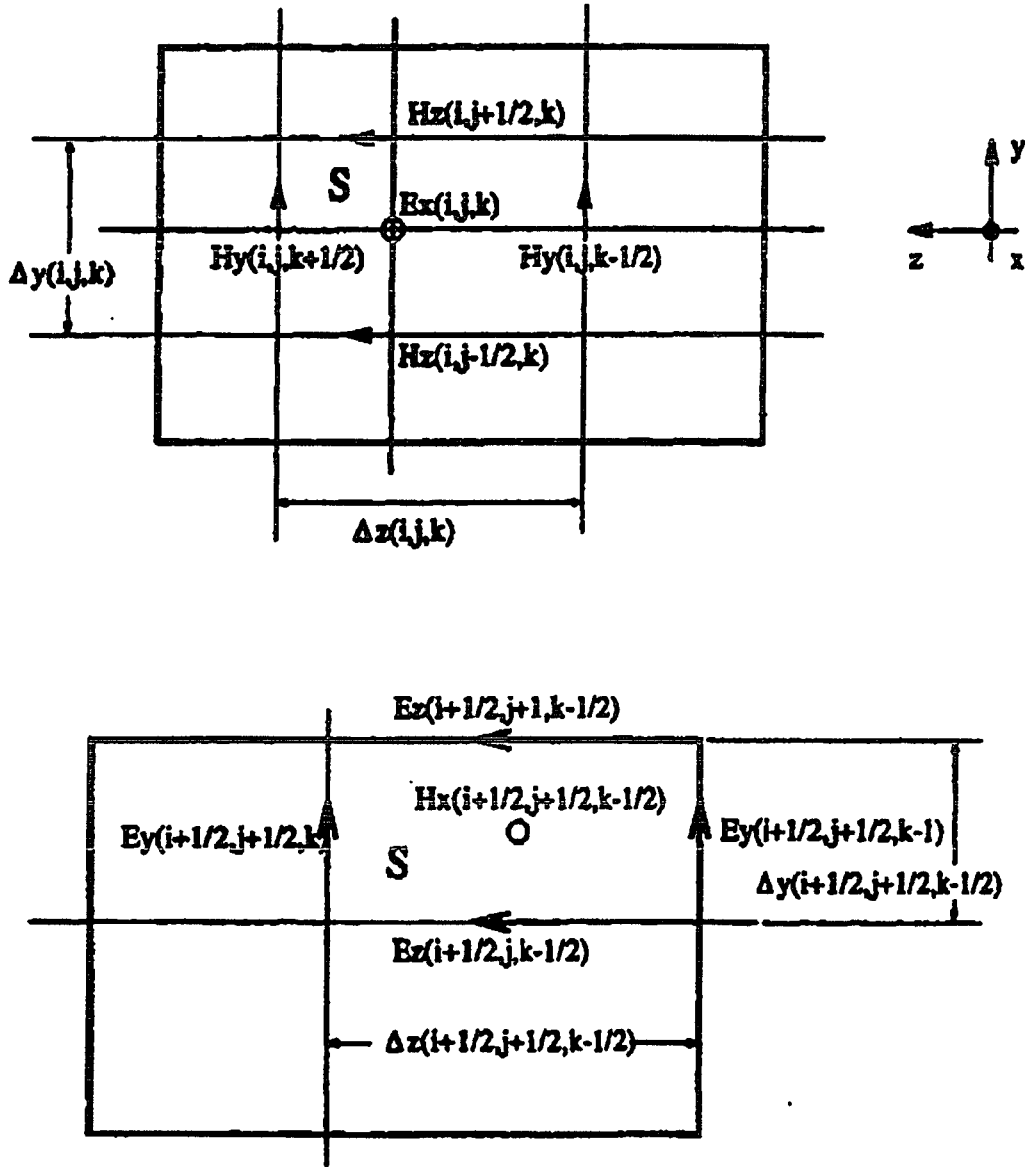
Figure 1.15 Examples of non-uniform mesh cells.

1.4 Absorbing Boundary Conditions (ABC)

1.4.1 Introduction

Since the computational domain cannot include the whole of space, the finite difference mesh must be truncated to be compatible with finite computer memories. The numerical

34

algorithm used on the truncation planes must simulate the propagation of outgoing waves. This is known as an artificial absorbing boundary condition.

The FDTD solutions of Maxwell's equations have been extensively applied to modeling open-region electromagnetic wave scattering problems. Here, a primary challenge has been the development of absorbing boundary conditions (ABCs) to effectively terminate the EM field that propagates at the outer grid boundaries. Techniques for improving the accuracy of ABCs have been suggested and a variety of existing analytical ABCs are documented. For example, Mur's ABC was introduced in [21]. Litva's dispersive ABC was used in [22] and [23] to absorb the incident wave at the designated frequencies. Berenger [24] introduced a revolutionary boundary condition called the Perfectly Matched Layer (PML) that gives remarkably low reflections. This method was validated in [25], extended to three dimensions in [26], and further extended to non-orthogonal 3-D meshes in [20], [27], [28] and [29]. In paper [30] a Modified-PML was introduced. Compared to Berenger's PML, the M-PML is more efficient in absorbing the evanescent energy and while keeping the same performance for propagating modes. The sophisticated properties of M-PML result in the reduction of the thickness of the matching layers used in PML, leading to less of a computer burden when carrying out FDTD modeling.

In this section Mur's first order ABC and Litva's dispersive ABC will be discussed briefly and then they will be used for simulating printed structures. The PML is used in waveguide structure designs. For details of PML and M-PML, please see the reference papers.

1.4.2 Mur's First Order ABC

As is well known when one considers a plane wave traveling with speed, v, it is quite easily to predict electromagnetic fields from plane #1 to plane #2 along the wave's direction of travel (for example in the x-direction) using following equation,

$$\left(\frac{\partial}{\partial x} + \frac{\partial}{v \partial t}\right)E = 0 \qquad (1.58)$$

where E represents the electric field components normal to the direction of travel (x-direction) and parallel to the plane #1 and plane #2. These two planes are separated by a distance $\Delta x \to 0$. Plane #2 can act as the outside boundary of the computational domain. To convert (1.58) into a finite difference form, one can use Mur's first order ABC [21],

$$E_M^n = E_{M-1}^{n-1} + \frac{v\Delta t - \Delta x}{v\Delta t + \Delta x}\left(E_{M-1}^n - E_M^{n-1}\right) \qquad (1.59)$$

where E_M^n = the unknown tangential **E** field on the boundary,

E_{M-1}^{n-1} = the previous known field one grid inside of the boundary,

E_M^{n-1} = the previous known field on the boundary,

E_{M-1}^n = the present known field one grid inside of the boundary,

Δt = time step,

Δx = the distance between grid #M and grid #M-1,

v   = the speed that the wave travels from grid #M-1 and grid #M.

1.4.3 Litva's Dispersive ABC

If Mur's first order ABC is used solely, it will be found that,

    1. when the wave is dispersive,

    2. when the wave hits the outside boundary with an angle,

the reflections from the boundary can be quite large because the boundary condition only acts as a good absorber at the velocity **v**. Therefore, a dispersive boundary condition which can absorb fields in a wide frequency band or wider incident angle needs to be used [22] [31].

By cascading two Mur's first order ABC together with different speeds, the following equation can be obtained,

$$\left(\frac{\partial}{\partial x} + \frac{\partial}{v_1 \partial t}\right)\left(\frac{\partial}{\partial x} + \frac{\partial}{v_2 \partial t}\right)E = 0. \qquad (1.60)$$

To rewrite equation (1.60) in finite difference form, one has Litva's Dispersive ABC,

$$E_M^n = 2E_{M-1}^{n-1} - E_{M-2}^{n-2} + (\gamma_1 + \gamma_2)\left(E_M^{n-1} - E_{M-1}^n - E_{M-1}^{n-2} + E_{M-2}^{n-1}\right)$$

$$(\gamma_1 \cdot \gamma_2)\left(E_M^{n-2} - E_{M-1}^{n-1} - E_{M-1}^{n-1} + E_{M-2}^n\right) \qquad (1.61)$$

where E_M^n = the unknown tangential **E** field on the boundary which is grid #M,

$E_M{}^{n-1}$ = the one time-step previously known field on the boundary,

$E_M{}^{n-2}$ = the two time-step previously known field on the boundary,

$E_{M-1}{}^{n}$ = the presently known field on one grid inside ($^\#$M-1) of the boundary,

$E_{M-1}{}^{n-1}$ = the one time-step previously known field on grid $^\#$M-1,

$E_{M-1}{}^{n-2}$ = the two time-step previously known field on grid $^\#$M-1,

$E_{M-2}{}^{n}$ = the presently known field on two grids inside ($^\#$M-2) of the boundary,

$E_{M-2}{}^{n-1}$ = the one time-step previously known field on grid $^\#$M-2,

$E_{M-2}{}^{n-2}$ = the two time-step previously known field on grid $^\#$M-2,

$$\gamma_i = \frac{v_i \cdot \Delta t - \Delta x}{v_i \cdot \Delta t + \Delta x}$$

Δt = time increment,

Δx = distance between grid points,

v_i = wave velocities (i = 1, 2). For a dispersive printed transmission line $v_i = \frac{c}{\sqrt{\varepsilon_{reff_i}}}$, where c is speed of light and ε_{reff_i} (i = 1, 2) are the effective dielectric constants for two separate frequencies [23]. Table 1.1 gives the results obtained for the test of Litva's ABC. To be specific, it gives the reflection coefficient (RC) for the ABC, when 50Ω microstrip lines are analyzed for different RT/duroid materials. It is noted that these materials correspond to widely varying dielectric constants and substrate thickness. It is conclusively proved that the ABC can be used for solving practical problems.

It is easily seen that the above boundary condition is fairly absorptive for any linear combination of plane waves propagating with velocity v_1 and v_2. By concatenating several absorbing boundary conditions, as given by (1.58), the number of velocities at which absorption is optimized can be increased.

37

RT/duroid	5870	5880	6006	6010	6010	6010
ϵ_r	2.33	2.20	6.15	10.5	10.5	10.8
h (mm)	0.787	1.575	0.635	0.635	1.905	0.635
dx (mm)	h/4	h/5	h/4	h/11	h/5	h/11
w (mm)	2.36	5.09	0.94	0.59	2.27	0.57
dy,dz (mm)	w/12	w/16	w/6	w/10	w/6	w/10
ϵ_{reff1} (1 Ghz)	1.97	1.88	4.42	6.98	7.04	7.15
ϵ_{reff2} (10 Ghz)	2.01	1.96	4.59	7.36	8.59	7.55
RC (dB) (5 Ghz)	−88.57	−92.82	−82.66	−57.66	−63.04	−51.46
RC (dB) (15 Ghz)	−85.78	−78.52	−74.06	−60.80	−65.80	−66.04

Table 1.1 Reflection coefficient (RC) of Litva's ABC.

1.5 Scattering Parameters

1.5.1 Introduction

For a high-frequency device the S-parameters are usually used to measure the network performance [32]. In the case of either the impedance or admittance matrices for an N-port network, the scattering matrix provides a complete description of the network as seen at its N ports. While the impedance and admittance matrices relate the total voltages and currents at the ports, the scattering matrix relates the waves incident on the ports to those reflected from the ports. The scattering parameters can be measured directly with a vector network analyzer. Once the scattering parameters of a network are known, conversion to other matrix parameters can be performed, if needed.

1.5.2 The Definition of S-parameters

Consider the N-port network shown in Figure 1.16, where $V_n^+(f)$ is the voltage wave incident on port n, and $V_n^-(f)$ is the voltage wave reflected from port n. The scattering matrix, or [S] matrix, is defined in relation to these incident and reflected voltage waves as,

$$[V^-] = [S][V^+] \tag{1.62}$$

A specific element of the [S] matrix can be determined as,

$$s_{ij}(f) = \left.\frac{v_i^-(f)}{v_j^+(f)}\right|_{v_k^+(f)=0}, \qquad (k \neq j) \tag{1.63}$$

s_{ij} is found by driving port j with an incident wave of voltage $v_j^+(f)$ and measuring the reflected wave $v_i^-(f)$ coming out from port i. The incident waves on all ports except the jth port are set to zero, which means that all ports should be terminated in matched loads to avoid reflections. Thus s_{ii} is the reflection coefficient seen looking into port i when all other ports are terminated in matched loads, and s_{ij} is the transmission coefficient from port j to port i, when all other ports are terminated by matched loads.
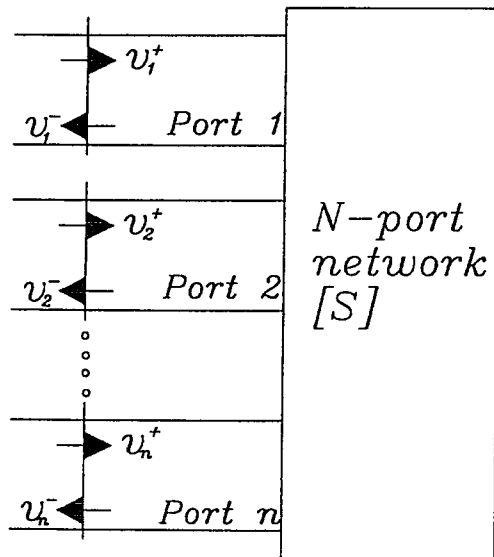
Figure 1.16 An N-port network.

1.5.3 N-Port Network with Different Characteristic Impedance

To demonstrate the case of a two-port network, which has different characteristic impedances (Z_{oi} and Z_{oj}) at each port, consider Figure 1.17 [33]. This example shows a microstrip line-fed patch antenna with coax-to-microstrip transition. In this case the frequency dependent generalized scattering matrix should be used, which is defined as,

$$s_{ij}(f) = \left[\frac{v_i^-(f)\sqrt{Z_{oj}(f)}}{v_j^+(f)\sqrt{Z_{oi}(f)}} \right]_{v_{others}^+(f)=0} \quad , \quad i, j = 1 \text{ or } 2. \tag{1.64}$$

Port 1 represents the input to the coaxial line at reference plane 1, and port 2 is the output taken on microstrip line at reference plane 2. Z_{oi} is the characteristic impedance of transmission line that is connected to the ith port. $v_i^+(f)$ and $v_i^-(f)$ are the incident and reflected voltage waves at the ith port, which are given from the Fourier transform of the voltages $v_i^+(t)$ and $v_i^-(t)$ in time domain,

$$v_i^\pm(f) = F\{v_i^\pm(t)\} \tag{1.65}$$

where $v_i^\pm(t)$ can be obtained from FDTD simulations. The coax-to-microstrip transition can be modeled by an equivalent circuit. In the circuit the transition is represented by a reciprocal two-port network (see Figure 1.17(b)). Reference plane 1 is located in the coaxial line, where the characteristic impedance is Z_{oc}, and Γ_{in} is the reflection coefficient looking into the antenna from plane 1. Once Γ_{in} and [S] of the transition are given, the reflection coefficient Γ_1, which is defined somewhere on the microstrip line, can be written as,

$$\Gamma_l = \left(s_{22} + \frac{s_{12}s_{21}}{\Gamma_{in} - s_{11}} \right)^{-1} . \tag{1.66}$$

Simple transmission line theory can then be used if the reference planes need to be shifted along the transmission lines.

The example shown in Figure 1.17(a) consists of two parts. One is a simple patch antenna, which has been studied extensively. The other is a coax-to-microstrip transition. The

first time full-wave studies of this transition over a wide frequency band were published in [33]. In practice, the transition is widely used in various printed antenna structures, as well as printed circuits. The de-embedding of the effects of the transition is very important for carrying out accurate practical designs. In the numerical FDTD analysis to follow, reference plane 1 is located at a distance of $19\Delta x$ from the ground plane, and plane 2 is located at a distance of $84\Delta z$ from the connector, where $\Delta x = 1.272\Delta h$, $\Delta z = \Delta y = \Delta h = 0.315$ mm. In this example, the characteristic impedance of the microstrip line is 63Ω at 6GHz. The first order absorbing boundary condition is applied at a distance of $64\Delta h$ away from the patch. The numerical coaxial line length is 100 Δx, and the Gaussian pulse is applied at the second grid with respect to the bottom of the coaxial line. The 5% pulse width of the pulse corresponds to 15 space steps with the pulse maximum at $100\Delta t$.

The transition from a coaxial line to a microstrip line can be described by using S-parameters. Due to the existence of surface and radiation waves, the network can be considered to be lossy, as well as being reciprocal. The S-parameters for this example, which are calculated by using the FDTD method, are shown in Figure 1.18. It can be clearly seen that at low frequencies there is efficient transmission electromagnetic energy between the coaxial line and the microstrip line. However, at higher frequencies the transmission characteristics degenerate due to the higher order modes at the discontinuity and radiation loss in the microstrip line. It is interesting to note that in this example the energy is seriously blocked at a frequency of around 18 GHz. This blockage is caused mainly by the open-end stub, which shorts the circuit at a length of about one-quarter of the waveguide wavelength.

The reflection coefficient Γ_{in} of the entire antenna is measured at the reference plane 1, which is located on the coaxial line. Figure 1.19 shows the magnitude and phase of Γ_{in} from 3 to 9 GHz (group 1). The measured results are in very good agreement with the FDTD calculated results. The reflection coefficient tells us that the antenna is resonant at frequency of 5.53GHz. By using the TRL calibration procedure, the reflection coefficient Γ_1 of the patch antenna defined at reference plane 2 is measured and is shown by the dashed line in group 2. With the help of Eq.(1.66), the numerical value for Γ_1 is obtained by converting Γ_{in}, which is calculated by the FDTD method (see solid line of group 1 in Figure 1.19), from reference plane 1 to reference plane 2, using the previously calculated S-parameters. It follows from the close agreement that the S-parameters of the transition obtained from the FDTD method are correct.
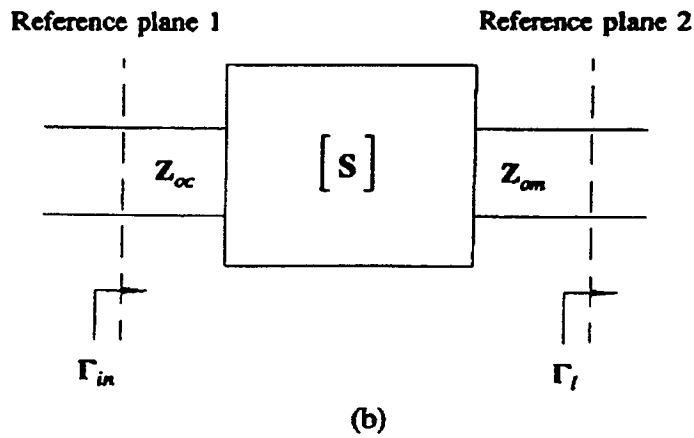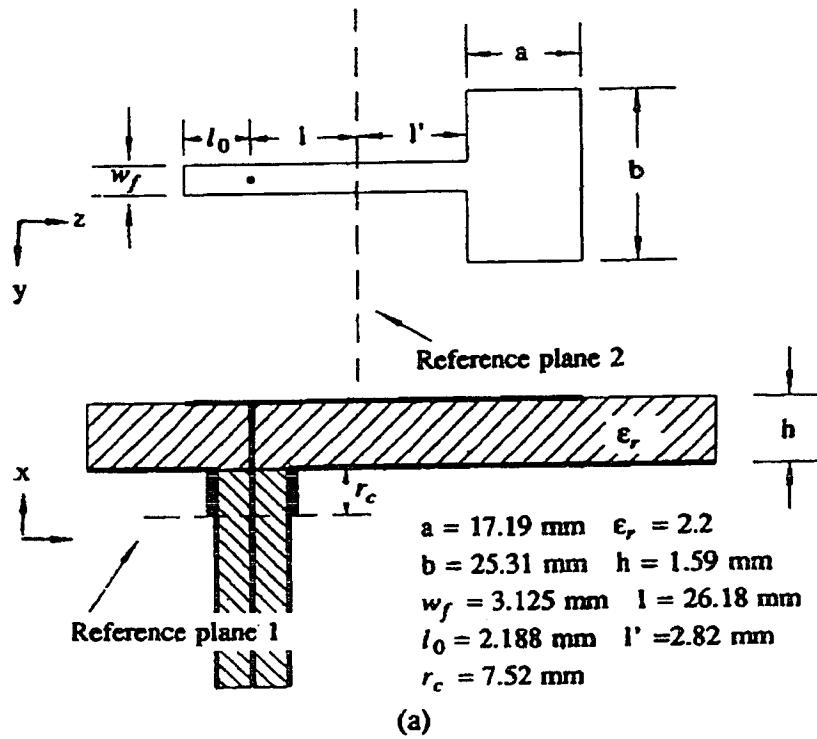
Figure 1.17 (a) Microstrip line fed patch antenna with coax-to-microstrip transition and (b) the equivalent two-port network of the coax-to-microstrip transition.
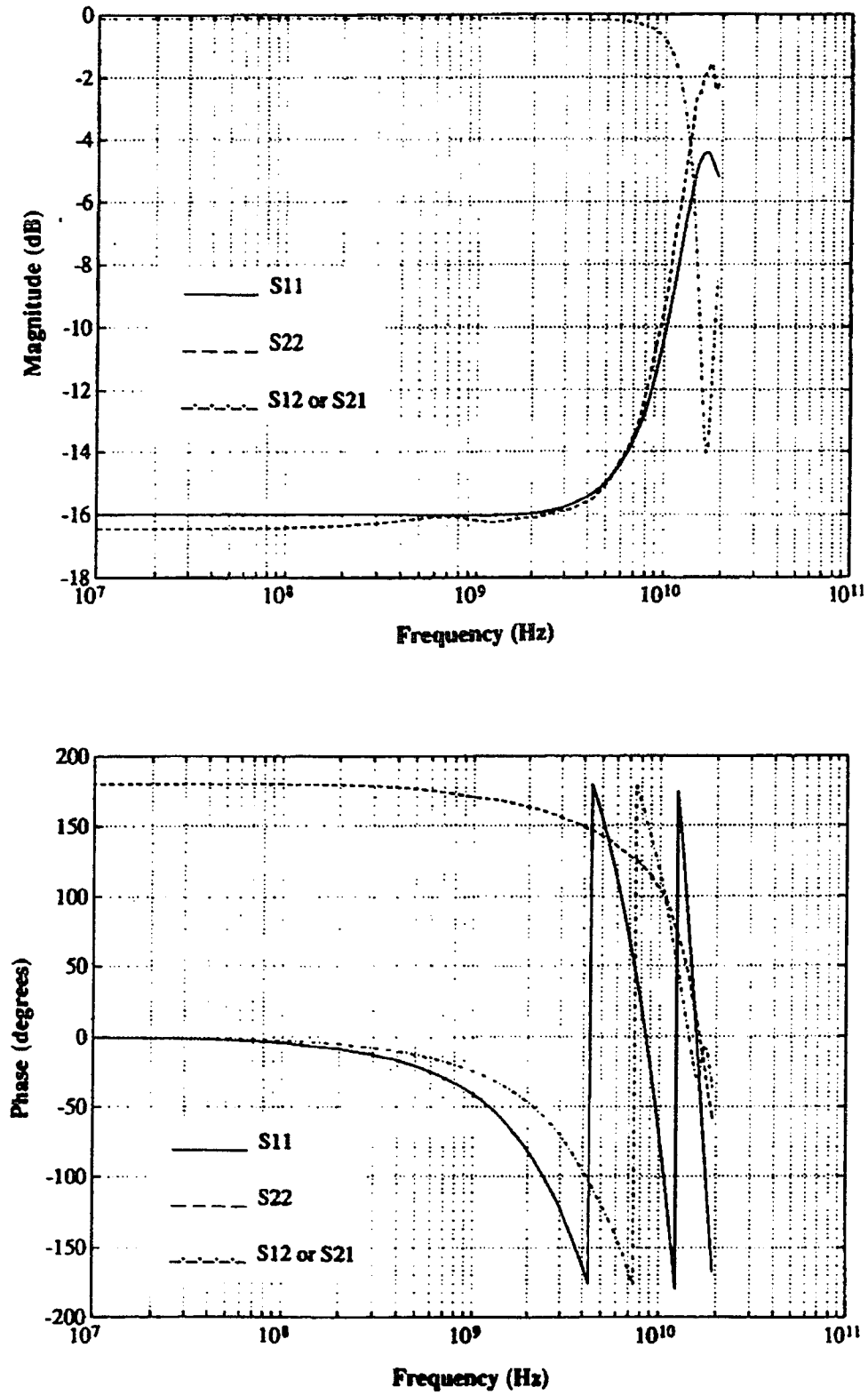
Figure 1.18 The S-parameters for the coax-to-microstrip transition
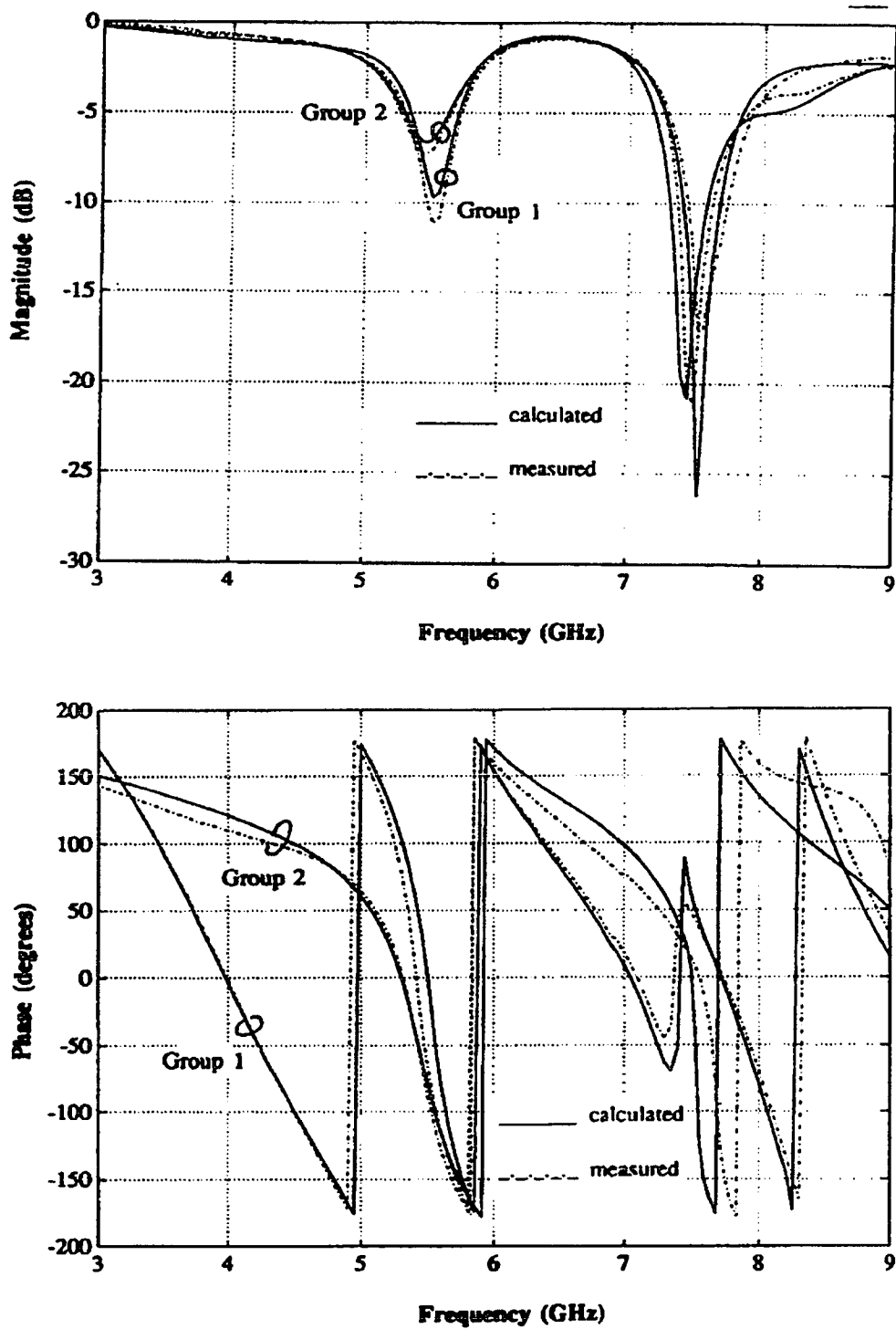
Figure 1.19 The reflection coefficients of the patch antenna with coax-to-microstrip transition. Group 1 and Group 2 are defined at reference planes 1 and 2, respectively.

1.6 The 3D FDTD Structure Simulator

1.6.1 Introduction

Based on the previous discussion it is very clear that the non-uniform FDTD algorithm with orthogonal grids represents an attractive approach for antenna and microwave device simulations and design. Since the grid size can be gradually changed between adjacent grids, the algorithm offers great flexibility for modeling the fine features of a complex structure. Compared with regular FDTD algorithm the orthogonal non-uniform FDTD method requires less computer memory and modeling time while providing good simulation results [34]. Compared with the non-orthogonal FDTD algorithm the orthogonal non-uniform FDTD method requires six field components, while the non-orthogonal FDTD algorithm needs twelve field components. Staircasing must be used with the orthogonal non-uniform FDTD method if it is used to simulate shaped edges. The decision of which method should be adopted when carrying out simulations is case dependent.

An orthogonal non-uniform FDTD-based design program termed the FDTD 3D Structure Simulator (FDTD 3D SS) has been developed. In this thesis all the antenna designs are performed by using this simulator. Without it, this research would have taken a much longer time.

1.6.2 The Simulator

The FDTD 3D Structure Simulator (FDTD 3D SS) has a PC based user interface. Figure 1.20 shows the main screen of the interface. Because the FDTD 3D SS uses the orthogonal non-uniform FDTD algorithm, the rectangular blocks are used to input the structure under simulation. For each block the user has to define dielectric constant or set the parameter to zero in the case of a metal object. The simulator requires 'staircase' patterns to describe structures whose edges are not parallel to the x, y, and z-axes. There is an automatic mesh generator that defines the grid once the user has defined the maximum adjacent grid ratio R_{max}. The default condition is equal to 1:4, which is the maximum allowed for this ratio. It then places m grids on the smallest gap between edges in the structure. The m parameter is under user control, as well. Its default value is 2. It is important that the user should pay attention to the smallest discontinuity in the structure under test. This determines the spacing between grid

45

points, which in turn determines the total number of computational nodes needed to model the structure. If the space increment Δh is chosen to be too small, this can lead to an excessively large CPU time and memory when simulating a complete structure.
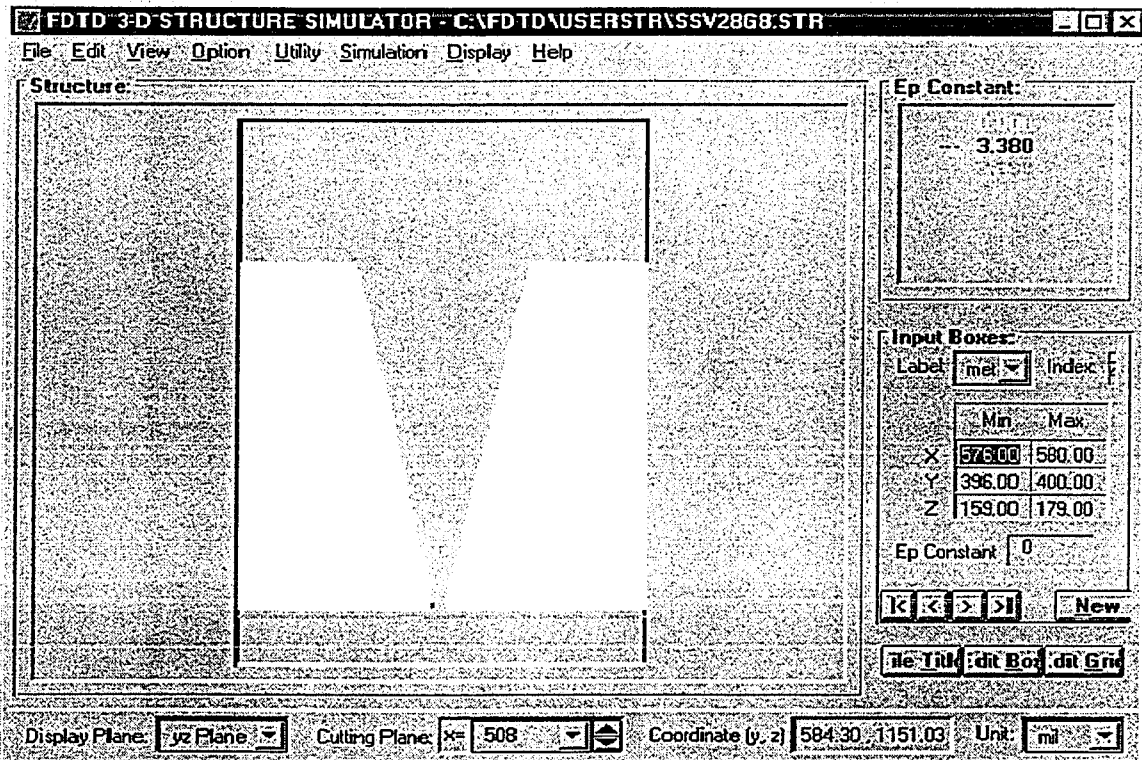
Figure 1.20 The interface of the FDTD 3D Structure Simulator

1.6.3 Using the Simulator to Model Some Antennas

Figure 1.21 shows a CPW antenna, which is configured without an adjacent ground plane. The antenna is fed by a 50Ω coaxial cable. Previous workers [35] have shown that a conventional coaxial cable with an SMA connector can be replaced by a square coaxial line, which has the same dielectric material, a similar size, and the same characteristic impedance. The reason for using a square coaxial line in the simulation is that it easily fits into the structure of a non-uniform FDTD grid. Further studies have also shown that square coaxial lines with different dielectric materials than those used in the cylindrical coaxial cable can be used to feed a PCS antenna in a simulation as long as the characteristic impedance of the square coaxial line equals that of the coaxial cable. The physical dimensions of a square coaxial line can be determined by [36],

$$Z_o = \frac{120\pi}{4\sqrt{\varepsilon_{rc}}} \left[\frac{1}{\dfrac{d}{D-d} + \dfrac{2}{\pi} \ln\left(\dfrac{D}{D-d} + \cosh\left(\dfrac{\pi}{2}\right) \right)} \right] \tag{1.67}$$

where:

d = dimension of inner conductor,

D = dimension of outer conductor,

ε_{rc} = the relative dielectric constant of the dielectric material.

In the CPW-antenna simulation example [37], the square coaxial line described by [35] is used. The return losses of the CPW antenna are given in Figure 1.22 for various computational-domain sizes and corresponding maximum adjacent-grid ratios for the non-uniform FDTD scheme. These results were compared to measurements obtained with a network analyzer. The total Central-Processing-Unit (CPU) time, given in Table 1.2, was obtained for each set of results based on an Alphaserver 1000 4/266 workstation from the Digital Equipment Corp.

From these results, it can be observed that the first resonant frequency of the antenna occurs at 2.25 GHz. It is evident that the choice of a maximum adjacent-grid-ratio, $R_{max} = 1:4$,

for the non-uniform FDTD grid, provides good results, while at the same time providing rapid convergence in the time domain. Therefore, a large adjacent-grid-ratio can be used initially in antenna design problems. Once the simulation approaches the design requirements, a finer mesh can be employed to complete the design.

X_{max} total grid in x-direction	196	159	134
y_{max} total grid in y-direction	210	157	123
Z_{max} total grid in z-direction	131	106	85
R_{max}	1 : 1.2	1 : 2	1 :4
CPU time (second)	18,500	9,000	4,725

Table 1.2 CPW-antenna simulation times
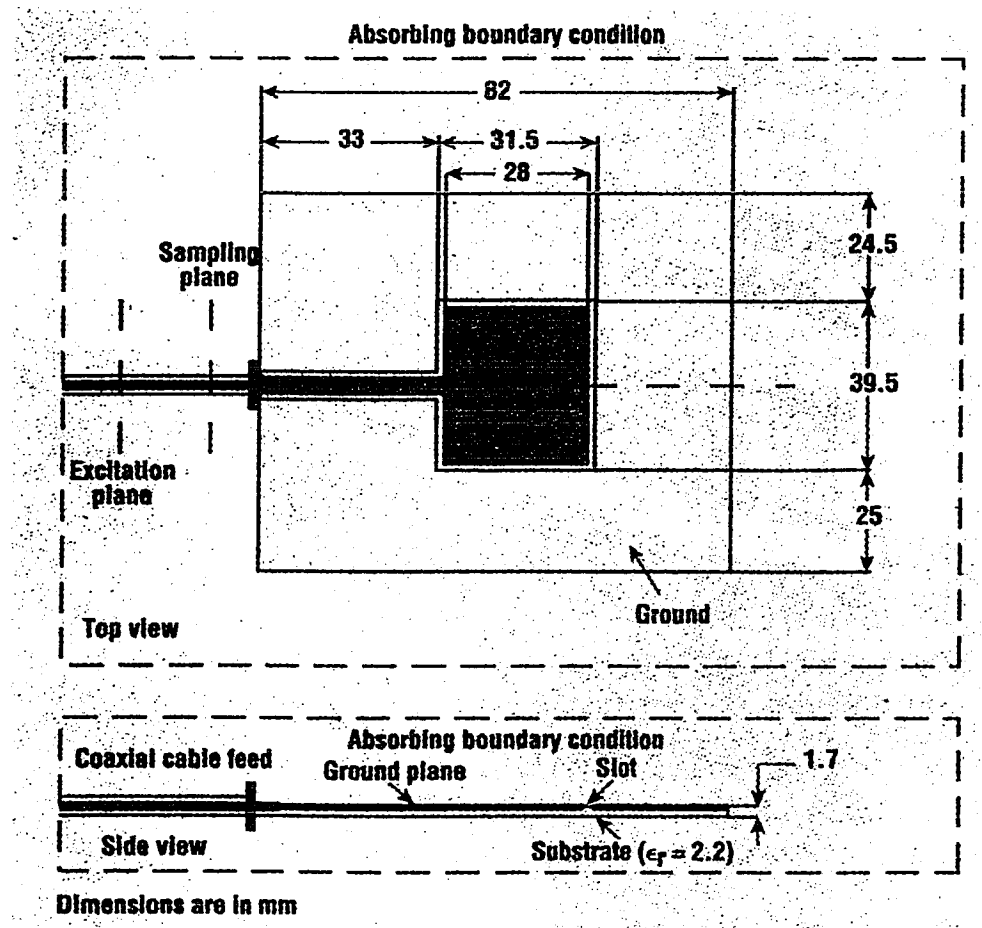
Figure 1.21 A CPW antenna fed by a coaxial cable.
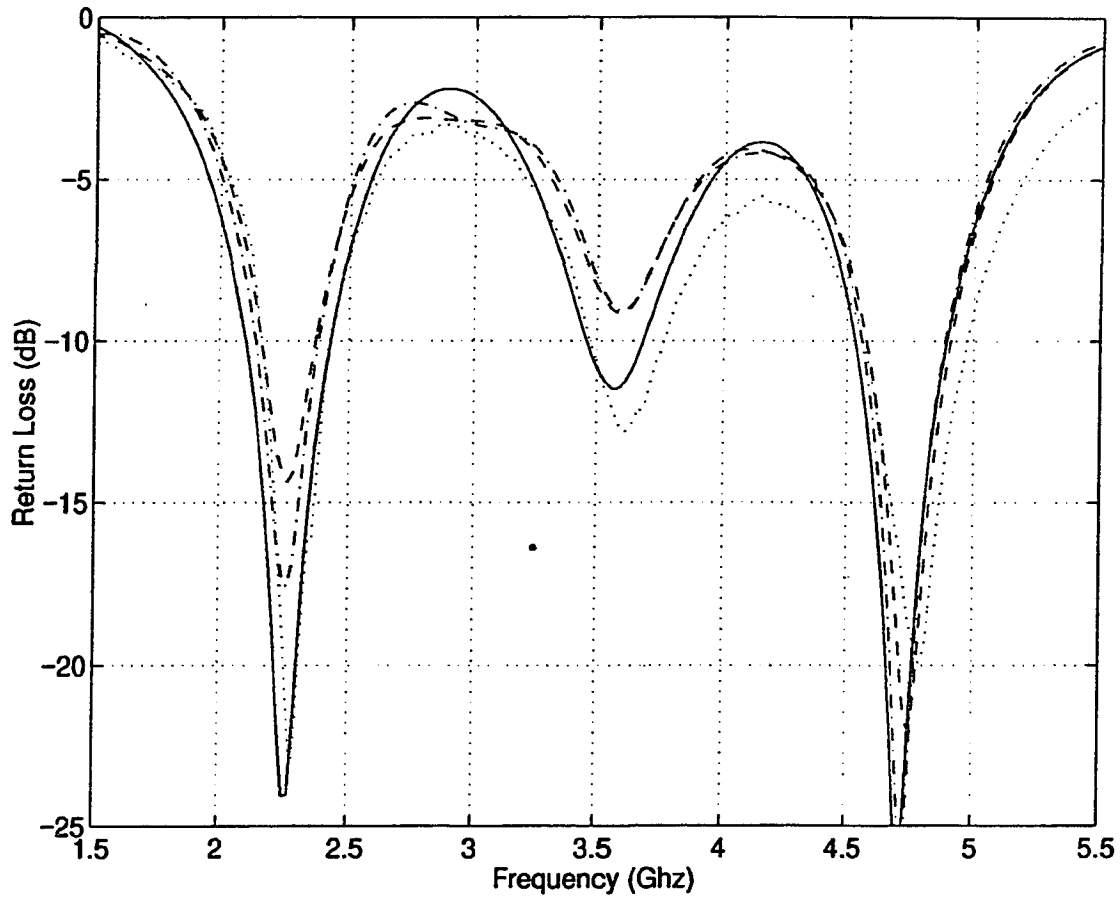
Figure 1.22 Comparison of simulated return loss for a CPW antenna. The simulations were carried out for three different values of R_{max}.

Solid line: $R_{max} = 1:1.2$;
Dot-dashed line: $R_{max} = 1:2$;
Dashed line: $R_{max} = 1:4$;
Dotted line: measured result.

The aperture-coupled patch antenna shown in Figure 1.23 provides the next example of FDTD modeling. The simulation is carried out with a R_{max} value of 1:2. The design parameters used for the square coaxial line are $\varepsilon_{rc} = 1.0$ and $D/d = 2.07$. The simulation is carried out with a value of $d = 3.72$ mm. From Figure 1.24, it follows that there is a good agreement between the values of return loss obtained by measurement and calculation. In Figure 1.25 shows the E-plane and H-plane radiation patterns for the aperture-coupled patch antenna at 2.2GHz. The

calculated patterns are obtained by determining equivalent electric and magnetic virtual currents [2].

From these examples it can be seem that the result from the FDTD 3D SS simulations agree very closely with measurements. It follows that this simulator can be used to greatly speed up the design of microwave and millimeter antennas and devices, thereby increasing the efficiency and effectiveness of the design procedure.
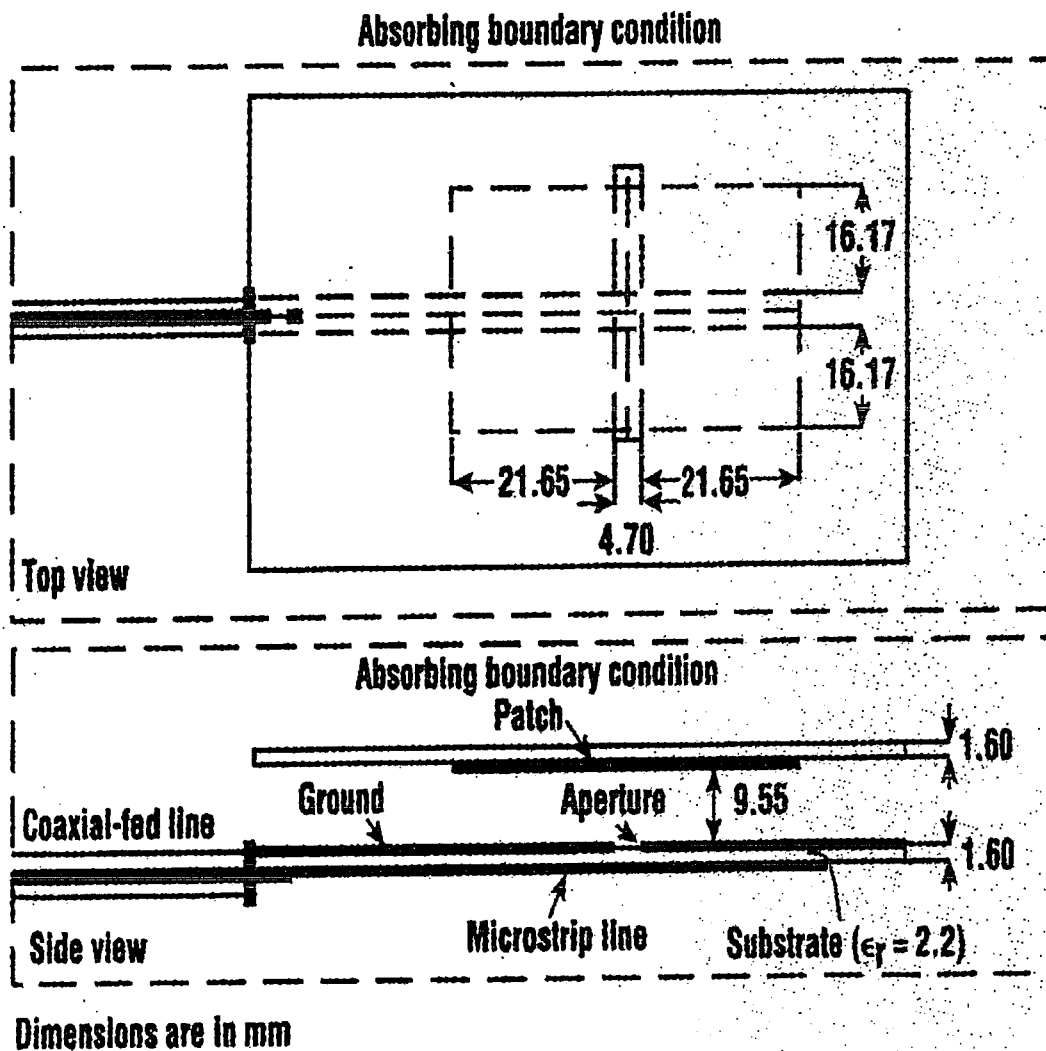
Figure 1.23 An aperture-coupled patch antenna was used to validate the accuracy of the FDTD 3D Structure Simulator.
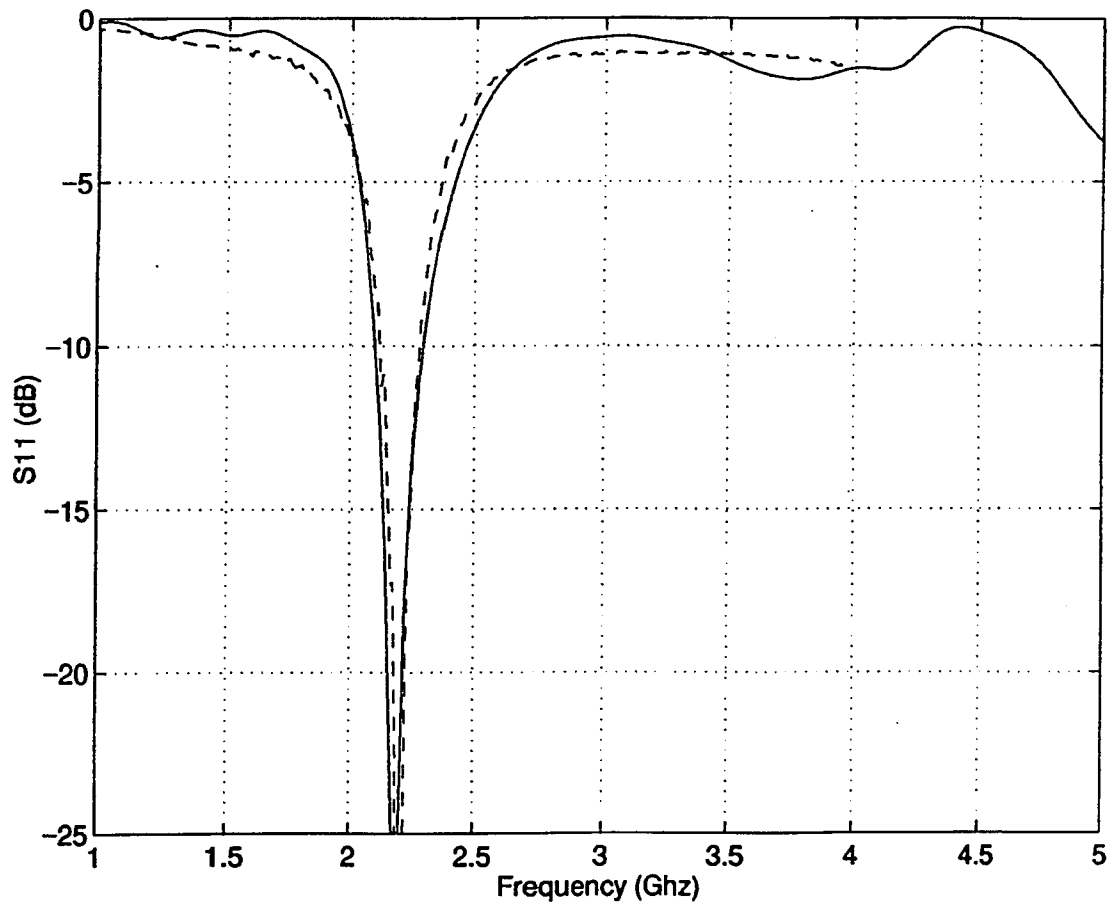
Figure 1.24 Good agreement between simulated and measured return loss of the aperture-coupled patch antenna.

Solid line: calculated result;
Dashed line: measured result.
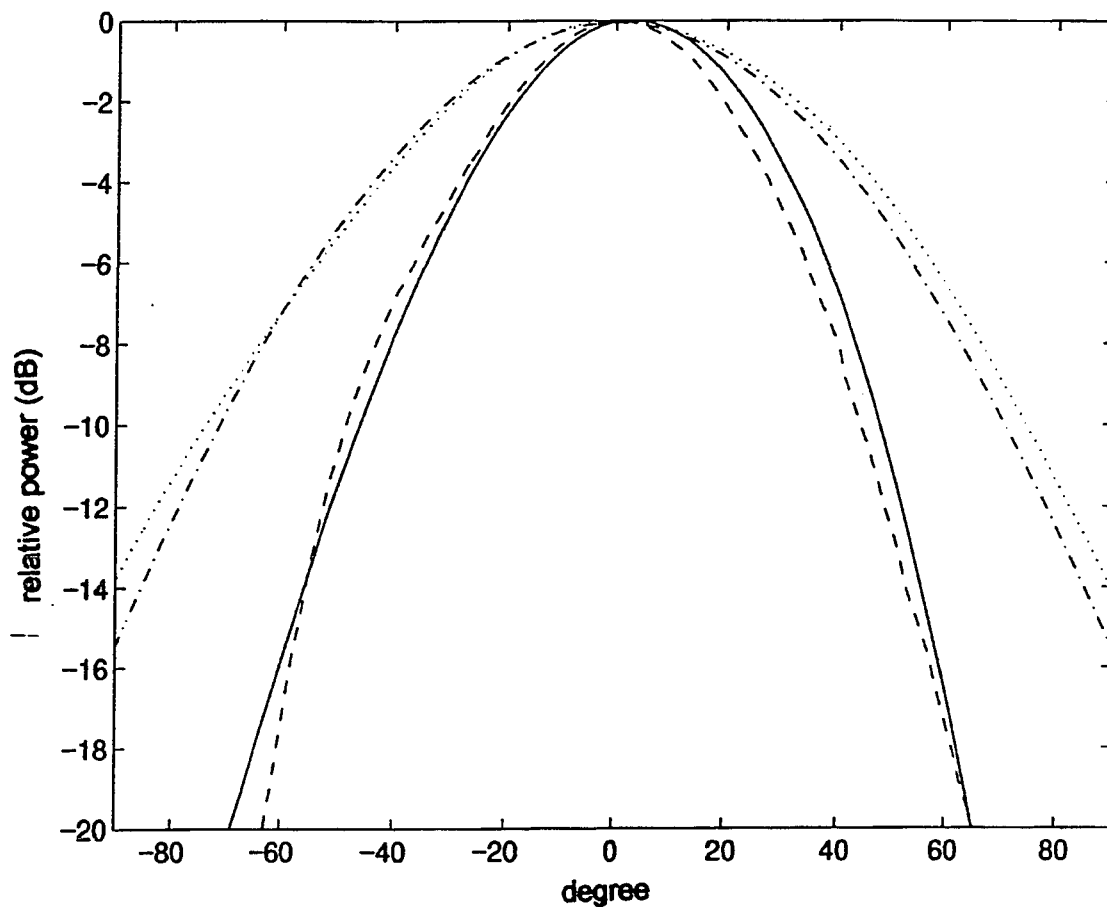
Figure 1.25 Comparison of computed and measured E- and H-plane radiation patterns for an aperture-coupled patch antenna.

Solid line: calculated E-plane pattern;
Dashed line: measured E-plane pattern;
Dot-dashed line: calculated H-plane pattern;
Dotted lined: measured H-plane pattern.

Chapter 2 . The Linear Tapered Slot Antenna Fed by Suspended Microstrip and Inverted Microstrip Lines

2.1 Introduction

The popularity of planar integrated antennas on dielectric substrates has steadily increased over the past two decades, or so, in the fields of microwaves and millimeter waves. To a considerable degree, this interest is tied to the potential being exhibited by fully monolithic circuits, as well as barrier diodes and field effect transistors (FET's) for transmitter applications. Many implementations currently visualized involve broadside-radiating elements such as printed dipoles, microstrip patches, slots, etc. These elements have a number of advantages, such as low cost, low weight, low profile, conformability with existing structures, and ease of fabrication and integration with active devices. On the other hand they usually have relative low gain and narrow bandwidth, because they are resonant structures in nature. Until the introduction of the 'Vivaldi' antenna by Gibson in 1979 [38], there was not a well known planar antenna element which could produce a symmetric endfire beam, with appreciable gain and low sidelobes. The Vivaldi antenna consists of a metalized dielectric substrate with an exponentially tapered slot cut in the metalization. The metalization can be on a single side or on both sides of substrate as shown in Figure 2.1. Since the work of Gibson a number of different printed tapered slot antennas have been developed and investigated by many researchers [39] [40] [41]. These antennas have the same characteristics as the Vivaldi antenna.

The antennas shown in Figure 2.2 belong to the general class of endfire traveling-wave antennas, and have moderately high (10-17dBi) directivity gain for a given cross section by virtue of their traveling wave nature. The manner in which tapered slot antennas achieve such

performance is very similar to that of a dielectric rod antenna fed by a waveguide [42]. Despite their planar geometry, it is the beauty of tapered slot antennas that they can produce a symmetric beam (in E- and H-planes), often over a wide band of frequencies under some necessary conditions, such as shape, total length, substrate thickness and dielectric constant.
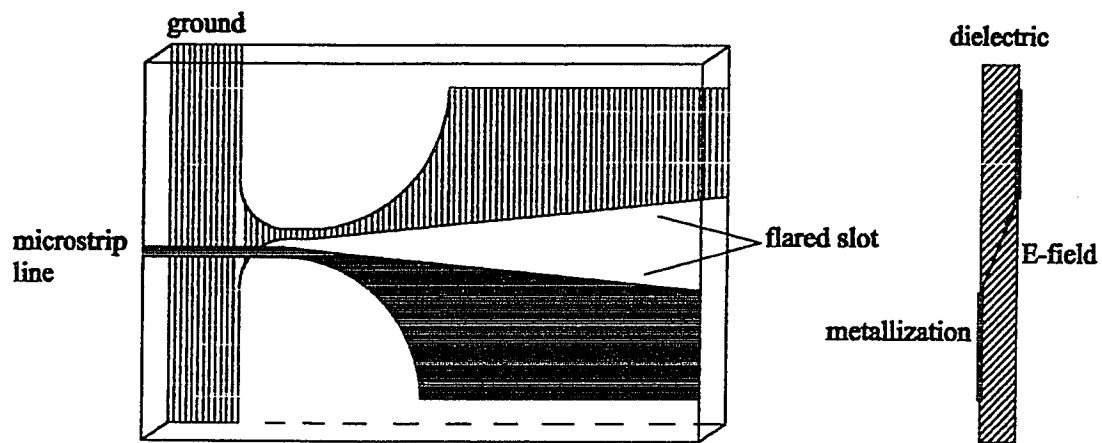
Figure 2.1 The Vivaldi antenna.
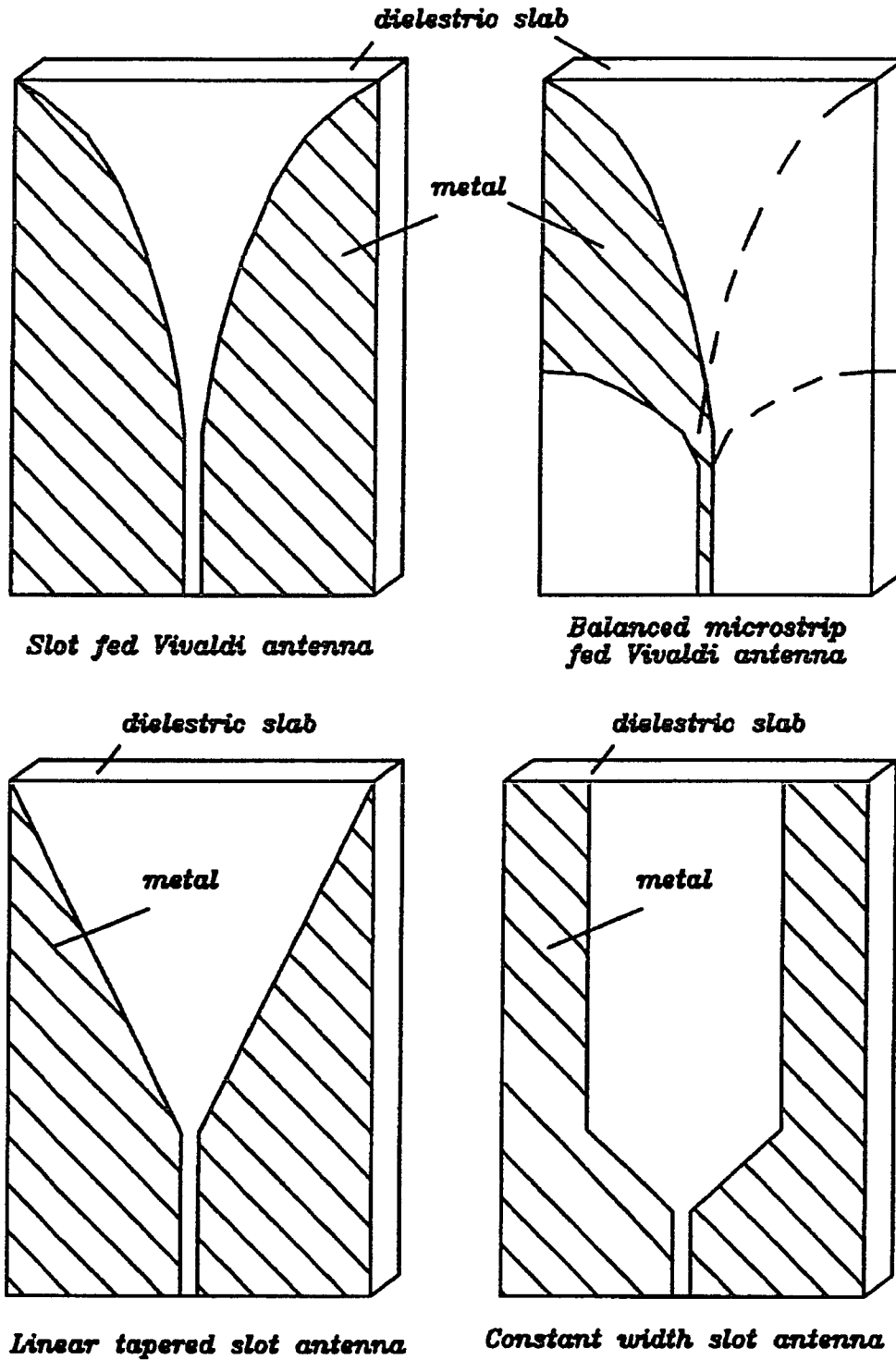
Figure 2.2 Different types of endfire tapered slot antenna.

2.2 A Review of Traveling Wave Antenna Properties

There are two main classes of traveling-wave antennas, traditionally called 'leaky-wave antennas,' and 'surface-wave antennas.' The first type typically utilizes a traveling wave that propagates along some antenna structure with a phase velocity $v_{ph} > c$, where c is the speed of light. Since the phase velocity is greater than c, it follows that the main beam occurs in a direction other than endfire. The second class consists of those that satisfy the condition $v_{ph} < c$. They can consist of a dielectric on a ground plane, or a periodic structure. These antennas, as well as those for the limiting condition $v_{ph} = c$, can produce endfire radiation.

Traveling-wave antennas are treated in many well known references, such as [43], but the review by Zucker in Jasik's *Antenna Engineering Handbook* [44] is the most useful for the purposes of this research. For an endfire traveling-wave antenna with a constant phase velocity, there is an optimum velocity ratio c/v_{ph}, which results in maximum directivity as shown by Hansen-Woodyard for very long antennas, and Ehrenspeck-Poehler for an antenna of arbitrary length [44]. Typical values for directivity are given by $D \approx 10 \cdot L/\lambda_0$, where the length (L) of the antenna is typically in the range $3\lambda_0$ to $8\lambda_0$ and $c/v_{ph} = 1.05$. For longer antennas, the coefficient multiplying L/λ_0 decreases somewhat. But the approximate linear dependence of D on L/λ_0 is an important characteristic of all endfire traveling-wave antennas. Zucker [44] has plotted the optimum gain and beamwidth for such antennas, as well as typical values for low sidelobe and broadband designs. In [40] after comparing 'standard data' given by Zucker [44] and measured data from a number of tapered slot antennas (TSA) the author arrived at the following conclusions,

1. Whether tapered slot antennas behave as optimized traveling-wave antennas or not, most of the antennas have a slot which is tapered. As a consequence, the phase velocity is not constant along the antenna and the propagation constant is complex due to radiation losses. The situation is similar to that of tapered rod antennas [42], classified by Zucker in Table 2.1, as low sidelobe and broadband traveling wave antennas.

2. The performance of a TSA, with constant angle and substrate thickness, as a function its length or frequency, may not be optimum. Nevertheless, practical TSA's often stay close to their optimum performance over a wide range of normalized lengths.

	Optimum (Max.	Low sidelobes

	gain)	(Broad bandwidth)
Directivity (dB)	$10\log\left(10\dfrac{L}{\lambda_o}\right)$	$10\log\left(4\dfrac{L}{\lambda_o}\right)$
Beamwidth (degree)	$55/\sqrt{\dfrac{L}{\lambda_o}}$	$77/\sqrt{\dfrac{L}{\lambda_o}}$
Optimum velocity ratio	$1+\dfrac{1}{2\dfrac{L}{\lambda_o}}$	

Table 2.1 Typical properties of endfire traveling-wave antennas [44].

2.3 The Linear Tapered Slot Antennas Fed by Different Printed Transmission Lines

2.3.1 Introduction

In this section we will focus on the Linear Tapered Slot Antenna (LTSA) and develop some new feed structures so that the antenna can operate in the millimeter and sub-millimeter wave bands.

The LTSA has been developed for potential millimeter wave applications. Up to now, in most applications of this antenna structure, workers have used it as the radiating elements for reflector or lens antennas [45] [46] [47], because it can produce high gain and symmetric radiation patterns in E- and H-planes. A number of feed structures have been developed to feed TSA's. The waveguide-to-finline [39] transition was the early feeding technique. As printed antennas and microwave integrated circuits became popular, the microstrip-to-slot transition was used to feed TSA's [46] [48] (see Figure 2.3). It is one of the simpler structures that can be used to feed the LTSA. By carefully choosing the length of the microstrip stub and the shape of the opening in the microstrip ground plane at the end of the LTSA, this transition can provide very good return loss over more than a 30% frequency bandwidth.

The coplanar waveguide (CPW) has emerged as an alternative to the microstrip line because of its many advantages [49]. In Lee and Simons [47] four excitation techniques was introduced: three for exciting planar LTSA's with CPW and one for exciting non-planar LTSA's with a balanced microstrip feed.

The first excitation technique described in Lee and Simons [47] is the planar LTSA which is excited by a finite coplanar waveguide (FCPW) [50]. The LTSA and the FCPW are etched on opposite sides of the substrate with the finite ground plane of the CPW tapered and connected to the antenna ground plane through via holes, which ensure a good impedance match and an odd mode operation. Power is coupled to the antenna through the center conductor of the CPW, which is extended to form a CPW-to-slot line transition with the LTSA. To provide a smooth transition, the slot line at the feeding end has a circular bend instead of a right angle bend. The measured results show that the return loss of this antenna is lower than −10dB (2:1 VSWR) from 10 to 28GHz.

The second excitation technique described in Lee and Simons [47] illustrates another feeding approach with the FCPW placed at a right angle to the slot line which connects the LTSA. To improve coupling, two notches, which are located above the slot line of the LTSA, are cut out from the FCPW ground plane. A pair of bonding wires are attached to both sides of the notch to suppress any spurious slot line modes generated at the discontinuity. The FCPW and the slot line are terminated in short circuits. The measured results show that the return loss of this antenna is lower than −10dB (2:1 VSWR) from 17.7 to 23.5GHz.

The third excitation technique given in Lee and Simons [47] is used to excite a planar LTSA by an air bridge. Power is coupled to the antenna through a 0.2mil wide gold ribbon that bridges over the slot line connecting the open end of the CPW. Here the LTSA is the same as the one shown in Figure 2.3. The measured return loss of this antenna is lower than −10dB (2:1 VSWR) from 16.7 to 20.2GHz.

One disadvantage of using a slot line to feed an LTSA is that it is difficult to fabricate when matching to a 50 Ohms input, especially if the substrate is of low ε_r. If the slot line is replaced by a balanced microstrip line, it is relatively easy to realize wideband impedance matching. Figure 2.4 shows the non-planar LTSA being excited by a microstrip-to-balanced microstrip transition [47]. The non-planar LTSA is formed by gradually flaring the strip conductors of the balanced microstrip on opposite side of the substrate by an angle. The feed

structure consists of a conventional microstrip on a dielectric substrate with the ground plane tapered to the strip width to form a balanced microstrip. The characteristic impedance of the balanced microstrip is chosen to be the same as the input impedance of the LTSA. The electric field distributions at various cross sections are shown in Figure 2.5. The measured return loss for the non-planar LTSA is better than −10dB over a frequency range extending from 8 to 32GHz.

In [51] the uniplanar microstrip-to-coplanar strip (CPS) line transition was introduced by Simons et al. First, the transition is uniplanar which simplifies series as well as shunt mounting of components. Second, since the feed is inline with the V-LTSA it is very compact and can be enclosed inside a small package. Third, the microstrip input simplifies integration of the V-LTSA with a MMIC microstrip oscillator chip or a mixer chip to form a compact transmitter or a receiver circuit. One advantage of the V-LTSA is that the antenna has finite conductor widths, which suppress surface wave modes and parallel plate modes between conductors. Additionally, adjacent elements in an array are DC isolated which facilitates biasing of semiconductor devices in an active array antenna. The measured return loss of the proof-of-concept antenna in [51] is better than −10dB from 5 to 15 GHz. Although the microstrip-to-CPS transition has a lot of advantages, it unfortunately has one disadvantage that makes it difficult to use in phased array applications. It is difficult to fit it into the available real estate in a phased array, when the element spacing is tight.

All the antennas with special designed feed transitions discussed in this section have a common advantage that the transitions can provide good antenna return loss performance for the antenna across a very wide frequency band. The microstrip-to-slot transition is the simplest feed technique, but the microstrip line usually has very high loss in the millimeter wave band. Typically a well-designed 50Ω feed line on a 5mil substrate will have an attenuation coefficient [52] (AC),

$$AC = \begin{cases} 0.12dB/\lambda_0 \rightarrow Duroid \\ 0.14dB/\lambda_0 \rightarrow quartz \\ 0.28dB/\lambda_0 \rightarrow alu\min a \end{cases} . \qquad (2.1)$$

So the microstrip line beam forming network (BFN) is not suitable for large millimeter-wave phased array applications. In general the CPW-to-slot transition has a wider input impedance bandwidth than the microstrip-to-slot transition, but it usually involves the use of via holes or

air bridges. So these transitions are also not appropriate for large antenna array applications. Although the microstrip-to-balanced microstrip transition gives the antenna a very wide input impedance bandwidth, the LTSA antenna usually has large cross-polarized component simply because the metalization used by the LTSA is located on different sides of the substrate. In Figure 2.6 a strip line-to-triple parallel strips transition is presented. The antenna retains the wide bandwidth characteristics while reducing the cross-polarization by 15dB across an 18:1 band, but an extra layer of substrate is required. This approach can double the cost of the antenna when compared to a microstrip-to-balanced microstrip fed LTSA.

In order to keep the simplicity of the microstrip-to-slot transition and to reduce the FBN loss in a large phased array, we will develop the suspended microstrip line (SML) and inverted microstrip line (IML) to slot transitions. Five-piece and three-piece assembled LTSA elements will be introduced in this section. Finally an SML-to-'Hockey stick' shaped slot transition will be presented and used to feed the non-dielectric slab LTSA. This novel transition is a very good feed structure to feed the LTSA element in a large flat panel antenna (FPA).
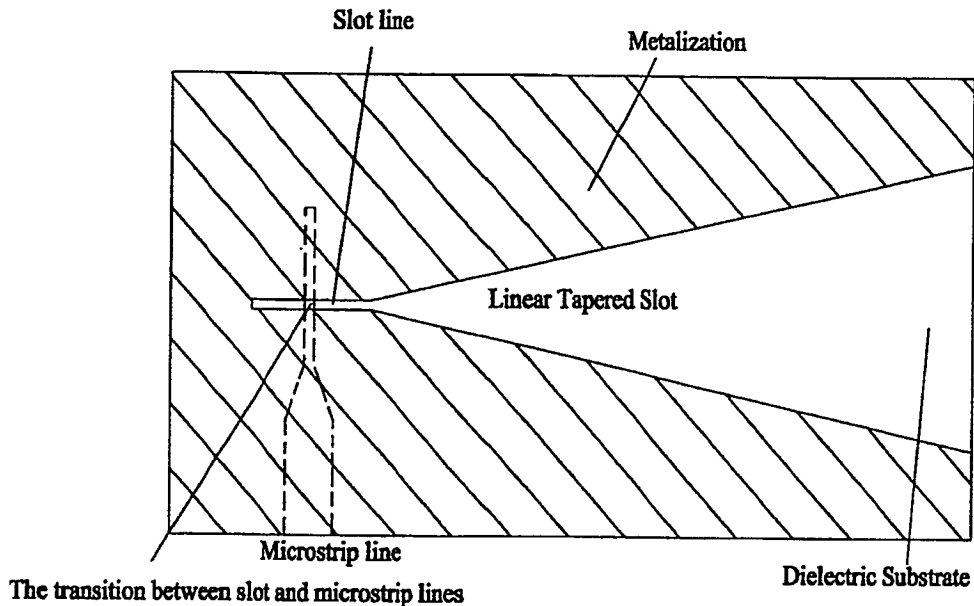
Figure 2.3 Schematic for the LTSA and microstrip line feed.
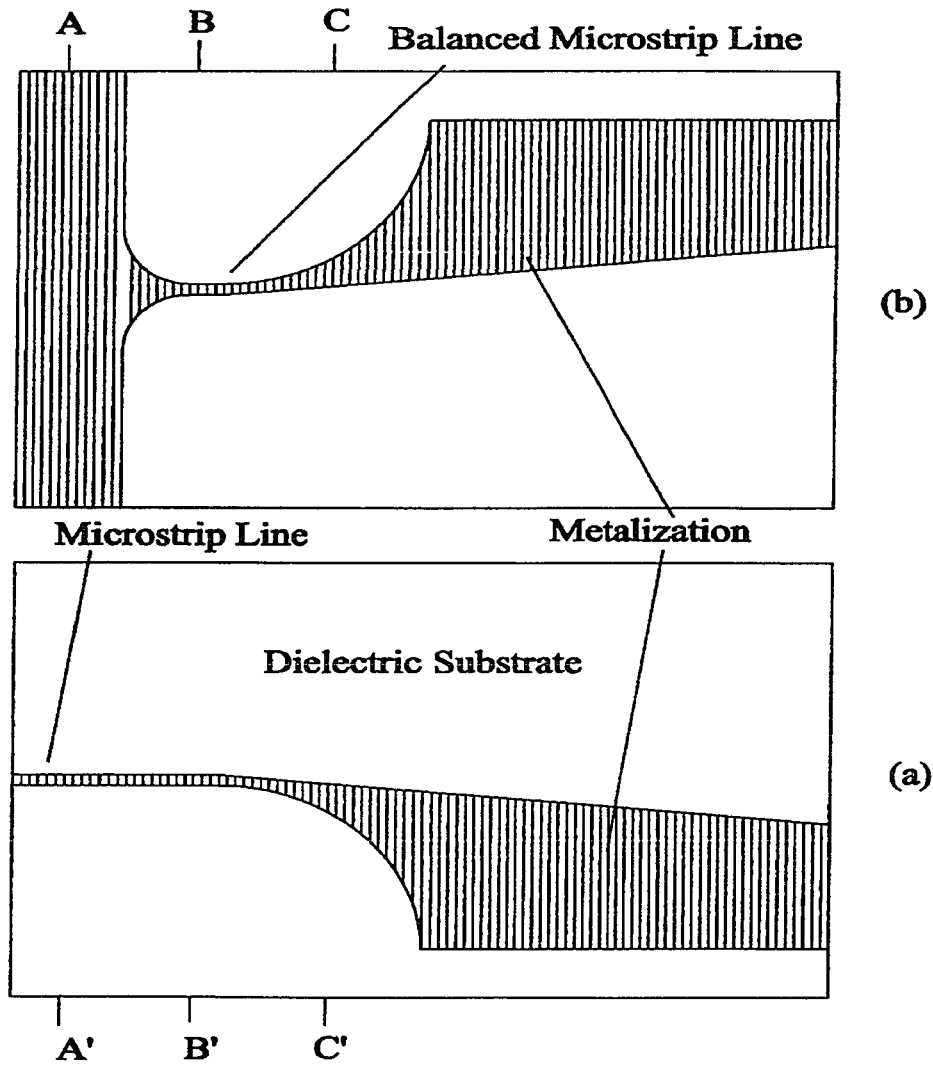
Figure 2.4 Non-planar LTSA and feed network.
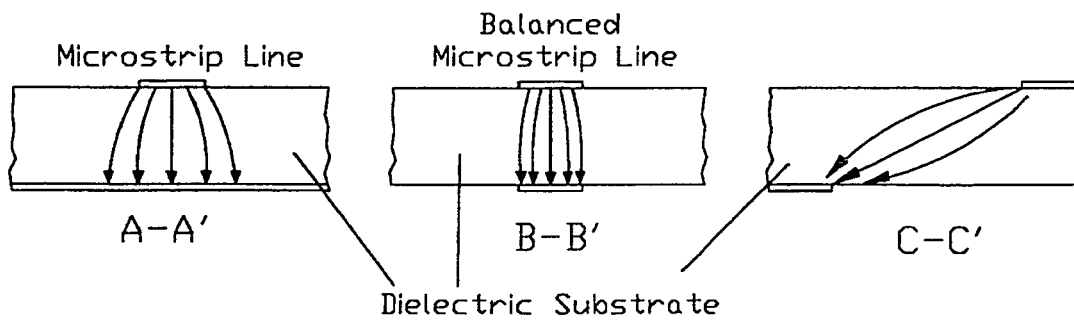
Figure 2.5 The Electric field distributions at various cross sections: (a) conventional microstrip line, (b) balanced microstrip and (c) antenna radiating edge.
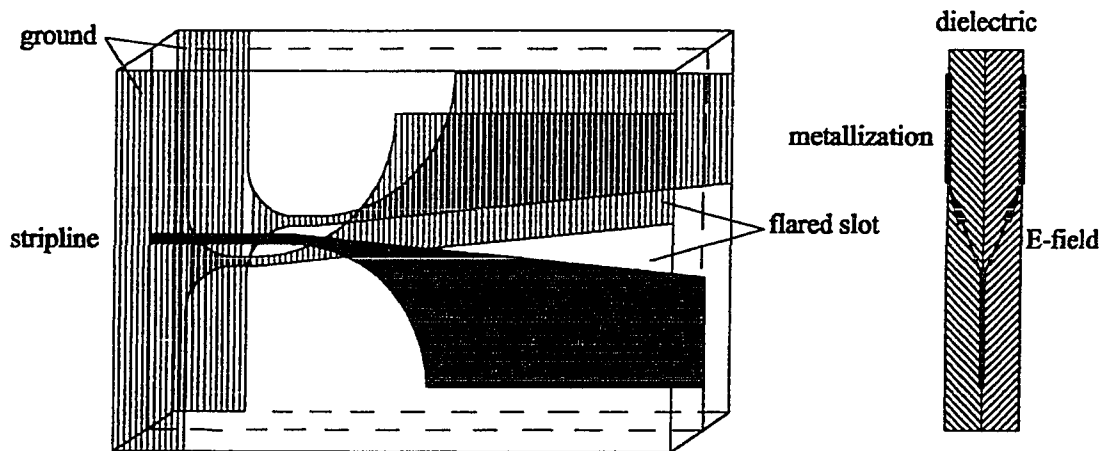
Figure 2.6 Diagrammatic view of balanced antipodal LTSA and direction of dominant E field across radiating slot.

2.3.2 Suspended Microstrip Line, Inverted Microstrip Line and Power Splitters

Suspended Microstrip Line and Inverted Microstrip Line

The suspended microstrip line (SML) and the inverted microstrip line (IML) structures are illustrated in Figure 2.7. Fields in these structures are no longer primarily confined to the dielectric slab, and dielectric losses are reduced. These lines have lower loss because a greater portions of the fields exists the air when compared to microstrip. In addition, a broader line-width is possible for a prescribed characteristic impedance, and the TEM mode propagation is more pronounced. However, the structures are less rugged than microstrip because of the likelihood of substrate breakage. Compared with waveguide, the dimension tolerances and requirement for a surface finish on metallic surroundings are not critical.

Because a substantial amount of the field exists in the air regions above and below the substrate, the dispersion is less pronounced than that in the SML and the IML structure. Thus, numerical quasi-TEM analysis can be applied to yield sufficiently accurate results up to the

millimeter-wave frequency range. Comparing the calculated results for the effective dielectric constant as a function of frequency with the static effective dielectric constant, Button [53] concluded that the dispersion of these lines is negligible over a very wide bandwidth for low ε_r and thin substrates.

Closed-form equations with adequate accuracy were presented by Pramanick and Bhartia [54] for the effective dielectric constant and the characteristic impedance. The expressions were derived using least-squares curve fitting to accurate numerical data available from the spectral domain analysis of transmission lines. The characteristic impedance for a homogeneous air-filled microstrip can be written as,

$$Z_o = 60 \ln \left\{ \frac{f(u)}{u} = \sqrt{1 + \left(\frac{2}{u}\right)^2} \right\}, \tag{2.2}$$

for SML $u = w / (a + b)$ (Figure 2.7(a)) and for IML $u = w / b$ (Figure 2.7(b));

$$f(u) = 6 + (2\pi - 6)\exp\left\{-\left(\frac{30.666}{u}\right)^{0.7528}\right\}. \tag{2.3}$$

The characteristic impedance for an inhomogeneous air-filled microstrip is given by,

$$Z = \frac{Z_o}{\sqrt{\varepsilon_e(0)}}, \tag{2.4}$$

where $\varepsilon_e(0)$ is the effective dielectric constant at zero frequency (the static TEM effective dielectric constant) of the line, the closed form expression for which follow,

(a) Suspended Microstrip

$$\sqrt{\varepsilon_e(0)} = \left[1 + \left(a_1 - b_1 \ln \frac{w}{b} \right) \left(\frac{1}{\sqrt{\varepsilon_r}} - 1 \right) \right]^{-1} \tag{2.5}$$

where the coefficients a_1 and b_1 are given by,

$$a_1 = 0.155 + 0.505\left(\frac{a}{b}\right)$$

$$b_1 = 0.023 + 0.1863\left(\frac{a}{b}\right) - 0.194\left(\frac{a}{b}\right)^2, \qquad \text{for } 0.2 \le \frac{a}{b} \le 0.6$$

and

$$a_1 = 0.307 + 0.239\left(\frac{a}{b}\right)$$

$$b_1 = 0.0727 + 0.0136\left(\frac{a}{b}\right), \qquad\qquad \text{for } 0.6 \le \frac{a}{b} \le 1.0.$$

(b) Inverted Microstrip

$$\sqrt{\varepsilon_e(0)} = 1 + \left(a_1 - b_1 \ln\frac{w}{b}\right)\left(\sqrt{\varepsilon_r} - 1\right) \qquad\qquad (2.6)$$

where the coefficients a_1 and b_1 are given by,

$$a_1 = 0.0669 + 0.2521\left(\frac{a}{b}\right)$$

$$b_1 = 0.02832 + 0.0884\left(\frac{a}{b}\right), \quad \text{for } 0.2 \le \frac{a}{b} \le 0.6$$

and

$$a_1 = 0.144 + 0.1231\left(\frac{a}{b}\right)$$

$$b_1 = 0.0642 + 0.0306\left(\frac{a}{b}\right), \quad \text{for } 0.6 \le \frac{a}{b} \le 1.0.$$

The above expressions can be used in range $1 \le w/b \le 8$, $0.2 \le a/b \le 1.0$ and $\varepsilon_r \le 3.8$.
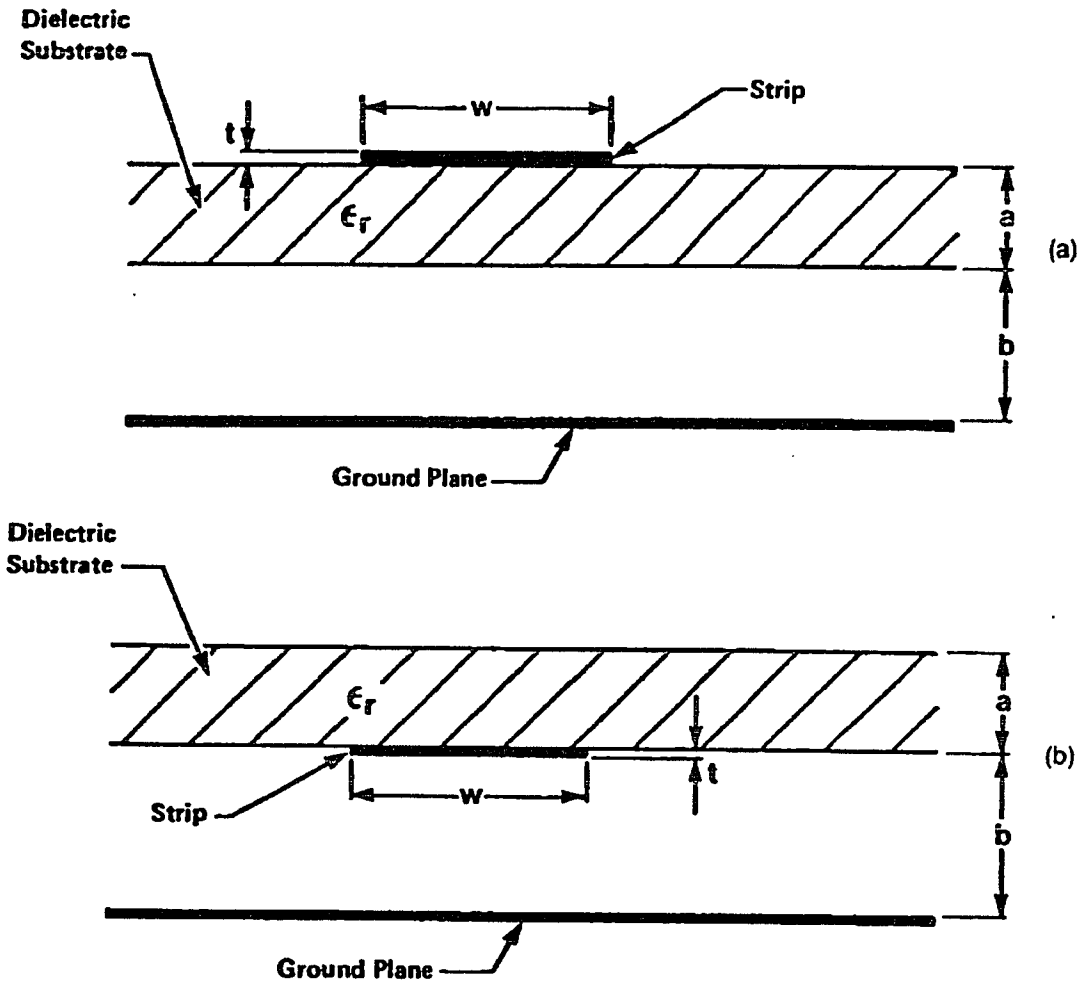
Figure 2.7 (a) Suspended microstrip line, (b) Inverted microstrip line.

The Power Splitter for IML and the SML Topology

A wide band non-isolating power splitter can be formed out of the T-junction as shown in Figure 2.8. The approximate design of this power splitter requires that,

$$\frac{1}{Z_{in}} = \frac{1}{Z_1} + \frac{1}{Z_2},$$ (2. 7)

where Z_{in}, Z_1 and Z_2 are the input and output line impedances of a T-junction before impedance transformers, respectively. Design of the corporate feed antenna beam-forming network requires

the correct selection of the power split ratio in each splitter to give the required power distribution over the aperture of the antenna array. If the output power ratio from port 1 and 2 is P_2/P_1, then one has,

$$\frac{P_2}{P_1} = \frac{Z_1}{Z_2},$$ (2. 8)

If the input port line impedance Z_{in} is given, for example 50Ω, using (2.7) and (2.8) one can determine Z_1 and Z_2.

After getting Z_{in}, Z_1 and Z_2, the line-widths, W's, for the input and output lines can be obtained from (2.2) to (2.6), if either IML or SML structure is chosen for the transmission line. Usually for 1/2oz and 1oz copper deposited on printed circuit broad, the copper thickness (t) is 0.7mil and 1.4mil, respectively. To obtain the optimum bandwidth and equal phase at the output ports, a notch at the center of splitter needs to be optimized. A full-wave numerical modeling tool: IE3D, was used to perform the optimizations and FDTD 3D SS was used for the final verifications. For example, an IML equal power splitter is shown in Figure 2.9. The impedance of input and output port lines of the T-junction are 50, 100 and 100Ω, respectively. Three-stage Chebyshev transformers are used at the output ports to transform the line impedance from 100Ω back to 50Ω. The line-widths of the $\lambda_o/4$ transformers are $W_{(57\Omega)}$ = 80mil, $W_{(70\Omega)}$ = 56mil and $W_{(87\Omega)}$ = 40mil.

Table 2.2 [57] gives the general Chebyshev transformer design parameters, which are used to achieve impedance matching from the input port (Z_0) to the output port (Z_L). N is the number used in the stages of transformer. Γ_m (= S_{11}) is the design goal for the reflection coefficient.
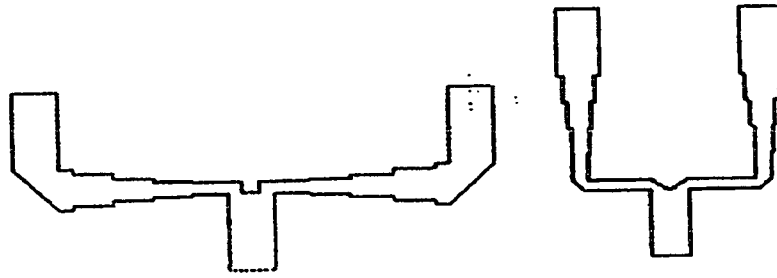
Figure 2.8 T-junction power splitter with impedance transformers at output ports.

	N = 2				N = 3					
	$\Gamma_m = 0.05$		$\Gamma_m = 0.20$		$\Gamma_m = 0.05$			$\Gamma_m = 0.20$		
Z_L/Z_0	Z_1/Z_0	Z_2/Z_0	Z_1/Z_0	Z_2/Z_0	Z_1/Z_0	Z_2/Z_0	Z_3/Z_0	Z_1/Z_0	Z_2/Z_0	Z_3/Z_0
1.0	1.0000	1.0000	1.0000	1.0000	1.0000	1.0000	1.0000	1.0000	1.0000	1.0000
1.5	1.1347	1.3219	1.2247	1.2247	1.1029	1.2247	1.3601	1.2247	1.2247	1.2247
2.0	1.2193	1.6402	1.3161	1.5197	1.1475	1.4142	1.7429	1.2855	1.4142	1.5558
3.0	1.3494	2.2232	1.4565	2.0598	1.2171	1.7321	2.4649	1.3743	1.7321	2.1829
4.0	1.4500	2.7585	1.5651	2.5558	1.2662	2.0000	3.1591	1.4333	2.0000	2.7908
6.0	1.6047	3.7389	1.7321	3.4641	1.3383	2.4495	4.4833	1.5193	2.4495	3.9492
8.0	1.7244	4.6393	1.8612	4.2983	1.3944	2.8284	5.7372	1.5766	2.8284	5.0742
10.0	1.8233	5.4845	1.9680	5.0813	1.4385	3.1623	6.9517	1.6415	3.1623	6.0920

	N = 4							
	$\Gamma_m = 0.05$				$\Gamma_m = 0.20$			
Z_L/Z_0	Z_1/Z_0	Z_2/Z_0	Z_3/Z_0	Z_4/Z_0	Z_1/Z_0	Z_2/Z_0	Z_3/Z_0	Z_4/Z_0
1.0	1.0000	1.0000	1.0000	1.0000	1.0000	1.0000	1.0000	1.0000
1.5	1.0892	1.1742	1.2775	1.3772	1.2247	1.2247	1.2247	1.2247
2.0	1.1201	1.2979	1.5409	1.7855	1.2727	1.3634	1.4669	1.5715
3.0	1.1586	1.4876	2.0167	2.5893	1.4879	1.5819	1.8965	2.0163
4.0	1.1906	1.6414	2.4369	3.3597	1.3692	1.7490	2.2870	2.9214
6.0	1.2290	1.8773	3.1961	4.8820	1.4415	2.0231	2.9657	4.1623
8.0	1.2583	2.0657	3.8728	6.3578	1.4914	2.2428	3.5670	5.3641
10.0	1.2832	2.2268	4.4907	7.7930	1.5163	2.4210	4.1305	6.5950

Table 2.2 The Chebyshev transformer design [32].
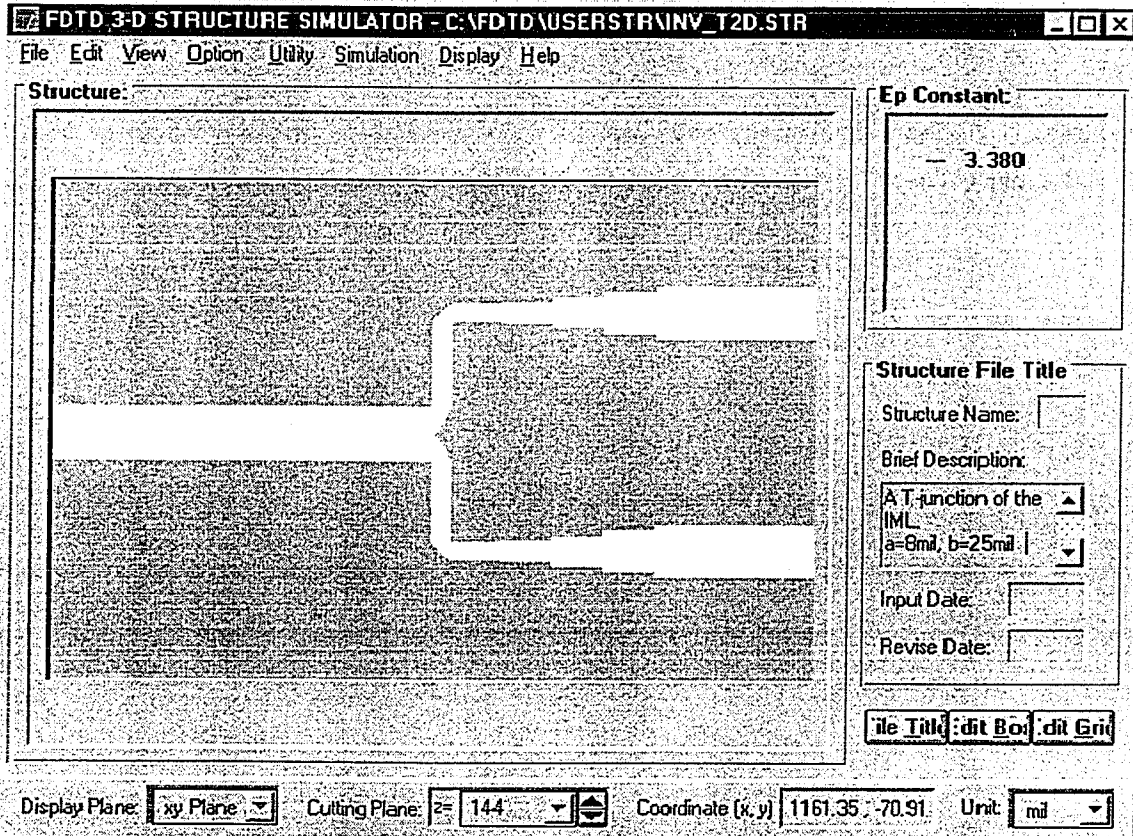
Figure 2.9 An IML equal power splitter.

a = 8mil, b = 20mil, ε_r = 3.38, $W_{in(50\Omega)}$ = 104mil, $W_{1(100\Omega)}$ = 32mil, and $W_{2(100\Omega)}$ = 32mil.
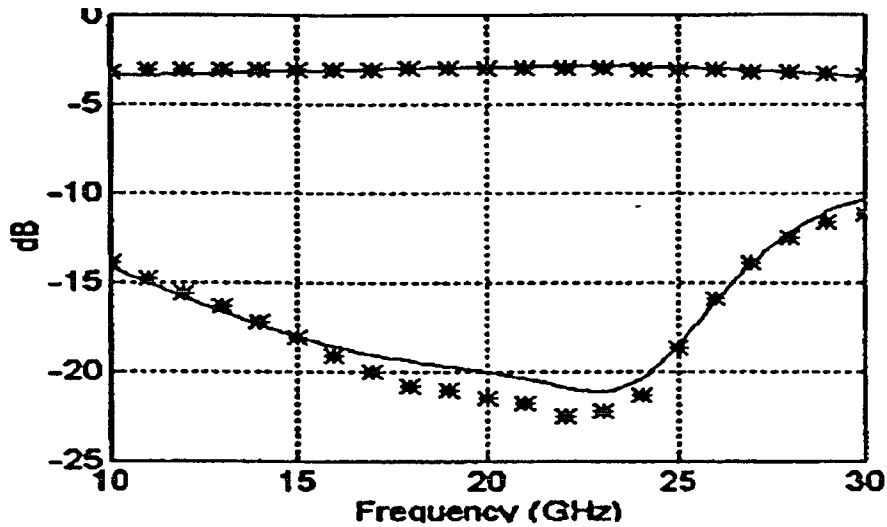
Figure 2.10 The S-parameters of the IML equal power splitter, *: IE3D results, solid line : FDTD results.**

2.3.3 Five-Piece Assembled SML Fed LTSA

Based on the microstrip-to-slot transition design in Figure 2.3, we introduced a LTSA in Figure 2.11, which is similar to Figure 2.3 except for the use of an SML-to-slot transition. The performance of the LTSA design is defined by L and W. When the aperture size (W) of any tapered slot antenna becomes of the order of $\lambda_o/2$, it no longer acts as a broadband traveling-wave antenna. Thus, a cutoff wavelength can be defined by,

$$\lambda_c = 2W .\tag{2.9}$$

For the wide-band traveling-wave antenna the designed lowest frequency should have a wavelength $\leq \lambda_c$. A typical high-gain antenna has $\lambda_c/\lambda_o \approx 3\text{-}4$. In Figure 2.11, 's' is the width of the slot line. Under the slot line there is a SML with line width 'W_m'. By changing l_s, l_m, l_o and the size of of the small patch at the end of the SML, u x v, a LTSA can operate over a wide-band starting from f_c (=c/ λ_c). The antenna presented in Figure 2.11 can be used from 17 to 24 GHz, which covers the 18 GHz band (17.7 - 19.7GHz) and 23GHz band (21.4 - 23.6GHz) in frequencies in K band. These bands are used for point-to-point communications.

Unlike the microstrip fed LTSA, in which the microstrip line and slot are simply etched on different sides of a printed circuit board (PCB), an SML fed LTSA needs an 'air-filled' dielectric layer. So a five-piece SML fed LTSA assembly was designed (Figure 2.12). In this design the top and bottom plates hold the LTSA (printed antenna) layer, spacer, and SML BFN layer together to form an SML fed LTSA. The spacer will ensure a uniform 'air-filled' dielectric gap.

In Figure 2.13, the FDTD 3D SS is used to find the optimum dimensions of the LTSA shown in Figure 2.11. The sampled time domain response is given in Figure 2.14. It is clear that after the incident pulse passes the sampling plane, during the time interval between 0 and 400Δt, the wave reflected from the discontinuities, consisting of the SML-to-slot transition and V-slot, returns back to the sampling plane between 400Δt and about 2000Δt. Some energy reflected by the abrupt endings of the V-slot and substrate is collected at the sampling plane after 2000Δt. Figure 2.15 gives the return loss of the SML-to-slot transition. The result was obtained by using the pulse from 0 to 400Δt as the incident wave and 400Δt to 2000Δt as the reflected wave in

69

Figure 2.14. It is clear that the energy is very smoothly coupled from the SML to slot line between 17 and 24 GHz. The return loss of the LTSA is given in Figure 2.16.
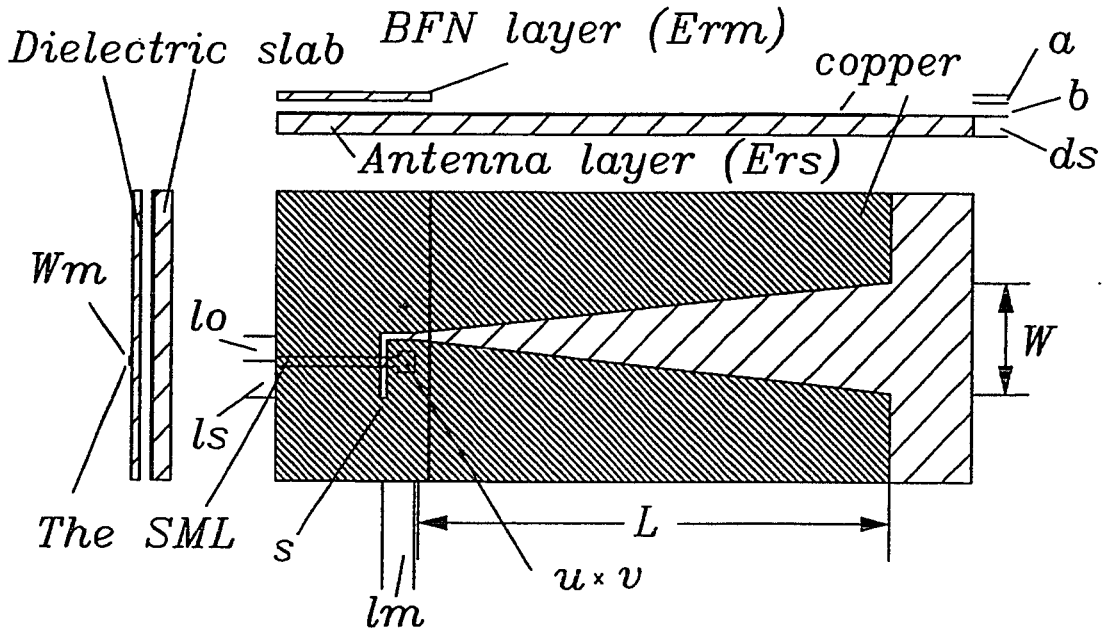
Figure 2.11 The LTSA fed by the SML-to-slot transition.

L = 1700mil	the length of the LTSA,
W = 386mil	the end opening of LTSA,
W_m = 32mil,	the width of 100Ω SML,
s = 24 mil,	the width of slot line,
l_o = 70mil,	the distance between center of the SML and center of slot line,
l_s = 120mil,	the distance between center of the SML and end of slot line,
l_m = 230mil,	the distance between center of slot line and end of the SML,
a = 8mil,	the substrate thickness of the SML,
b = 20mil,	the thickness of air gap,
d_s = 20mil,	the substrate thickness of the LTSA,
ε_{rm} = 3.38,	the dielectric constant of the substrate for the SML,
ε_{rs} = 3.38,	the dielectric constant of the substrate for the LTSA,
u x v = 60x45mil,	the size of the patch at the end of the SML.
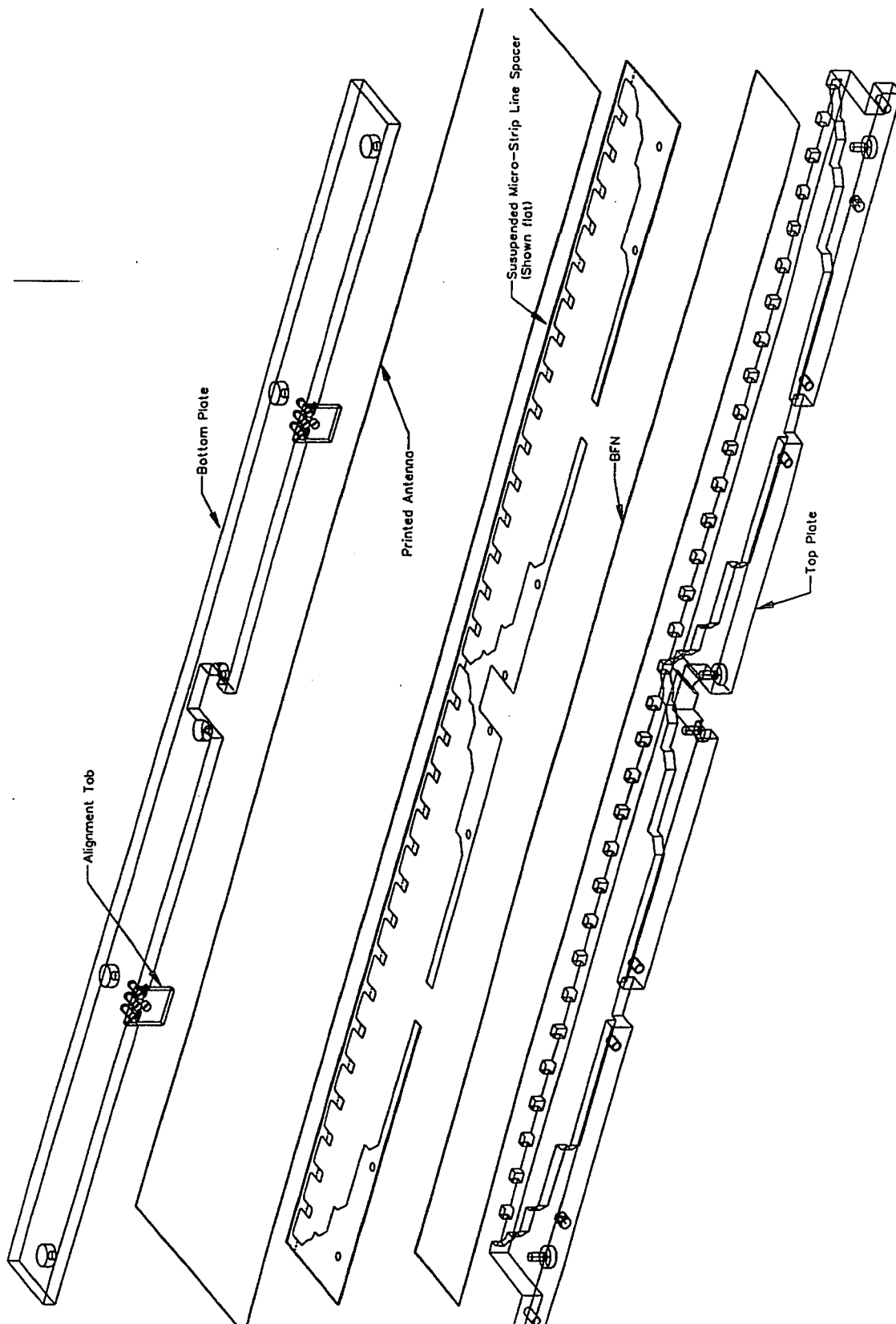
Figure 2.12 Five-piece SML fed LTSA assembly.
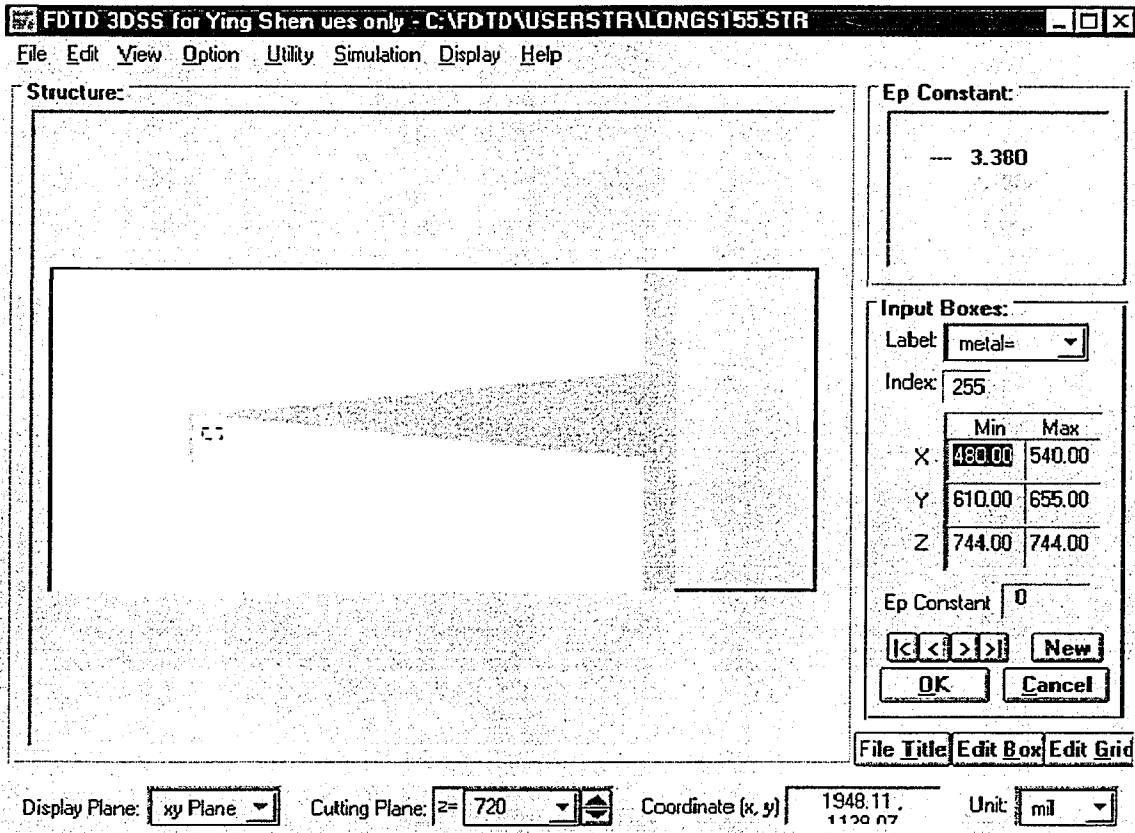
Figure 2.13 The LTSA shown on FDTD 3D SS interface.
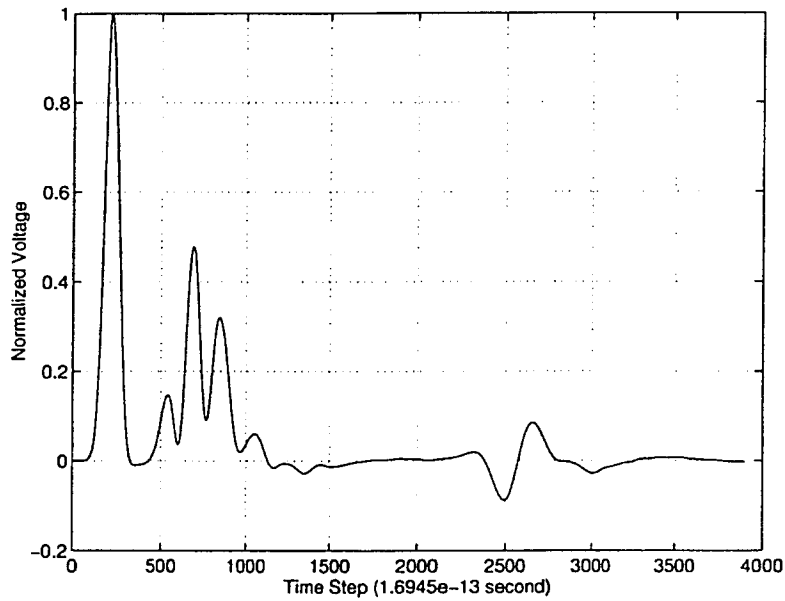
Figure 2.14 The time domain response sampled at the SML.
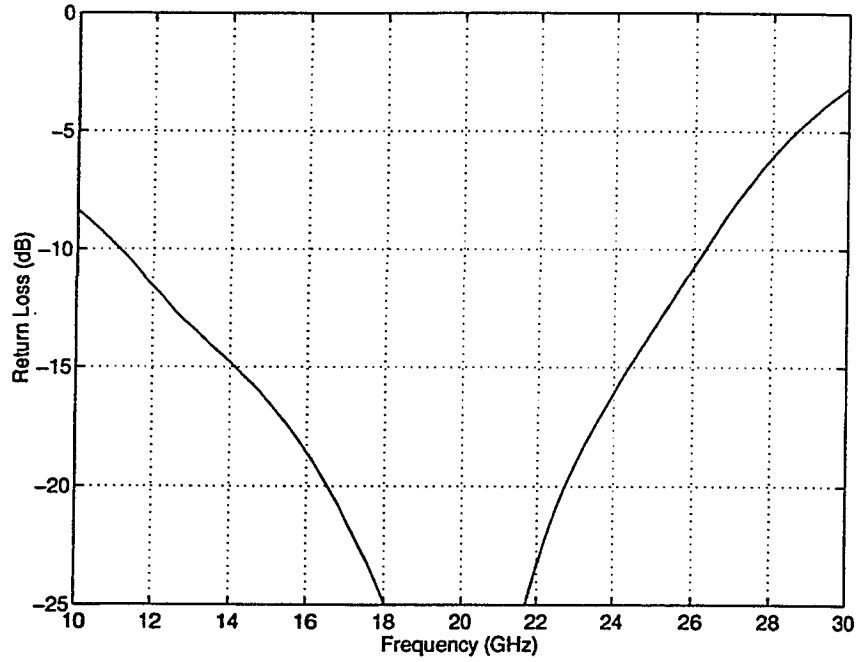
Figure 2.15 The return loss of the SML-to-slot transition calculated with the V-slot, using the pulse from 0 to 400Δt as the incident wave and 400Δt to 2000Δt as the reflected wave in Figure 2.14
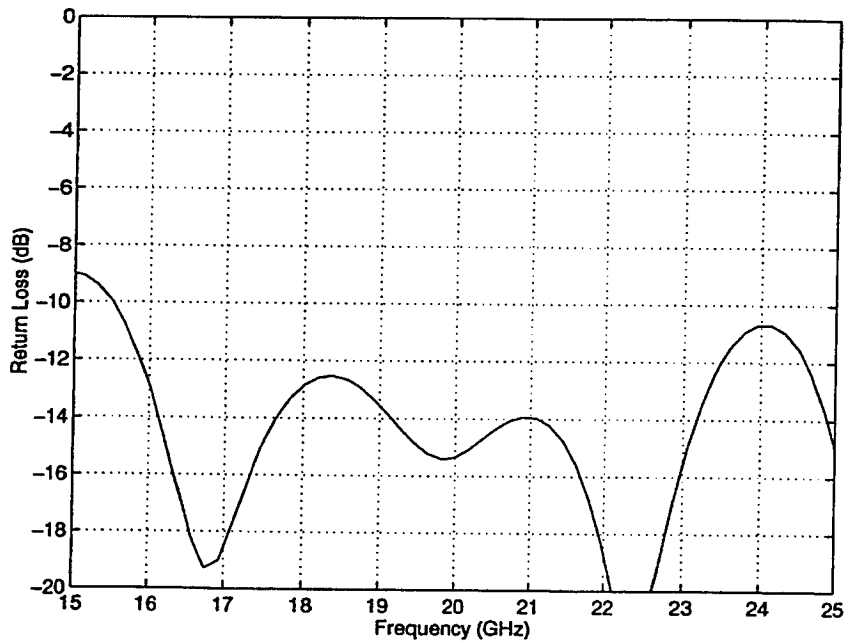
Figure 2.16 The return loss of the LTSA in Figure 2.11.

73

2.3.4 Three-Piece Assembled the IML Fed LTSA

Although the five-piece SML fed LTSA assembly has wide-band characteristics, the major drawback of the design is that it has too many components. It would be too costly to use in a very large phased array. (A 32 x 32 Flat Panel Antenna (FPA) was designed and built using this element and is reported in Chapter 3.) If the metalization of the SML and V-slot can be etched on the same side of a PCB, it can save some of the components used in the five-piece design, thereby getting around the problem of aligning the SML and the slot line, as well as reducing the time for assembly.

A Wide-band IML-to-Coplanar Double Strips (CDS) Transition

In Figure 2.17 is shown a transition between a IML and a Coplanar Double Strip transmission line (CDS). There is a bottom metal plate used in this design. It has the following functions,

1. To act as supporter to hold the dielectric slab;
2. To act as the ground of the IML;
3. A spacer, which size is u x v with thickness b, can either rests or be built into the plate to form an air gap of the IML.

The IML line links to one strip of the CDS. The other strip of the CDS is connected to a copper patch (u x v), which is grounded by a metal spacer that is in contact with the copper patch. A size #2 copper screw is used to tighten the bottom plate and the dielectric slab together. The transition is designed and simulated using the FDTD 3D SS as shown in Figure 2.18. By adjusting W_c, s_1 and s the transition can be optimized to provide operation over a very wide frequency band. The FDTD simulation was setup by first implementing Litva's ABC at both ends of the transmission lines. The return loss of the transition shown in Figure 2.18 was then simulated. It is given in Figure 2.19, with the simulation carried out with the observer looking into the structure from the left hand side, i.e. from the IML port.
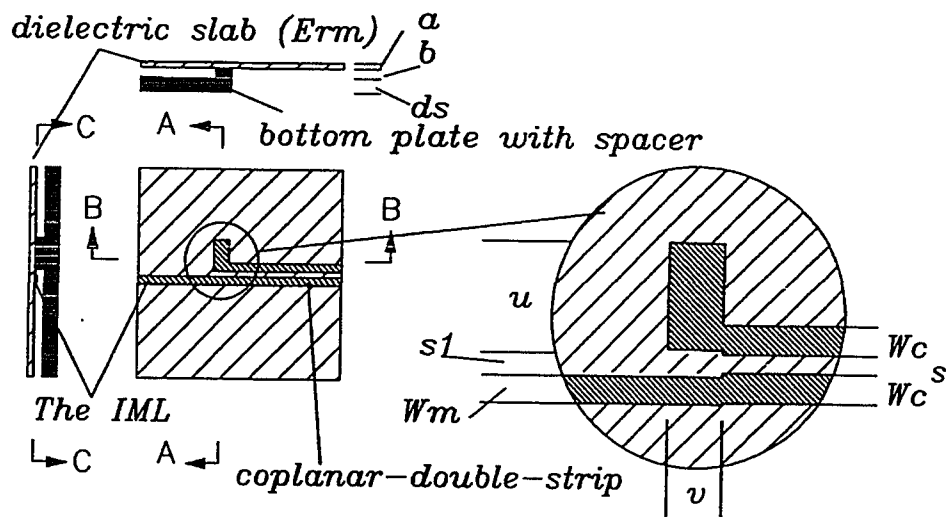
Figure 2.17 The IML-to-Coplanar Double Strip (CDS) Transition

a = 8mil, b = 25mil, ε_r = 3.38, d_s = 100mil, W_m = 30mil,
Wc = 40mil, s1 = 40mil, s = 20mil, u x v = 200 x 150mil.

Figure 2.18 The IML-to-CDS transition as represented by the FDTD 3D SS interface.
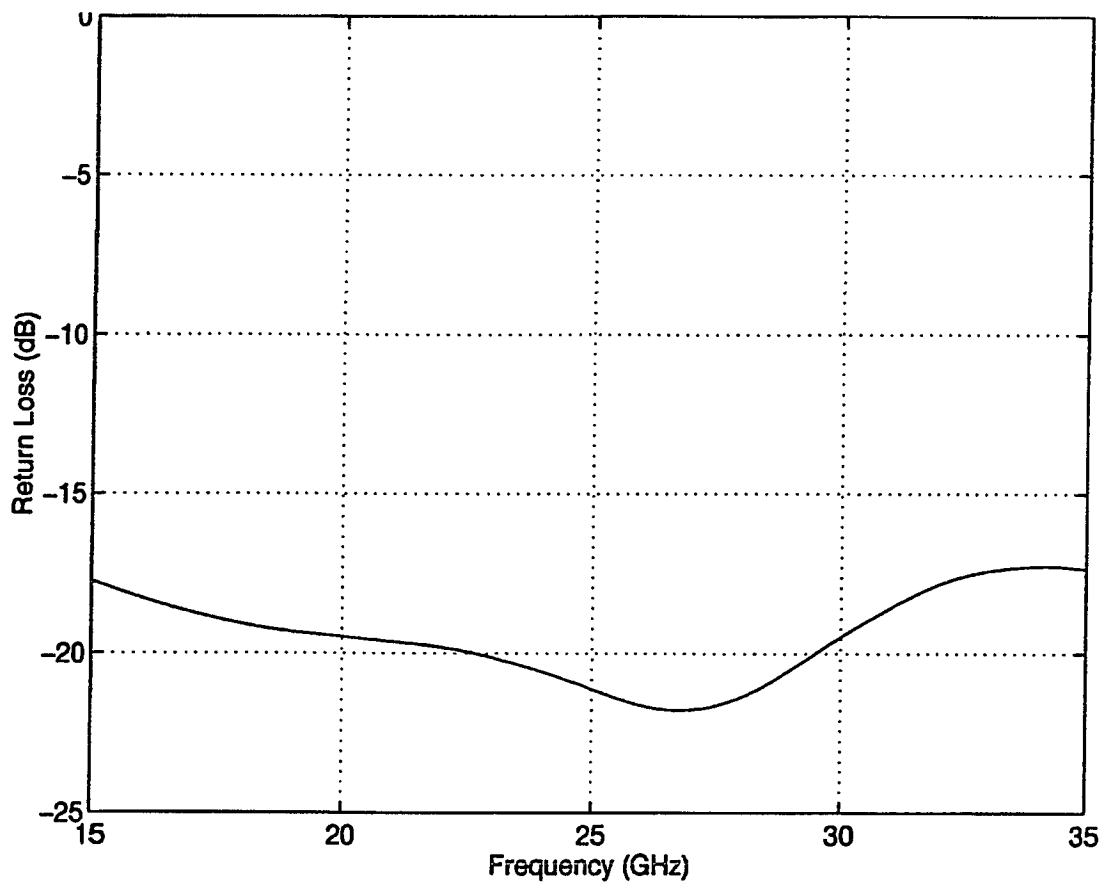
Figure 2.19 The return loss of the IML-to-CDS transition.

A LTSA Fed by the IML-to-CDS Transition

After finding a good transition, the LTSA was designed, as shown in Figure 2.20, by using the FDTD 3D SS. In Figure 2.21 is shown the antenna as it was entered into the FDTD 3D SS simulator. The return loss of the antenna is presented in Figure 2.22. It can be seen that the antenna element has very good return loss when L_{cds}, which is the length of the CDS, is very small. Including the top cover, a three-piece LTSA one-dimensional array has been designed and is shown in Figure 2.23. It is a 1x16 element linear array and is fed by an IML beamforming network. Starting from left to right we identify the components. The first component is the bottom plate, which has small islands. These protrusions are the spacers. Each

spacer has a threaded hole. The height of the spacers is 25mil. The middle component is a PCB. The linear tapered slot and IML BFN are etched on the board. The right-hand-side component is the top cover. The small islands on the top cover have the same shape as those on the bottom plate with a height of about 200mil. Thirty-two size #2 screws are used to bind the three piece assembly together, thereby producing a 1 x 16 element linear array. For details refer to Chapter 3.
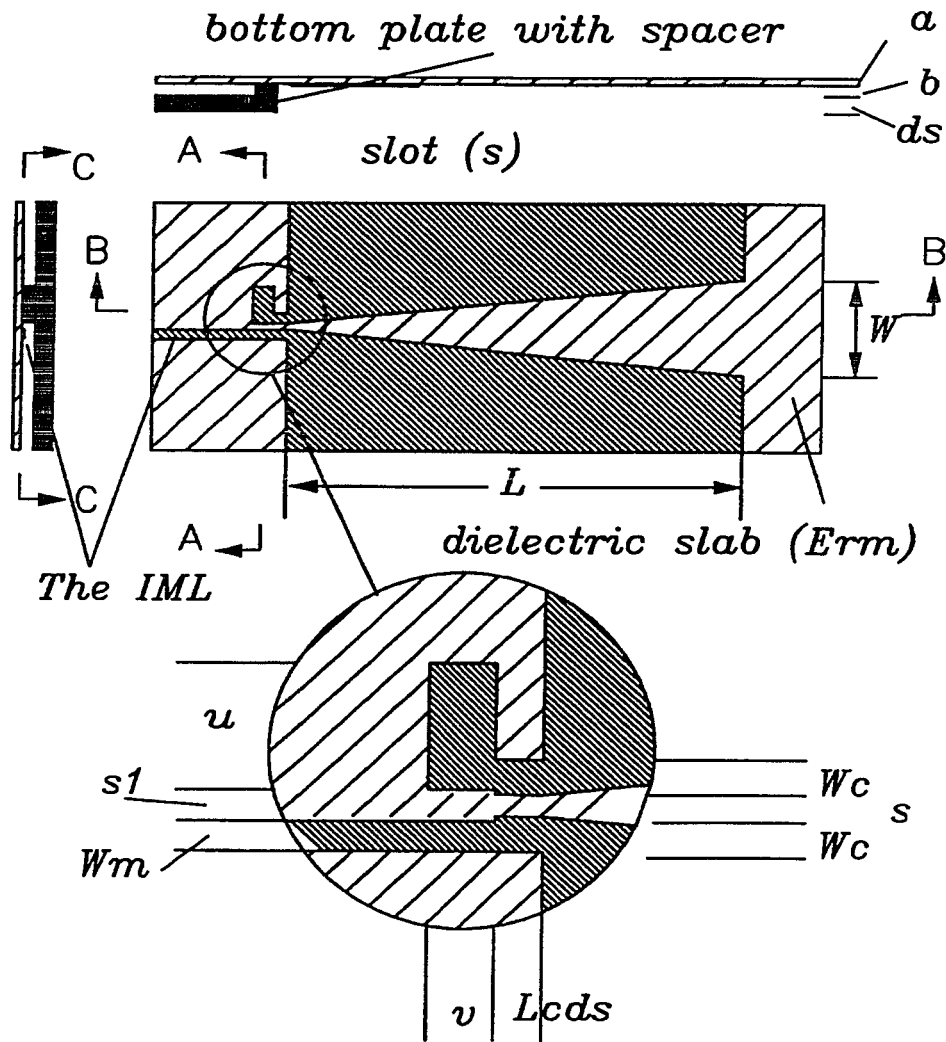
Figure 2.20 An LTSA fed by the IML-to-CDS Transition

$a = 8\text{mil}$, $b = 25\text{mil}$, $\varepsilon_r = 3.38$, $W_m = 30\text{mil}$, $s_1 = 40\text{mil}$, $s = 20\text{mil}$, $u \times v = 200 \times 150\text{mil}$, $L = 1200\text{mil}$, $W = 468\text{mil}$, $L_{cds} = 50\text{mil}$, $W_c = 40\text{mil}$.
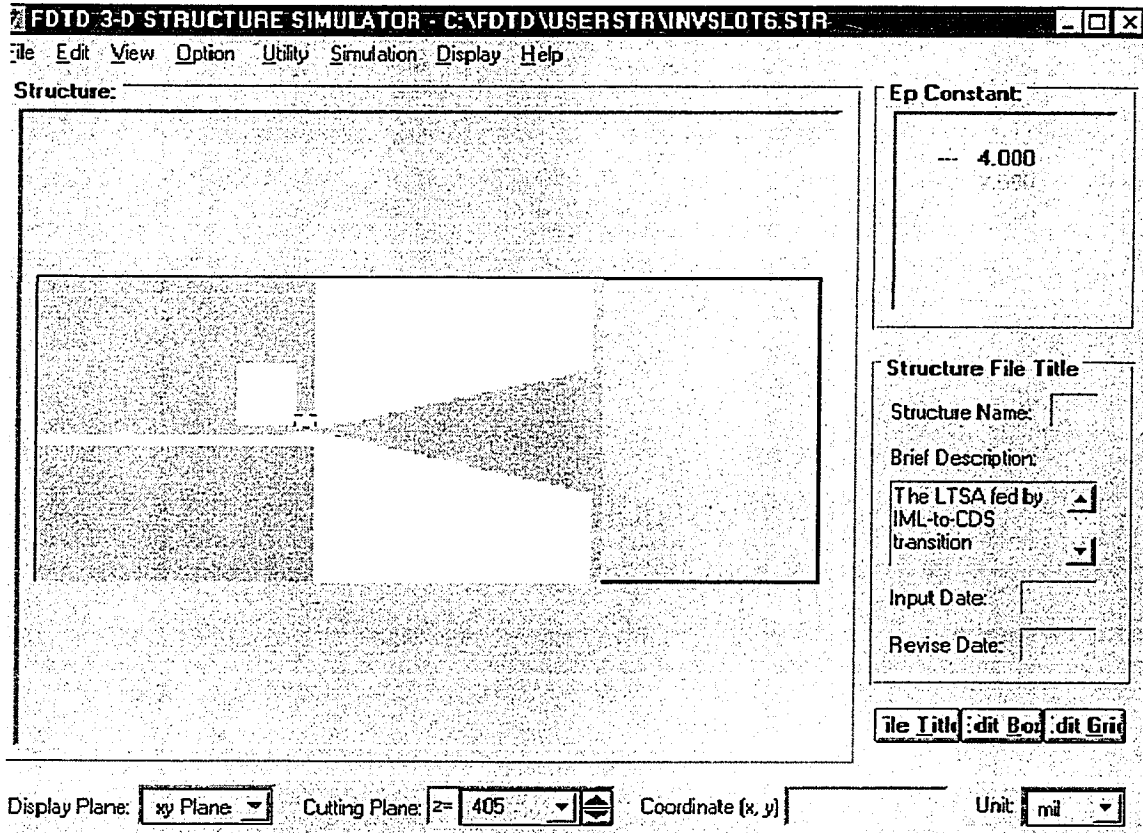
Figure 2.21 The LTSA as shown when entered into the FDTD 3D SS simulator.
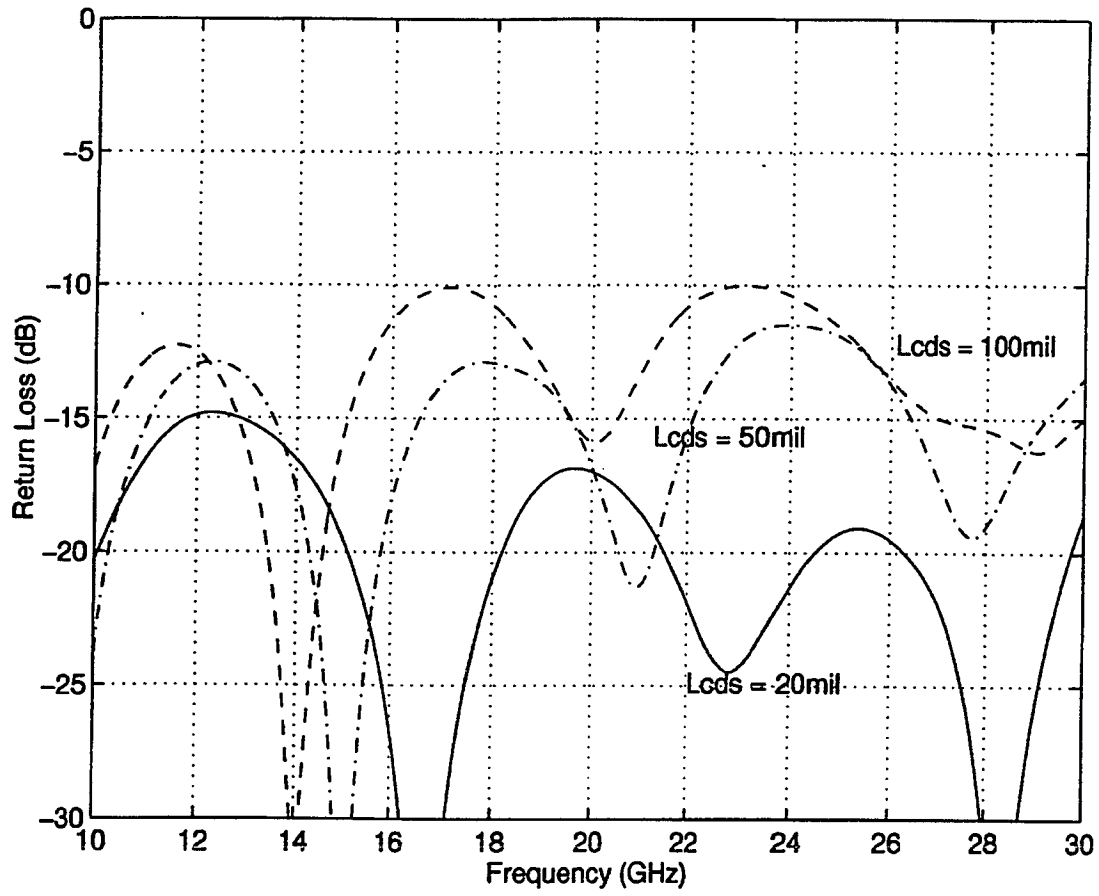
Figure 2.22 The return loss of the LTSA fed by the IML-to-CDS transition.

Bottom Plate   **PCB Board**   **Top Plate**
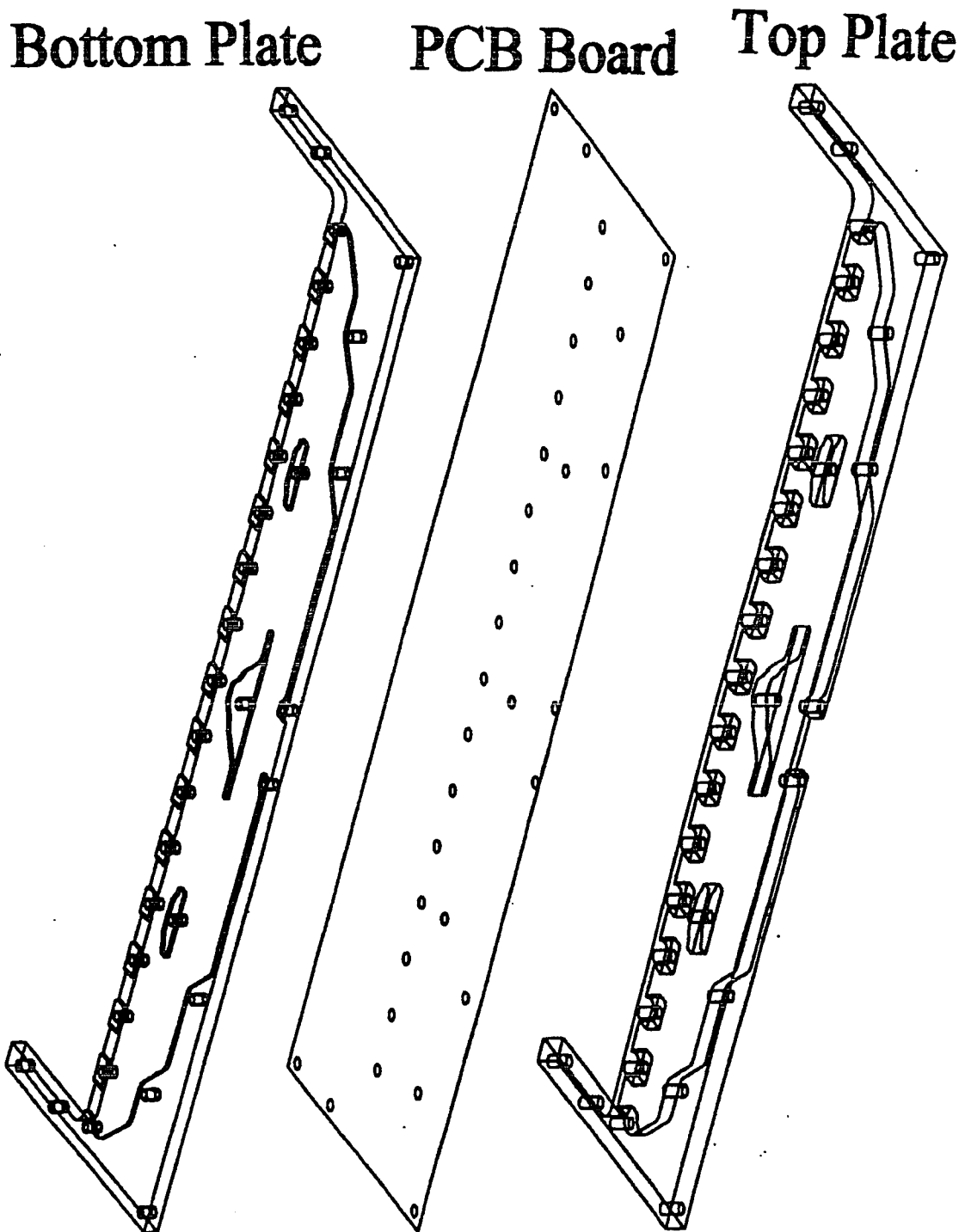
Figure 2.23 Three-piece assembly for the IML fed LTSA.

As shown in Figure 2.24 the performance of a two-element (1x2) array was simulated using the FDTD 3D SS. The objective was to evaluate the performance of the IML equal power divider, which is connected to the LTSAs. The inter-element spacing used in the array was 468mil. It follows from Figure 2.25 that the subarray has a good return loss in the 18/23 GHz frequency bands. Therefore it is expected to have good performance over these two bands.
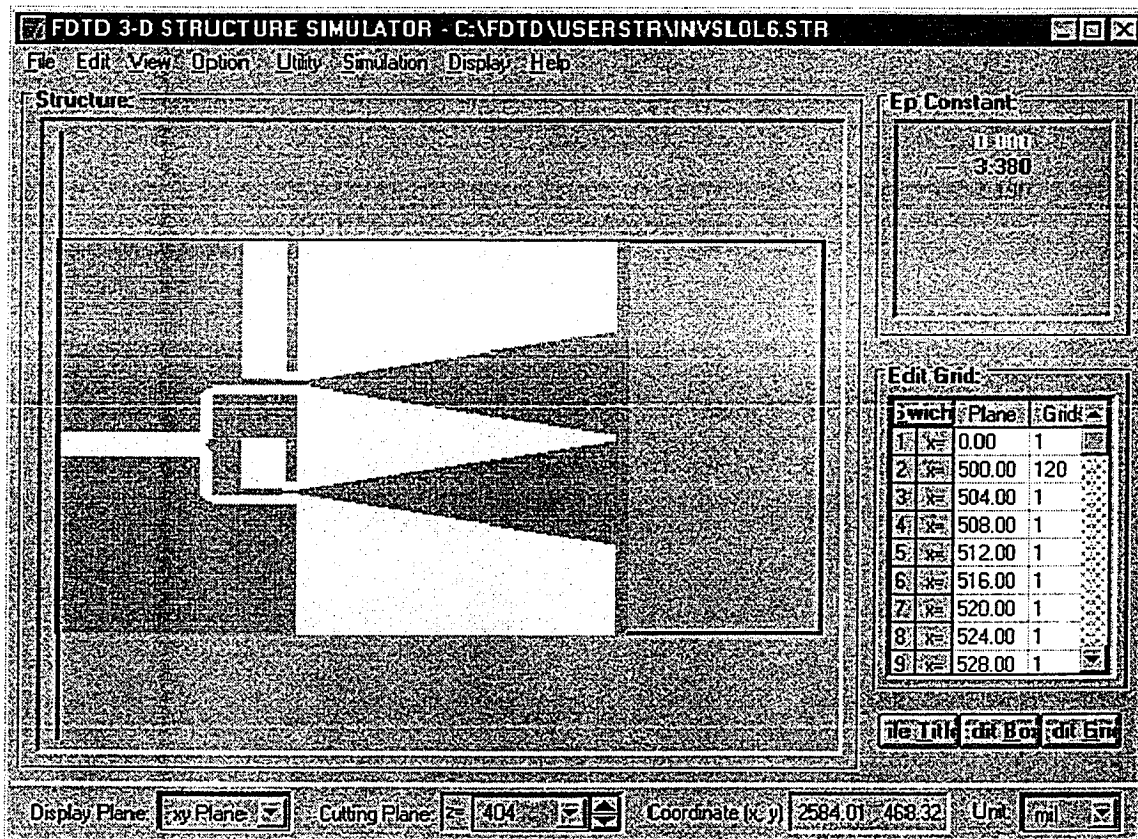
Figure 2.24 An 1 x 2 E-plane LTSA subarray.
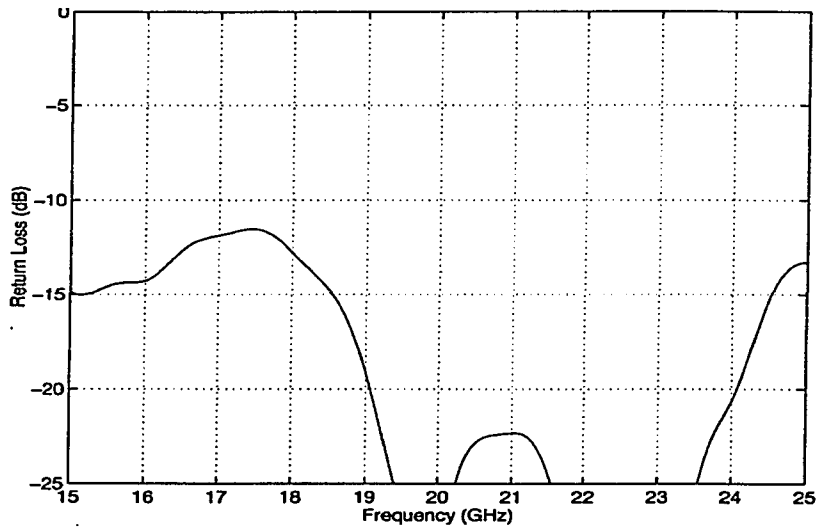
Figure 2.25 The return loss of the 1 x 2 E-plane LTSA subarray.

The mutual coupling in E-plane subarray was studied by using the 1 x 3 E-plane subarray shown in Figure 2.26. The element spacing was also 468mil. Litva's ABC was used at the end of each IML feed line to simulate matched loads. A pulse was lunched on the IML of the center element. It can be observed in Figure 2.27 that the coupling between adjacent elements is lower than −15dB. The results observed here for the mutual coupling between the LTSAs in an array environment are the same as the conclusion given in [55].
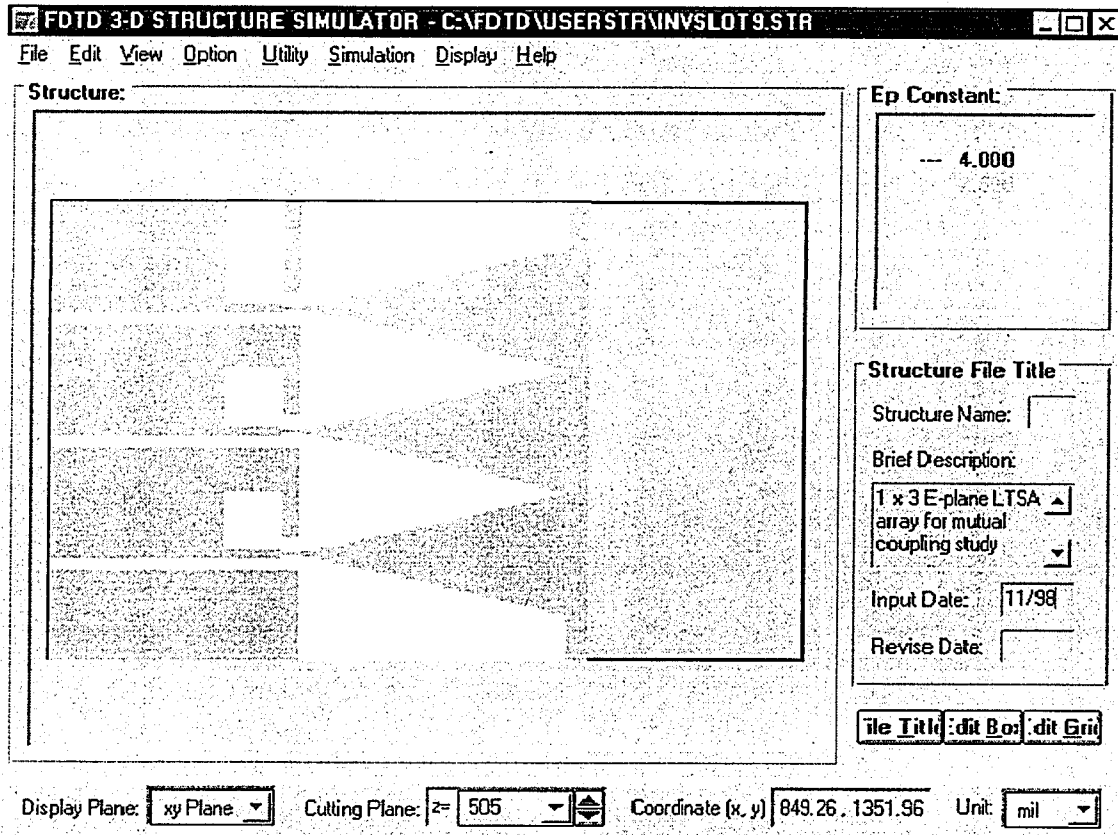
Figure 2.26 An 1 x 3 E-plane LTSA subarray.
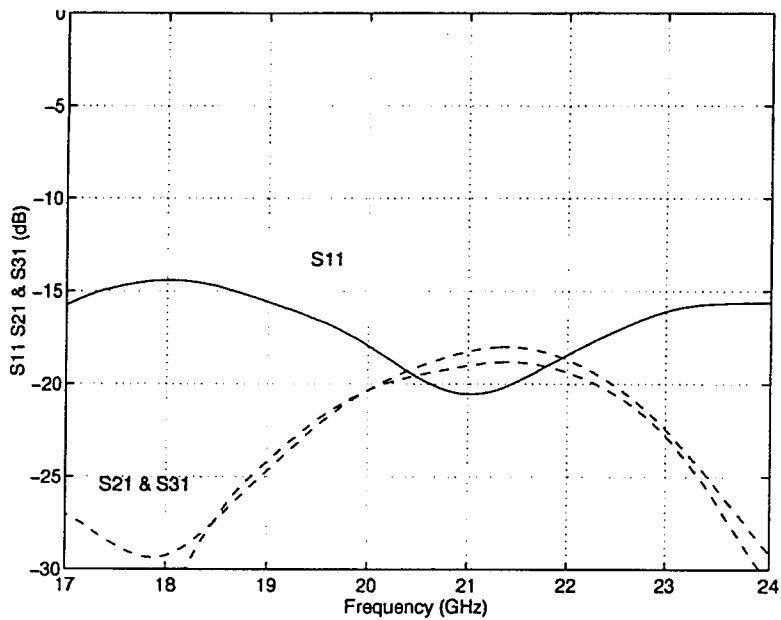
Figure 2.27 The mutual coupling between LTSAs in an array environment.

An SML-to-CDS transition was also designed to feed LTSAs. The only difference between these two transitions, i.e. the IML-to-CDS and SML-to-CDS, is that the copper patch (u x v) does not directly touch spacer (u x v) on the SML-to-CDS transition. As shown in Figure 2.28 a metal pin must be used to connect the copper patch to the ground. Figure 2.29 gives the simulated return loss for the antenna element.
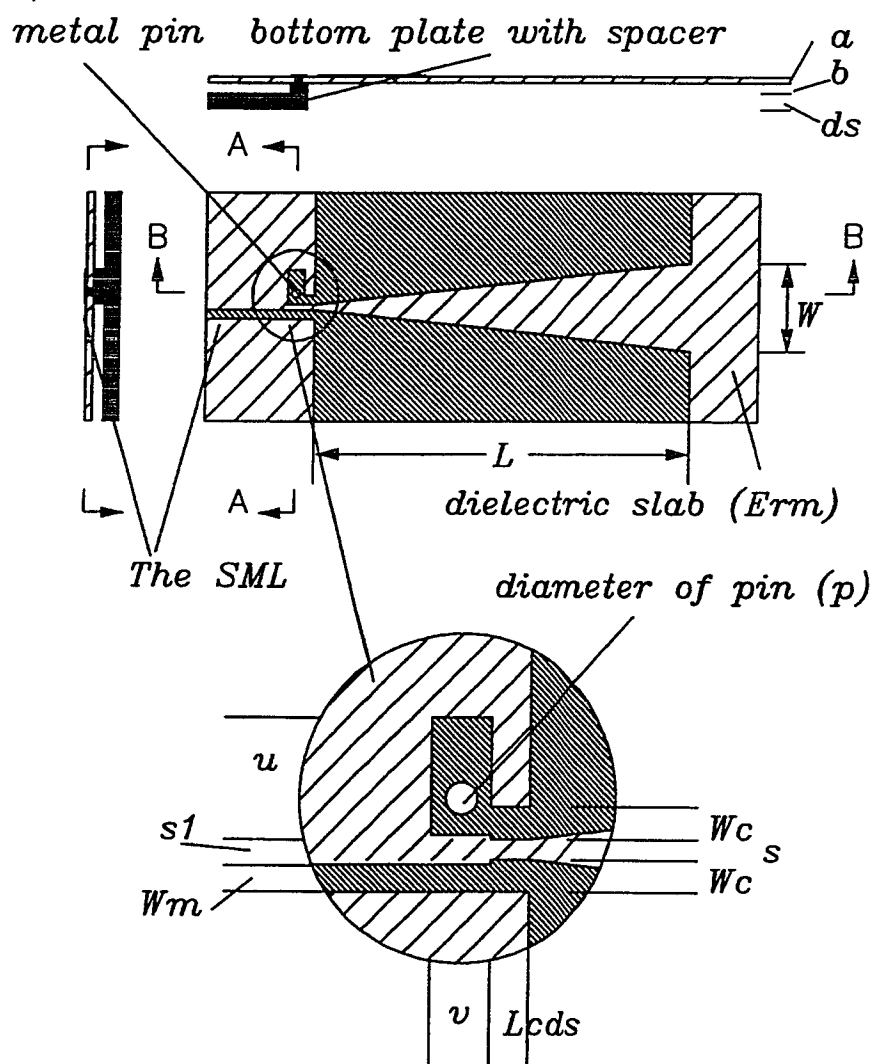
Figure 2.28 The LTSA fed by the SML-to-CDS transition.

a = 8mil, b = 20mil, εr = 3.38, Lcds = 50mil, Wm = 25mil, Wc = 40mil, s1 = s = 20mil, u x v = 200 x 150mil. Pin is a size #2 screw.
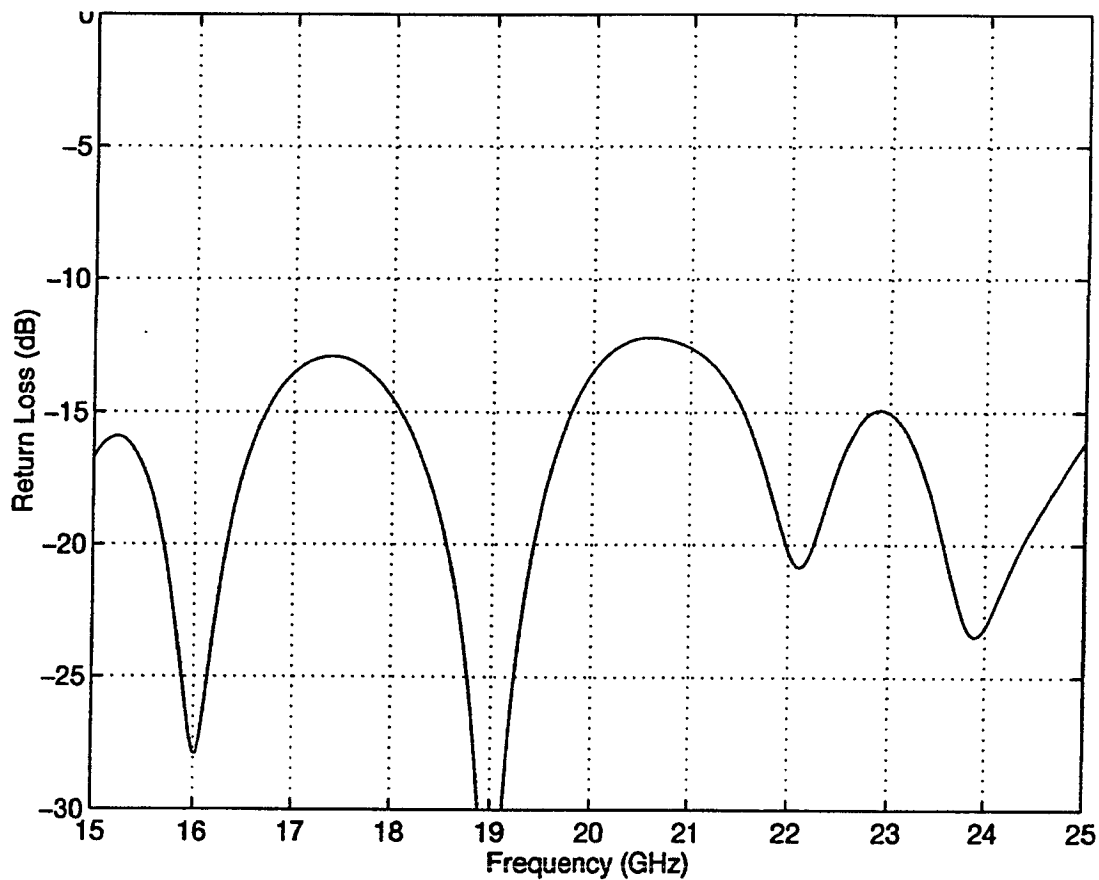
Figure 2.29 Return loss of the LTSA fed by the SML-to-CDS transition.

2.3.5 The SML Fed 'Hockey Stick' Slot Coupled LTSA Design

The SML-to-slot, SML-to-CDS and IML-to-CDS transitions can be used to feed the LTSAs in many applications, but they have some drawbacks for Flat Panel Antenna (FPA) applications. First, although it is easy to use these transitions to form E-plane LTSA arrays, it is difficult to use them to form H-plane LTSA arrays. Secondly, if these transitions are used in millimeter wave FPA designs, the final array usually becomes very thick. For example, the total thickness of a 32 x 32 FPA (the five-piece structure described in Chapter 3) is about 3.5 inches when designed for the 18/32GHz bands. In the array there are 32 1x32-E-plane-subarrays that are aligned side by side. The length of the LTSA radiating element is about 1.2 ~ 1.7 inches.

The E-plane BFN is about 1.3 ~ 1.5 inches thick. The H-plane BFN, that lies under the E-plane subarrays, plus the radome add another 0.3 ~ 0.5 inch. In addition to thickness, this array assembly has the disadvantage of being costly to build simply because of the large number of components.

A panel microstrip patch antenna array [56] [57] [58] can be easily fed by printed transmission lines using a parallel feed or a series feed, or the combination of parallel and series feeds. It is very useful to design a transition, which is similar to the transition used in an aperture-coupled patch antenna, to couple energy from transmission line to the LTSA through a slot in the printed transmission line ground. It means that the printed transmission line and radiating element (tapered slot) are on two orthogonal planes. The transition should have the following features:

1. Relatively wide frequency bandwidth, because the LTSA is a wideband radiating element.

2. Very low profile, because the FPA needs to have as low a profile as possible.

3. Easy to fabricate, because cost is always an important factor for antenna design.

4. Very compact size, because sometimes for a large phased array the radiating elements need to fit into a very tight space.

Figure 2.30 shows a unique LTSA design fed by a SML. The IML or microstrip line topologies also can be used. The radiating element composed of a V-slot is formed by two metal fins. The length of the fin is L and width of the end opening of V-slot is W. The thickness of metal fin is T. In this case v_{ph} is equal to the speed of light, because there is no dielectric slab at the back of the fins. At the bottom of V-slot there is a 'Hockey Stick' shaped slot, which is engraved in the ground of the SML. The ground could be a piece of metal sheet with thickness t. There are four walls of height, h, and width, w, surrounding the 'Hockey Stick' slot. These walls have three functions:

1. to support the fins,

2. to form a grid structure to support the whole antenna array, because the ground plate of the SML can be very thin;

3. to provide some isolation between the slots.

86

Energy travelling along the SML is coupled through the 'Hockey Stick' slot and radiated by the V-slot. If the size of V-slot and the parameters of the SML are fixed, then by changing the size of 'Hockey Stick' slot, the element can be used in any frequency band as long as the condition $W \geq \lambda_c/2$ is being met.
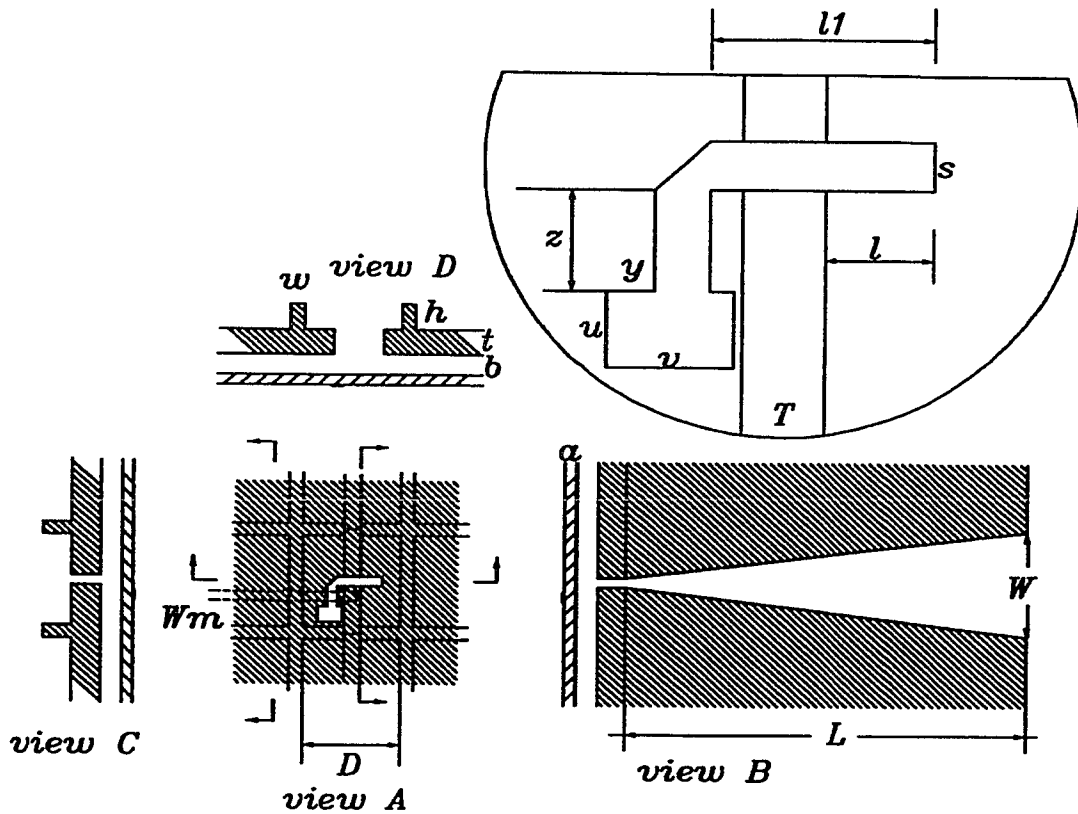
Figure 2.30 A SML fed 'Hockey Stick' slot coupled LTSA.

A design for the 18 and 23 GHz bands

The detailed dimensions of a SML fed 'Hockey Stick' slot coupled LTSA are shown in Figure 2.31. The total thickness of an FPA that is designed to operate in the 18/23 GHz bands is 1.5 ~ 2.0 inches. It depends on the length of the V-slot. The stub length of the SML after the

'Hockey Stick' slot is about $\lambda_o/4$. From the return loss of the antenna shown in Figure 2.32, it is obvious that this design can be used in the 18/23GHz bands. The three curves shown in Figure 2.32 present the results of three different sampling planes along the SML.
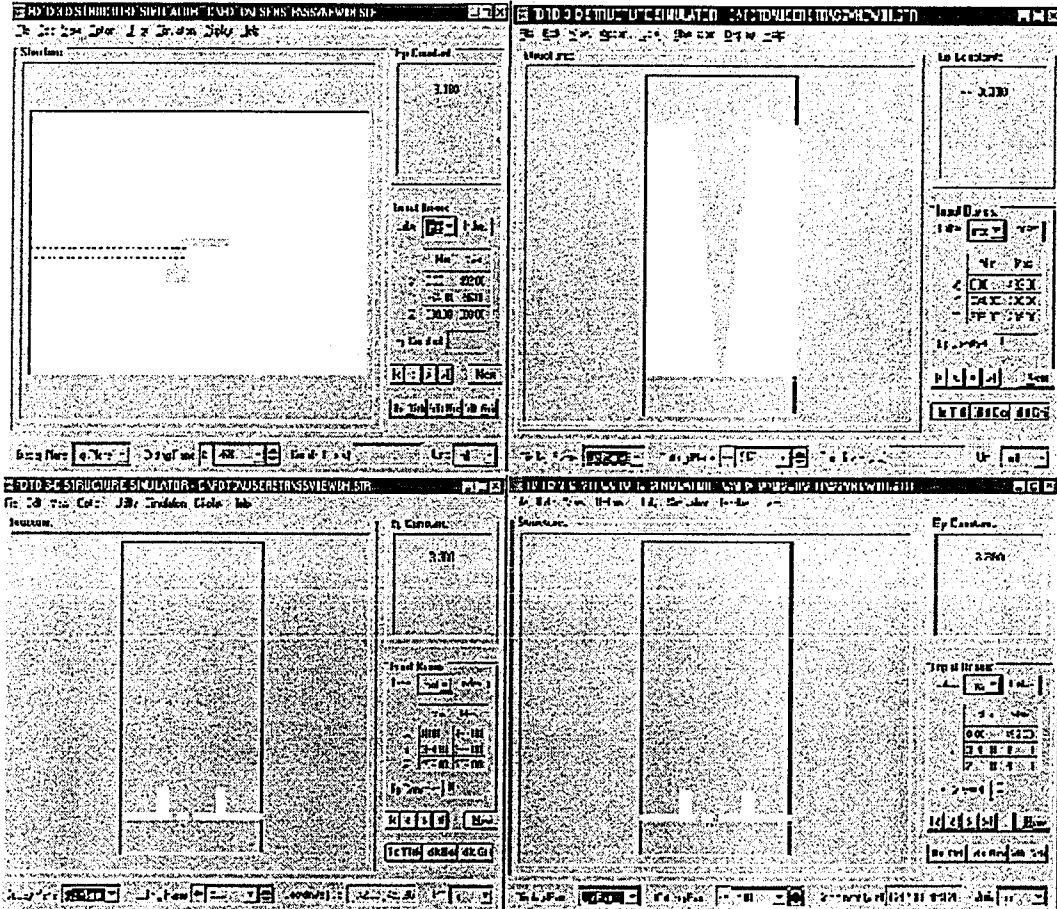
Figure 2.31 Four different views of the SML fed 'Hockey Stick' slot coupled LTSA in FDTD 3D SS.

Upper-left: 'Hockey Stick' slot in the ground of the SML for view-A in Figure.2.30; **Upper-right**: Radiation element of the LTSA for view-B in Figure 2.30; **Lower-left**: view-C in Figure 2.30; **Lower-right**: view-D in Figure 2.30

a = 8mil, b = 20mil, ε_r = 3.38, t = 32mil, h = 168mil, w = 56mil, W_m = 32mil, s = 32mil, u = 48mil, v = 84mil, y = 32mil, z = 64mil, l = 72mil, ll = 144mil, W = 344mil, L = 1484mil, T = 44mil, D = 288mil, d = 32mil.

(a)

(b)

(c)
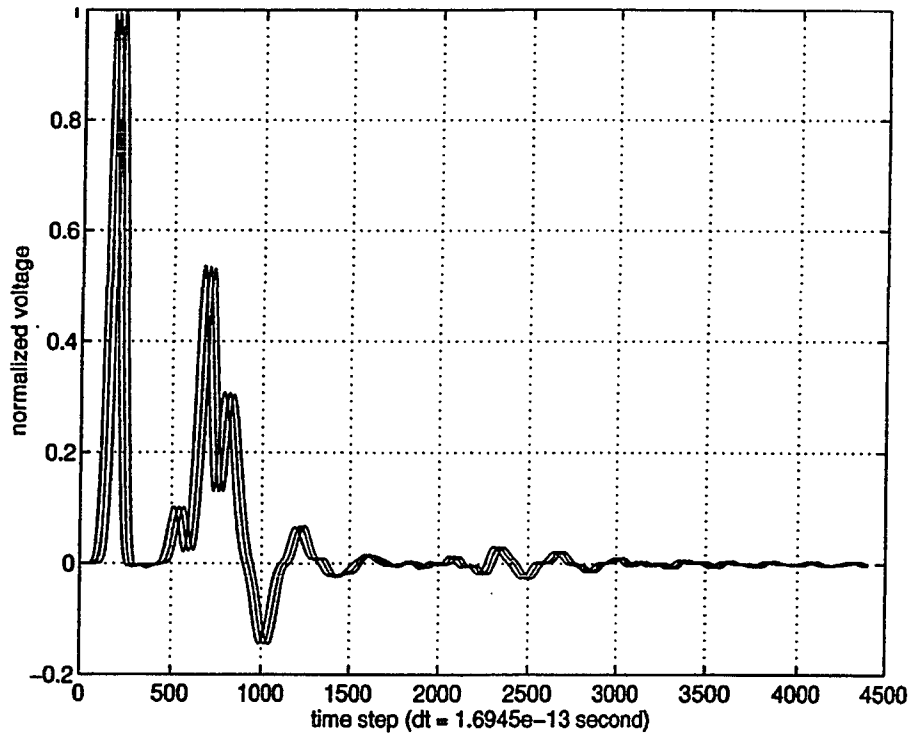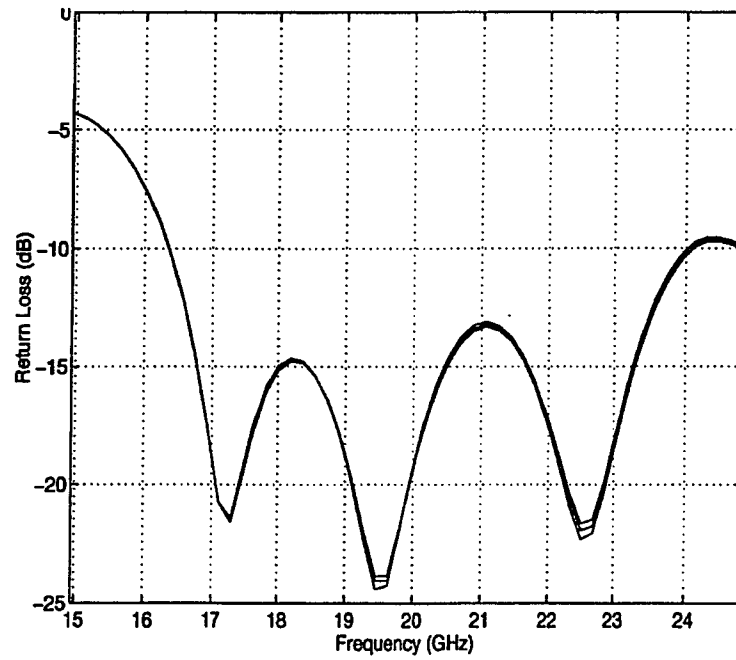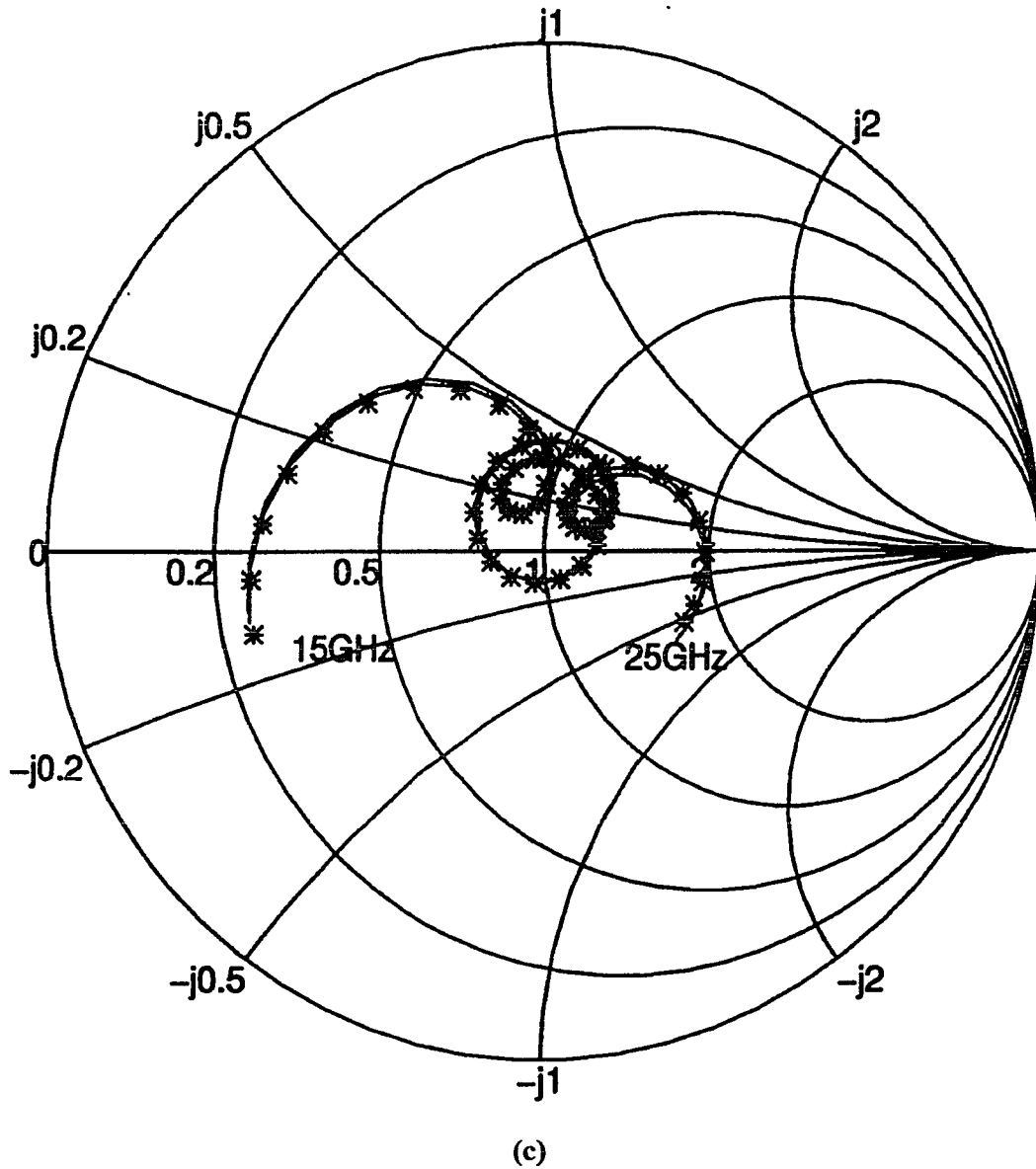
Figure 2.32 (a) Time domain data sampled on the SML, (b) return loss, (c) input impedance, the reference plane is at the center of the slot.

A 2 x 2 subarray is shown in Figure 2.33. The spacing between the elements is 346 mil. The SML BFN of the 2x2 array is shown in Figure 2.34. The FDTD simulated return loss for the 2 x 2 array is given in Figure 2.35.
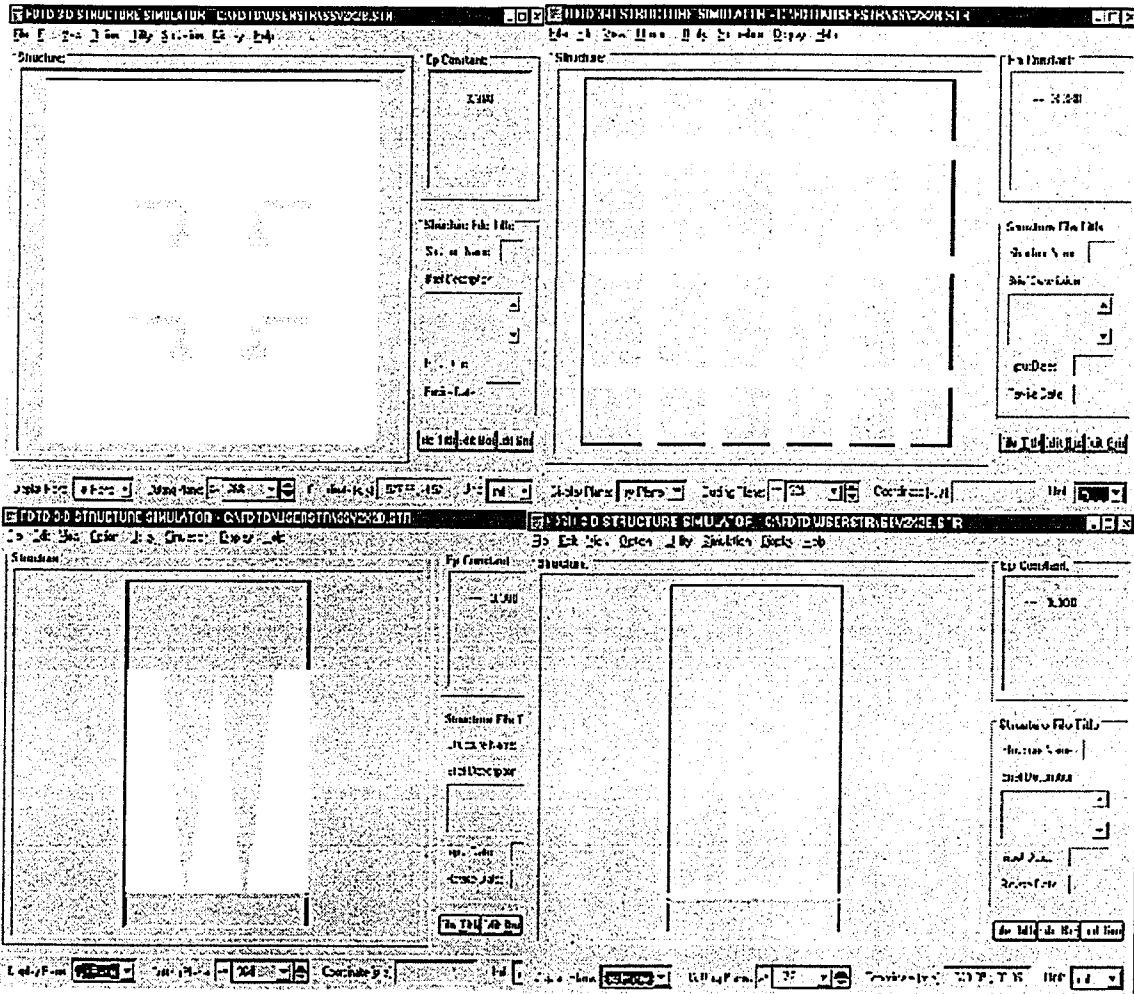
Figure 2.33 A 2 x 2 SML fed 'Hockey Stick' slot coupled LTSA array using the element in Figure 2.31.
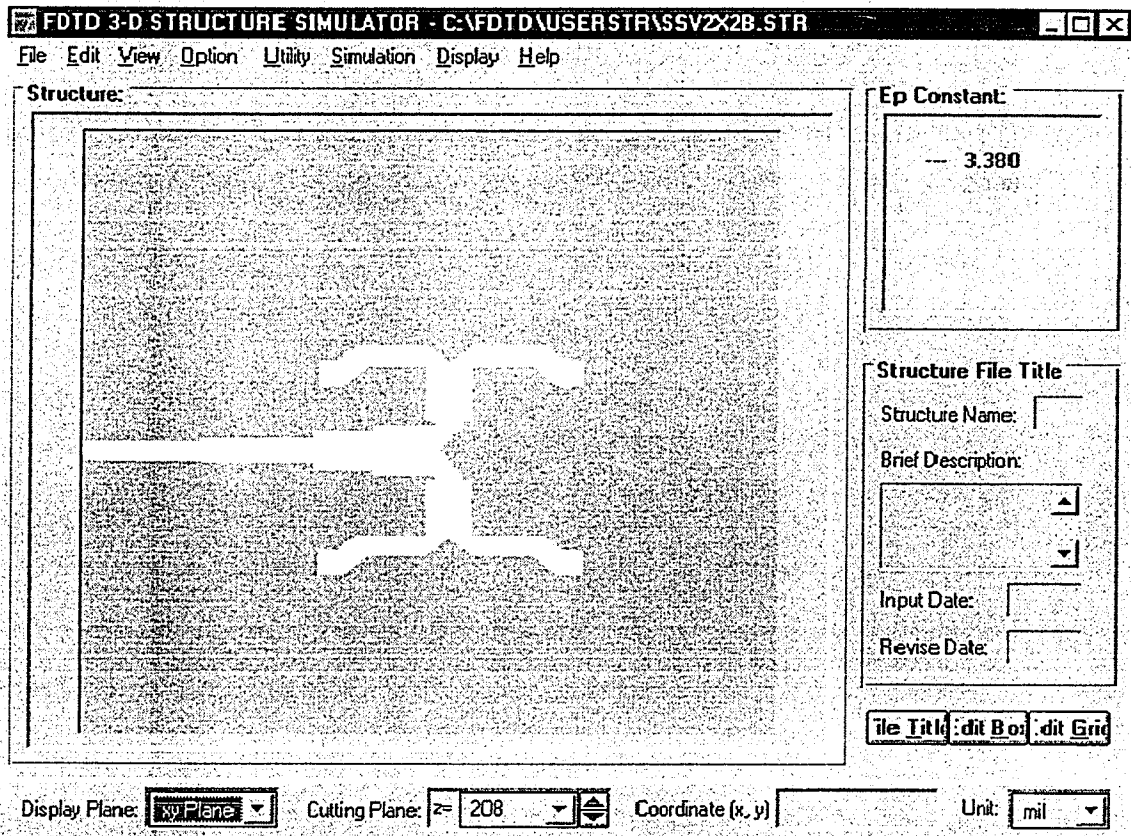
Figure 2.34 The SML BFN for the 2 x 2 SML fed 'Hockey Stick' slot coupled LTSA.
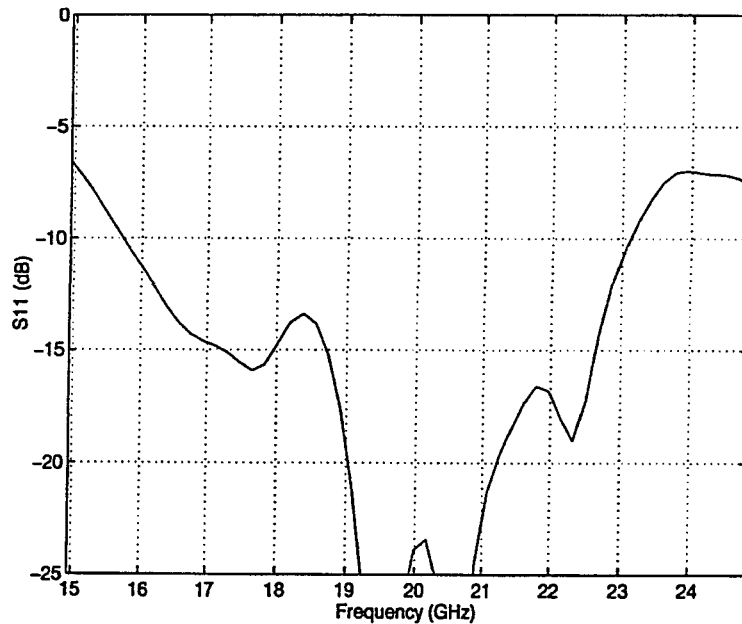
Figure 2.35 Return loss for the 2 x 2 SML fed 'Hockey Stick' slot coupled LTSA array.

To verify the new concept, a 4 x 4 SML fed 'Hockey Stick' slot coupled LTSA array was made from copper shown in Figure 2.36. The measured return loss and E- and H-plane patterns are shown in Figures 2.38, 2.39 and 2.40, respectively. The cross-polarization level in E-plane is better than −18dB, and better than −20dB in H-plane. In Figure 2.41 the measured gain is compared with the directivity, which is given by $4\pi A/\lambda_o^2$, where A is the size of array aperture. From the comparison it can be seen that the antenna has good aperture efficiency. Two sets of the metal fins were made for the 4 x 4 array given in Figure 2.37. Because of the copper material used for the fin, their thickness was 50 mil instead of 44mil. There was very little change in the measured performance of the 4x4 array using the different sets of fins. From Figure 2.37 it can be seen that side walls of the shorter fins have an about 1 degree slope. The reason for this is that if the fins were made using an injection plastic mold, then the mold would be easily opened once the molding process had been completed.
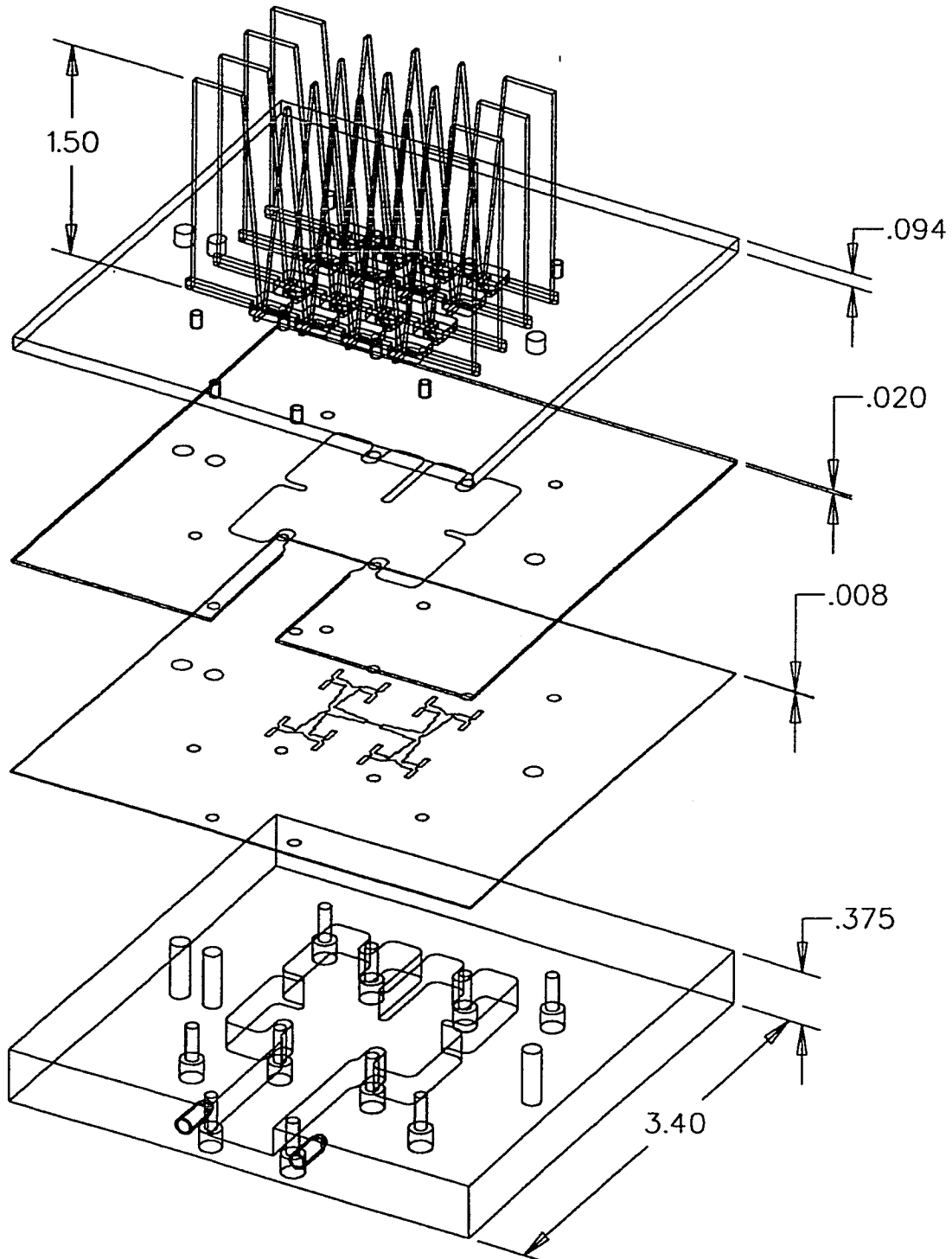
Figure 2.36 The line model of a SML fed 'Hockey Stick' slot coupled LTSA array.
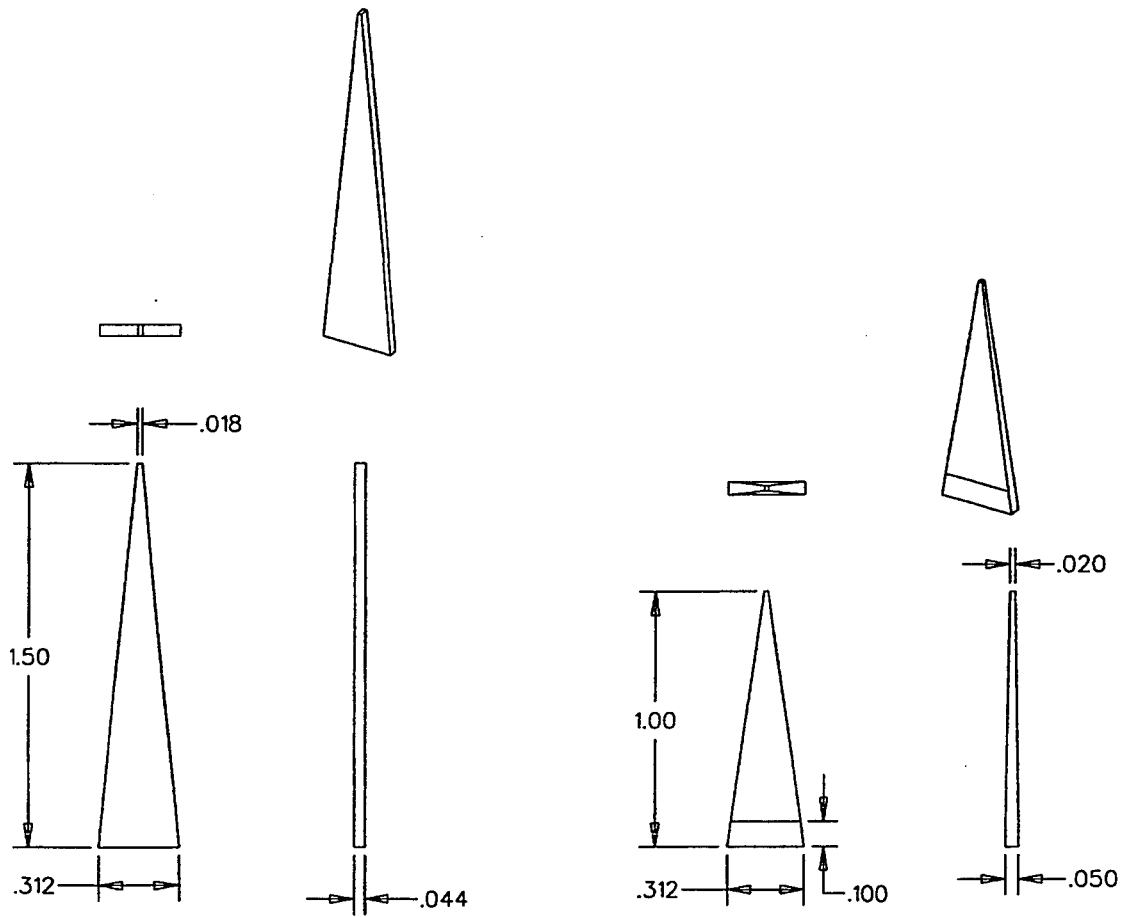
Figure 2.37 The metal fins used in the design of the 4 x 4 SML fed 'Hockey Stick' slot coupled LTSA array.
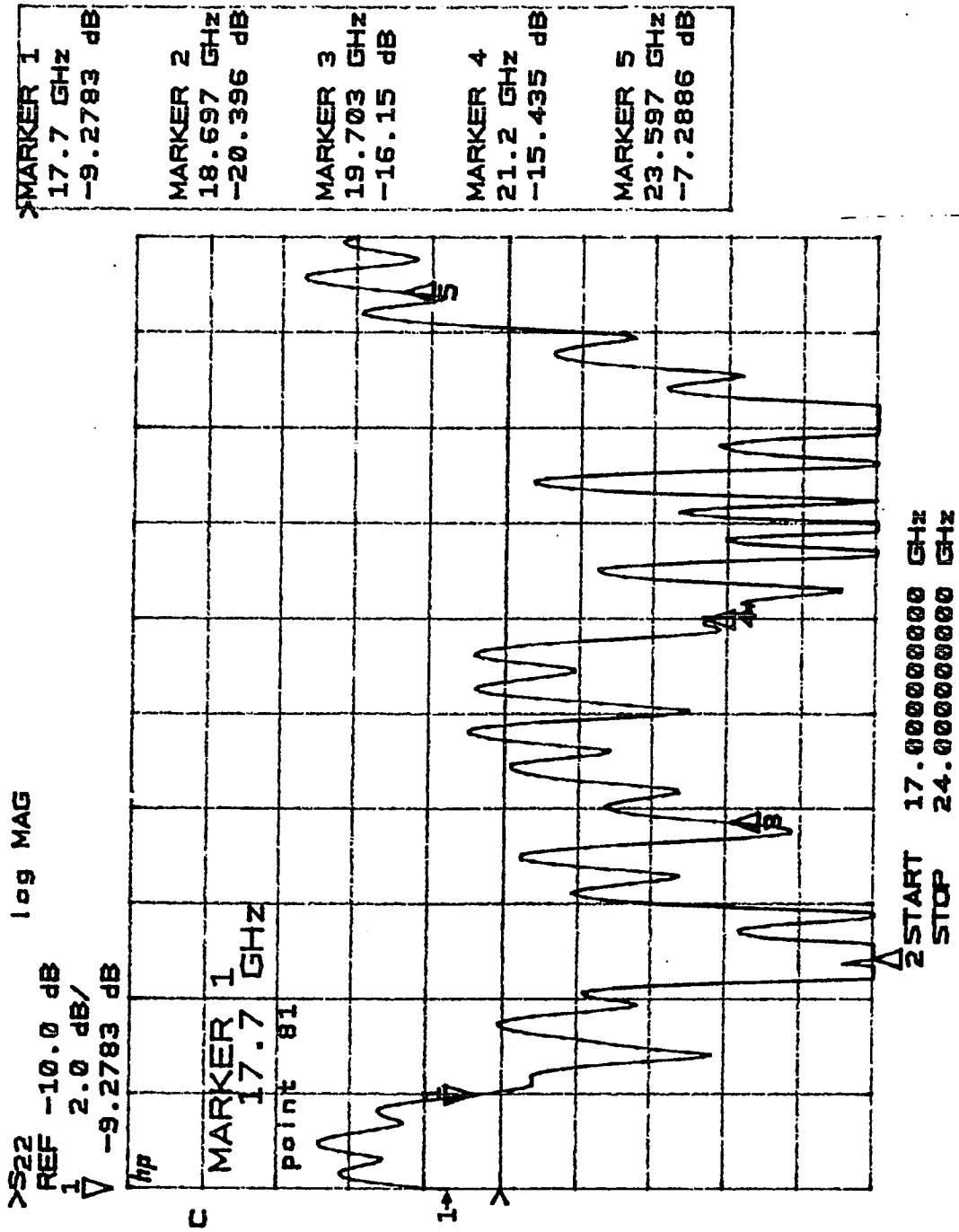
Figure 2.38 The measured return loss of the 4 x 4 SML fed 'Hockey Stick' slot coupled LTSA array.
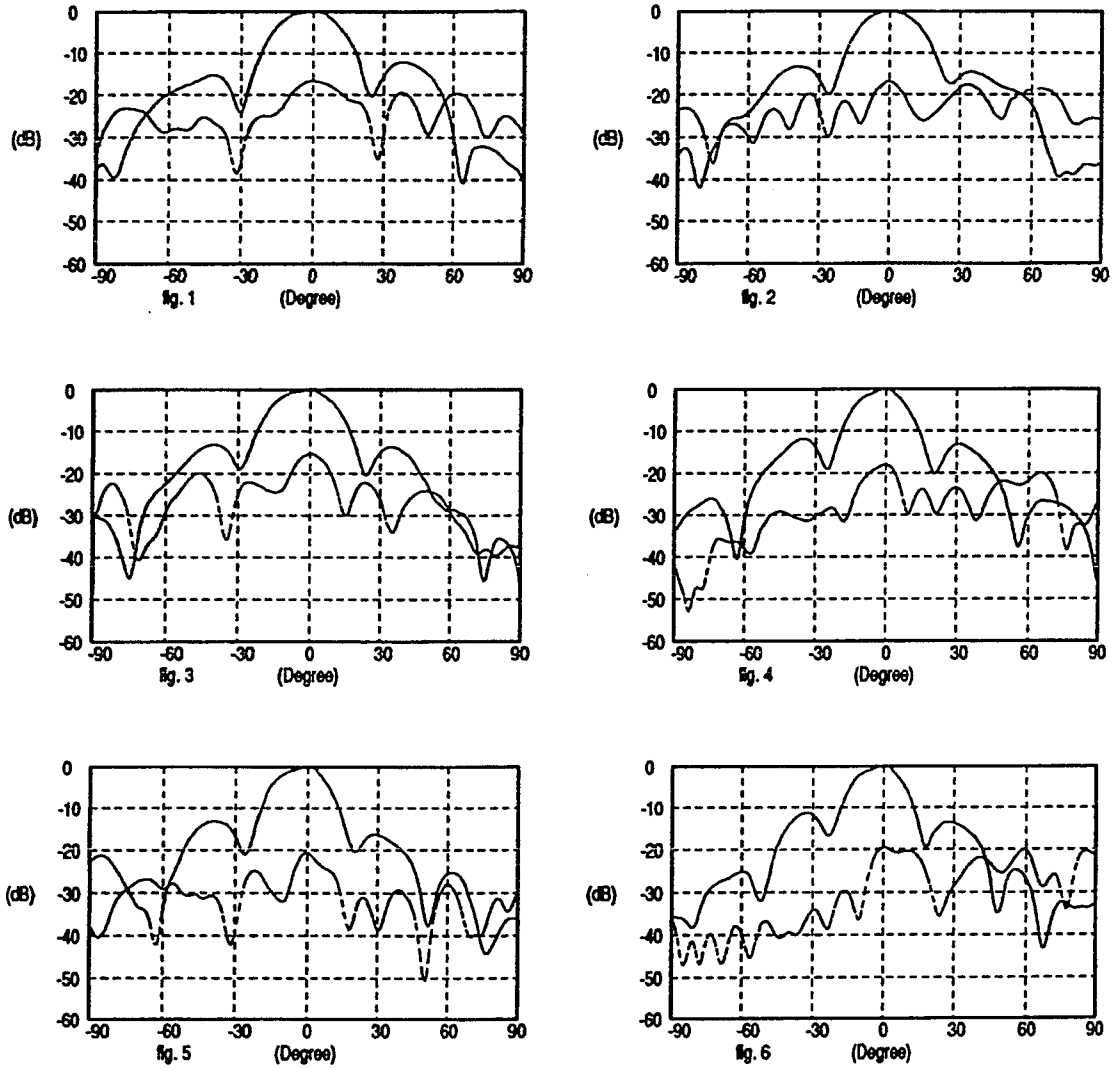
Figure 2.39 The E-plane co- and cross-polarization patterns of the 4 x 4 array. From fig1 to 6, the frequencies are 17.7, 18.7, 19.7, 21.2, 22.4and 23.6 GHz.
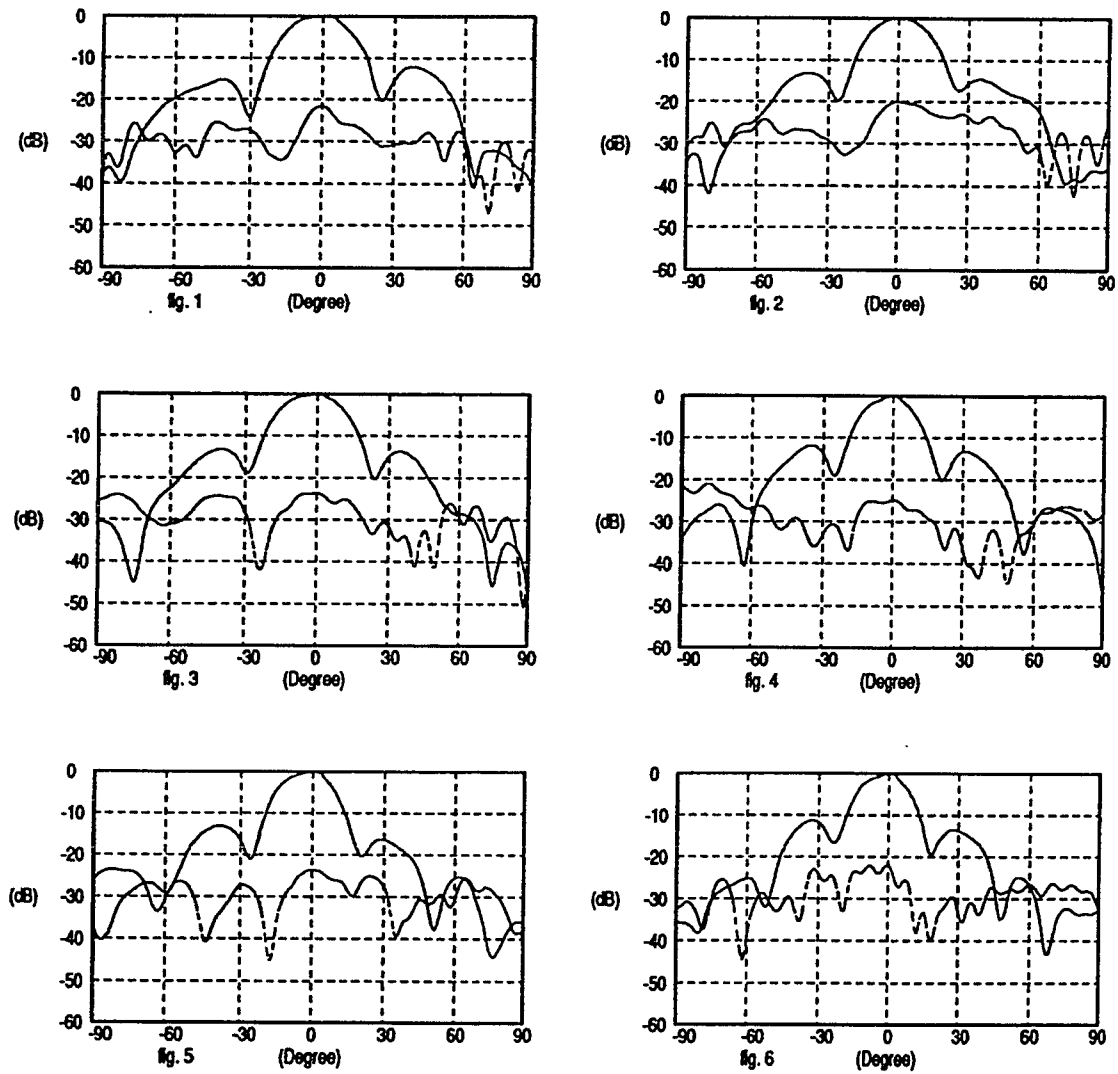
Figure 2.40 The H-plane co- and cross-polarization patterns of the 4 x 4 array. From fig1 to 6, the frequencies are 17.7, 18.7, 19.7, 21.2, 22.4and 23.6 GHz.
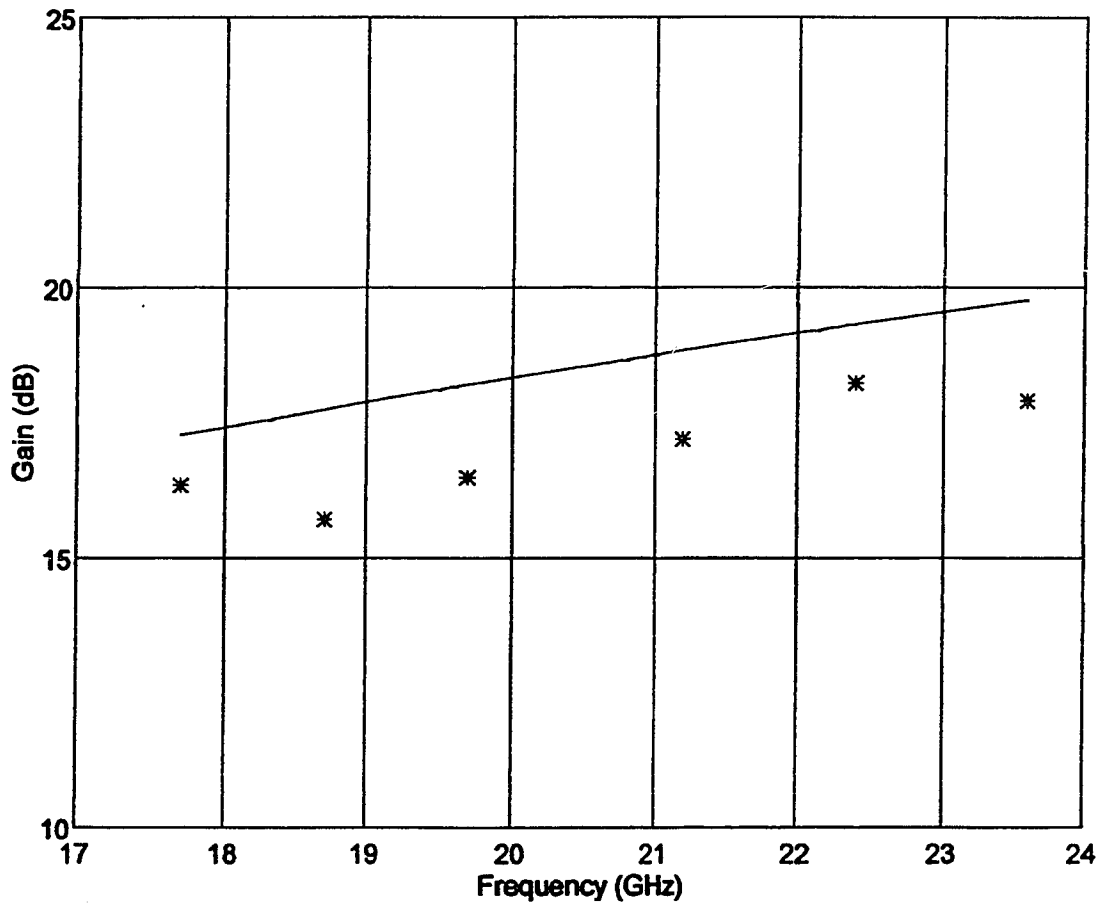
Figure 2.41 The measured gain of the 4 x 4 array.

A design for the 26 and 28GHz bands

The SML fed Hockey Stick' slot coupled LTSA shown in Figure 2.31 can also be used in 26/28GHz bands by simply changing the dimensions of the slot as follows: u = 36mil, v = 60mil, y = 28mil, z = 48mil, l = 32mil and $l1$ = 104mil. The FDTD simulated results are shown in Figure 2.42. It is obvious that the 'Hockey slot' plays an important role in this antenna structure. The size of the slot determines the operating frequency band of the antenna. It is an advantage for antenna manufacturing that the antenna element can be used in different frequency bands.

(a)

(b)

(c)
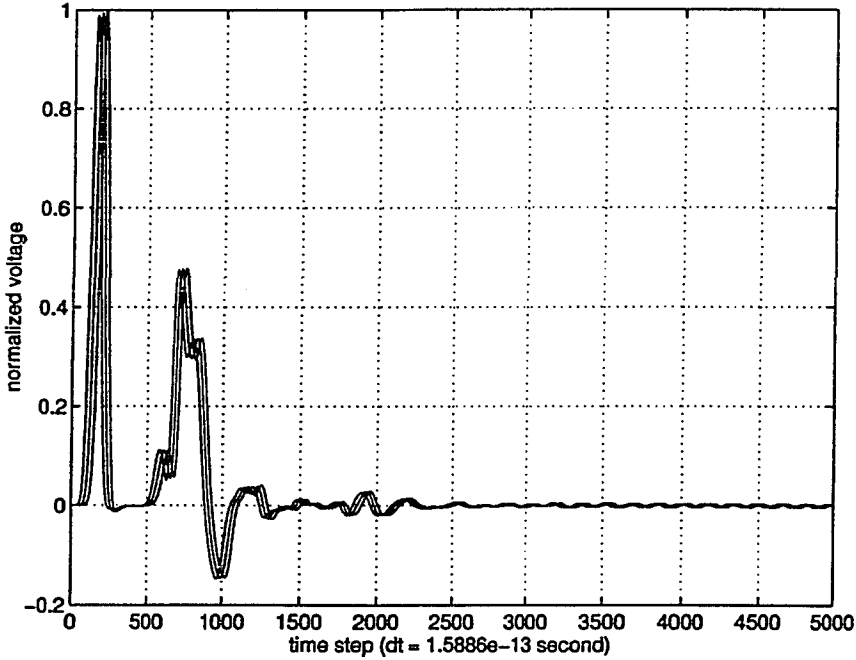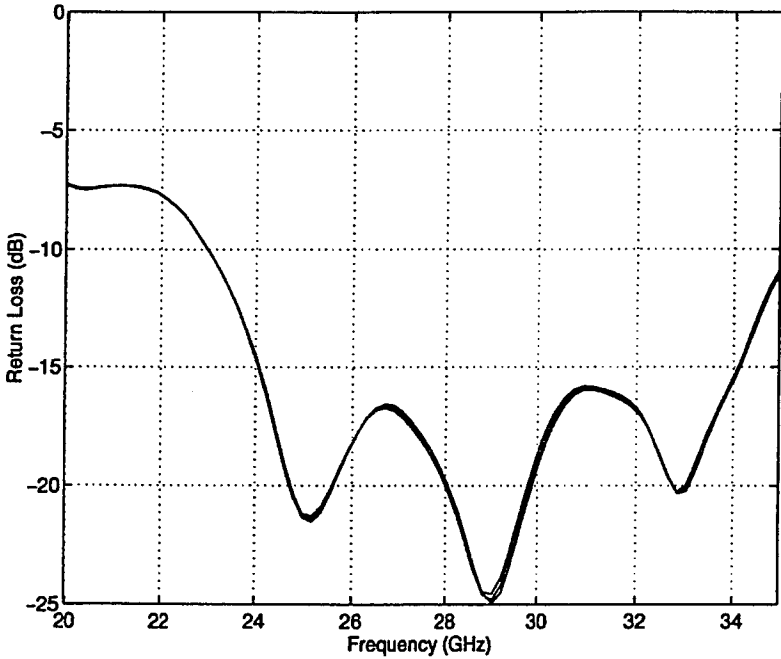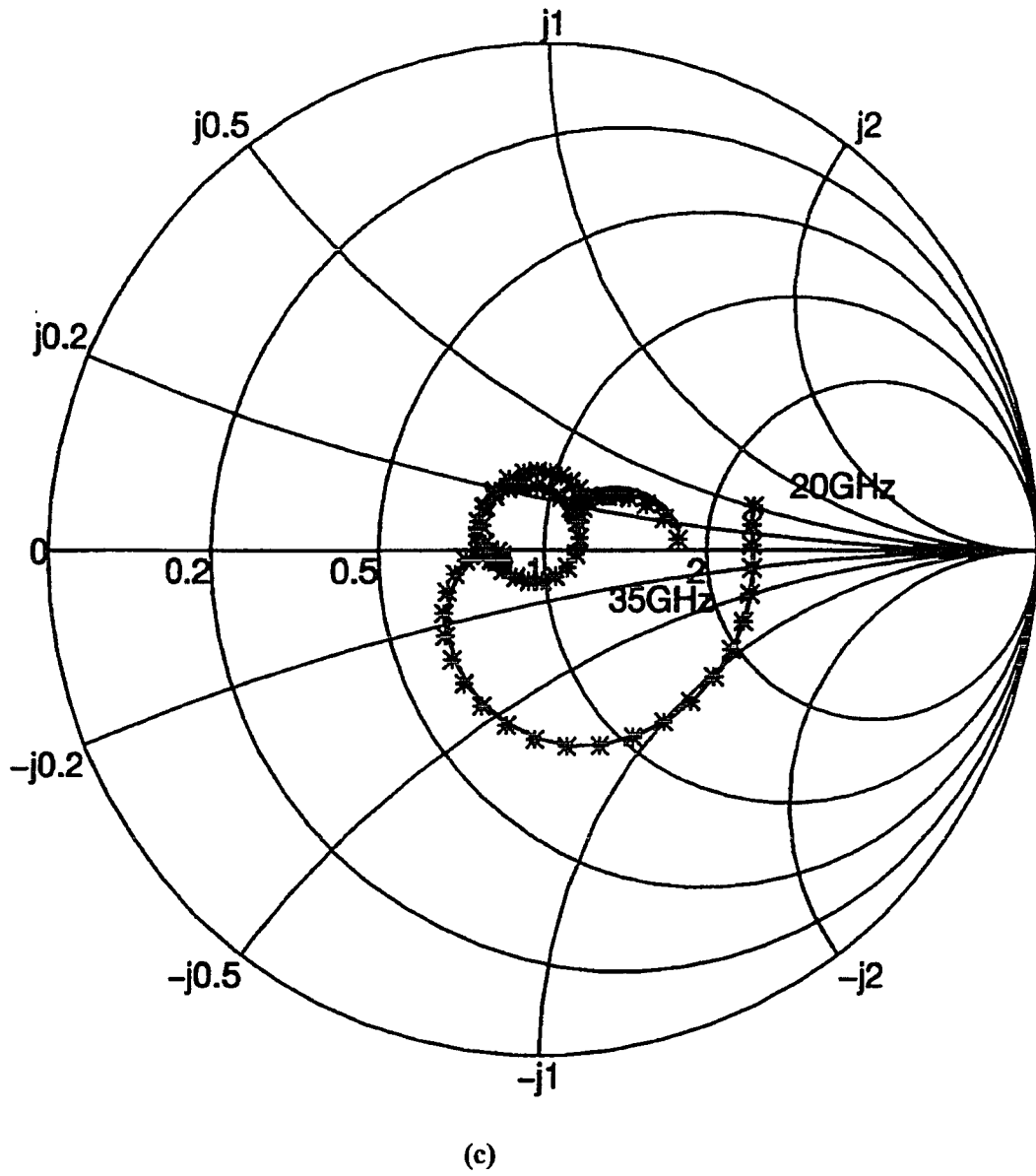
Figure 2.42 The simulated return of the 26/28GHz bands SML fed 'Hockey Stick' slot coupled LTSA. (a) time domain data sampled on SML, (b) return loss, (c) input impedance (the reference plane is at the center of the slot.)

Chapter 3 . The Applications of the Linear Tapered Slot Antennas Fed by Different Printed Transmission Lines

3.1 Introduction

Fixed point-to-point microwave communications technology has been under development for about 20 to 30 years. As the popularity of wireless communications has increased in the last few years, the importance of broadband communication has increased as well. More and more point-to-point and point-to-multipoint communication systems, in the millimeter or sub-millimeter bands, are being used for transmission of data, TV and the internet. For example, The data communication between PCS (Personal Communication Service) basestations needs 38GHz point-to-point communication systems. The Local Multipoint Distribution Service (LMDS), which can provide interactive video and high speed data access service along with broadcast and telephony, requires 28GHz point-to-multipoint communication systems. The Wireless Local Network (WLN) also requires point-to-point or point-to-multipoint communication systems.

The parabolic reflector antenna is currently the most popularly high-gain antenna used for fixed point-to-point communications. As flat panel antenna (FPA) technology develops, more and more users are likely to adopt FPAs mainly because FPAs have a low profile, light weight and reasonably cheaper than parabolic reflector antennas, etc. Sometimes FPA also means Flat Plate Antenna.

3.1.1 A Brief Review of the Flat Panel Antenna Technology

The printed antenna is possibly the most recognizable FPA technology. The concept of creating antennas from printed circuits provides the antenna engineer with an opportunity to

102

construct very thin planar antenna structures [59] [60] [61] [62]. These antennas are usually cheaper, have a low profile and will conform to the supporting structure. There are a number of printed shapes, which can be used as radiating elements, for example, rectangular patches, circular patches, printed dipoles, printed folded dipoles, CPW antennas, slots etched in a metal ground plane etc. Most of these radiating elements are resonant structures, so these antennas usually have impedance bandwidths that extend over a few percentage points.

Anyone contemplating the design of some new form of FPA should first get acquainted with waveguide array configurations [63]. A linear array can be formed by placing several slots periodically along a waveguide transmission line with suitable orientations. The slots radiate power from the incident waveguide mode that may then be reflected by a terminal short circuit to create a narrow-band resonant array. Alternatively, if the residue of the incident wave is absorbed by a matched load, then a broadband travelling-wave array is produced. If the power radiated by the elements has a shaped distribution across the array then the sidelobes can be reduced. The cost of a waveguide slot array is higher than that of a printed antenna, but it gives much better antenna efficiency, because waveguides have transmission losses that are lower than those of printed transmission lines. Although the dimensions of standard waveguide are very small, for example, WR42 waveguide (420 x 170mil) and WR28 waveguide (280 x 140mil), the final array thickness may be quite thick. It is because the E-and H-plane BFN may have to be very complicated in order to achieve very low side-lobe patterns.

Periodic dielectric antennas [64] [65] [66] [67] [68] [69] consist of a uniform dielectric waveguide with a periodic surface perturbation. The uniform waveguide supports a traveling wave. The surface perturbation acts as a grating that radiates the guided energy outwords. As is true for dielectric-rod antennas [44], these grating antennas are directly compatible with a dielectric waveguide. Additional advantages include ruggedness and a low profile, the antennas can be installed conformably with a (planar) metal surface, and a capability for beam scanning by frequency variation [61].

Although a 'long' element (usually $> 3\lambda_o$) is common for traveling-wave antennas (the LTSA or dielectric-rod antennas), it becomes very short when an antenna is designed for the millimeter wave band. An FPA antenna can be constructed by placing the traveling-wave elements side by side and using waveguide or printed transmission lines to feed them.

In this Chapter, the radiating elements discussed in Chapter 2 will be employed to build antenna arrays. After presenting the five-piece SML fed LTSA and the three-piece IML fed LTSA linear arrays, a 32 x 32 five-piece SML fed LTSA and a 16 x 16 SML fed 'Hockey Stick' slot coupled V-slot antenna will be described in detail. A 120-degree horizontal beamwidth and vertical polarized Vivaldi antenna will be discussed. This antenna can be used as a sector antenna in a point-to-multipoint communication circuit.

3.1.2 Parallel-fed Beam Forming Network

A parallel (or corporate) feed beam-forming network supplies excitation to each array element individually. Most parallel feed networks use equal line lengths and power dividers for directing power to each element. This means that the amplitude and phase tracking with frequency are usually quite good. The commonly used binary printed transmission line feed network is an example of such a parallel feed. The result is that a parallel-fed array will usually have good pattern and gain bandwidth. The impedance bandwidth of the overall array will be approximately limited to that of a single radiating element. The loss in a parallel feed network is usually higher than that in series feed network because a parallel feed network needs longer line lengths than a series feed network to feed the same array.

To reduce transmission line losses a combined multi-stage feed network can be used [70]. Because waveguide has much lower loss than a printed transmission line, a waveguide parallel feed network can be used to feed subarrays, and in each subarray, printed transmission lines can be used to feed the elements. In this combined feed structure a good waveguide-to-printed line transition is required and the transitions in the final array need a high degree of consistency. Another example is the use of a series and parallel feed network together to reduce transmission line loss[71].

3.2 Experimental Study of the Uniform Weighting Linear Array Using the SML Fed Five-Piece Structure

The endfire LTSA is of considerable interest as a wideband antenna element and has many potential applications. In this section the experimental investigation of the LTSA in an array environment is presented. The element developed in section 2.3.3 is used. The aim of the

work is to investigate the feasibility and performance of large LTSA arrays for MMW applications. Experimental results for 1 x 4, 1 x 8, 1 x 16 and 1 x 32 element arrays fed by the SML are presented herein.

The single LTSA element, as shown in Figure 2.11, consists of an SML, an SML-to-slot line transition and a LTSA element. The LTSA has length (L) and width (W). In order to obtain good sidelobes in the H-plane, the top cover is used to cover the SML feed network. The spacing between the SML and cover is 150~200mil. The coupling between the SML stub and LSTA was designed by using the FDTD simulator. The results show the input impedance of the LTSA element operating in the travelling mode is nearly constant (about 100 ohms) over a wide range of frequencies when the length of the antenna is more than 2 wavelengths. Table 3.1 gives the measured results for the beamwidths, gains and sidelobes of LSTA elements with different L and W, while the other dimensions are kept constant and are as shown in Figure 2.11. When the length of the antenna is increased, the beamwidth becomes narrower and the directivity is higher, but the difference between the E-plane and H-plane beamwidths are increased at the low frequency end. When L equals $3\lambda_o$ and W changes from 0.6 to $0.8\lambda_o$, the beamwidth remains almost the same at each frequency for both planes. In the 18/23 GHz bands, an optimum LTSA element has W/L = 0.2 ~ 0.25 and the length is about 3 wavelengths using an 8mil thick ε_r = 3.38 substrate to support the SML. It is very interesting to note that gains for different elements (in Table 3.1) agree closely with the gain of broadband traveling wave antenna given in Table 2.1.

A series of 1 x n (n = 4, 8, 16, 32) element arrays have been designed and built using the element described above. The element spacing is 486mil. The BFN is a parallel feed equal line length network which consists of 3dB power dividers fabricated on 8mil thick substrate (ε_r = 3.38) with a 20mil air gap to the ground as shown in Figure 2.11. The LTSA is fabricated on 20mil thick substrate (ε_r = 3.38). It is also found that the LTSA continues to provide good performance, even if a less expensive laminate is used, such as FR4 substrate (d_s = 10mil). Figure 3.1 shows the printed BFN and the LTSA elements used in the 1 x 32 element linear array, which consists of two 1 x 16 element linear arrays. Table 3.2 shows measured results of gain, beamwidth, sidelobe level and cross-polarization level for 1 x n (n = 1, 4, 8, 16, 32) element arrays. As the number of elements increases the beamwidth of H-plane does not change.

Figure 3.2 shows the measured return loss at port #1 and #2 of the 1 x 32 element array shown in Figure 3.1. It can be seen that the return loss from two output ports of the 1 x 16 element subarrays have good consistency. The typical E- and H-plane co- and cross-polarization patterns of the 1 x 32 element linear array are given in Figure 3.3. While measuring the antenna patterns, a 3dB coaxial power combiner was used to combine signals from the two output ports of the 1 x 16 element subarrays.

		$L=3\lambda_o$, W=0.6λ_o			$L=3\lambda_o$, W=0.8λ_o			$L=2.5\lambda_o$, W=0.7λ_o			$L=2\lambda_o$, W=0.7λ_o		
F (GHz)		17	21	24	17	21	24	17	21	24	17	21	24
BW	E	48	36	30	47	39	32	49	38	32	50	41	38
(^{0})	H	27	33	20	36	32	30	46	39	35	57	49	42
Gain (dBi)		9.5	9.7	10.1	9.4	9.5	10.3	8.9	9.1	9.3	8.1	8.4	8.7
SLL	E	13	14	15	14	14	15	12	11	12	10	10	9
(dB)	H	11	10	9	10	9	12	12	12	12	13	13	10

Table 3.1 Measured results of beamwidth, gain and sidelobe level for different LTSA elements.

Element		1 x 1			1 x 4			1 x 8			1 x 16			1 x 32		
F (GHz)		17	21	24	17	21	24	17	21	24	17	21	24	17	21	24
BW	E	47	39	32	19	16	13	8.7	7.8	6.3	4.4	3.6	3.2	2.2	1.8	1.6
(^{0})	H	36	33	30	37	34	31	38	35	31	38	34	31	38	36	30
G (dBi)		9.5	9.7	10.1	15	14.2	15	17	18.9	19.1	19.7	20.9	21.5	22.0	23.2	24.1
SLL	E	13	14	15	15	18	14	13	14	16	15	14	15	13	13	14
(dB)	H	11	10	9	11	10	10	12	10	9	11	12	11	18	15	15
Cross-pol	E	16	23	22	20	18	17	20	12	21	16	17	18	16	21	23
(dB)	H	10	9	10	11	10	11	9	10	11	10	11	12	13	16	19

Table 3.2 Measured results of beamwidth, gain, sidelobe level and cross-polarization level for the arrays with different number of elements.

The LTSA radiating elements

2.8"

16.16"

1.195"

The spacers

Printed SML BFN

port #1

prit #2
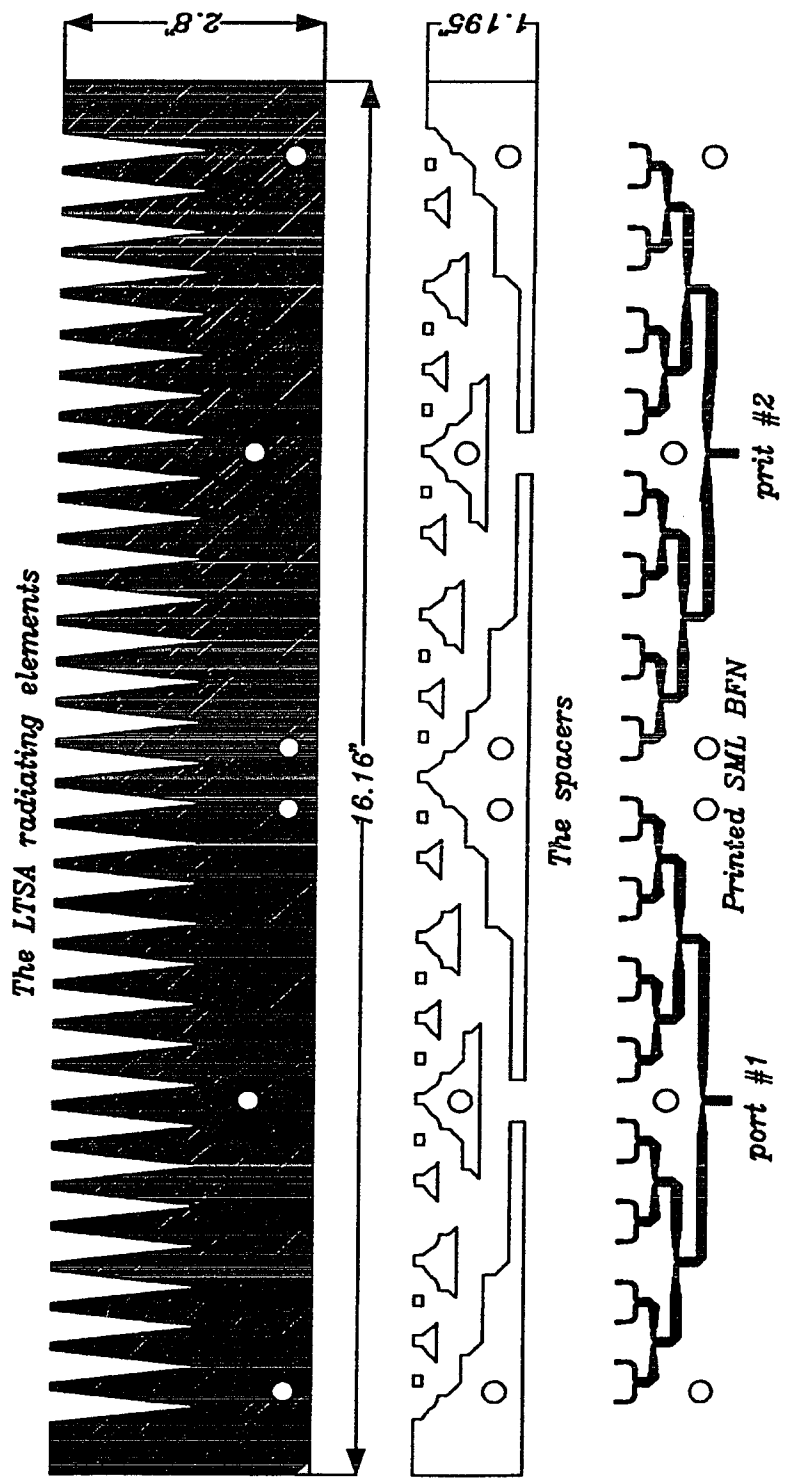
(a)
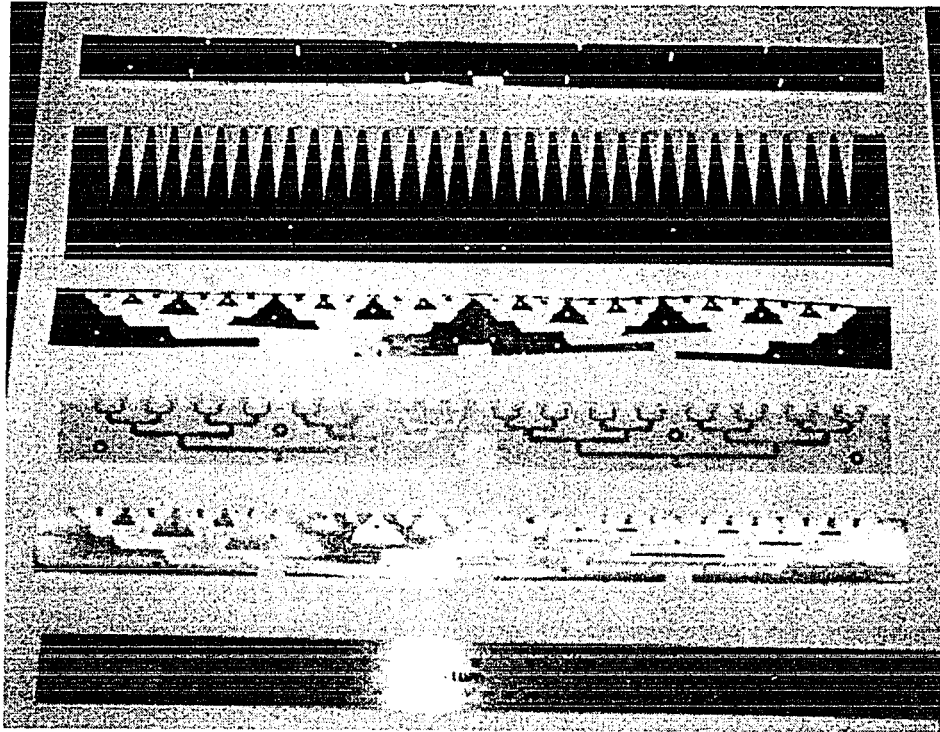
(b)

Figure 3.1 (a) The layout of the 1 x 32 element uniform weighting LTSA array, which is formed by two 1 x 16 element subarrays. The SML BFN, top view of spacers (middle) and the LTSA elements with coupling slots, (b) A photo of the 1 x 32 element SML fed LTSA array.
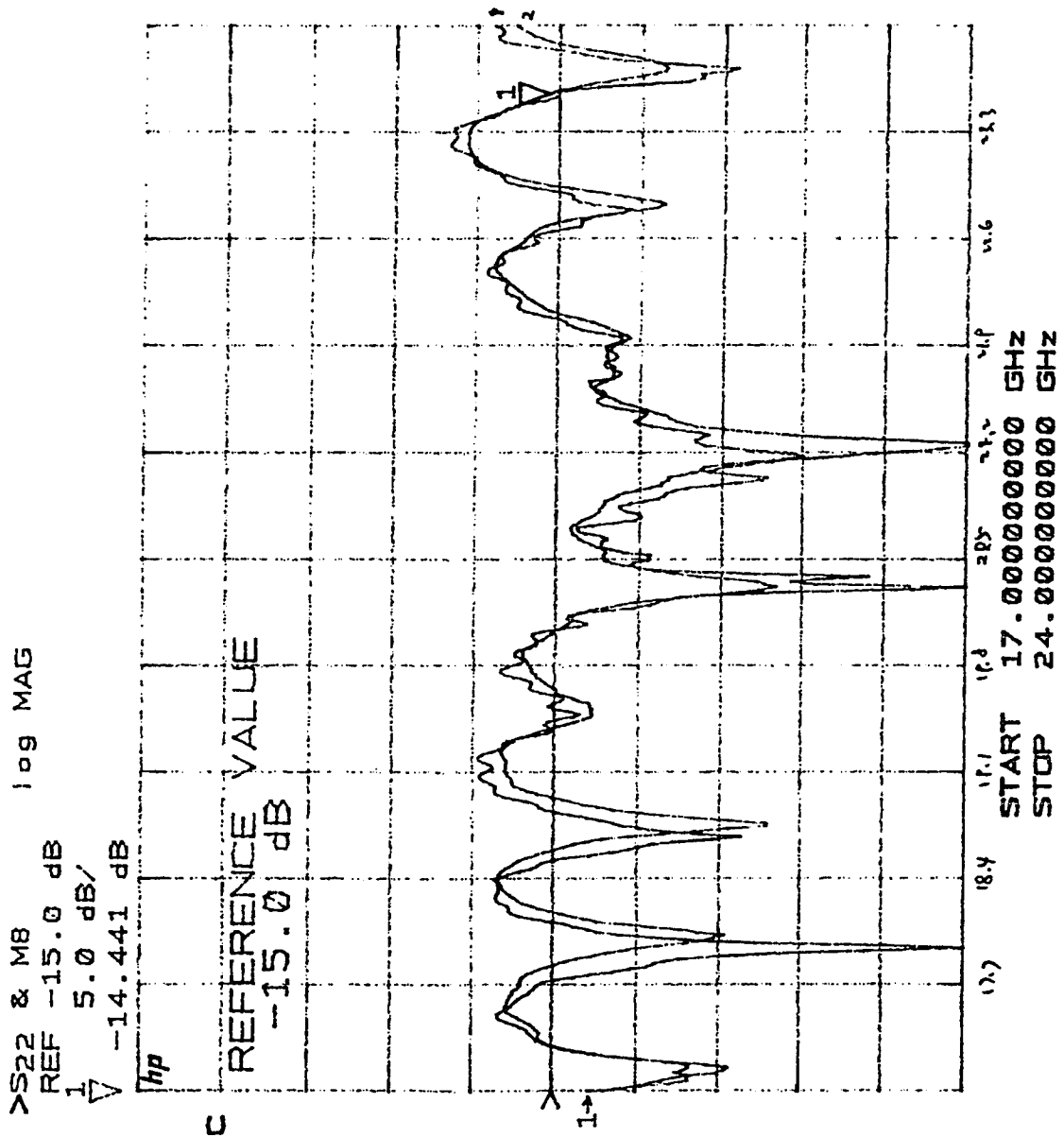
Figure 3.2 The measured return loss at port #1 and #2 for the 1 x 32 element LTSA array.
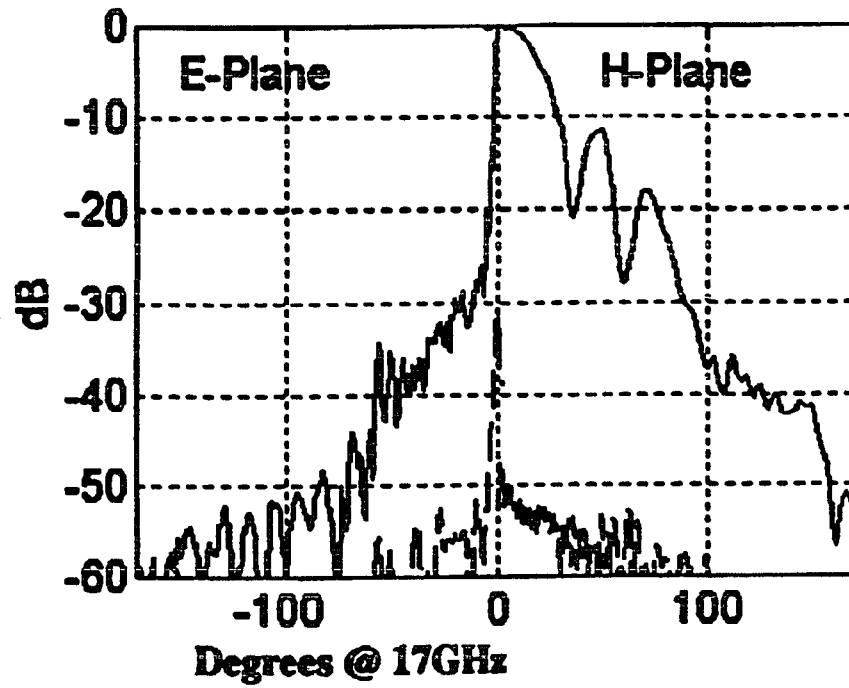
(a)
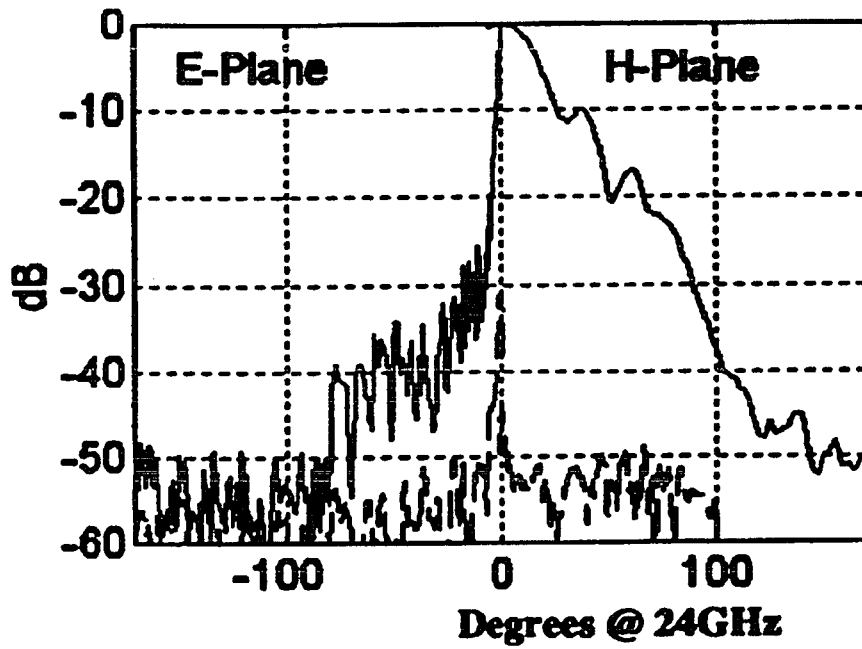
(b)

Figure 3.3 The typical measured (a) E- and (b) H-plane co-polarization and cross-polarization patterns of the 1 x 32 element array.

3.3 An 1 x 16 Element Uniform Weighting Array Fed by IML (the Three-Piece Structure)

In Chapter 2 we discussed the design of the three-piece IML fed LTSA element using FDTD 3D SS, and investigated the mutual coupling between elements. To prove the concept a 1 x 16 element uniform linear array was built. The radiating elements and the bottom plate are shown in Figure 3.4. The element spacing in the array is 468mil, as well.

The measured return loss, gain and E-plane patterns are given in Figures 3.5, 3.6 and 3.7, respectively. It can be seen that the array has very good input impedance bandwidth and gain. The measured gain is better than the 1 x 16 element SML fed LTSA array in Table 3.2. It is because the IML usually has a little less loss than that of the SML. The H-plane patterns are basically the same as those for a single element.

The conclusion is that the three-piece IML fed LTSA is a very good antenna element. It can be very easily used in an array environment, and the array will have excellent performance. Another advantage of an array formed by the three-piece IML fed LTSA is that all the metallic parts of the array are grounded. This is a very important feature for a large array to avoid static accumulation, which often damages printed antenna arrays.
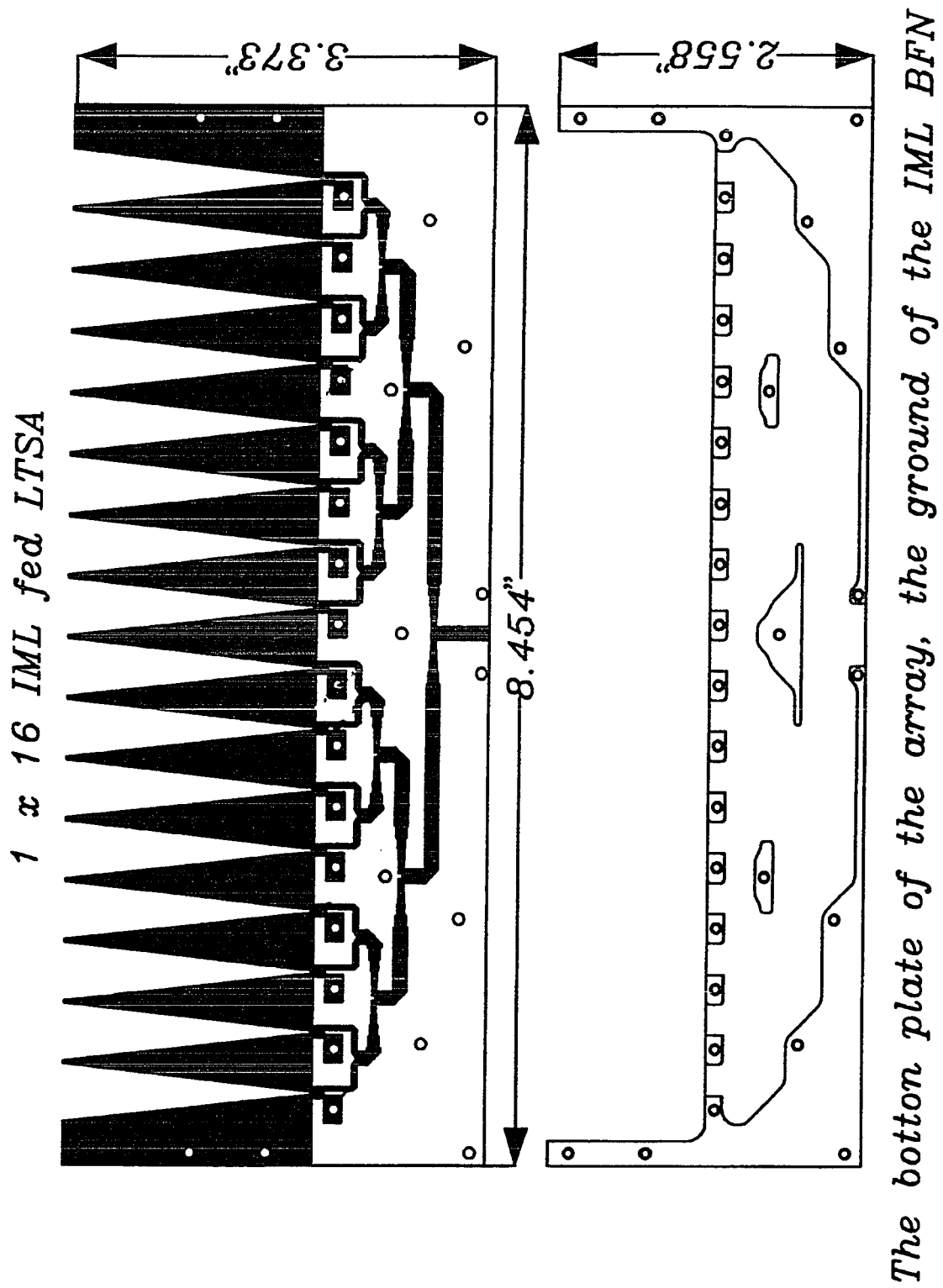
Figure 3.4 A 1 x 16 element uniform linear LTSA array fed by IML.
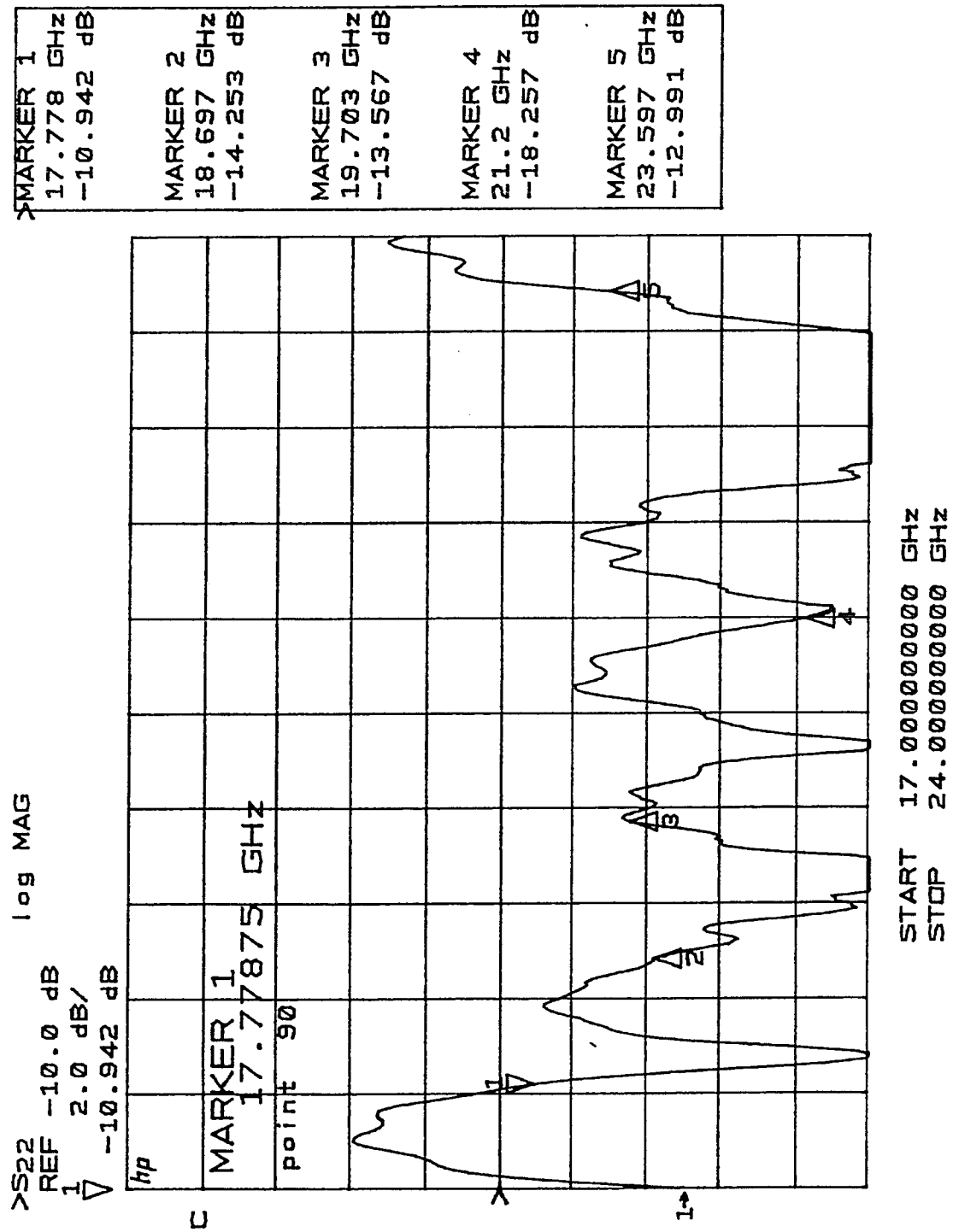
Figure 3.5 The return Loss of the 1 x 16 element IML fed LTSA array.
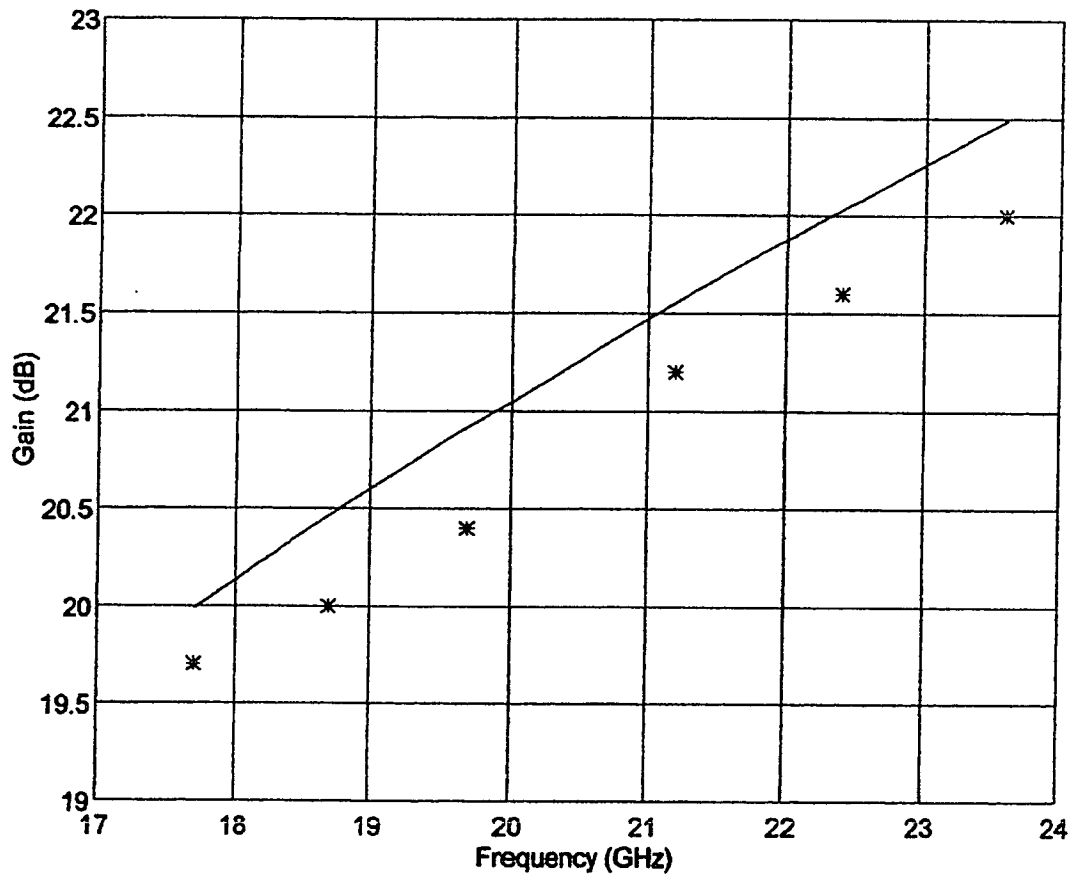
Figure 3.6 Measured gain of the 1 x 16 element array IML fed LTSA array, solid line: the directivity of the array, ***: the measured gain.
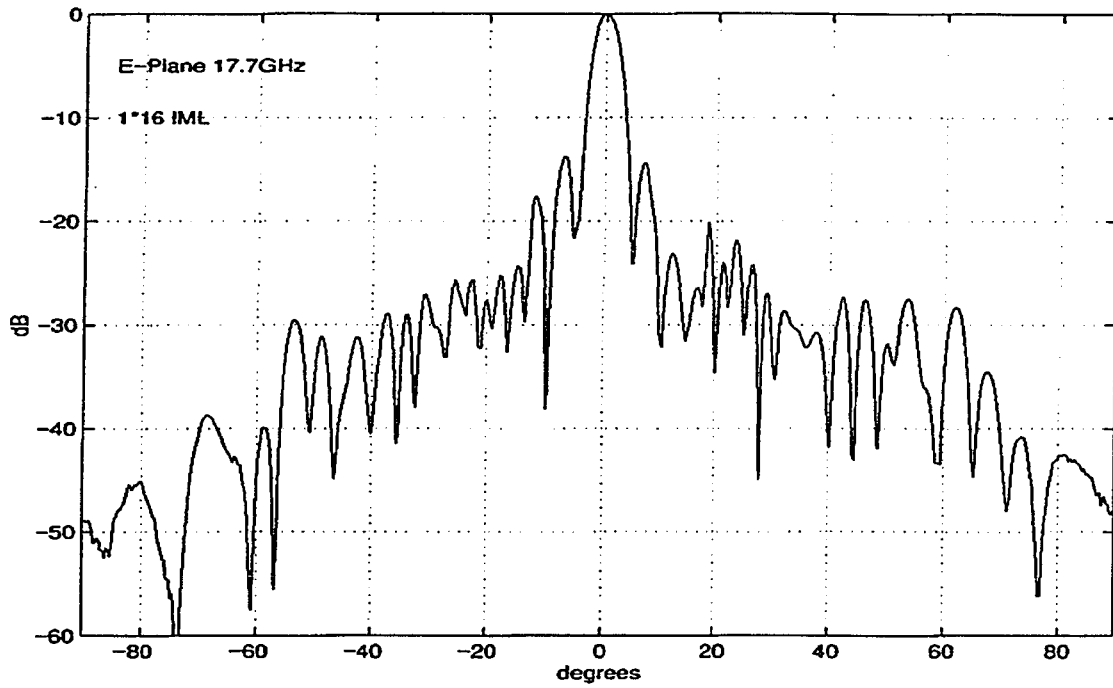
(a)
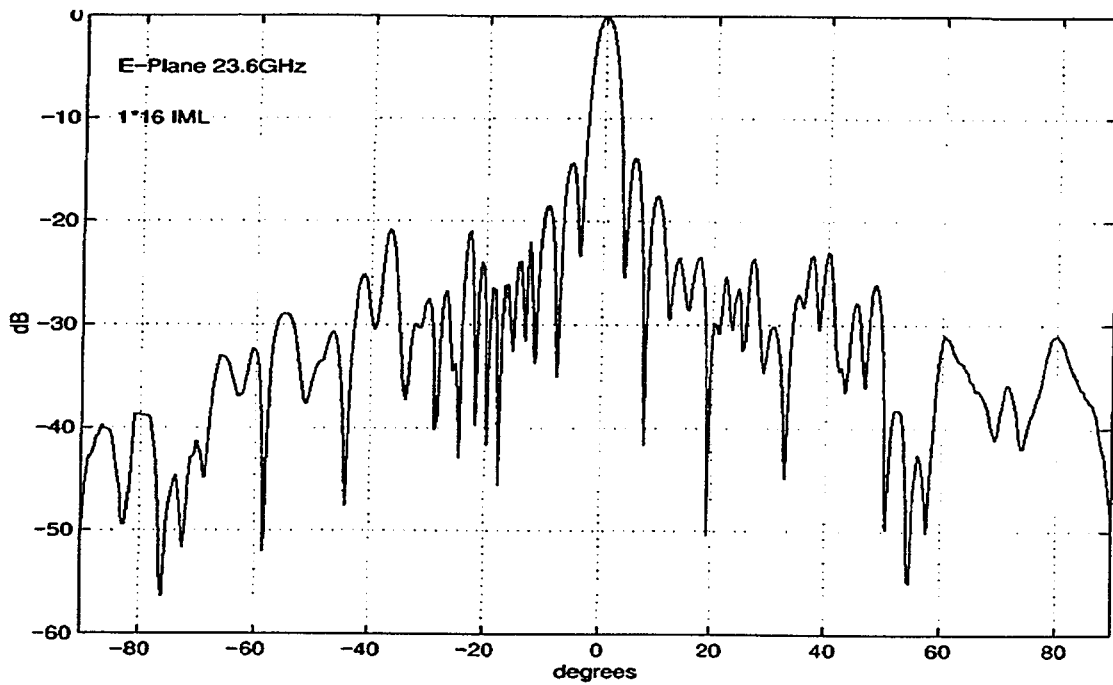
(b)

Figure 3.7 The typical E-plane patterns of the 1 x 16 element IML fed LTSA array.

3.4 A 32 x 32 Element Uniform Weighting LTSA Array

3.4.1 The Array Structure

In Figure 3.8 is shown the 3-dimensional-line model of a 32 x 32 element LTSA array fed by SML. For simplicity only one of the 1 x 32 element five-piece LTSA subarray is drawn in the model. The details of the subarray are given in Figure 2.11 and Figure 3.1. Figure 3.9 gives the top and side views of the array. From the top view of the array it can be seen that the H-plane BFN lies on the bottom of the box. The H-plane BFN is formed by a parallel-fed SML, as well. The antenna is fed by a WR42 waveguide. A waveguide-to-SML transition is used to couple energy from waveguide to SML. Once energy is coupled to the SML it is divided by two parts in the H-plane BFN, half is fed to the upper 32 output ports and another half is fed to the lower 32 output ports in Figure 3.9. A 90-degree bend, UT 141-A, semi-rigid coaxial cable is used at each output port of the H-plane BFN. 64 short cables act as transitions to connect the output ports of the H-plane BFN in the main array to the input ports of the E-plane BFN in subarrays. The array has the following main components:

Name of component	Number of piece required
Waveguide-to-SML transition [72][73][74][75][76]	1
H-plane SML BFN	1
H-plane BFN to E-plane BFN transition	64
1 x 32 five-piece SML fed LTSA subarray	32
Bottom plate	1
Radome	1
Polarizer	1
Side wall	4

Table 3.3 Name of components used in the 32 x 32 element LTSA array.

The actual size of the radiating aperture is about 15.5" x 15.5" and thickness of the array is 3.5". Figure 3.10 shows a picture of the array. The design specifications are given in Table 3.4.

Frequency band	18 and 23 GHz bands
Gain (min. dBi)	34
Beamwidth (max. ^{0})	2.2 x 2.2
Polarization	V or H
Cross-pol Level	< -30dB
SLL	FCC and MPT
Front-to-back ratio	> 50dB
VSWR	1.5 : 1
Input connector	WR42 waveguide

Table 3.4 The design specifications
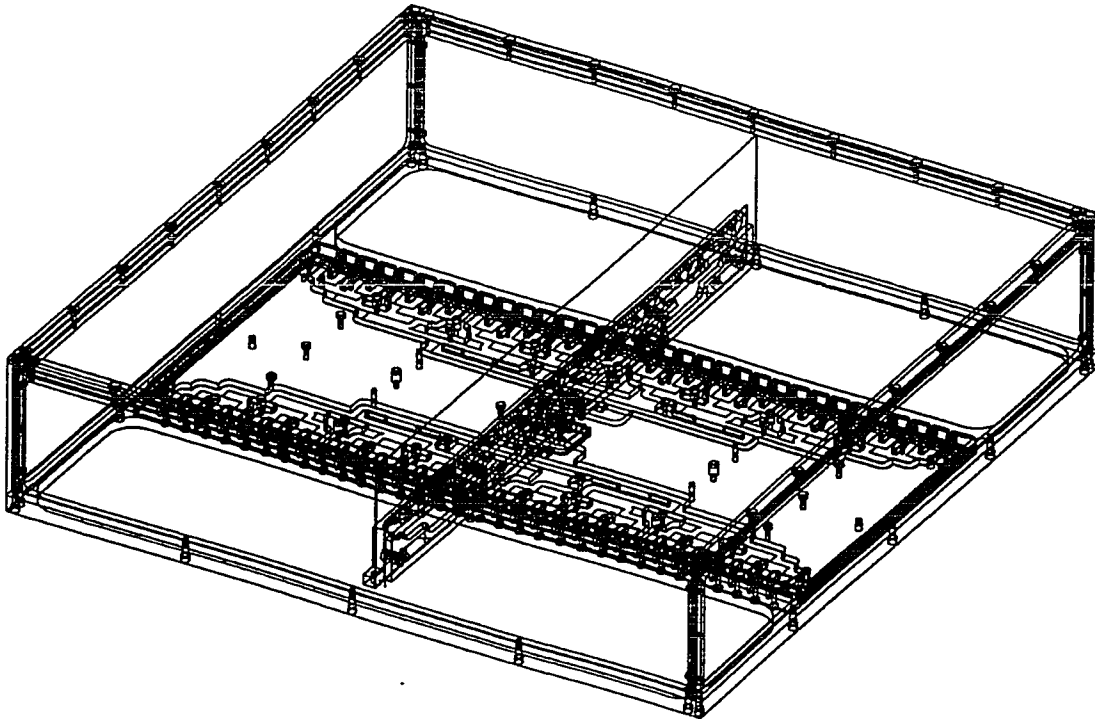
Figure 3.8 A 3D line model of a 32 x 32 element LTSA fed by the SML BFN.
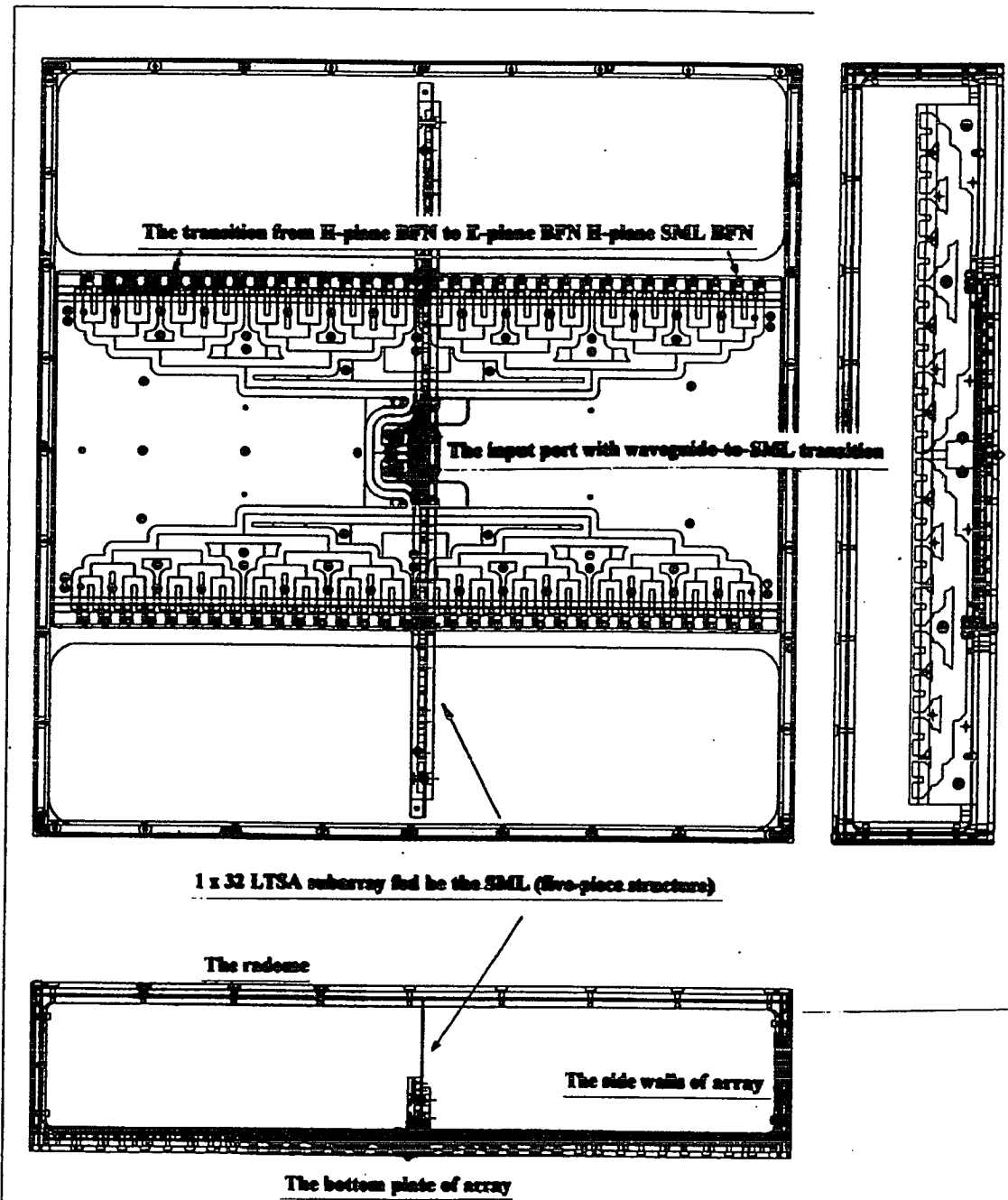
Figure 3.9 The top and side views of the 32 x 32 element LTSA fed by the SML BFN.
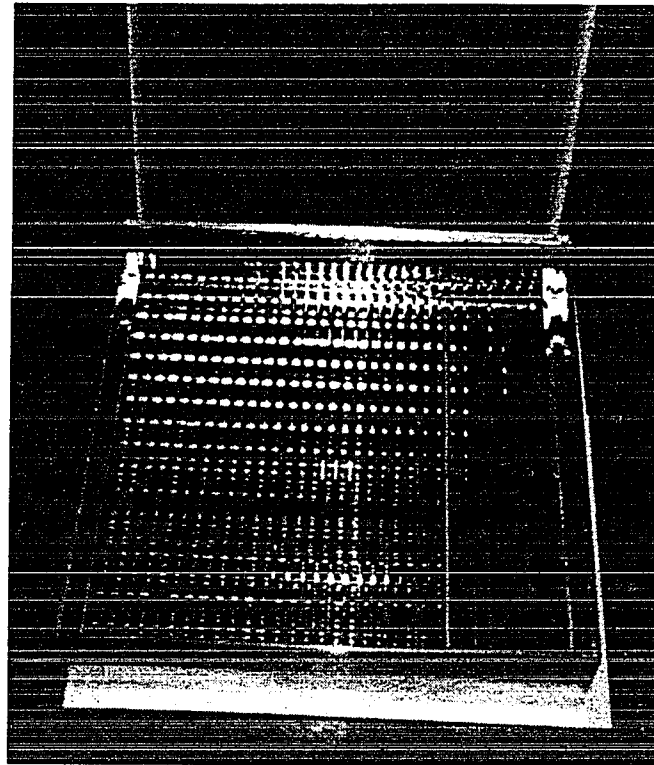
(a)
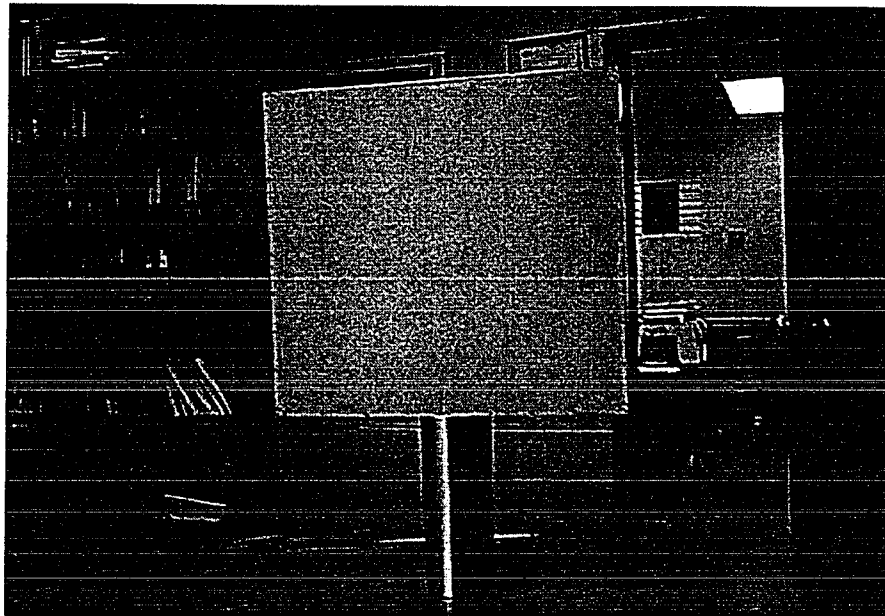
(b)

Figure 3.10 Pictures of 32 x 32 elemenet LTSA fed by the SML.

3.4.2 The Measured Results and Discussions

The measured gain, return loss, and E- and H-plane patterns are presented in Figures 3.11, 3.12 and 3.13, respectively. In Figure 3.13 the MTP1409 high performance and standard, (which is very close to FCC category-A and B antenna pattern masks), are shown with measured patterns. It is clearly seen that the array has good measured results. When comparing the measured results with the design specifications we arrive at the following conclusions:

1. From 18.1 to 23.2 GHz the antenna gain is better than 34dBi.

2. In the 18 and 32 GHz bands the E- and H-plane beamwidth are all less than 2.2^0.

3. The array can be used with either Vertical or Horizontal polarization by simply turning array 90^0, because the WR42 waveguide input port is at the center of the array.

4. All measured cross-polarization levels in both E- and H-plane are less than -30dB.

5. Measured front-to-back ratios are better than 50dB.

6. In the 18 and 23 GHz bands the VSWR is better than 2:1.

7. In general, the E- and H- plane radiation patterns are good, but some small peaks can be observed at the angles away from zero degrees.

From Table 3.2 it can be seen that the 1 x 32 element subarray has very good gain and efficiency. Based on the 3dB rule of thumb, the 32 x 32 element array should have a gain of about, 22dBi + 15dB = 37dBi at 17.7GHz. The reasons for the small peaks in patterns and also for the lower than expected gain:

i. Although some alignment tools and mechanical methods were used, we found that both the E- and H-plane elements still were not will aligned. It is difficult to keep the spacing between the subarrays a constant.

ii. It was found to be very difficult to keep uniformity among the 64 H-plane BFN to E-plane BFN transitions, because of the soldering at each of the transitions.

Items (i and ii) will cause both phase and magnitude errors in the array. The waveguide-to SML, H-plane BFN to E-plane BFN transitions and H-plane BFN introduce extra loss, as well.

From the above discussions we conclude that the design of the five-piece SML fed LTSA is not suitable for large array applications, because the design has a large component requirements, its assembly is time consuming and it is difficult to maintain consistency. But the design is a very good candidate for sector antenna applications. Please see section 3.6.
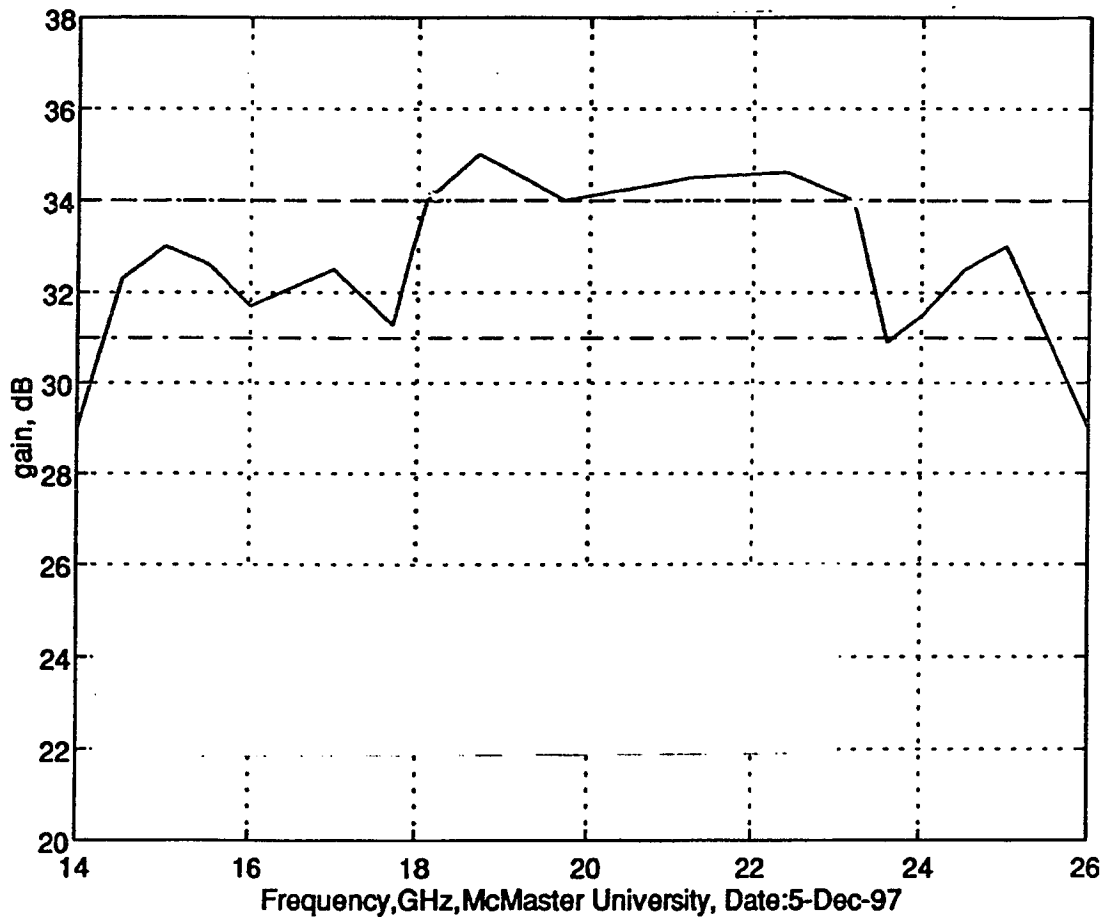
Figure 3.11 Gain of the 32 x 32 element LTSA array.
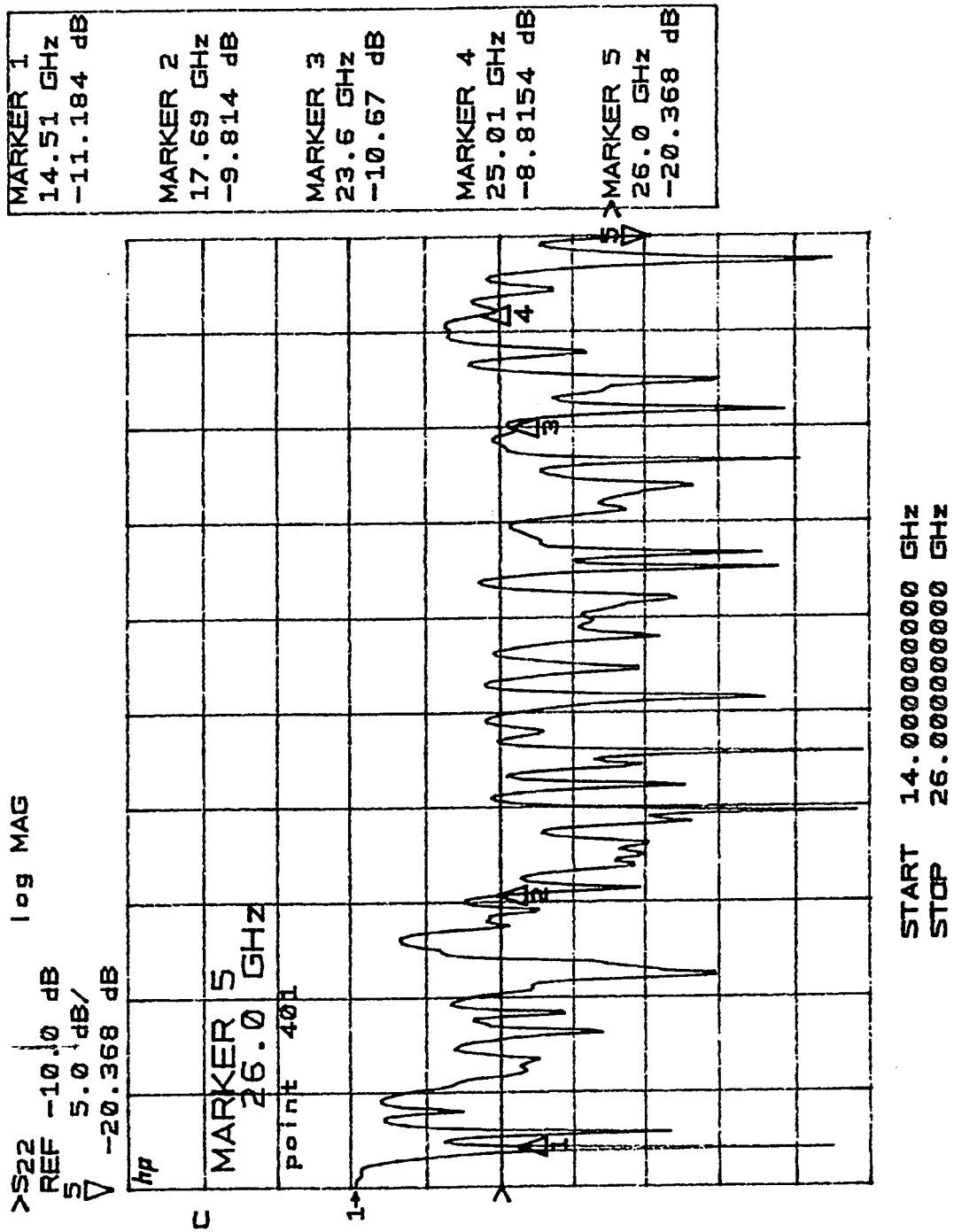
Figure 3.12 Measured return of the 32 x 32 element LTSA array.

Ant.Pat.(E-plane) of array:32*32@ 17.7GHz

Beamwith:2.2Degree

Cross.Pol.:-32.0dB

Co.pol

----Cross.pol

Degrees,McMaster University, Date:2-Nov-97

(a)

(b)

(c)

Ant.Pat.(E-plane) of array:32*32@ 21.2GHz

(d)

Ant.Pat.(E-plane) of array:32*32@ 22.4GHz

Beamwith:1.7Degree

Cross.Pol.:-30.7dB

Co.pol

Cross.pol

Degrees,McMaster University, Date:2-Nov-97

(e)

(f)

(g)

Ant.Pat.(H-plane) of array:32*32@ 18.7GHz

Beamwith:1.9Degree

Cross.Pol.:-38.6dB

_____Co.pol

----Cross.pol

Degrees,McMaster University, Date:5-Nov-97

(b)

Ant.Pat.(H-plane) of array:32*32@ 19.7GHz

(i)

(j)

(k)

Ant.Pat.(H-plane) of array:32*32@ 23.6GHz

Beamwith:1.7Degree

Cross.Pol.:-39.0dB

Co.pol

Cross.pol

dB

Degrees,McMaster University, Date:5-Nov-97

(l)

Figure 3.13 E- (a, b, c, d, e, f) and H-plane (g, h, i, j, k, l) co- and cross-polarization patterns of the 32 x 32 element LTSA array at 17.7, 18.7, 19.7, 21.2, 22.4 and 23.6GHz.

3.5 A 16 x 16 Element SML Fed 'Hockey Stick' Slot Coupled LTSA Array

3.5.1 The Array Structure

The SML fed 'Hockey Stick' slot coupled LTSA design has some advantages over the five-piece SML fed LTSA and three-piece IML fed LTSA designs. They are:

1. There are no H-plane BFN to E-plane BFN transitions;

2. There is no requirement for soldering;

3. The sub-systems are easily assembled;

4. An array can be built to be much thinner than 3.5".

After finishing the proof-of-concept, which was a 4 x 4 element array, a 16 x 16 element SML fed 'Hockey Stick' slot coupled LTSA array were designed and built. Figure 3.14 shows the line-model of the fully assembled array without side walls and a radome. A picture of the antenna is given in Figure 3.15. There are four main parts in this design. They are:

1. Main plate with fins (Figure 3.16);

2. Printed circuit board (Figure 3.18);

3. Bottom plate (Figure 3.20).

4. An SML-to-UT86 cable transition [75] [76] (Figure 3.15)

In Figure 3.16 the main plate can be made from metal or injection ABS plastic finished with copper plating. This subassembly consists of five components. They are:

1. The base plate which has alignment holes and holes for screws,

2. Fins (on the front of base plate, short version in Figure 2.37) to form the V-slots for the radiating elements,

3. Square grids (on the front of base plate) - to hold fins and support ground of SML,

4. 'Hockey-Stick' slots (in base plate, for details see Figure 3.17) - to cut current in the ground of SML and coupled energy to the V-slots,

5. Spacers (on the back of base plate) - to form an air gap of the SML .

135

In Figure 3.18 is shown a SML BFN (also see photo in Figure 3.19) which is etched on a substrate (8mil and $\varepsilon_r = 3.38$). The printed lines, spacers and back side of the base plate form the SML BFN, which is used to feed the antenna array. The functions of the bottom plate in are:

1. To act as a base-plate, to which all components are attached.

2. To act as a solid foundation, which ensures that a constant air gap thickness can be maintained for the SML BFN, and

3. To act as a cover to shield the SML BFN.
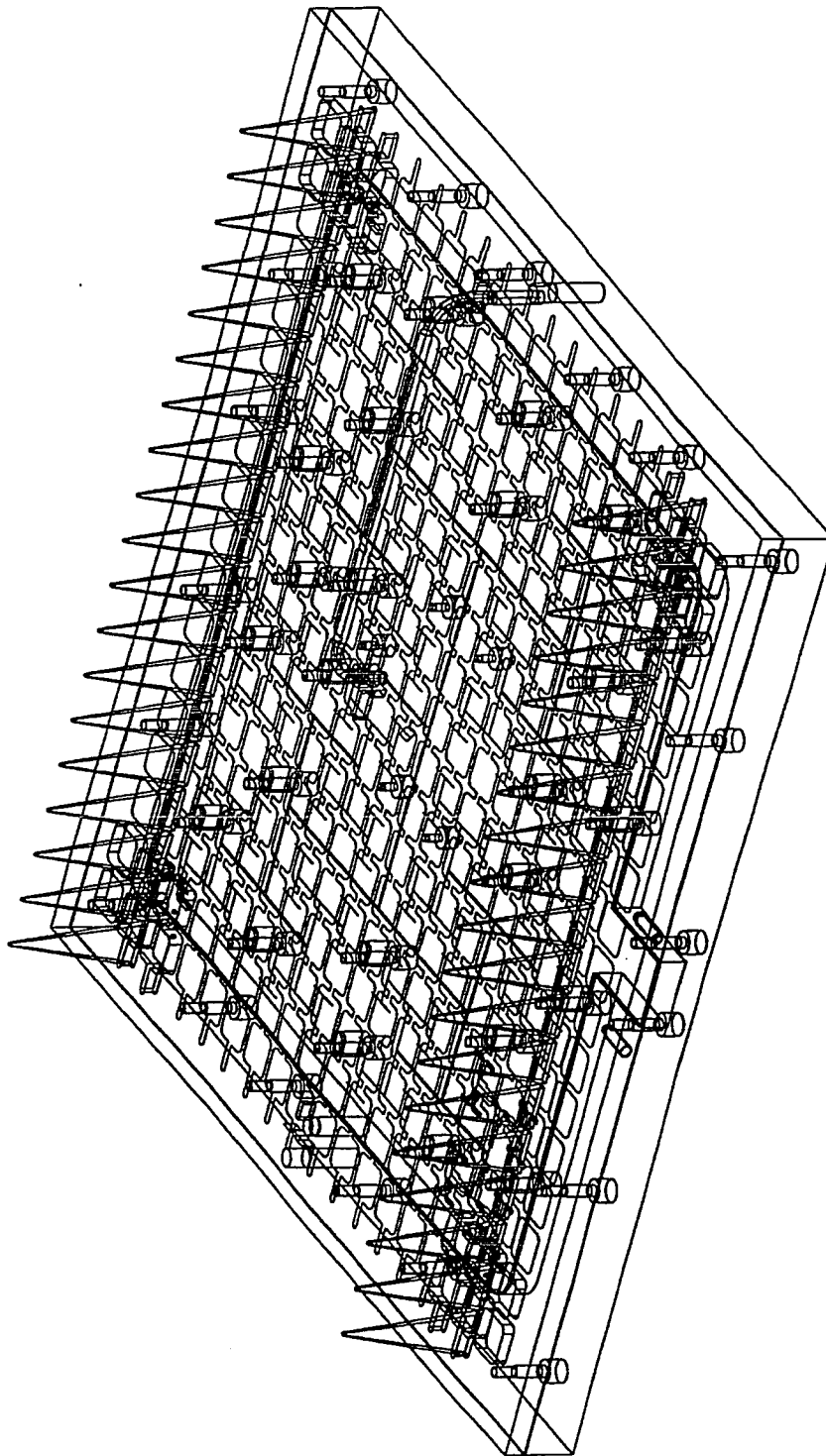
Figure 3.14 The line-model of a 16 x 16 element SML fed 'Hockey Stick' slot coupled LTSA array.

The array input port can be one of the followings, an SML, a waveguide or a coax-cable. In Figure 3.15 the antenna input port starts with an SMA connector → an one foot long UT86 low loss cable (loss about 1dB at 20GHz) → a SML-to-UT86 cable transition → the SML BFN → to each element. The SML-to-UT86 cable transition was designed using the FDTD 3D SS, as well. The FDTD 3D SS simulated the insertion loss of the transition from 15 to 25GHz to be between 0.2 to 0.4dB. The reason for using cable is that the 16 x 16 array can be used as a subarray in a large array. The results that follow were measured from the SMA connector. The array was designed to operate in the 18/23GHz bands. All the element dimensions are the same as those given in Figure 2.31. The overall size of the array is about 6 x 6 inches and overall thickness is less than 2 inches.
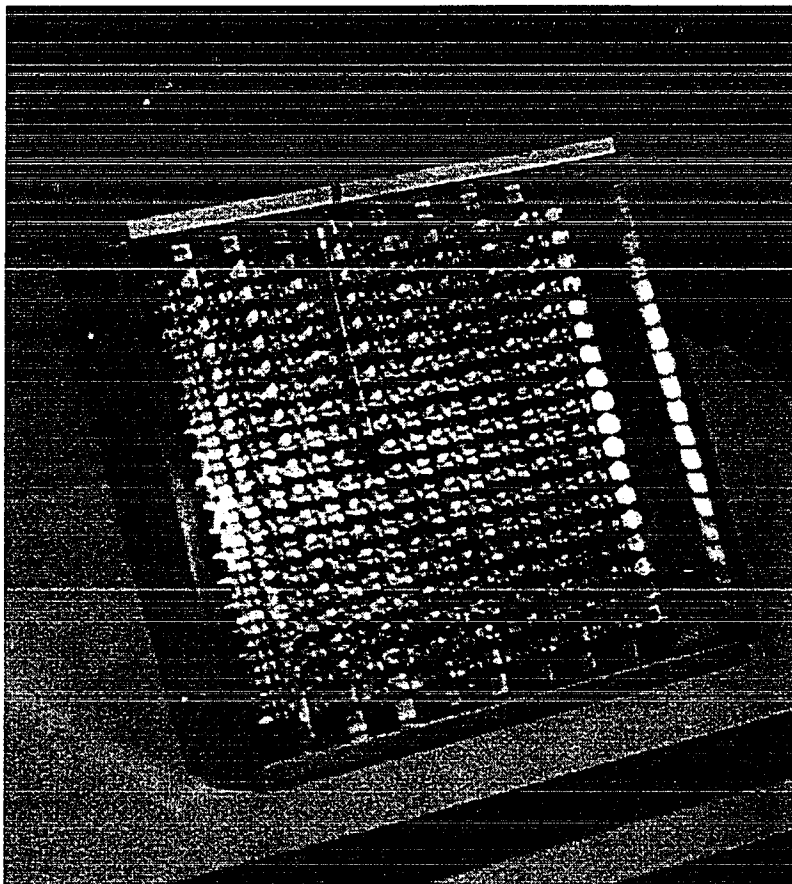
Figure 3.15 A photo of the 16 x 16 element SML fed 'Hockey Stick' slot coupled LTSA array.
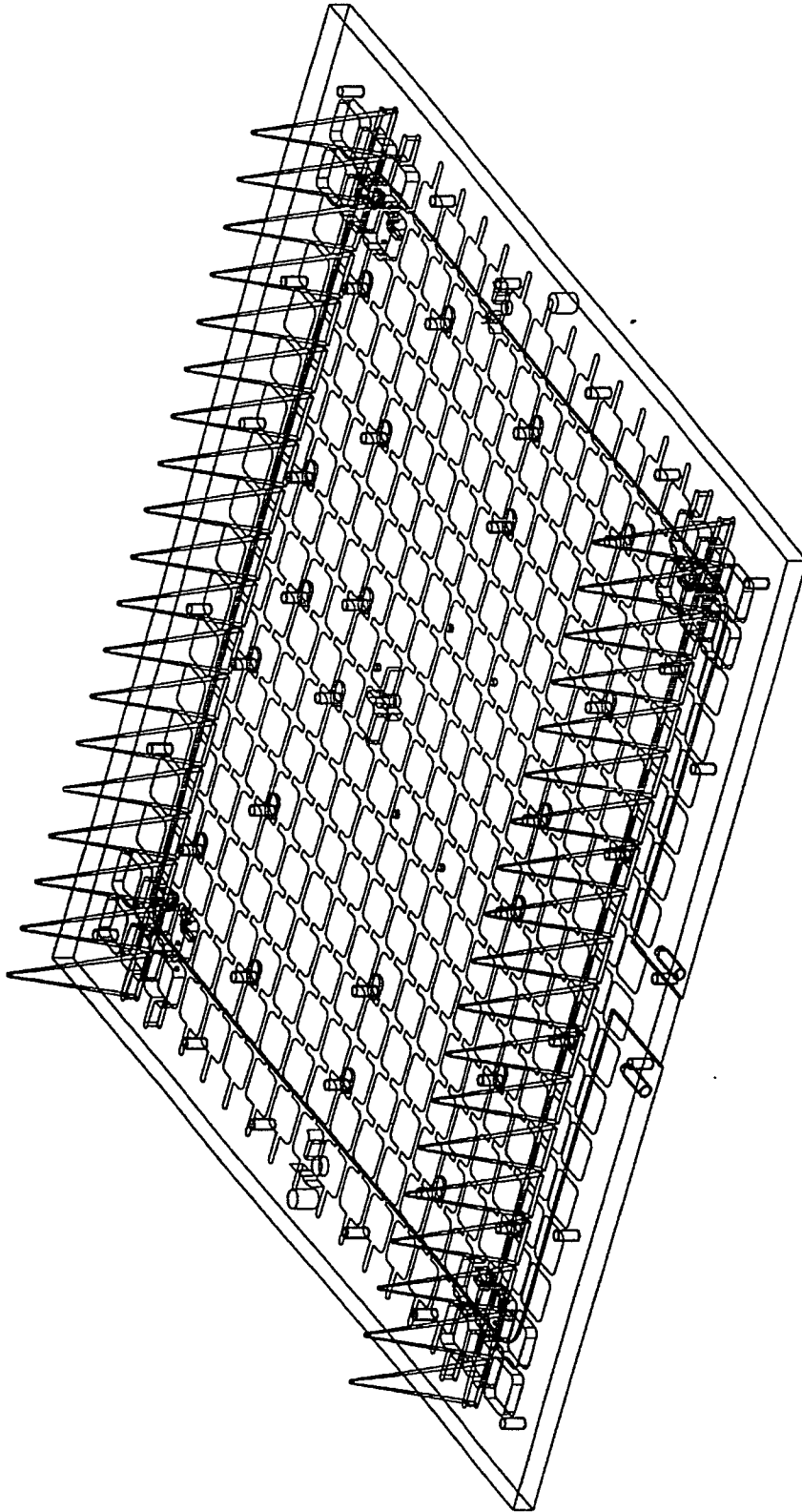
Figure 3.16 The main plate with fins of the 16 x 16 element array.
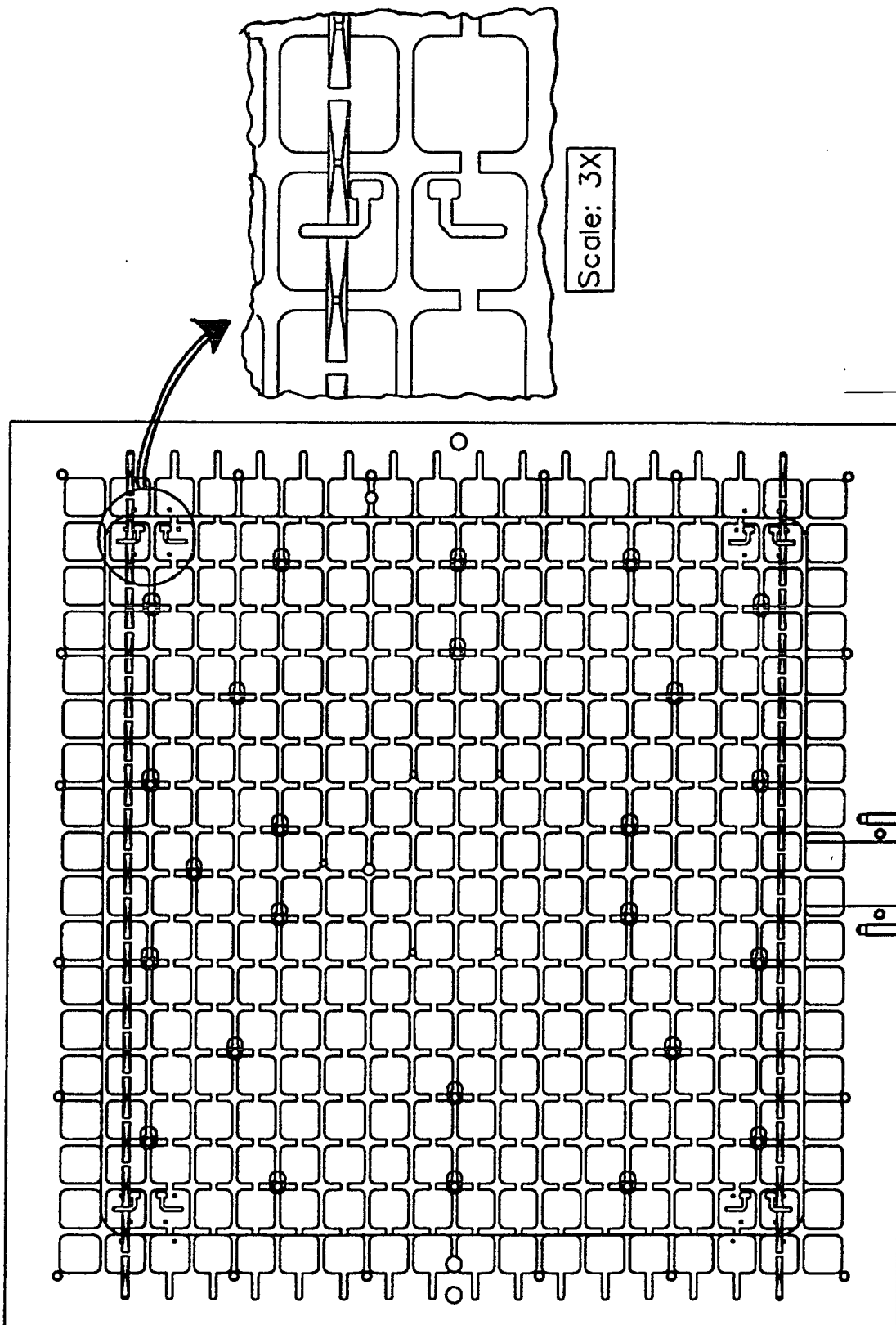
Figure 3.17 The top-view of the copper part with detail view of 'Hockey Stick' slot.
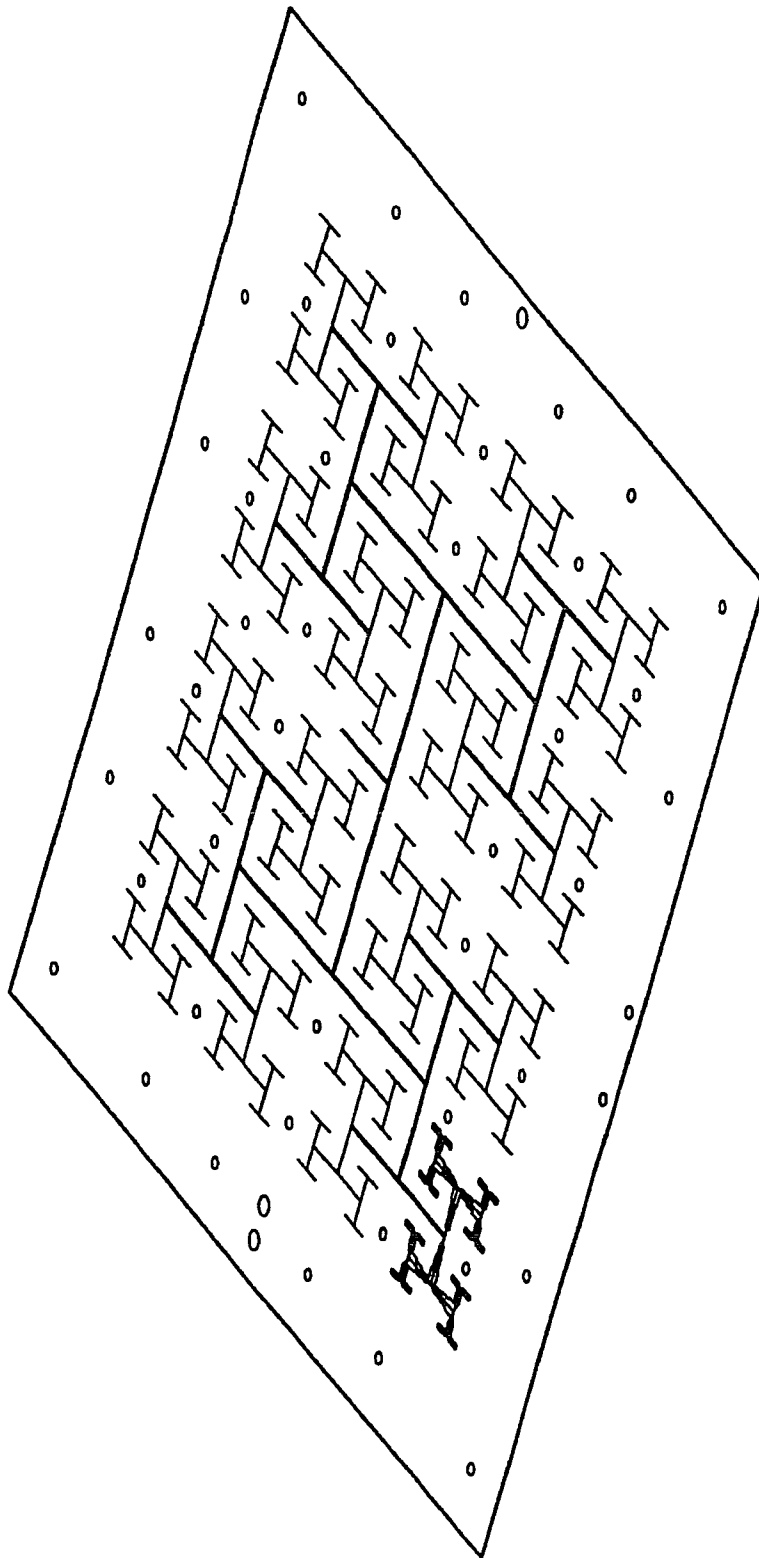
Figure 3.18 The printed BFN of the 16 x 16 element array.
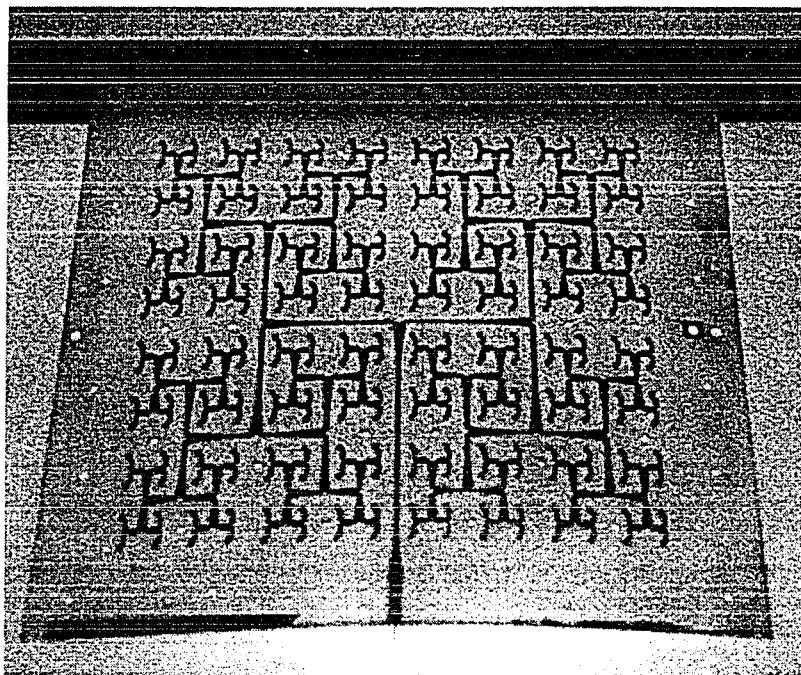
Figure 3.19 The photo of the printed BFN in the 16 x 16 element array.
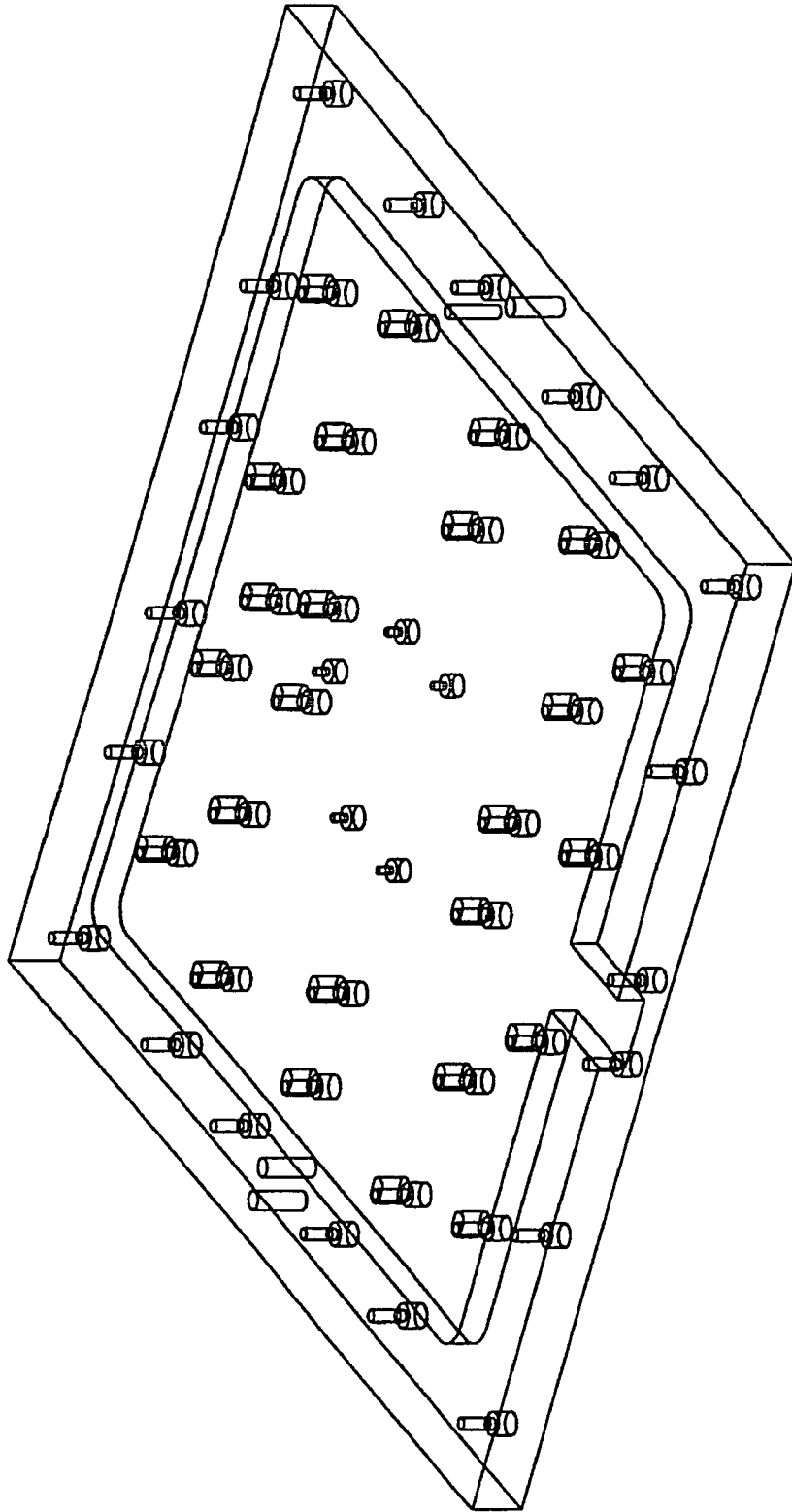
Figure 3.20 The bottom plate of the 16 x 16 element array.

3.5.2 The Measured Results and Discussions

Extensive measurements were carried out on the 16 x 16 element array from 17GHz to 24GHz. The measured return loss and gain are given in Figures 3.21, and 3.22. The radiation patterns in both E- and H-planes were measured from 17 to 24GH with 0.2GHz increment. The typical E- and H-plane co- and cross-polarization patterns are shown in Figures 3.23 and 3.24, respectively. From Figure 3.21 it can be observed that the array has good impedance bandwidth. The reasons for the return loss being degraded at the higher frequencies are:

1. The consistency of the soldering for the SML-to-UT86 cable transition needs upgrading,

2. The transition needs to have a wider bandwidth, (It is a challenging topic.)

3. The coupling between the main branch SML in BFN and 'Hockey Stick' slots needs to be further reduced by increasing the array element spacing.

The array has good gain if the cable loss (about 1dB at 20GHz) and the transition insertion loss are taken into account. The main reason for the drop-off in gain at the higher frequencies is a degeneration in the return loss.

The radiation patterns and beamwidth in both E- and H-plane are very close to the theoretical ones. Basically we found that −30dB cross-polarization levels can be achieved, if a polarizer (Figure 3.25) is placed in front of the 16 x 16 element array. The polarizer is made from 5mil FR4 printed circuit board with single-sided copper. The copper strip size and the spacing between the copper stripes are all about 8mil to 9mil with ±1mil accuracy. The distance between the polarizer and the array is 200mil. Without the polarizer in place, the H-plane cross-polarization levels will increase to about −18 to −22dB level in around the ±(30 to 60) degree regions. The reason for this is the head area of the 'Hockey Stick' slot leaks energy. The arrangement shown in Figure 3.17 for the 'Hockey Stick' slots can be used to reduce the H-plane cross-polarization level on the broadside of the array. There is little improvement observed in the E-plane cross-polarization level with the incorporation of the polarizer.
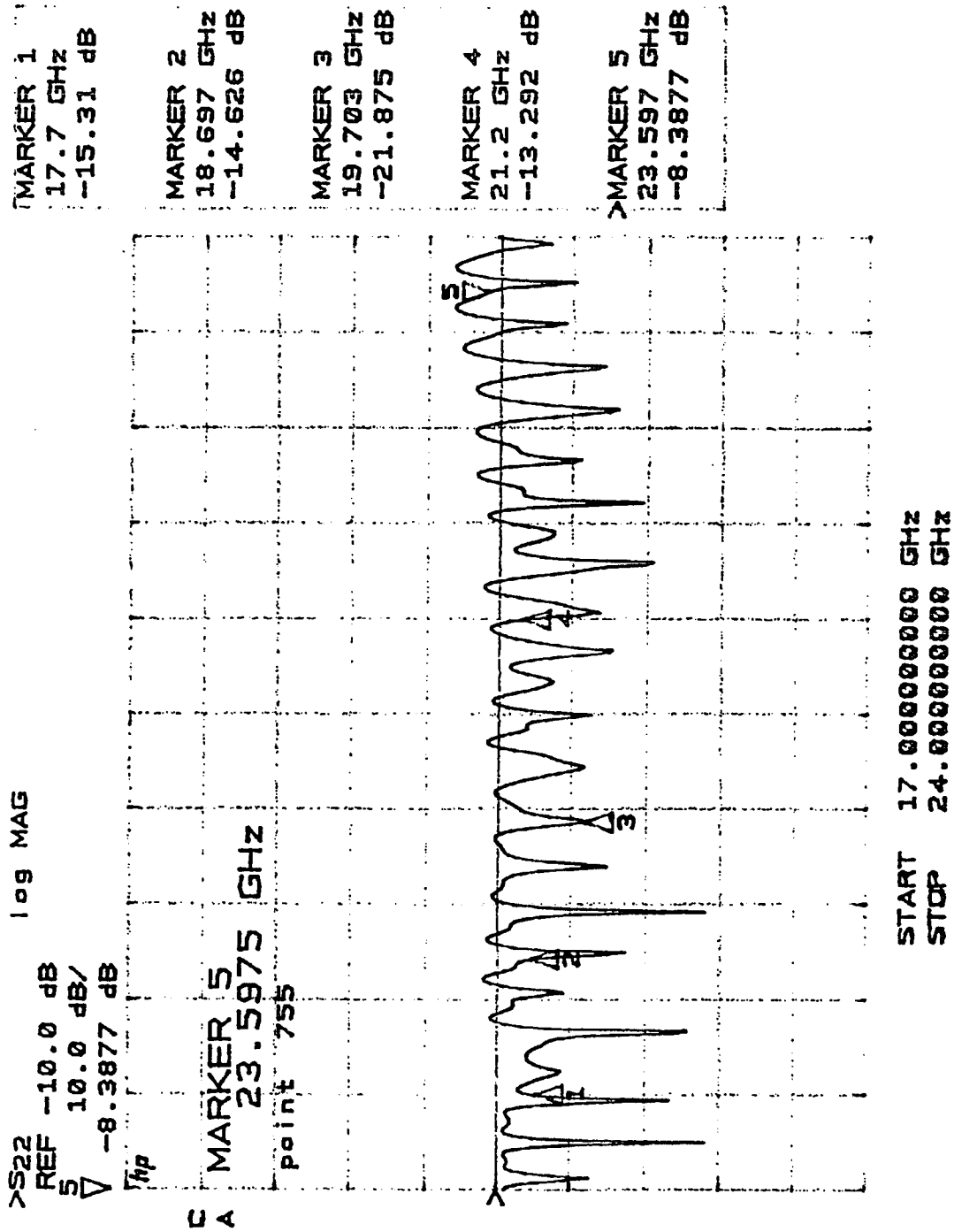
Figure 3.21 Measured return loss of the 16 x 16 element SML fed 'Hockey Stick' slot coupled LTSA array.
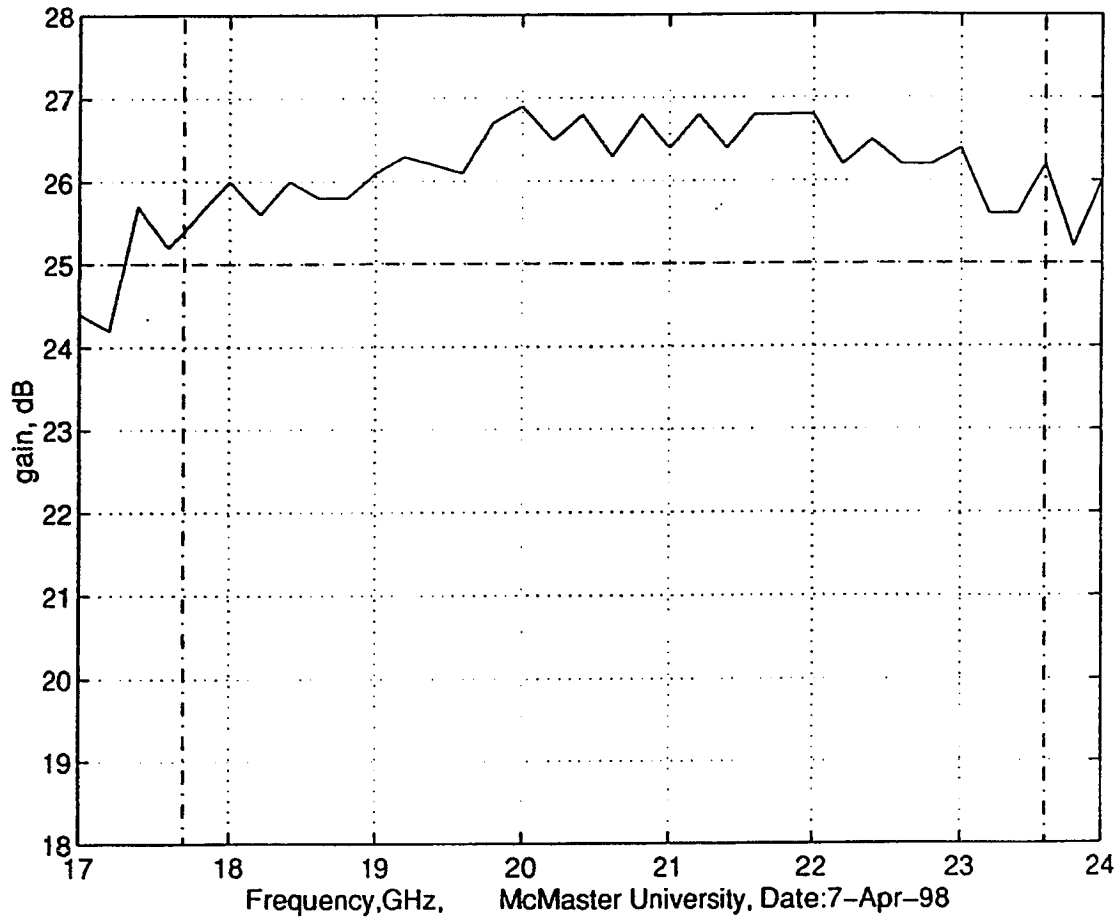
Figure 3.22 Measured gain of the 16 x 16 element SML fed 'Hockey Stick' slot coupled LTSA array.
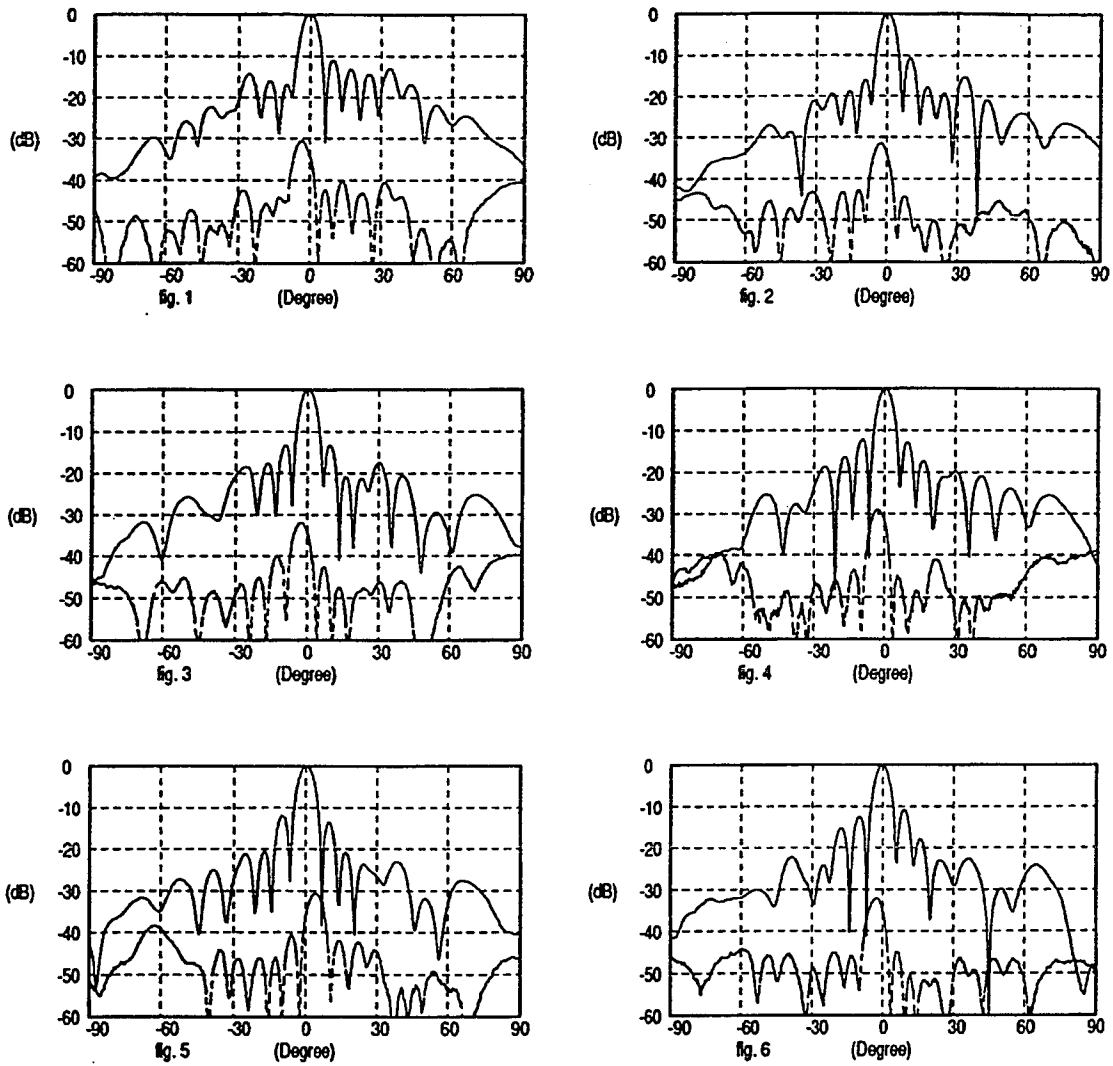
Number	Frequency	Gain	Beamwidth	Cross.pol	Filename(Col.pol)
1	17.00 GHz	24.52 dB	6.33 deg	30.48 dB	d:\pafta700001.pat
2	17.20 GHz	24.01 dB	5.89 deg	31.45 dB	d:\pafta710101.pat
3	17.40 GHz	25.72 dB	5.98 deg	31.90 dB	d:\pafta720201.pat
4	17.60 GHz	25.12 dB	5.80 deg	29.13 dB	d:\pafta730301.pat
5	17.80 GHz	25.59 dB	6.15 deg	30.59 dB	d:\paftA740401.pat
6	18.00 GHz	25.82 dB	5.63 deg	32.07 dB	d:\pafta750501.pat

Figure 3.23 E-plane co- and cross-polarization patterns of the 16 x 16 element SML fed 'Hockey Stick' slot coupled LTSA array.
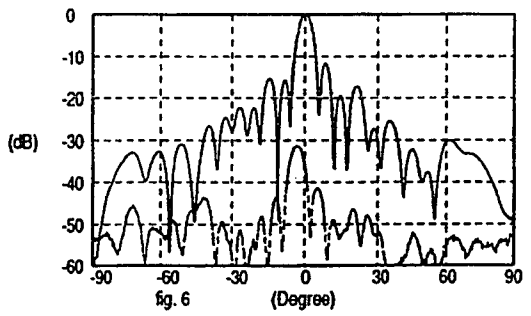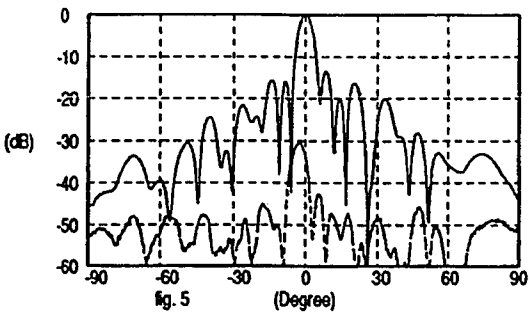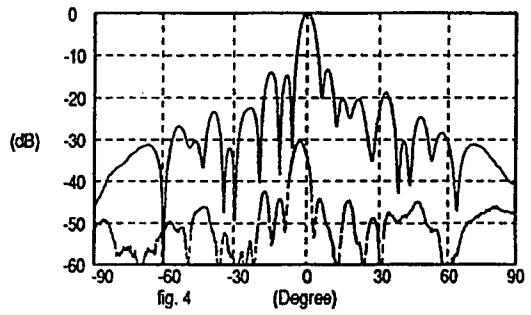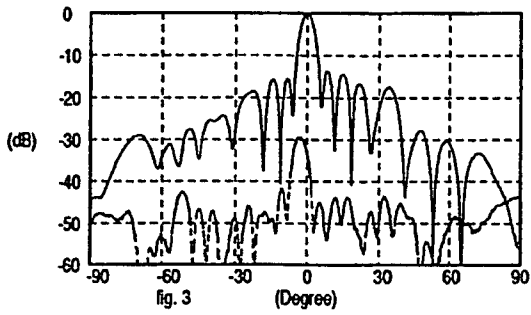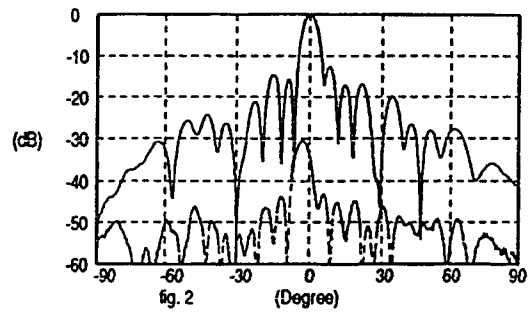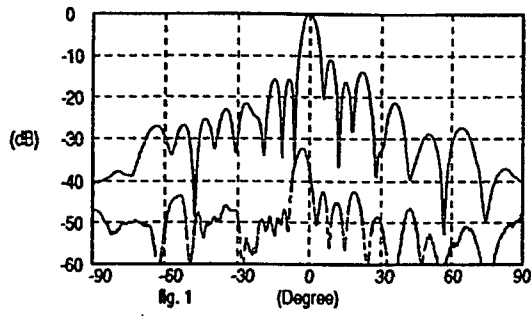
Number	Frequency	Gain	Beamwidth	Cross.pol	Filename(Col.pol)
1	20.60 GHz	25.37 dB	5.45 deg	32.21 dB	d:\pa\a7181801.pat
2	20.80 GHz	26.26 dB	5.45 deg	30.56 dB	d:\pa\a7191901.pat
3	21.00 GHz	25.46 dB	5.01 deg	29.42 dB	d:\pa\a7202001.pat
4	21.20 GHz	26.27 dB	5.10 deg	30.46 dB	d:\pa\a7212101.pat
5	21.40 GHz	25.97 dB	5.01 deg	30.55 dB	d:\pa\a7222201.pat
6	21.60 GHz	26.69 dB	5.10 deg	31.29 dB	d:\pa\a7232301.pat

Figure 3.23 continue ...

148
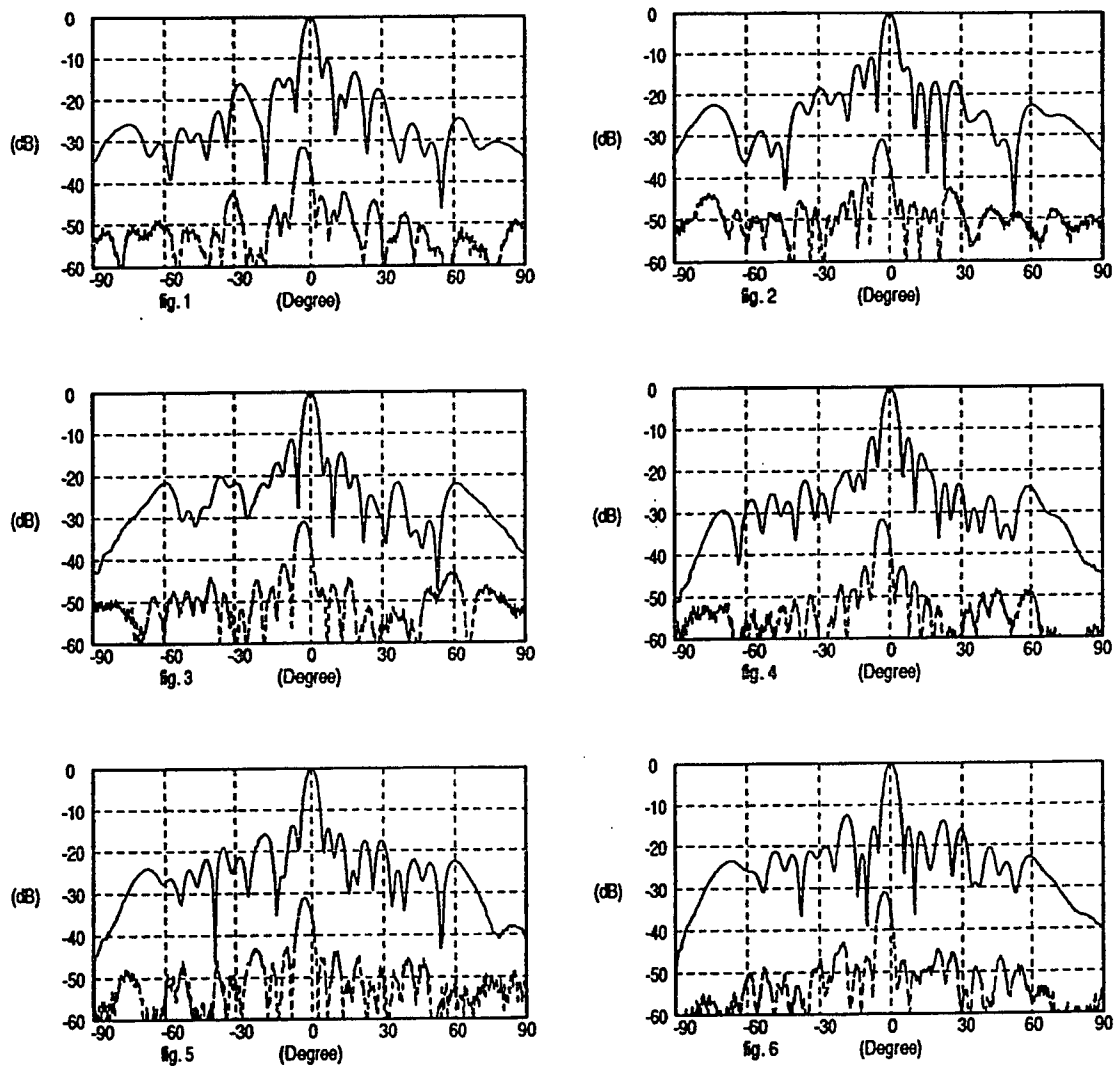
Number	Frequency	Gain	Beamwidth	Cross.pol	Filename(Col.pol)
1	23.00 GHz	25.57 dB	4.83 deg	31.53 dB	d:\pa\ta7303001.pat
2	23.20 GHz	25.03 dB	4.83 deg	30.82 dB	d:\pa\ta7313101.pat
3	23.40 GHz	24.97 dB	4.66 deg	30.86 dB	d:\pa\ta7323201.pat
4	23.60 GHz	25.83 dB	4.75 deg	31.75 dB	d:\pa\ta7333301.pat
5	23.80 GHz	24.58 dB	4.66 deg	31.01 dB	d:\pa\ta7343401.pat
6	24.00 GHz	25.51 dB	4.57 deg	30.93 dB	d:\pa\ta7353501.pat

Figure 3.23 continue.

149
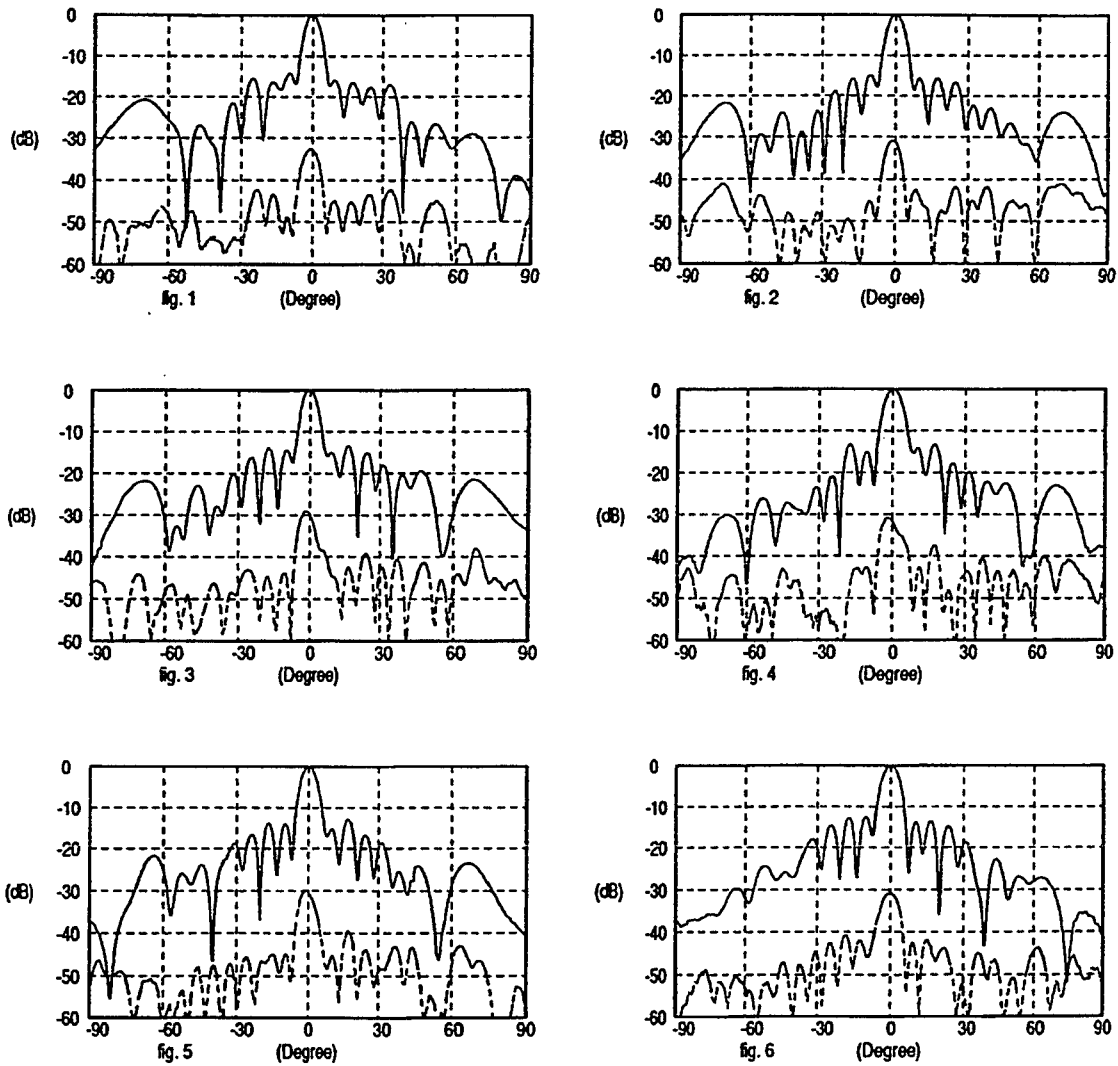
Number	Frequency	Gain	Beamwidth	Cross.pol	Filename(Col.pol)
1	17.00 GHz	24.39 dB	6.15 deg	32.47 dB	d:\pa\ta400001.pat
2	17.20 GHz	24.12 dB	6.15 deg	30.72 dB	d:\pa\ta410101.pat
3	17.40 GHz	25.51 dB	6.15 deg	29.07 dB	d:\pa\ta420201.pat
4	17.60 GHz	24.95 dB	6.59 deg	30.75 dB	d:\pa\ta430301.pat
5	17.80 GHz	25.41 dB	6.77 deg	29.85 dB	d:\pa\ta440401.pat
6	18.00 GHz	25.89 dB	6.59 deg	30.75 dB	d:\pa\ta450501.pat

Figure 3.24 H-plane co- and cross-polarization patterns of the 16 x 16 element SML fed 'Hockey Stick' slot coupled LTSA array.

150
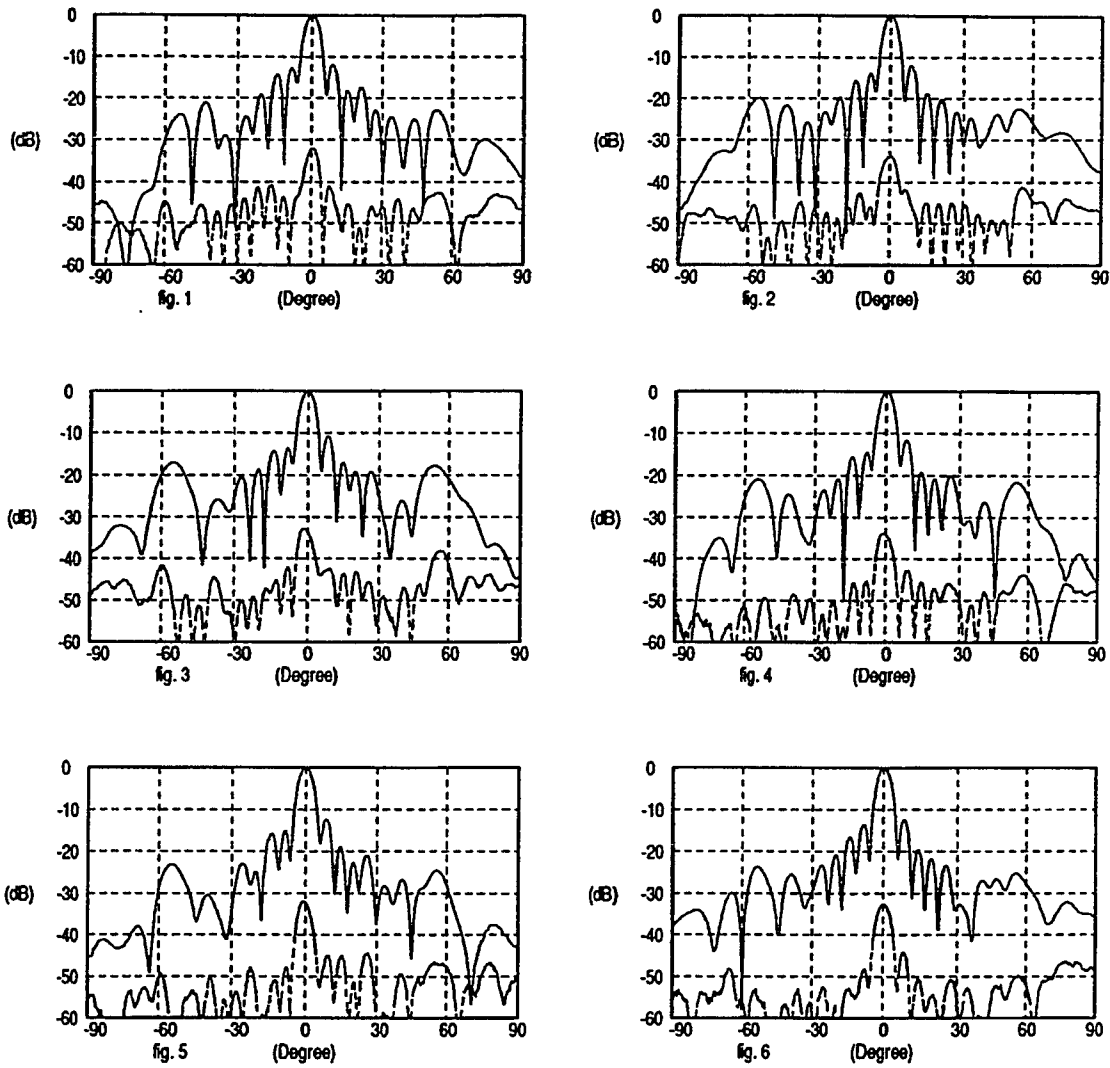
Number	Frequency	Gain	Beamwidth	Cross.pol	Filename(Col.pol)
1	20.60 GHz	25.89 dB	5.10 deg	32.09 dB	d:\pafta4181801.pat
2	20.80 GHz	26.78 dB	5.01 deg	33.82 dB	d:\pafta4191901.pat
3	21.00 GHz	25.98 dB	5.18 deg	32.76 dB	d:\pafta4202001.pat
4	21.20 GHz	26.80 dB	4.83 deg	33.82 dB	d:\pafta4212101.pat
5	21.40 GHz	26.42 dB	5.45 deg	31.91 dB	d:\pafta4222201.pat
6	21.60 GHz	26.87 dB	5.36 deg	32.59 dB	d:\pafta500001.pat

Figure 3.24   continue ...

fig. 1   (Degree)

fig. 2   (Degree)

fig. 3   (Degree)

fig. 4   (Degree)

fig. 5   (Degree)

fig. 6   (Degree)
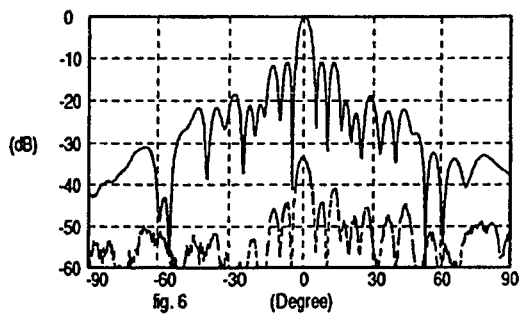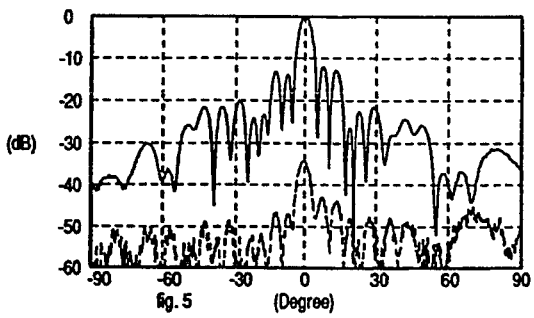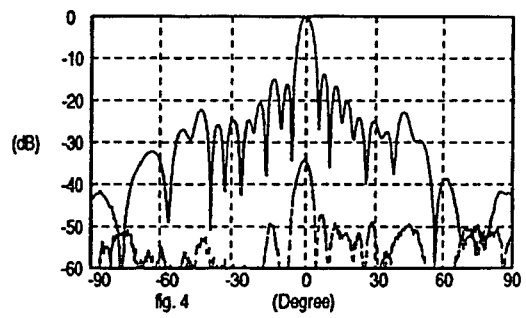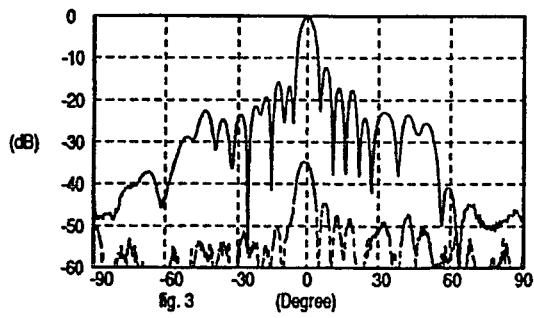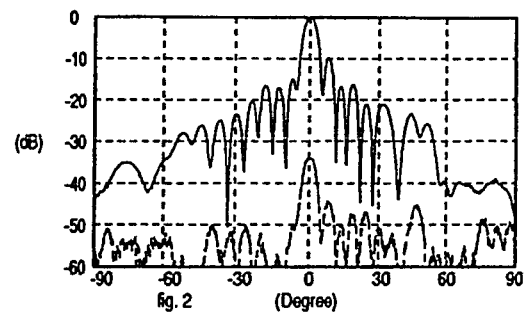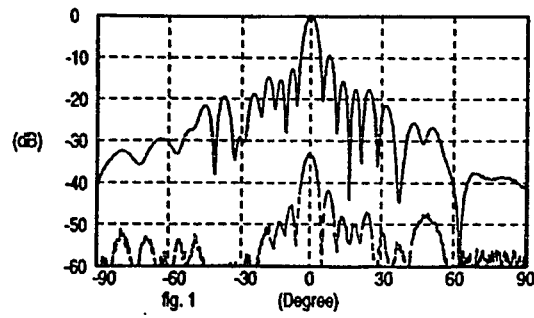
Number	Frequency	Gain	Beamwidth	Cross.pol	Filename(Col.pol)
1	23.00 GHz	26.34 dB	5.10 deg	33.14 dB	d:\pafta570701.pat
2	23.20 GHz	25.60 dB	4.75 deg	34.03 dB	d:\pafta580801.pat
3	23.40 GHz	25.63 dB	5.27 deg	34.76 dB	d:\pafta590901.pat
4	23.60 GHz	26.22 dB	4.75 deg	34.25 dB	d:\pafta5101001.pat
5	23.80 GHz	25.20 dB	4.75 deg	34.35 dB	d:\pafta5111101.pat
6	24.00 GHz	26.04 dB	4.13 deg	33.16 dB	d:\pafta5121201.pat

Figure 3.24 continue.

152
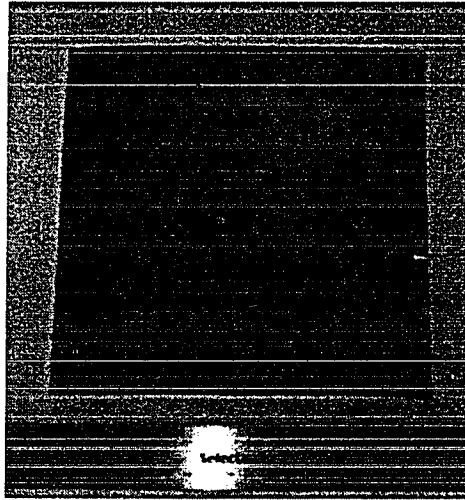
Figure 3.25 A picture of the polarizer used in the 16 x 16 element SML fed 'Hockey Stick' slot coupled LTSA array.

3.6. A Sector Antenna

3.6.1 Introduction

The sector antenna plays a very important role in point-to-multipoint communications. The main reason is that the horizontal-plane can be divided into n sectors. Each sector is 360/n (degrees) in width and is covered by a sector antenna, whose 3dB beamwidth is about 360/n (degrees). This means the frequency can be reused in the different sectors, [77] [78] thereby increasing spectrum capacity. The specifications of the sector antenna in our design are given in Table 3.5.

Frequency (GHz)	18.86 ~ 19.26
Gain (min. dBi)	> 15
Beamwidth (max. ^{0})	Horizontal $120^0 \pm 5^0$, Vertical $\sim 5^0$
Polarization	V
Cross-pol Level	< -30dB
Front-to-back ratio	> 50dB
VSWR	1.5 : 1
Input connector	WR42 waveguide

Table 3.5 The specifications of sector antennas

3.6.2 A Design of 120-degree Vertical Polarized Sector Antenna Using Very Short Balanced Antipodal Vivaldi Antenna

3.6.2.1 The Array Structure

The Vivaldi antenna can be used for those applications requiring a high-gain traveling wave antenna. The antenna usually has very long length L ($\geq 3\lambda_0$). Following basic traveling-wave antenna principles, the longer L, the higher the gain and narrower the beamwidth. Very few references appear in the literature where this antenna element is used in its very short form, i.e. (L $\leq \lambda_0/2$). Figure 3.26 shows a picture of three 120-degree sector antennas. A line-model of

the 120-degree sector antenna is given in Figure 3.27. In this design, there are the following components:

1. ABS radome with polarizer,

2. 1 x 16 element short Vivaldi array fed by strip line BFN

3. waveguide-to-strip line transition

4. two reflectors

5. aluminum base

6. bottom plate

A detailed assembly drawing is given in Figure 3.28. The polarizer design is the same as the one used in the 16 x 16 SML fed 'Hockey Stick' slot coupled LTSA array. It is installed under the dome-shaped radome. The details of radiating array are given in Figure 3.29. The spacing between elements is 362mil. The two reflectors on each side of the radiating element play a very important role in forming a beam with a beamwidth of 120^0 in the H-plane. Two mirror symmetrical aluminum blocks form the aluminum base, which have following functions:

1. to hold the Vivaldi antenna array and two reflectors in place,

2. to form the input waveguide,

3. to house the waveguide-to-strip line transition,

4. to house a slider waveguide shorted terminal in the waveguide,

5. to secure the array to the bottom plate.
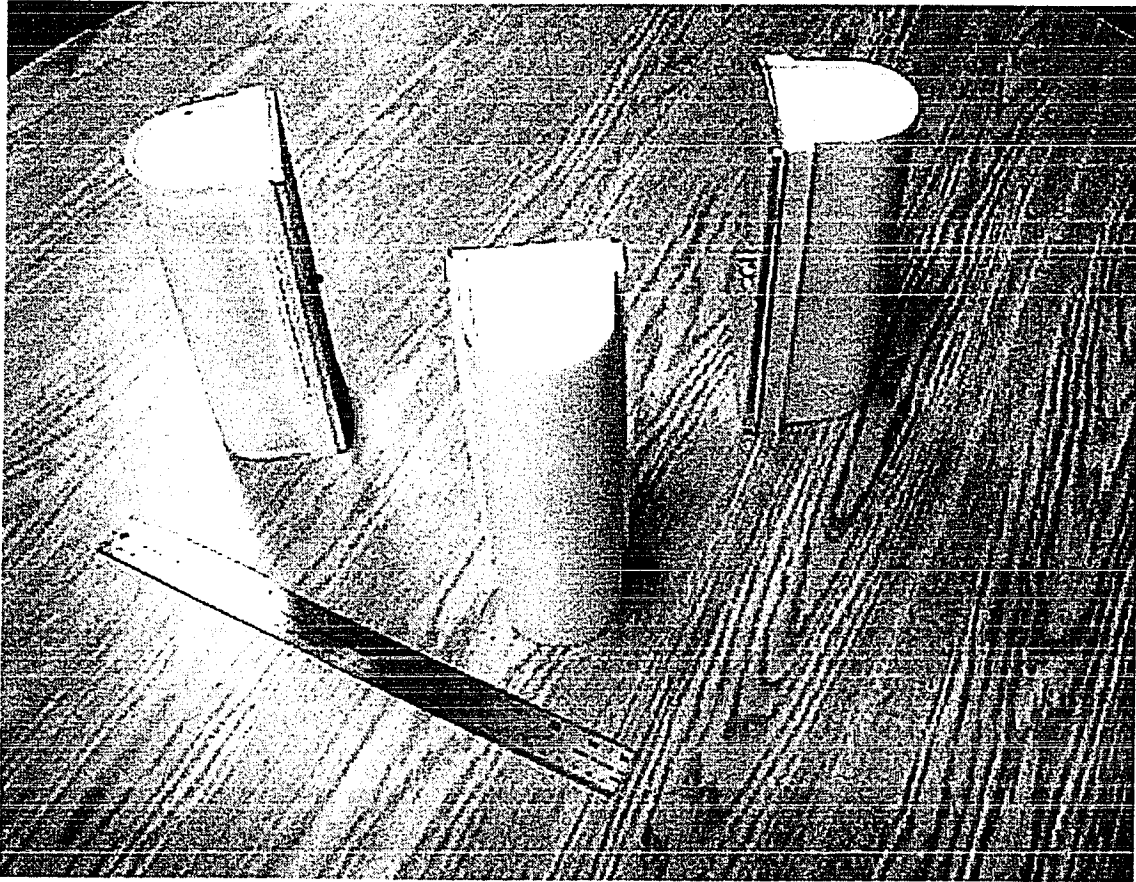
Figure 3.26 A picture of three 120-degree sector antennas.
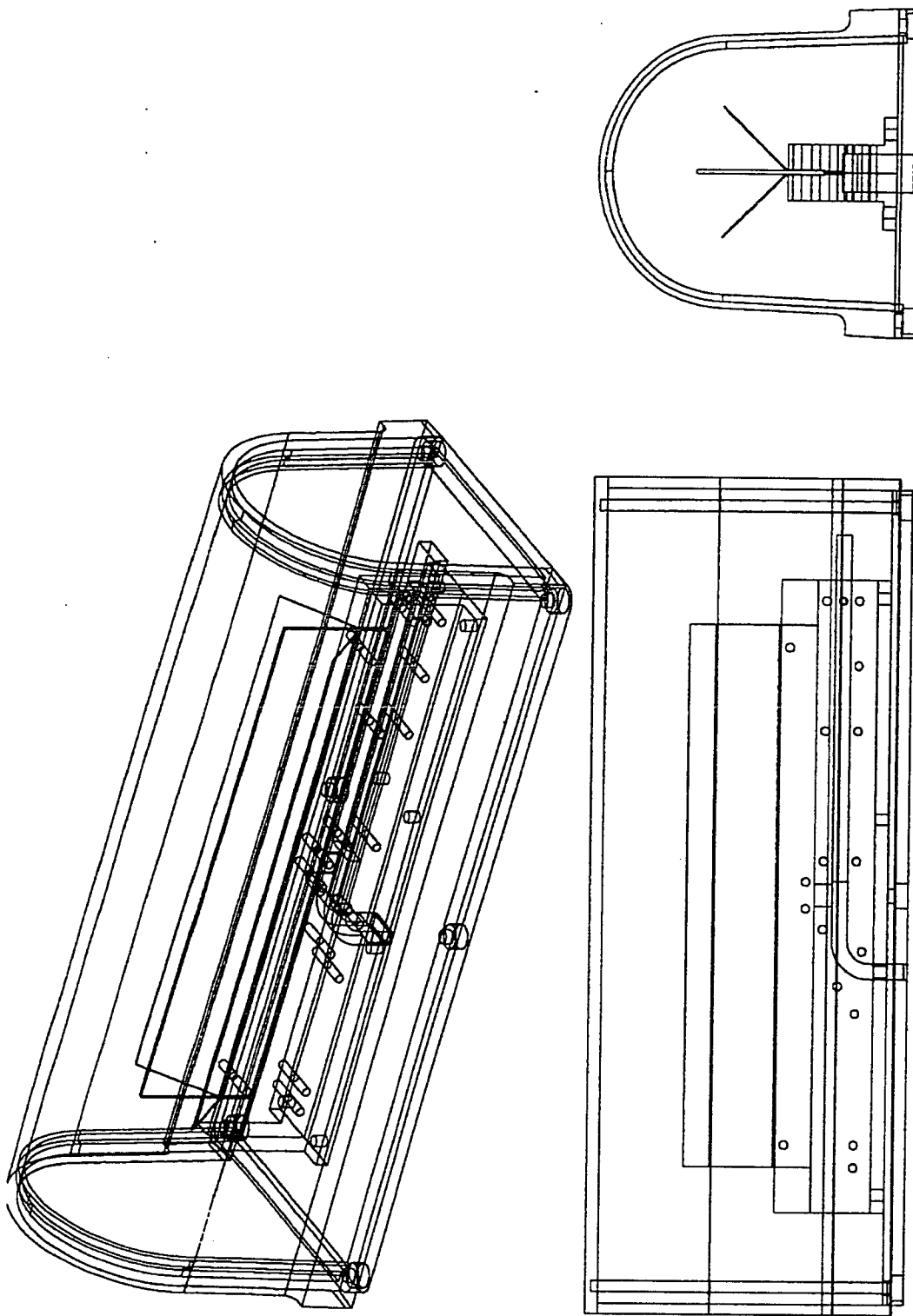
Figure 3.27 A line-model of the 120-degree sector antennas.
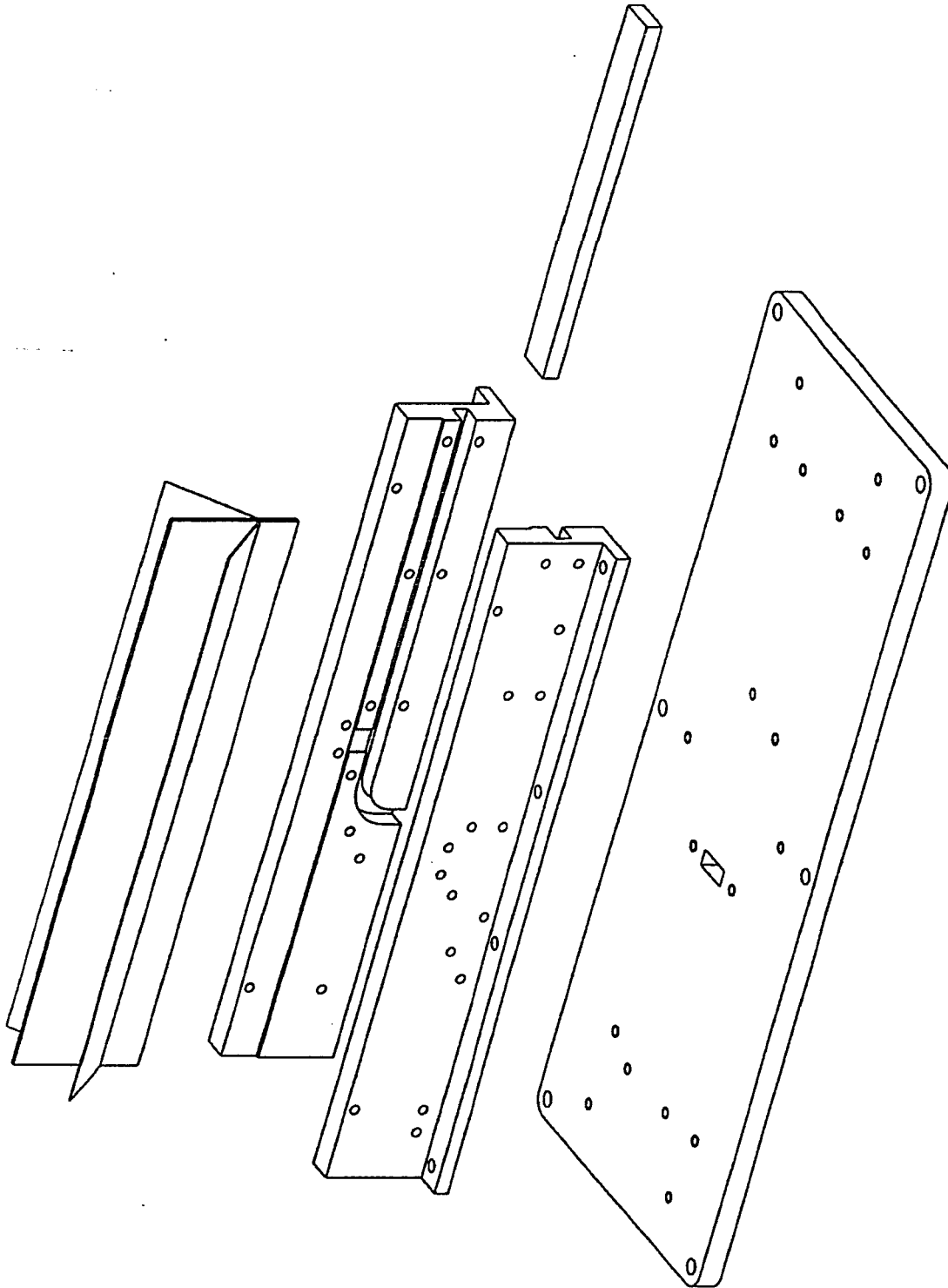
Figure 3.28 The detail assembly draw of the 120-degree sector antennas.
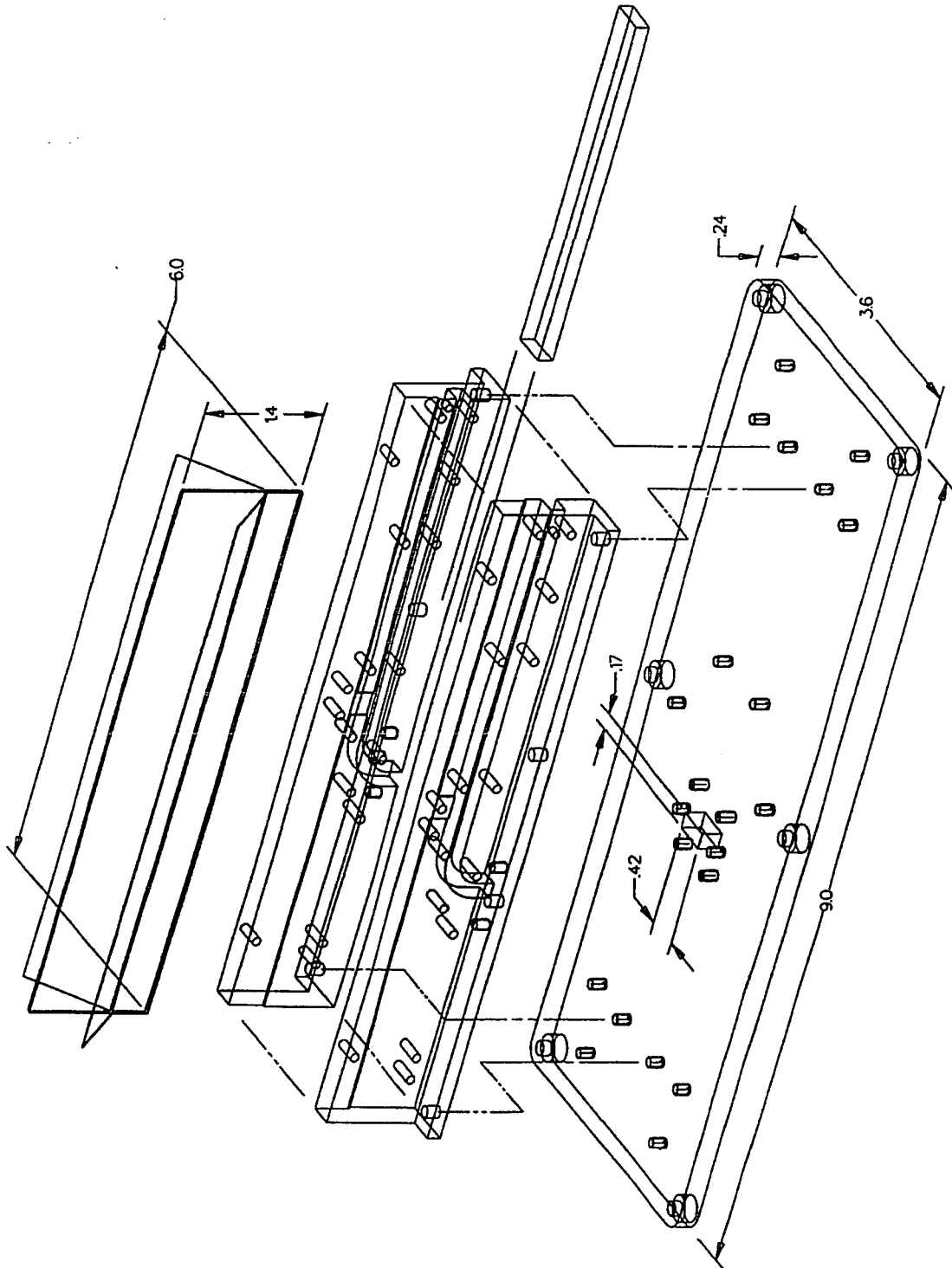
Figure 3.28 continue.
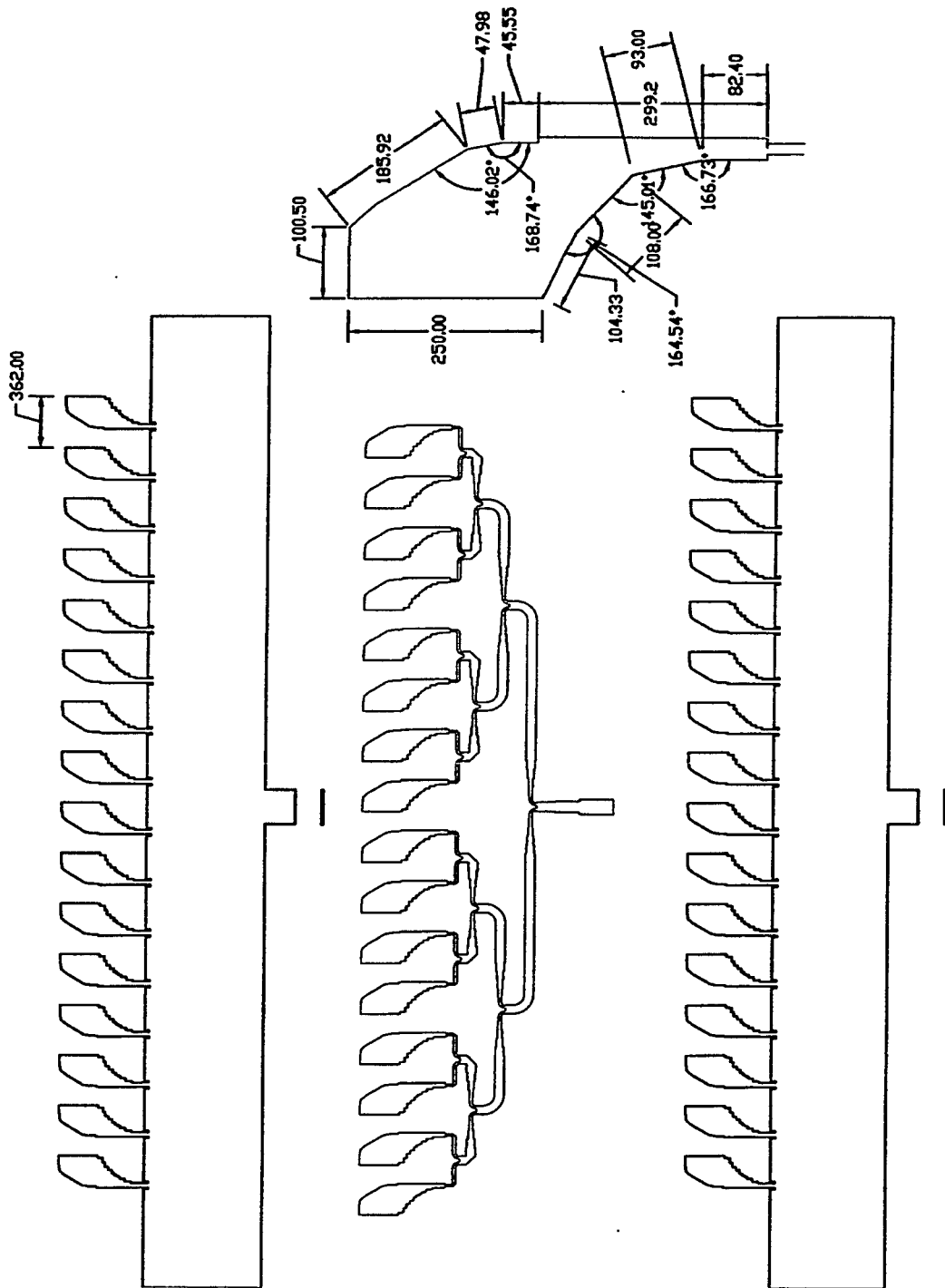
Figure 3.29 The 1 x 16 balanced antipodal Vivaldi array fed by strip line FBN, The dielectric slab thickness is 40mil and $\varepsilon_r = 2.2$.

3.6.2.2 The Measured Results and Discussions

A total of six of the 120-degree sector antennas have been built. The typical measured return loss, gain, beamwidth and E- and H-plane radiating patterns are shown in Figures 3.30 and 3.31, respectively. These antennas meet the design specifications, as can be seen by comparing the measured results with specifications given in Table 3.1.

Although the waveguide-to-strip line transition was designed by using the FDTD simulator, each array needed some touch-up tuning. This is accomplished by changing the position of the shorted terminal in the waveguide. The requirement for tuning is mainly due to the E-plane waveguide band (see Figures 3.27 and 3.28) was not involved in FDTD simulation [79]. The results of experimental study show that by changing the length of the reflectors and the angle between the reflectors the beamwidth can be altered with little accompanying change in the return loss.
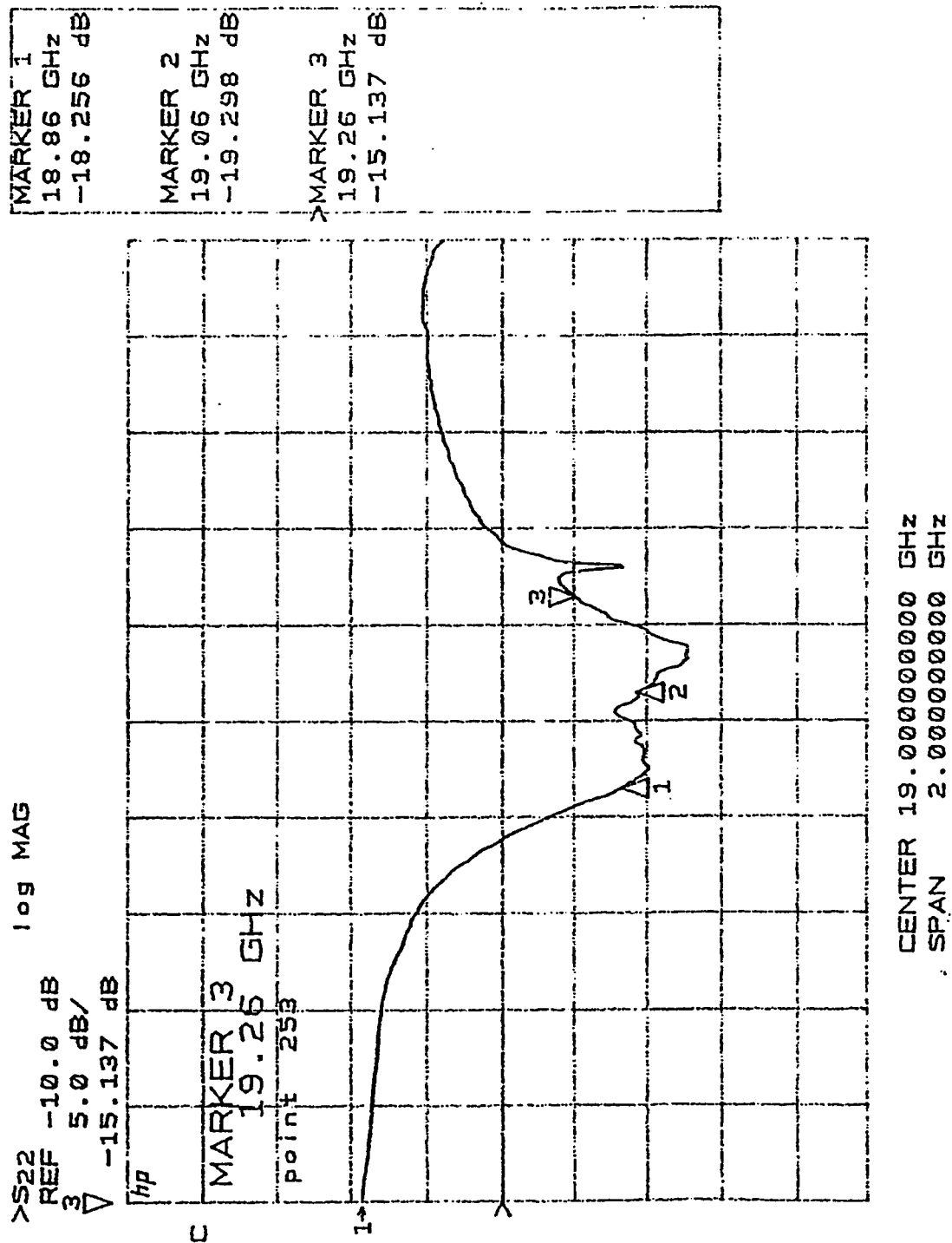
Figure 3.30 Measured return loss the sector antenna.
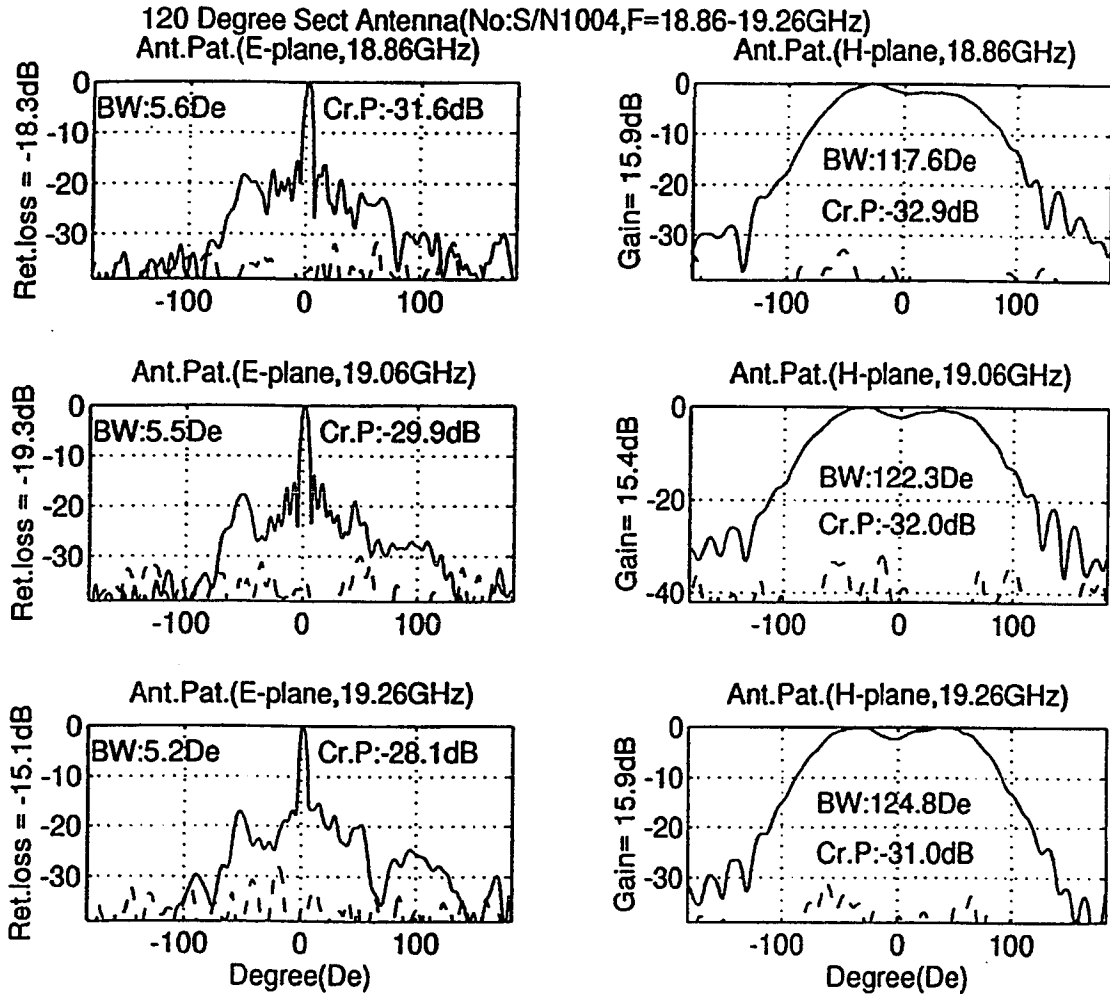
Figure 3.31 Gain, E- and H-plane patterns and beamwidth of the sector antenna.

Chapter 4 . Conclusions

.

Based on extensive research in developing and using the Finite Difference Time Domain method, we reached the conclusion that the FDTD method may be the most powerful numerical modeling algorithm for solving complex EM problems that has been developed in the 20th century. It is because this numerical method is quite simple and can deliver very reliable results in both time and frequency domains simultaneously. After a number of years of ongoing research on the method; particularly, in applying the method to solve complex EM problems, a research based FDTD 3-dimensional Structure Simulator (FDTD 3D SS) has been developed. Without this tool it would have been not possible to achieve the antenna research and development, which have been given in Chapter 2 and 3 of this thesis, within a time period of less than one year. More than 500 computer simulations have been carried out using this design tool.

In Appendix A is given a list of the research topics that the author carried out using the FDTD method to solve different EM problems. In Appendix B gives the published journal and conference papers that relate to his research topics. His contributions to the FDTD research and other developments are mainly in two areas, they are:

1. Applying digital signal processing (DSP) techniques with the FDTD method to solve EM problems;

2. Applying of the FDTD method designing and developing antennas and microwave passive components.

In the first contribution, DSP techniques are used as post processing methods to process the information obtained from the FDTD method in the time domain. There are two major achievements:

- Using DSP techniques, such as the AR model, Total Least Square (TLS) and Neural Networks, etc, to enhance the FDTD method and solve EM problems. For example, when using the FDTD method to simulate high-Q microwave devices, very long simulation times are required to achieve convergence. By using DSP techniques or Neural Networks one can use early time-domain information given by the FDTD method to predict later information in order to arrive at convergence more quickly. It has been demonstrated that up to 90% of the FDTD simulation time can be saved.

- Using the FDTD method to model wave propagation and signal processing techniques for estimating angle of arrival and delay spread of radio wave in multi-path environment. The combination of the FDTD and DSP methods can give remarkable resolutions of the results in the time, spectrum and spatial domains. It is because the mesh sizes used in the FDTD method are usually smaller than $\lambda_{min}/10$, where λ_{min} is the wavelength of highest frequency component in a designed frequency band. If one puts sampling point at each node of the mesh used in the FDTD method, one can easily put more than 10 'sensors' in each wavelength and sample at each Δt that is the time step of the FDTD method. It is a practical impossibility to use experimental to realize the high-resolution results, which are obtained using the FDTD and DSP methods.

In the second contribution, a large number of antennas and microwave components are simulated and designs carried out for different applications. They includes:

- Printed antennas and printed feed networks;

  A US patent, which is based on this development, has been applied.

- Design software for square-coaxial TEM line components, used for C-band satellite BFNs, based on the non-orthogonal FDTD method;

  This achievement received the Telecommunications Research Institute of Ontario award and saved a Canadian space company 2.5 million dollars to develop antenna beamforming networks for satellite communications.

- Waveguide components and BFN;

  A novel waveguide BFN for antenna array applications has been developed. Based on this invention, another US patent has been filed.

- Microwave transitions and other discontinuities;

This thesis focuses on using the FDTD method to investigate and develop novel antenna feed structures and antenna elements, and to apply them to different millimeter wave arrays, i.e. FPAs and sector antennas, for point-to-point and point-to-multipoint communications. It actually is a rich fruit, consisting of the combination of (1) the might of the FDTD method, (2) the experiences gained in using the method, (3) EM theory, (4) antenna theory and (5) digital computer technology.

The contributions of this thesis can be summarized as followings:

1. In Chapter 1 the applications of the FDTD method to solve different microwave and millimeter wave circuit and antenna problems have been successfully realized. When Litva's ABC was first published in 1992 [22], people criticized it because they said that it was not stable and could not be used in real FDTD simulations for printed circuit design. One of the author's contributions was to carry out extensively detailed research, based on numerical experimental studies and proving that it is a very good ABC for the FDTD method when simulating microwave printed circuits. The study found that this ABC is stable for all the microwave dielectric substrate materials available in the market. It gives better than −50dB return loss at the designed frequency, when it is used as a terminal of a microstrip line [23]. The non-orthogonal FDTD method has for the first time been applied to square-coaxial waveguide components [11]. This application greatly reduced the number of iterations that were required to design square-coaxial BFNs for satellite communications.

2. In Chapter 2 broadband traveling wave antenna elements and novel feed structures have been developed using the FDTD method. They are: (1) the suspended microstrip line fed slot line coupled LTSA element, (2) the inverted microstrip line-to-coplanar double strips fed LTSA element, and (3) the suspended microstrip line fed 'Hockey Stick' slot coupled V-slot element. These three new inventions are superior to previous designs, which were available in the literature. The advance is due to the fact that the designs are simple and use low loss transmission feed lines. The design of the third antenna structure was a challenging problem, since the feed transmission line and the radiating element are in two orthogonal planes. The 'Hockey Stick' slot coupling structure in the transition occupies a very small

amount of real estate and gives very wide bandwidth. The impedance bandwidth for a 2:1 VSWR was found to be about 37%, while the designs of other researchers currently reached only around 6% [80]. These designs can be used in other frequency bands. The transmission line to radiating element transitions can be used to feed different antenna elements, as well. It is very important to note that the FDTD method is a very powerful design tool, which gives designers a very efficient way to try different ideas without spending a lot of money for making prototype hardware. It was found that almost every design solution developed using the FDTD design tool resulted in a piece of hardware that worked after the first design iteration.

3. The antenna designs developed in Chapter 2 have been successfully used in the flat panel antenna arrays described in Chapter 3. Example arrays are the 32 x 32 element suspended microstrip line fed slot line coupled LTSA, and the 16 x 16 element suspended microstrip line fed 'Hockey Stick' slot coupled LTSA. The measurement studies prove that the designs of the antenna elements given in Chapter 2 are correct and usable, and the antenna arrays presented in Chapter 3 demonstrate good performance in terms of gain, impedance and antenna patterns. Some of these arrays can be incorporated into millimeter systems for point-to-point communication.

4. The concept of using very short Vivaldi or Linear Tapered Slot elements to design sector antennas given in Chapter 3 can give antenna engineers a very simple way to design wideband sector antennas with different horizontal beam-widths. From published literatures, it is the first time that the short ($L \leq \lambda_0/2$) Tapered Slot Antennas are used in antenna applications. Although only short Vivaldi sector antenna has been presented in Chapter 3, the short LTSA sector antennas have been designed and fabricated with 90-degree beamwidth, as well. They have been used in real field trial in South American.

Appendix A

In this appendix the author gives a list of the research that was carried for the purpose of using the Finite Difference Time Domain method to solve complex EM problems.

A.1 Applying Digital Signal Processing Techniques to Enhance the FDTD Method

A.1.1. List of Techniques That Have Been Successfully Applied to FDTD to Save Simulation Time

1. Auto-regression Analysis (AR Model)

2. Principal Component Analysis (PCA)

3. Total Least Square Method (TLS)

4. The Finite Impulse Response Neural Network (FIR NN) Method

5. Back-propagation Neural Network

A.1.2. Examples of the Use of Signal Processing with FDTD for Simulating Complex Environments

1. The first time to use FDTD for modeling indoor radio wave propagation (2D) with the objective of estimating angle of arrival and delay spread

2. The first time to use FDTD to simulate a smart antenna in a multi-path environment

A.2. Applications of FDTD to Antennas and Microwave Devices

A.2.1. Printed Antennas and Printed Feed Networks

1. Microstrip line fed patch antennas in different frequency bands

2. Coaxial line fed patch antennas

3. Aperture-coupled patch antenna in different frequency bands

4. Coaxial line fed multi-layer patch antennas

5. Aperture-coupled multi-layer patch antennas in different frequency bands

6. Microstrip line fed slot antennas

7. Coplanar-waveguide antennas

8. Coplanar-waveguide fed multi-slot antennas

9. 4 x 4 coaxial line fed microstrip patch array (mutual coupling study)

10. Antenna for PCMCIA Card at 2GHz

11. Microstrip line fed folded printed dipole for PCS basestation sector antenna

12. Suspended microstrip line fed printed linear tapered slot antennas used at millimeter wave frequency

13. Inverted microstrip line fed printed linear tapered slot antennas used at millimeter wave frequency

14. Microstrip and strip line Butler matrix at 2GHz

15. Microstrip line filters

A.2.2. TEM Line (Square-Coaxial) Components for Satellite Beam Forming Networks in C-band

1. TEM bends (with different angles)

2. Rat-Race coupler

3. Proximity coupler

4. Branch Line coupler

5. Feed through (with 0, 90, 180 and 270-degree angles)

6. Phased slope equalizer (Type 1)

7. Phased slope equalizer (Type 2)

A.2.3. Waveguide Components

1. Waveguide U-bend (with PML absorbing boundary conditions)

2. Waveguide E and H bends

3. Waveguide band pass filters

4. Waveguide low pass filter (Waffle-Iron filter)

5. Waveguide E-plane 3dB power dividers

A.2.4. Microwave Transitions and Other Discontinuities

1. Coaxial line-to-microstrip line transition

2. Microstrip line-to-coplanar waveguide transition

3. Microstrip line-to-strip line transition

4. Microstrip Line-to-waveguide (WR42 and WR28 waveguide) transition (E- and H-plane)

5. Suspended microstrip line-to-waveguide (WR42 and WR28 waveguide) transitions

6. Inverted microstrip line –to-waveguide (WR42 and WR28 waveguide) transitions

7. Inverted Microstrip Line-to-Coplanar Double Line transition

8. Fin line-to-waveguide transition

9. Microstrip line T-junctions

10. Suspended microstrip line T-junctions

11. Inverted Microstrip Line T-junctions

12. Rectangular Waveguide magic-T

A.3. Other FDTD Modeling

1. Microwave Tube

2. MMIC package modeling

3. Active device modeling

Appendix B

Following is a list of papers published in different journals and conference proceedings. The author was either as the first or second author of the papers. He was very actively involved in the research, contributed to the ideas and developed experiments to support the concepts described in each paper.

Refereed Journals:

1. C. Wu, J. Wang, R. Fralich and J. Litva, "A rigorous analysis of an aperture-coupled stacked microstrip antenna", Microwave and Optical Technology Letters, 3(11), 400- 404, November, 1990.

2. C. Wu, J. Wang, R. Fralich and J. Litva, "Analysis of a series-fed aperture-coupled patch array antenna", Microwave and Optical Technology Letters, 4(3), 110-113, February, 1991.

3. C. Wu, K. L. Wu, Z. Bi and J. Litva, "Modeling of coaxial-fed microstrip patch antenna by finite difference time domain method", IEE Electronics Letters, 27(19), 1691-1692, September., 1991.

4. C. Wu, K L. Wu, Z. Q. Bi and J. Litva, "Accurate characterization of planar printed antennas using finite-difference time-domain method", IEEE Trans. on Antennas & Propagat., 40(5), 526-534, May, 1992.

5. K. L. Wu, C. Wu and J. Litva, "Characterizing microwave planar circuits using the coupled finite-boundary element method", IEEE Trans. on Microwave Theory & Tech., 40(10), 1963-1966, October, 1992.

6. J. Litva, C. Wu, K. L. Wu and J. Chen, "Some considerations for using the finite difference time domain technique to analyze microwave integrated circuits", IEEE Microwave and Guided Wave Letters, 3(12), 438-440, December, 1993.

7. P. Y. Zhao, C. Wu and J. Litva, "Improved computational efficiency for the FDTD method", Microwave & Optical Tech. Letters, 7(2), 60-62, February, 1994.

8. E. A. Navarro, C. Wu, P.Y. Chung and J. Litva, "Application of the PML super-absorbing boundary condition to non-orthogonal meshes", IEE Electronics Letters, 30(20), 1654-1656. Augugst, 1994.

9. J. Chen, C. Wu, T. Lo, K. L. Wu and J. Litva, "Using linear and nonlinear predictors to improve the computational efficiency of the FD-TD algorithm", IEEE MTT, 42(10), 1992-1997, October, 1994.

10. K. L. Wu, C. Wu and J. Litva, "An application of FD-TD method for studying the effects of packages on the performance of microwave and high speed digital circuits", IEEE MTT, 42(10), 2007-2009, October, 1994.

11. E. A. Navarro, C. Wu, P.Y. Chung and J. Litva, "Some considerations about the finite-difference time-domain method in general curvilinear coordinates", IEEE Trans. on Microwave and Guided Wave Letters, 4(12), 396-398, December, 1994.

12. E. A. Navarro, C. Wu, P.Y. Chung and J. Litva, "A study of the use of non-regular grids with the FDTD algorithm", IEEE MGWL, August, 1994.

13. C. Wu, E.A. Navarro, P.Y. Chung and J. Litva, "Modeling of waveguide structures using the non-orthogonal FDTD method with a PML absorbing boundary", IEE Electronics Letters Microwave and Optical Technology, March, 1995.

14. E. A. Navarro, C. Wu, P.Y. Chung and J. Litva, "Sensitivity analysis of the non-orthogonal FDTD method applied to the study of square coaxial waveguide structures", IEE Electronics Letters Microwave & Optical Technology, March, 1995.

15. E. A. Navarro, C. Wu, P.Y. Chung and J. Litva, "Application of PML super-absorbing boundary condition to non-orthogonal FDTD method", IEE Electronics Letters, 30(20), 1654-1656, August, 1995.

16. Z. N. Li, C. Wu and J. Litva, "Adjustable frequency dielectric resonator antenna", IEE Electronic Letters, 32(7), 606-607, March 28, 1996.

17. J. Litva, C. Wu and A. Ghaforian, "Use of FDTD for simulating the angle-of-arrival and time delay of signals propagating in indoor environments", IEE Electronics Letters, 32(10), 930-932, May, 1996.

18. E. Navarro, C. Wu, P.Y. Chung and J. Litva, "Efficient FDTD analysis of discontinuities in a square coaxial waveguide", Microwave & Optical Technology Letters, 13(1), 1-7, September, 1996.

19. C. Wu, M. Nguyen and J. Litva, "Use of FDTD technique in PCS antenna design," Microwave & RF, vol. 35, no. 11, November, 1996.

Conference/Symposium Papers:

20. C. Wu, J. Wang, R. Fralich and J. Litva, "Study on a series-fed aperture-coupled microstrip patch array", 1990 AP-S Symp. Digest, Dallas, TX, pp. 1762-1765, May, 1990.

21. C. Wu, J. Litva, R. Fralich and C. Wu, "Full wave numerical model of arbitrary- shaped proximity coupled microstrip antenna", Proc. Canadian Conference Electrical and Computer Engineering, Quebec, PQ, September, 1991.

22. C. Wu, K. L. Wu, Z. Bi and J. Litva, "Modeling of coaxial-fed microstrip patch antenna by the finite-difference time-domain method", Proc. Canadian Conference Electrical and Computer Engineering, Quebec, PQ, September, 1991.

23. C. Wu, Z. Q. Bi, K. Wu, R. Fralich and J. Litva, "A study of the characteristics of microstrip line on grounded semiconductor slab by FD-TD method", 1991 North American Radio Science Mtg., 193, London, ON, June, 1991.

24. K. L. Wu, C. Wu and J. Litva, "Characterizing microwave planar circuits by coupled finite-boundary element method", Proc. IEEE MTT-S Interntl. Microwave Symp., 865-868, Albuquerque, NM, June, 1992.

25. M. Zhang, C. Wu, K. L. Wu and J. Litva, "Losses in GaAs microstrip and coplanar waveguide", Proc. IEEE MTT-S Interntl. Microwave Symp., 971-974, Albuquerque, NM, June, 1992.

26. J. Chen, C. Wu, K. L. Wu and John Litva, "Combining an autoregressive (AR) model with the FD-TD algorithm for improved computational efficiency", Proc. IEEE MTT-S Intl. Microwave Symp., 749-752, Atlanta, GA, June, 1993.

27. J. Chen, C, Wu, K. L. Wu and J. Litva, "Combining the FD-TD algorithm with AR model to analyze the microstrip problems, Proc. URSI Radio Science Mtg., 141, Ann Arbor, MI, June/July, 1993.

28. C. Wu, K. L. Wu and J. Litva, "The application of finite-difference time-domain method with autoregressive technique to design the rectangular coaxial line components", Proc. URSI Radio Science Mtg., 145, Ann Arbor, MI, June/July, 1993.

29. C. Wu, K. L. Wu, J. Chen and J. Litva, "Some considerations with regards of using the FD-TD analysis microstrip passive circuits", Proc. IEEE Antennas & Propagation Soc. Intl. Symp., 1171-1174, Ann Arbor, MI, June/July, 1993.

30. Z. L. Cai, C. Wu, Y. H. Qi, N. T. Sangary and J. Litva, "Investigations of wave propagation characteristics in microcell environments for PCS applications", IEEE AP-S Interntl. Symp., Seattle, WA., June, 1994.

31. C. Wu and J. Litva, "Experimental investigations of radio wave propagation in some special environments", IEEE URSI Radio Science Mtg., Seattle, WA, June, 1994.

32. Y. H. Qi, C. Wu and J. Litva, "Shaped beam base station antenna for cellular and PCS signal coverage", IEEE Pacific Rim 1995 Conference, Victoria, B.C., May, 1995.

33. P. Chung, C. Wu, E. Navarro and J. Litva, "A circular mesh scheme for the nonorthogonal finite difference time domain method", 1995 IEEE AP-S Interntl. Symp. and USNC/URSI Radio Science Mtg., Newport Beach, CA, June 1995.

34. J. Litva, C. Wu and E. Navarro, "On incorporating signal processing and neural network techniques with the FDTD method for solving electromagnetic problems", Interntl. Symp. on Signals, Systems and Electronics, (ISSSE'95), San Francisco, CA, Oct., 1995

35. J. Litva, C. Wu and E. Navarro, "On incorporating signal processing and neural network techniques with the FDTD method for solving electromagnetic problems", Interntl. Symp. on Signals, Systems and Electronics, (ISSSE'95), San Francisco, CA, October, 1995.

36. J. Litva, C. Wu and Amir Ghaforian, "The use of FDTD for simulating the angle-of-arrival and time-delay of signals propagating in indoor environments", Wireless'96, Calgary, AL, July, 1996.

37. J. Yang, C. Wu and J. Litva, "Microstrip ring antennas for PCS application", 1996 IEEE AP-s/URSI radio Science Symp., Baltimore, MA, July, 1996.

38. C. Wu, P. Yau, Y. Zhuang and J. Litva, "The Design of multi-beam microstrip antennas using finite difference time domain 3D structure simulator", 1996 IEEE AP-S/URSI Radio Science Symp., Baltimore, MA, July, 1996.

39. C. Wu, M. Nguyen and J. Litva, "On incorporating finite impulse response neural network with finite difference time domain method for simulating EM problems", 1996 IEEE AP-S/URSI Radio Science Symp., Baltimore, MA, July, 1996.

40. Z. N. Li, C. Wu and J. Litva, "A study of the frequency adjustable cylindrical and ring dielectric resonator antenna", 1996 IEEE AP-S/URSI Radio Science Symp., Baltimore, MA, July, 1996.

41. J. Litva, C. Wu, V. Kezys and M. Nguyen, "The use of FDTD method to simulate smart antennas in multipath channels", 1997 IEEE AP-S / URSI Radio Science Symp., Montreal, P.Q., July, 1997.

42. C. Wu and J. Litva, "A study of a new suspended microstrip line fed slot coupled linear tapered slot antenna for millimeter wave applications", 1999 IEEE AP-S/ URSI Radio Science Symp., Orlando, FL, July, 1999.

Following is a list of papers published on different journals and conference proceedings, which the author was involved in discussions and contributed the ideas.

Refereed Journals:

a. K. L. Wu, J. Litva, R. Fralich and C. Wu, "Full wave analysis of arbitrarily shaped line-fed microstrip antennas using triangular finite-element method", IEE Proceedings-H, 138(5), 421-428, October, 1991.

b. Z. Q. Bi, K. L. Wu, C. Wu and J. Litva, "A new finite-difference time-domain algorithm for solving Maxwell's equations", IEEE Microwave and Guided Wave Letters, 1(12), 382-384, December, 1991.

c. Z. Q. Bi, K. L. Wu, C. Wu and J. Litva, "A dispersive absorbing boundary condition for microstrip component analysis using the FD-TD method", IEEE Trans. Microwave Theory Tech., 40(4), 774-777, April, 1992.

d. Y. Shen, R. Fralich, C. Wu and J. Litva, "Active radiating oscillator using a reflection amplifier module", IEE Electronics Letters, 28(11), 991-992, May 21, 1992.

e. Y. Zhuang, K. L. Wu, C. Wu and J. Litva, "Full-wave analysis of finite large printed dipole arrays using the conjugate gradient-FFT method", Microwave and Optical Technology Letters, 6(4), 235-238, March 20, 1993.

f. E. A. Navarro, N. T. Sangary, C. Wu and J. Litva, "Analysis of a coupled patch antenna with application in personal communications", IEE Proc. Microwave. Antennas Propag. 142(6), 495-497, Dec., 1995.

g. Y. Zhuang, K. L. Wu, C. Wu and J. Litva, "A combined full-wave CG-FFT method for rigorous analysis of large microstrip antenna arrays", IEEE Trans. on Antennas & Propagation, 44(1), 102-109, 1996.

Conference/Symposium Papers:

h. J. Litva, Z. Q. Bi, K. Wu, R. Fralich and C. Wu, "Full-wave analysis of an assortment of printed antenna structures using the FD-TD method", Proc. IEEE AP-S Interntl. Symp., 410-413, London, ON, June, 1991.

i. J. Wang, R. Fralich, C. Wu and J. Litva, "Multifunctional aperture coupled stacked antenna", Proc. IEEE AP-S Interntl. Symp., 727-730, London, ON, June, 1991.

j.   Z. Bi, J. Litva, K.L. Wu and C. Wu, "FD-TD analysis of waveguide components using dispersive boundary conditions (DBC)", Proc. ANTEM'92, pp. 261-264, Winnipeg, MN, August, 1992.

k.   Y. Zhuang, K. L. Wu, C. Wu and J. Litva, "Full-wave analysis of finite large printed dipole arrays using the conjugate gradient - FFT method", Proc. ANTEM'92, pp. 529-533, Winnipeg, MN, August, 1992.

l.   J. Litva, Y. Zhuang and C. Wu, "Theoretical and experimental studies of microstrip reflectarrays for use in mobile satellite communications", 1993 Symp., on Antenna Applications, May, 1993

m.   Y. Shen, K. Nickerson, C. Wu, J. Litva and D. Conn, "Full-wave analysis of optically controlled semiconductor coplanar waveguides", Proc. IEEE Antennas & Propagation Soc. Intl. Symp., 838-841, Ann Arbor, MI, June/July, 1993.

n.   Y. Zhang, K. L. Wu, C. Wu and J. Litva, "Microstrip reflectarrays: full-wave analysis and design scheme", Proc. IEEE Antennas & Propagation Soc. Interntl. Symp., 1386-1387, Ann Arbor, MI, June/July, 1993.

o.   Y. H. Qi, Z. L. Cai, C. Wu, J. Chen, B. Currie and J. Litva, "Simulation and measurements of radio wave propagation in urban environment", IEEE URSI Radio Science Mtg., Seattle, WA, June, 1994.

p.   N. Sangary, E. Navarro, C. Wu and J. Litva, "Application of Non-Uniform Method to PCS Antennas", 1995 IEEE AP-S Interntl. Symp. and USNC/URSI Radio Science Mtg., Newport Beach, CA, June 1995.

q.   Y. H. Qi, B. Currie, W. Wang, P. Chung, C. Wu and J. Litva, "Measurement and simulation of radio wave propagation in two indoor environments", 6th IEEE PIMRC'95, 1171-1174, Toronto, ON, Sept. 1995.

Bibliography

[1] K. S. Yee, 'Numerical solution of initial boundary value problems involving Maxwell's equations in isotropic media,' IEEE *Trans. on Antennas and Propagation*, vol. AP-14, pp. 302-307, May 1966.

[2] A. Taflove, 'Computational electrodynamics – The Finite-Difference Time-Domain Method,' *Artech House, Inc.* 1995.

[3] J. Litva, C. Wu and A. Ghaforian,' Use of FDTD for simulating the angle of arrival and time delay of signals propagating in indoor environments,' IEE *Electronics Letters*, 32(10), 930-932, 1996.

[4] C. Wu, J. Litva and V. Kezys, 'The use of FDTD method to simulate smart antennas in multipath channels' submitted to IEE *Electronics Letters*.

[5] J. Chen, C. Wu, T. Lo, K. L. Wu and J. Litva, "Using linear and nonlinear predictors to improve the computational efficiency of the FD-TD algorithm", IEEE *Trans. Microwave Theory Tech.*, vol. MTT-42, pp. 1992-1997, 1994.

[6] K. L. Wu, C. Wu and J. Litva, "An application of FD-TD method for studying the effects of packages on the performance of microwave and high speed digital circuits", IEEE *Trans. Microwave Theory Tech.*, vol. MTT-42, pp. 2007-2009, 1994.

[7] C. Wu, K. L. Wu and J. Litva, "The application of finite-difference time-domain method with autoregressive technique to design the rectangular coaxial line components", Proc. URSI Radio Science Mtg., 145, Ann Arbor, MI, June/July, 1993.

[8] V. J. Brankovic, D. V. Krupezevic and F. Arndt, 'An efficient two-dimensional graded mesh finite-difference time-domain algorithm for shielded or open waveguide structures,' IEEE *Trans. Microwave Theory Tech.*, vol. MTT-40, pp. 2272-2277, 1992.

[9] D. L. Paul, N. M. Pothecary and C. J. Railton, 'Calculation of the dispersive characteristics of open dielectric structures by the finite-difference time-domain method,' IEEE *Trans. Microwave Theory Tech.*, vol. MTT-42, pp. 1207-1212, 1994.

[10] P. Chung, C. Wu, E. Navarro and J. Litva, "A circular mesh scheme for the non-orthogonal finite difference time domain method", 1995 IEEE AP-S Interntl. Symp. and USNC/URSI Radio Science Mtg., Newport Beach, CA, June 1995.

[11] C. Wu, P. Y. Chung and J. Litva, 'Optimization for Beam Forming Network for C-band Array-Fed Contoured Beam Antennas,' Contract Report for Spar Aerospace, November 1994.

[12] J. A. Stratton, *Electromagnetic Theory*, New York, McGraw-Hill, 1941.

[13] R. Holland, 'Finite-difference solution of Maxwell's equations in generalized non-orthogonal coordinates,' IEEE *Trans. Nucl. Sci.*, vol. NS-30, no. 6, 1983.

[14] M. Fusco, 'FDTD algorithm in curvilinear coordinates,' IEEE *Trans. Antennas Propagat.*, vol. AP-38, pp. 76-88, 1990.

[15] J. F. Lee, R. Palandech and R. Mittra, " Modeling three-dimensional discontinuities in waveguide using non-orthogonal FDTD algorithm,' IEEE *Trans. Microwave Theory Tech.*, vol. MTT-40, pp. 346-352, 1992.

[16] P. Monk and E. Suli, "A convergence analysis of Yee's scheme on non-uniform grid,' *SIMA J. on Numerical Analysis*, vol. 31, pp. 393-412, 1994.

[17] T. A. Manteuffel and A. B. Jr. White, 'Calculus of difference schemes for the solution of boundary-value problem on irregular meshes,' *SIMA J. on Numerical Analysis*, vol. 29, pp. 1321-1346, 1992.

[18] P. Y. Chung, 'Modeling electromagnetic wave interactions using the finite-difference time-domain method in general coordinates,' A Master Thesis, McMaster University, Feb. 1995.

[19] E. Suli, 'Convergence of finite volume scheme for Poisson's equation on non-uniform meshes,' *SIMA J. on Numerical Analysis*, vol. 28, pp. 1419-1430, 1991.

[20] E. A. Navarro, N. T, Sangary, and J. Litva, 'Some Considerations on the Accuracy of the Non-uniform FDTD Method and Its Application to Waveguide Analysis When Combined with the Perfectly Matched Layer Technique,' IEEE, *Trans. Microwave Theory Tech.*, vol. MTT-44., pp. 1115-1124, 1996.

[21] G. Mur, 'The modeling of singularities in the finite-difference approximation of the time domain electromagnetic-field equations,' IEEE *Trans. Electromagn. Compat.*, vol. EMC-23, pp. 377-382, 1981.

[22] Z. Bi, K. L. Wu, C. Wu and J. Litva, 'A dispersive boundary condition for microstrip component analysis using FDTD method,' IEEE *Trans. Microwave Theory Tech.*, vol. MTT-40, pp. 774-777, 1992.,

[23] J. Litva, C. Wu, K.L. Wu and J. Chen, "Some considerations for using the finite difference time domain technique to analyze microwave integrated circuits", IEEE *Microwave and Guided Wave Letters*, 3(12), 438-440, 1993.

[24] J. Berenger, 'A perfectly matched layer for absorbing of electromagnetic waves,' *J. Computat. Phys.*, vol. 114, pp. 185-200, 1994.

[25] C. Reuter, R. M. Joseph, E. T. Thiele, D. S. Katz and A. Taflove, 'Ultrawideband absorbing boundary condition for termination of waveguide structures in FD-TD simulations,' submitted to *IEEE Microwave and Guided Wave Lett.*

[26] D. S. Katz, E. T. Thiele, and A. Taflove, 'Validation and extension to three dimensions of the Berenger PML absorbing boundary condition for FD-TD meshes,' submitted to IEEE *Microwave and Guided Wave Lett.*

[27] E. A. Navarro, C. Wu, P. Y. Chung, and J. Litva, 'Application of PML superabsorbing boundary condition to non-orthogonal FDTD method,' *Electron Lett.*, vol. 30, no. 20, pp. 1654-1656, Sept. 1994.

[28] E. A. Navarro, C. Wu, P.Y. Chung and J. Litva, "Some considerations about the finite-difference time-domain method in general curvilinear coordinates", IEEE *Trans. on Microwave and Guided Wave Letters*, Vol. 4, pp. 396-398, 1994.

[29] C. Wu, E. A. Navarro, P. Y. Chung and J. Litva, "Modeling of waveguide structures using the non-orthogonal FDTD method with a PML absorbing boundary", *Microwave and Optical Technology*, March, 1995.

[30] B. Chen, D. G. Fang and B. H. Zhou, ' Modified Berenger PML absorbing boundary condition for FD-TD meshes,' IEEE *Microwave and Guide Wave Letter*, vol. 5, pp. 339-401, 1995.

[31] R. L. Higdon, 'Numerical absorbing boundary conditions for the wave equation,' *Math. Comput.*, vol. 49, pp. 65-91, 1987.

[32] D. M. Pozar, *Microwave Engineering*, 1st edition, Addison-Wesley, Reading, Massachusetts, 1990.

[33] C. Wu, K. L. Wu, Z. Q. Bi and J. Litva, 'Accurate characterization of planar printed antennas using finite-difference time-domain method', IEEE *Trans. on Antennas & Propagat.*, vol. AP-40, pp. 526-534, 1992.

[34] S. Chebolu and R. Mittra, 'The Analysis of microwave antenna using the FDTD method,' *Microwave Journal*, pp. 134-150, Jan., 1996.

[35] C. Wu, K.L. Wu, Z. Bi and J. Litva, "Modeling of coaxial-fed microstrip patch antenna by finite difference time domain method", IEE *Electronics Letters*, 27(19), pp. 1691-1692, 1991.

[36] B. C. Wadell, *Transmission Line Design Handbook*, Artech House, Inc., pp. 58-59, 1991.

[37] C. Wu, M. Nguyen and J. Litva, "Use of FDTD technique in PCS antenna design," Microwave & RF, vol. 35, no. 11, Nov. 1996.

[38] P. J. Gibson, 'The Vivaldi aerial,' presented at 9th Eur. Microw. Conf., Brighton, U.K., pp.101-105, 1997.

[39] A. Beyer, 'Millimeter-wave antenna in finline technique,' ICAP'83, pp. 44-46.

[40] K. S. Yngvesson, D H. Schaubert, T. L. Korzeniowski, E. L. Kollberg, T. Thunhren and J. F. Johasson, 'Endfire tapered slot antennas on dielectric substrates,' IEEE *Trans. Antennas. Prpoagat.*, vol. AP-33, pp. 1392-1400, 1985.

[41] R. J. Janaswamy et al, 'Analysis of the transverse electromagnetic mode linearly taped antenna,' *Radio Science*, vol. 21, no. 5, pp797-804, 1986.

[42] K. Kobayashi, R. Mittra and R. Lampe, 'Dielectric tapered rod antennas for millimeter-wave applications,' IEEE *Trans. Antennas Propagat.*, vol. AP-30, pp. 54-58, 1982.

[43] C. H. Walter, *Traveling Wave Antenna*. New York: McGraw-Hill, 1965.

[44] F. J. Zucher, 'Surface- and leaky-wave antennas,' in *Antenna Engineering Handbook*, H. Jasik, Ed. New York: McGraw-Hill, 1961.

[45] K. S. Yngvesson et al, 'The Tapered Slot Antenna--A new integrated element for millimeter wave applications,' IEEE *Trans. Microwave Theory Tech..*, vol. MTT-37, pp. 365-374, 1989.

[46] Y. S. Kim and K. S. Yngvesson, ' Characterization of tapered slot antenna feeds and feed arrays,' IEEE Trans. *Antennas. Prpoagat.*, vol. AP-38, pp. 1559-1564, 1990.

[47] R. Q. Lee and R. N. Simons, 'Linearly tapered slot antenna and feed networks,' *Antenna Application Symposium*, 1994.

[48] P. S. Kooi, T. S. Yeo and M. S. Leong, 'Parametric studies of the linearly tapered slot antenna (LTSA),' *Microwave and Optical Technology Letters*, vol. 4, pp. 200-207, 1991.

[49] C. P. Wen, 'Coplanar waveguide: A surface strip transmission line suitable for non-reciprocal geomagnetic device applications,' IEEE *Trans. Microwave Theory Tech.*, vol. MTT-17, pp. 1087-1090, 1969.

[50] R. N. Simons and R. Q. Lee, 'Couplanar waveguide aperture coupled patch antenna with ground plane / substrate of finite extent,' IEE *Electronics Lett.*, vol. 28, pp. 75-76.

[51] R. N. Simons, N. I. Dib, R. Q. Lee and L. P. B. Katehi, 'Integrated uniplanar transition for linearly tapered slot antenn,' IEEE Trans. . *Antennas. Prpoagat .*, vol. AP-.43, pp. 998-1002, 1995.

[52] F. Lalezari and T. Pett, 'Millimeter microstrip antennas for use in mil-spec environment,' final report to Battelle Columbus Labs/US Army CECOM, November 21, 1983.

[53] K. J. Button, *Topics in Millimeter Wave Technology*, vol. 1, Academic Press Inc., 1988.

[54] P. Pramanick and P. Bhartia, 'Computer-aided design models for millimeter-wave fin lines and suspended substrate microstrip lines,' IEEE Trans. *Microwave Theory Tech.*, vol. MTT-33, pp. 1429-1435, 1985.

[55] R. Q. Lee etal: Measured Mutual coupling between linearly Tapered Slot Antennas. IEEE Trans. on AP, vol.45, no 8, August 1997, pp. 1320-1322.

[56] J. R. James, P. S. Hall and C. Wood, *Microstrip Antenna* – theory and design, Peter Peregerinus LTD., IEE, 1981.

[57] D. M. Pozar and D. H. Shaubert, *Microstrip Antennas* – the analysis and design of microstrip antennas and arrays, IEEE Press, 1995.

[58] Y. T. Lo and S. W. Lee, Antenna Handbook – theory, applications and design, Van Nostrand Reinhold Company Inc., 1988.

[59] J. R. James, P. S. Hall and C. Wood, *Microstrip Antenna* – theory and design, Peter Peregerinus LTD., IEE, 1981.

[60] D. M. Pozar and D. H. Shaubert, *Microstrip Antennas* – the analysis and design of microstrip antennas and arrays, IEEE Press, 1995.

[61] Y. T. Lo and S. W. Lee, Antenna Handbook – theory, applications and design, Van Nostrand Reinhold Company Inc., 1988.

[62] J. R. James and P. S. Hall, '*Handbook of Microstrip Antennas,*' Peter Peregrinus Ltd. London, United Kingdom, 1989.

[63] H. Jasik, '*Antenna Engineering Handbook,*' McGraw-Hill, New York, 1961.

[64] K. L. Klohn, R. E. Horn, H. Jacobs, and E. Freibergs, 'Silicon waveguide frequency scanning linear array antenna,' IEEE Trans. *Microwave Theory Tech.*, vol. MTT-26, pp. 764-773, 1978.

[65] R. E. Horn, H. Jacobs, E. Freibergs, and K. L. Klohn, 'Electronic modulated beam-steering silicon waveguide array antenna,' IEEE Trans. *Microwave Theory Tech.*, vol. MTT-28, pp. 647-653, 1980.

[66] F. Schwering and S. T. Peng, 'Design of dielectric grating antennas for millimeter wave applications,' IEEE Trans. *Microwave Theory Tech.*, vol. MTT-31, pp.199-209, 1983.

[67] S. Kobayashi, R. Lampe, R. Mittra, and S. Ray, "Dielectric-rod leaky-wave antennas for millimeter-wave applications," IEEE Trans. *Antennas Propag.*, vol.AP-29, pp. 822-824, 1981.

[68] T. N. Trinh, R. Mittra, and R. J. Paleta, "Horn image-guide leaky-wave antenna," IEEE Trans. *Microwave Theory Tech.*, vol. MTT-29, pp. 1310-1314, 1981.

[69] T. Itoh and B. Adelseck, 'Trapped image-guide leaky-wave antennas for millimeter wave applications,' IEEE Trans. *Antennas Propag.*, vol. AP-30, pp. 505-509, 1982.

[70] M. A. Weiss and R. B. Cassell, 'Microstrip millimeter-wave antenna study,' R&D *Tech. Rep.*, *CORADCOM*-77-0158-F, 1979.

[71] J. Huang, 'A parallel-series-fed microstrip array with high efficiency and low cross-polarization,' *Microwave and Optical Technology Letters*, vol. 5, pp. 230-233, 1992.

[72] F. Lin, D. G. Fang and S. F. Li, 'Analysis of microstrip-to-waveguide transition by line integral method in spectral domain,' Chinese Microwave J. (in Chinese).

[73] Q. Xue, J. Xu, L. G. Xue and W. G. Lin, 'Analysis on waveguide cross-section-plane microstrip probe,' *Microwave and Optical Technology Letters.*, vol. 9, pp. 214-217, 1995.

[74] L. Fan M. Y. Li and K. Chang, 'Circular waveguide-to-microstrip transitions,' IEE *Electronics Lett.*

[75] J. S. Izadian and S. M. Izadin, '*Microwave Transition Design,*' Artech House, 1988.

[76] R. K. Hoffmann, (English Translation Edited by H. H. Howe, Jr.), '*Handbook of Microwave Integrated circuits,*' Artech House, 1987.

[77] W. C. Y. Lee, 'Spectrum and technology of a wireless local loop system,' IEEE *Personal Communications*, vol. 5, pp. 49-54, 1998.

[78] W. C. Y. Lee, '*Mobile Communication Design Fundamentals*', Wiley & Sons, 1993.

[79] W. B. W. Alison, '*A handbook for the Mechanical Tolerancing of Waveguide Components,*' Artech House, 1972.

[80] R. O. Lee and R. N. Simons, 'Design of broadband vertical transitions for tapered slot antennas', IEEE *Antennas & Propagation Soc. Interntl. Symp.*, URSI digest, pp. 242, 1999.